The Thesis committee for Chih-Chieh Chou

Certifies that this is the approved version of the following thesis

Improvements to Wireless, Passive Sensors for Monitoring

Conditions within Reinforced Concrete Structures

APPROVED BY

SUPERVISING COMMITTEE:

Sharon L. Wood

Dean P. Neikirk

Improvements to Wireless, Passive Sensors for Monitoring

Conditions within Reinforced Concrete Structures

by

Chih-Chieh Chou, B.S., M.S.C.E.

Thesis

Presented to the Faculty of the Graduate School of

The University of Texas at Austin

in Partial Fulfillment

of the Requirements

for the Degree of

Master of Science in Engineering

The University of Texas at Austin

August 2010

Dedication

To my family, without whom not.

Acknowledgements

Improvements to Wireless, Passive Sensors for Monitoring Conditions within Reinforced Concrete Structures

Chih-Chieh Chou, M.S.E.

The University of Texas at Austin, 2010

SUPERVISOR: Sharon L. Wood

The corrosion of steel reinforcement in reinforced concrete structures constitutes an alarming problem. To combat this problem, researchers at the University of Texas at Austin developed two, low-cost, passive, wireless sensors: a threshold, corrosion sensor and an analog conductivity sensor. Today, the basic circuit designs for both sensors are finished and their reliabilities are confirmed. However, multiple problems regarding the durability of the sensors remain. This research project: (a) identifies these problems, (b) proposes enhancements for each type of passive, wireless sensor, (c) tests and evaluates the proposed modifications to the sensors, and (d) proposes potential improvements and areas of research regarding the future development of these two sensors.

Table of Contents

List of Tables

List of Figures

xvi

xviii

xxi

CHAPTER 1

Introduction

1.1 Introduction

Reinforced concrete is the most widely-used construction material in the world. This composite material inherits most of the advantages of concrete and steel reinforcement and it unifies perfectly to provide sufficient safety and performance in buildings and other infrastructure systems. Typically, reinforced concrete structures remain durable and perform well throughout their service life. However, in some cases, reinforced concrete structures do not perform as intended.

The corrosion of the reinforcing steel in reinforced concrete structures is wide-spread problem which is caused by either the penetration of corrosive agents or severe environmental conditions. The durability of reinforced concrete structures is limited by chloride attack and carbonation and the subsequent spalling of the cover concrete. However, the corrosion initiation process is quite slow, and it is difficult for engineers to detect the presence of corrosion until after structural damage has occurred. In the most serious circumstances, corrosion of the reinforcement may cause the collapse of structures. The collapse of the highway overpass near Montreal in 2006 (Figure 1.1) is a tragic and representative example (New Civil Engineer Magazine 2006). To combat this problem, a cost-effective method for detecting the onset of corrosion of the embedded reinforcement is necessary.

Figure 1.1. Collapse of a highway overpass near Montreal, Canada (From New Civil Engineer Magazine 2006)

Governments around the world spend billions of dollars each year to maintain infrastructure systems and prevent corrosion deterioration of concrete structures. The United States in 2002, for example, spent 4.0 billion dollars (Figure 1.2) on maintaining overall bridge conditions (Koch et al. 2002). Yunovich et al. (1998) hypothesize that this amount will increase to 5.2 billion dollars by 2011. Both reports imply that the corrosion of steel reinforcement in infrastructural systems will worsen in the next decades and assert that advanced technologies for corrosion detection of reinforced concrete structures (compared to the conventional visual inspection) must be developed.
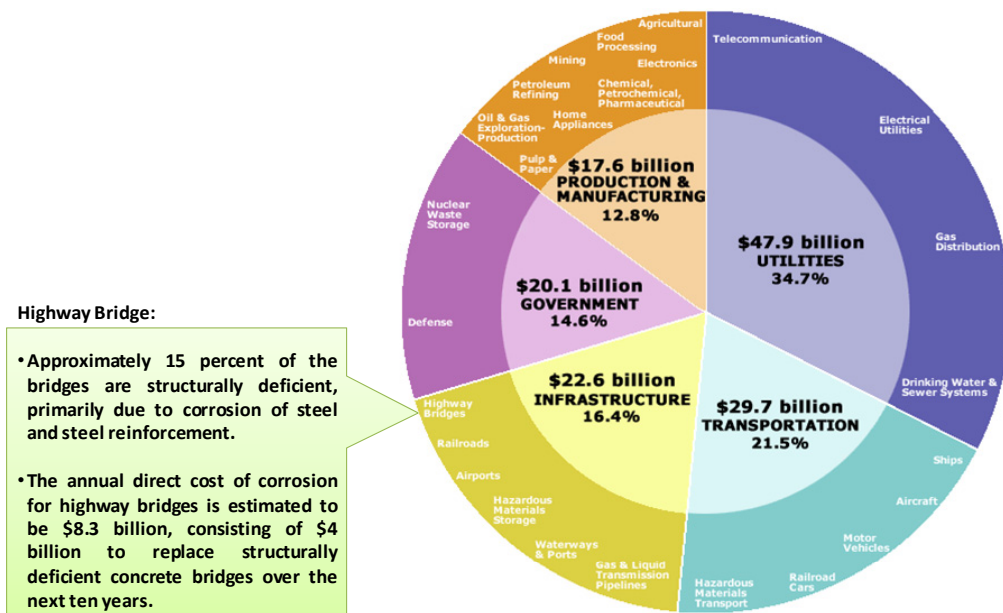
Figure 1.2. Average annual direct cost of corrosion in the US. (Yunovich et al. 2001).

The non-destructive technology/evaluation (NDT or NDE) is the most popular reinforced concrete inspection technology today. It enables inspectors to understand the internal status of a reinforced concrete structure (including steel reinforcement) without damaging the structure itself. Through the application of different concepts, the NDT can be grouped into four types (Song and Saraswathy 2007). These types are summarized in Table 1.1.

Table 1.1. Non-destructive methods for detecting corrosion in reinforced concrete structures (Song and Saraswathy 2007).

Category	Concepts Applied	Methods/Measurements	Method Deficiency
Type 1	Open Circuit Potential Concrete Resistance /Impedance Change	1. Half-cell potential measurement 2. Surface potential measurement 3. Concrete resistivity measurement 4. Linear polarization resistance measurement 5. Tafel extrapolation 6. Galvanostatic pulse transient method 7. Electrochemical impedance spectroscopy 8. Harmonic Analysis 9. Noise Analysis	1. No consensus in corrosion level definition 2. Need other methods to double check
Type 2	Magnetic Change Wave Velocity Change	1. Cover thickness measurement 2. Ultrasonic pulse velocity technique	1. Indirect corrosion detection 2. Only effective for serious corrosion situation (large concrete defects)
Type 3	Attenuation coefficient Thermal diffusivity Reflection coefficient	1. X-ray, Gamma radiography measurement 2. Infrared thermograph electrochemical 3. Ground penetrating radar	1. Environmental application limitation 2. Needs interpretation expertise 3. Instrument is expensive 4. Radiation hazard protection required
Type 4	Embedded Sensor	1. Embedded Corrosion Instrument (ECI)	1. Indirect corrosion measurement 2. External power required 3. Expensive

Type 1 of the NDT inspection methods monitors the open circuit potential or the impedance/resistance of a section of concrete. The half-cell potential (HCP) measurement and linear polarization resistance (LPR) measurement are two of the measurements grouped under Type 1. This type of method is easily applied and the results are easy to interpret. However, there is no consensus in the definition of corrosion levels, and the readings very with the moisture content within the concrete.

Type 2 involves measuring changes in the magnetic pull or wave velocity of the concrete. This type of method was originally designed for concrete quality investigation. Since the corrosion of steel reinforcement will cause stress cracking in concrete, Type 2 methods are based on the assumption that the structure was constructed to high quality standards. Cover meter measurement and Ultrasonic Pulse Velocity (UPV) measurements are examples of Type 2 methods.

The third category of method used to monitor the corrosion of steel reinforcement in concrete involves the application of a state-of-the-art imaging system (Pla-Rucki and Eberhard 1995) such as X-ray/Gamma Radiography, Ground Penetrating Radar (GPR) (He et al. 2009) and Infrared Thermograph (IT). Different properties of materials, such as attenuation coefficient, thermal diffusivity or reflection coefficient and the internal state of reinforced concrete (including steel reinforcement), can be captured in a 2D image (Figure 1.3). Although Type 3 methods are reliable, a large number of limitations exist. There are significant environmental restrictions and proper interpretation of the results requires

considerable experience. These limitations need to be overcome in order to enable the practical application of this type of corrosion detection method. More importantly for the application of corrosion detection of steel reinforcement, 2D images are not always sufficient to detect the onset of corrosion.

Type 4 methods involve the use of embedded sensors. Corrosion ladders are one form of commercially available embedded sensor. These sensors must be positioned carefully before placement of the concrete and most require wiring to data acquisition systems.
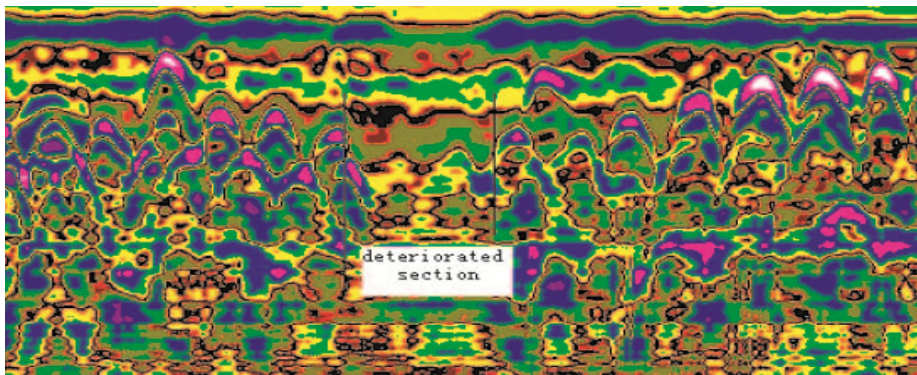
Figure 1.3. Example of a 2D ground penetrating radar image for good and corroded rebar (He et al. 2009).

Compared with the first three methods, embedded sensors seem to have the most potential for early detection of corrosion within concrete. However, the price of the sensors ranges from hundreds to thousand dollars per unit, which prevent this type of technology from being widely adopted. Therefore, researchers at the University of Texas at Austin are working to develop low-cost, embedded sensors for detecting

corrosion. These sensors are described and detailed in this thesis.

1.2 Scope of Research

For the past two years, the research team at University of Texas at Austin has worked to develop different kinds of sensors for detecting the onset of corrosion in reinforced concrete structures. These sensors are based on the design of electronic article surveillance (EAS) tags. To date, two prototype sensors have been developed. The first sensor is the threshold sensor which detects the onset of corrosion of steel reinforcement. The second is an analog sensor which measures the conductivity of the concrete.

The objective of this research project is to continue the development and testing of both these sensor platforms. Chapter 2 contains the literature review, divided into two parts. The first part surveys literature related to the causes, mechanisms, and the process of reinforcement corrosion in reinforced concrete. The second part reviews the design requirements and configurations of the two forms of prototype sensors. The second part of Chapter 2 also summarizes previous research results and remaining challenges.

Previous investigators (Dickerson 2005, Puryear 2007) have conducted long-term exposure tests of the passive sensors embedded in reinforced concrete members to evaluate the reliability of the sensors. Puryear (2007) constructed four slabs during his research, but the exposure tests were ongoing for three slabs at the

time of his graduation. The autopsy of Slab 3 and the measured response of the sensors are discussed in Chapter 3 of this thesis.

Based on the observed response of the sensors in Slab 3, two primary areas for improvement were identified for the threshold corrosion sensors. The first part of Chapter 4 attempts to extend the read range of the embedded sensor by selecting different capacitors. The second part of Chapter 4 addresses changes to improve the durability of the sensor by redesigning the protective housing.

The conductivity sensor is addressed in Chapter 5. The prototype conductivity sensor was proposed by Andringa in 2006. Refinements to improve the read range and characterize the sensitivity of the readings to thermal changes are discussed in Chapter 5.

Finally, Chapter 6 summarizes the most pertinent results from the thesis and provides recommendations for future research.

CHAPTER 2

Literature Review

2.1 Introduction

In order to reach an appropriate design for a corrosion sensor, it is necessary to thoroughly understand the characteristics of corrosion and to have clear design attributes and ideas. For the purpose of improving requirements in the future, this chapter will detail the corrosion properties and relevant design concepts of corrosion sensors.

Section 2.2 explains the causes, mechanism and processes of corrosion in steel reinforcement in concrete. The design attributes and passive wireless sensor design concepts are illustrated in Section 2.3. Section 2.4 expounds the theoretical basis of the two passive sensors: the threshold corrosion sensor and the analog conductivity sensor. Section 2.5 discusses the method used to extract quantitative data from the passive sensors and Section 2.6 summarizes the importance of the environmental protection system.

2.2 Corrosion Process and Corrosion Mechanism

Concrete is a permeable material. Any gas or liquid substance can penetrate concrete through its pores. This permeability is not only a vital part of the durability of concrete structures but is also a decisive factor in the corrosion of steel

reinforcement in concrete. Normally, the pore solution of the concrete has a high pH (13 to 13.9) due to the presence of sodium and potassium hydroxides. (Bertolini et al. 2004). In this environment, a thin, dense protective oxide film forms on the surface of embedded steel reinforcement. This passive layer protects the steel reinforcement from attack by intrusive corrosion agents. However, this oxide film protection is not permanent. As corrosion agents penetrate into the concrete, the passive layer is destroyed (Broomfield 2006).

2.2.1 The Corrosion Process

The corrosion process starts when oxygen, water and corrosive agents reach the surface of steel reinforcement. Because the passive layer around the steel reinforcement is not broken, there is no indication of corrosion. This stage is called the "Initiation period." However, once the rate to generate the passive layer is smaller than the rate to lose it, corrosion products will start to develop. This is the second phase of the corrosion, called the "Propagation of corrosion" period (Figure 2.1) (Kuutti 1982).
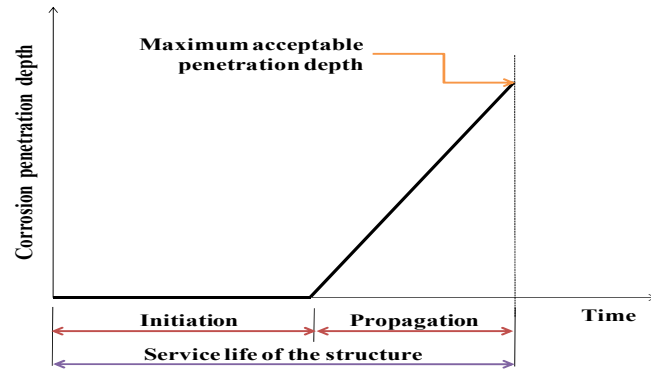
Figure 2.1. The initiation and propagation periods for corrosion in a reinforced concrete structure (Kuutti 1982).

Compared with the first phase of corrosion, the second phase of corrosion causes significant changes to the concrete environment. The most obvious characteristics are the anodic and cathodic corrosion reactions (Eqs. 2.1 and 2.2) which occur on the surface of steel reinforcement (Broomfield, 2006). These reactions are illustrated in Figure 2.2.

$$Fe \rightarrow Fe^{2+} + 2e^- \quad \text{(Anode)} \tag{2.1}$$

$$2e^- + H_2O + \frac{1}{2} O_2 \rightarrow 2\,OH^- \quad \text{(Cathode)} \tag{2.2}$$
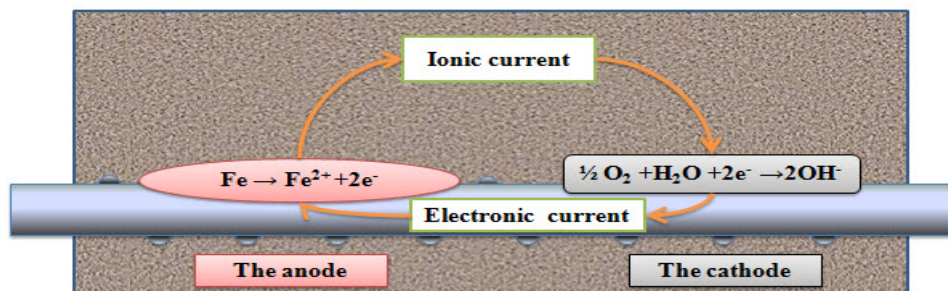
Figure 2.2. Anodic and cathodic reactions on corroding steel (Broomfield 2006).

11

Broomfield (2006) describes the corrosion process as "The anodic reaction causes the loss of steel reinforcement since iron releases two electrons and then dissolves into the pore solution. The cathodic reaction, however, maintains the high alkaline environment for the production of hydroxyl from the cathode which prevents the corrosion of steel reinforcement. Both corrosion reactions not only clearly express the status of steel reinforcement after the passive layer is broken, but provide vital information which can help engineers detect corrosion in steel reinforcement inside concrete. First, the corrosion reaction will cause the loss of steel reinforcement only occur at the anode. Second, the resistance/conductivity of the concrete changes during this second phase of the corrosion process.

The hydroxyl, on the other hand, reacts with bivalent irons and produces the iron compound of ferrous and ferric hydroxide (Eqs. 2.3 to 2.5). In this environment, since ferric oxide (Fe_2O_3) and hydrated ferric oxide ($Fe_2O_3 \cdot H_2O$) are the final stable iron compounds (Figure 2.3), the ferrous and ferric hydroxide will continuously react until stable iron compounds are formed. The resulting hydrated ferric oxide $Fe_2O_3 \cdot H_2O$ is "the rust"."

$$Fe^{2+} + 2\,OH^- \rightarrow Fe(OH)_2 \tag{2.3}$$

$$Fe(OH)_2 + O_2 + 2\,H_2O \rightarrow Fe(OH)_3 \tag{2.4}$$

$$Fe(OH)_3 \rightarrow Fe_2O_3 \cdot H_2O + 2H_2O \tag{2.5}$$
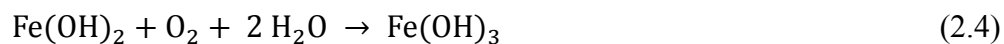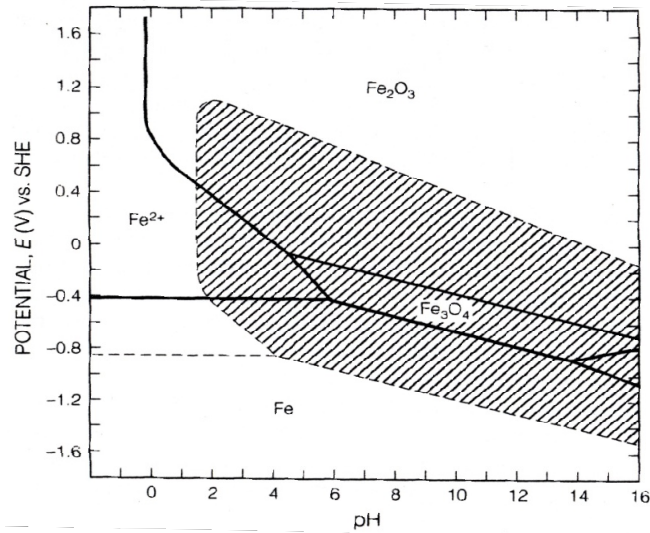
Figure 2.3. The Pourbaix Diagram of Iron (Pourbaix 1974)

By investigating the volumes of iron and its oxides, Mansfield (1981) proved that ferric oxide (Fe_2O_3) has two times the volume of the original iron and that, due to swelling during the hydration process, hydrated ferric oxide has more than six times the volume of the original iron (Figure 2.4). Since the corrosion process mixes ferrous and ferric oxide, the average volume at the steel/concrete interface expands six to ten times after the corrosion process occurs. This explains why concrete structures crack and spall after corrosion occurs in the steel reinforcement in concrete. It also conveys that stress changes in reinforced concrete may be a good indicator of corrosion activity within the concrete.

13
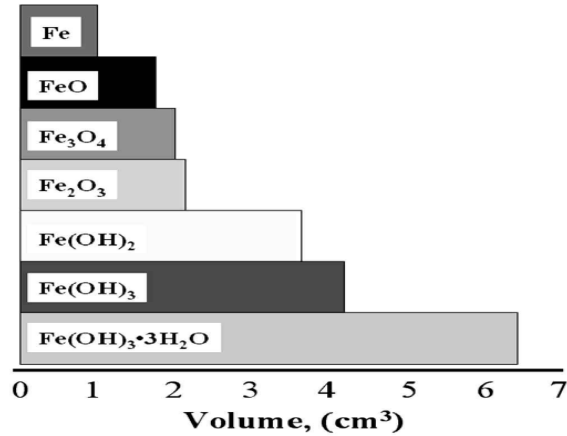
Figure 2.4. The relative volumes of iron and its oxides (Mansfield 1981).

2.2.2 The Corrosion Mechanism

Broomfield (2006) describes the corrosion mechanism as "The range of the anode on the surface of steel reinforcement is one of the major concerns when designing a corrosion sensor. If it is large enough, only a small amount of sensors are required to detect the corrosion situation of steel reinforcement in concrete. In general, the range of the anodic corrosion reaction is decided by the corrosion mechanism. The intrusion of different corrosive agents and the roles that they play during the reaction determines the range of the anodic reaction.

Carbon dioxide produces a large area attack as it decreases the alkalinity of the concrete environment to break down the stable phase of iron oxide. Consequently, the range of the anode will be larger. Chloride ions, however, produce a small area attack. Chloride ions serve as catalysts which help to depassivate the passive layer of steel

14

reinforcement and accelerate the corrosion process (Figure 2.5). Chloride attack, however, is effective only when the chloride content on the surface of steel reinforcement has reached a threshold value. The threshold value is variable due to the concentrations of tricalcium aluminate (C3A) and hydroxide ion (OH-) in the concrete, but the soluble chloride ion level usually at which steel reinforcement corrosion begins in concrete is about 0.2 to 0.4 percent by mass of cement. For both reasons, chloride attack usually results in a local breakdown (small active zone) of the passive layer on the surface of steel reinforcement in alkaline concrete. This is called pitting corrosion.
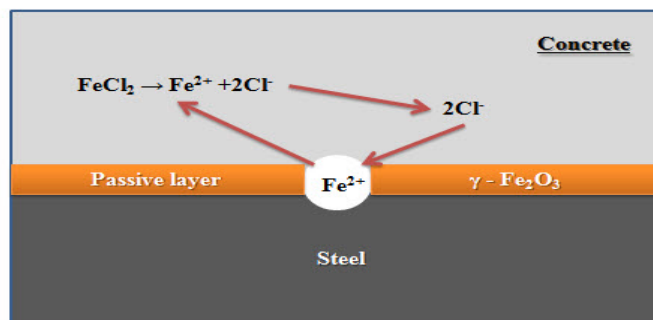
Figure 2.5. A chloride ion working as a catalyst to accelerate the corrosion process and causing pitting corrosion (Broomfield 1996).

Chloride attack always dominates the corrosion situation of steel reinforcement in concrete as it is more rapid and violent. Therefore, a large amount of sensors are needed if engineers aspire to thoroughly understand the corrosion situation in a reinforced concrete structure."

2.2.3 The Corrosion Behavior of Other Metals

In order to develop a corrosion sensor, metal is needed. Metal works as a transducer to detect environmental changes resulting from contamination by corrosive agents such as chloride ions. In addition, to limit the steel sensing wire of a threshold sensor corroded in the assigned area, a non-corrosive metal coating material used to protect for the rest of the steel sensing wire is also necessary. For both reasons, the behavior of metallic materials other than those used in steel reinforcement will be briefly examined.

Copper and its alloys do not corrode since they produce sufficient chemical compounds, such as cupric oxide and copper (II) chloride, on their surfaces to combat attacks from corrosive agents. The only exception occurs when ammonia compounds contained in some admixtures are in the presence of copper or copper alloys. In this situation, the phenomenon of stress-corrosion cracking can occur (Denney 1996).

Tin is a soft, pliable, silvery-white metal. It is not easily oxidized and resists corrosion because it is protected by an oxide film (SnO_2). Tin resists corrosion from distilled sea and soft tap water, and can be attacked by strong acids, alkalis and acid (oxidizing) salts such as potassium peroxysulfate and ferric chloride (Tan 1993). Therefore, if this metal wants to be applied in a chloride-contaminant-filled concrete environment, further tests need to be conducted.

2.3 Sensor Concept

2.3.1 Design Attributes

Compared to other non-destructive technologies, embedded corrosion sensors provide more accurate information about the corrosion situation of steel reinforcement in concrete based on their location next to the steel reinforcement. In order for this type of sensor to be widely used in infrastructure structural health monitoring, however, the sensors need to meet specific design attributes. These attributes are: (a) long service life, (b) reliable information and easy interpretation, (c) low impact to structures and (d) low cost.

2.3.1.1 Service Life

Once a corrosion sensor is embedded in concrete, there are no more chances to take it out. Accordingly, the first attribute of the embedded corrosion sensor is a long service life. Both the power supply and durability of the sensor must be considered during design.

Power supplies, generally, can be solved by an onboard power system or by non-contact magnetic power. If the onboard power system is used, high-tech wireless devices can be installed for data transmission, because sufficient power is available. The Embedded Corrosion Instrument (ECI-1) developed by Virginia Tech is an

example of an embedded sensor with an onboard power system (Kelly et al. 2002). The onboard power system, however, has its own problems. First, the life of its rechargeable battery is limited. Second, the "connecting" wire for power transmission may become a medium for corrosive agents to penetrate into the concrete.

If the onboard power system is eliminated, the sensor must rely on non-contact magnetic power — passive sensors. Under this expectation, only limited information can be transmitted from the embedded corrosion sensor.

Durability is also a critical factor in the design of an embedded corrosion sensor in order to meet the service life design criterion. The design life for infrastructure systems ranges from 75 to 100 years. Many extreme weather or environmental conditions may occur during this period. Therefore, the sensor must be provided with complete protection. Its protective covering must demonstrate sufficient strength when subjected to a rigorous testing (e.g. extreme temperature or high concentration corrosion environments) to ensure its durability before it can be embedded into reinforced concrete. A simple and direct way to effectively protect the sensor is to seal the entire sensor (except for its sensing components) with epoxy or other non-corrosive materials.

2.3.1.2 Reliable Information and Easy Interpretation

Obtaining the reliable test results is the basic criteria in a sensor design. To reach

this goal, the designed sensor needs to be confined its application range through a series of comprehensive performance tests in different assumed conditions encountered in the future. For this research project, since the sensor is designed to embedded in the reinforced concrete environment and exposed in a chloride-ions-filled environment, two major conditions will be tested: (a) the detection limit of the concentration of chloride ions in concrete structures. (b) the applicable read distance of the designed sensor.

Once a sensor is applied in practice, the sensor signal must be easily interpreted for widely spread. To achieve this, intuitive judgments must be adopted to express the state of reinforcement corrosion.

2.3.1.3 Low Impact to Structures

Engineers use embedded sensors to ensure the safety of a reinforced concrete structure. Therefore, a sensor must be designed in such a way that the sensor itself does not adversely affect the safety of the structure. To accomplish this, the size of the sensor is limited and any impact on the structural safety of the concrete caused by the embedding of the sensor (e.g. the accumulation of corrosion contents at the bottom of the sensor) must be eliminated.

2.3.1.4 Low Cost

In light of the fact that pitting corrosion is the main characteristic of reinforcement corrosion, a large number of corrosion sensors are required in order to establish an effective corrosion monitoring system in a concrete structure. However, the market price of a corrosion sensor today is extremely high (cost range from several hundred to thousands of dollars). This is a heavy burden for a government to carry under a limited budget each year. Consequently, the development of a low-cost sensor for infrastructural health monitoring is an urgent need.

In order to fulfill this goal, the prototype passive sensors have been developed. Through the implementation of a simple inductor-resistor-capacitor (LRC) circuit, the corrosion state of steel reinforcement in concrete can be effectively monitored and the price of a corrosion sensor can be reduced to less than $1.50.

2.3.2 The Passive Sensor Platform

The electronic article surveillance (EAS) tag (shown in Figure 2.6) is a low-cost, highly effective anti-theft sensor used to prevent shoplifting from retail stores or the pilferage of books from libraries. Because it is a 1-bit transponder, this tag can only convey information within a 1-bit memory or an effective message for a two-option situation, e.g. "Yes" or "No" (Finkenzeller 2003). In general, four major types of EAS systems are commonly used: (a) microwave, (b) electro-magnetic, (c)

acousto-magnetic, and (c) radio frequency (RF) (Dubendorf 2003). Among these types, only RF systems are easily converted for use in other applications.
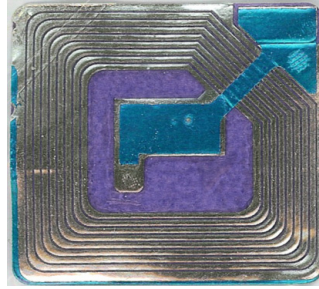
Figure 2.6. An anti-theft electronic article surveillance tag (radio frequency tag)

A typical RF system primarily consists of a reader and a separate tag. The reader produces different magnetic fields corresponding to its frequencies and scans for specific EAS tags. The tag is a sensing coil constituted by an LC circuit composed of an inductor (L) and a capacitor (C) and has its own unique resonant frequency (Eq. 2.6). The idealized circuit model of a RF system is illustrated in Figure 2.7.

$$f_0 = \frac{1}{2\pi\sqrt{L \cdot C}} \quad \text{or} \quad \omega_0 = \frac{1}{\sqrt{L \cdot C}} \tag{2.6}$$
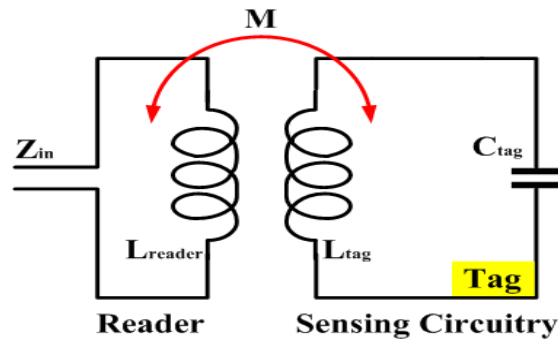
Figure 2.7. Idealized model of a RF system including a reader and a resonant tag.

When the RF system is operating, the reader sweeps a particular range of frequency. Sensing can be achieved only when the sweeping frequency matches the resonant frequencies of the tag. At this frequency, the tag and reader will have sympathetic oscillations. Meanwhile, since the impedance of the reader changes due to magnetic coupling with the tag, the phase response of the tag will suddenly decrease at the resonance frequency as shown in Figure 2.8. In other words, the phase dip will suddenly increase in quantity.
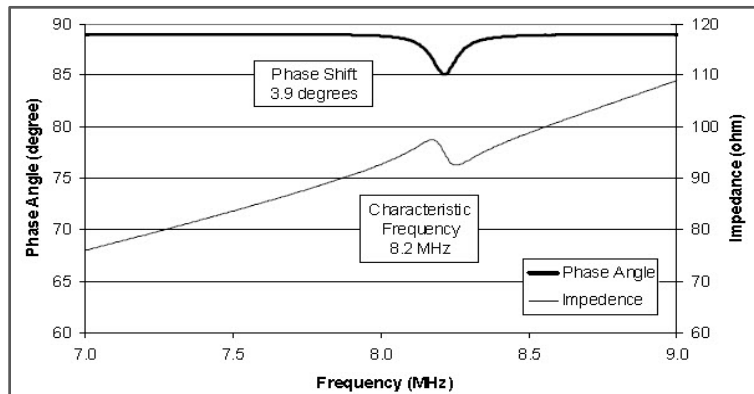
Figure 2.8. The phase response of the RF tag (Grizzle 2003).

The concept of the passive sensor platform including its framework and operation is crucial to this research project because it clearly points out a design concept for the passive wireless sensor and it provides a complete framework for sensor design in the future. Figure 2.9 shows how the passive sensor is interrogated in a wireless manner through the surrounding concrete.
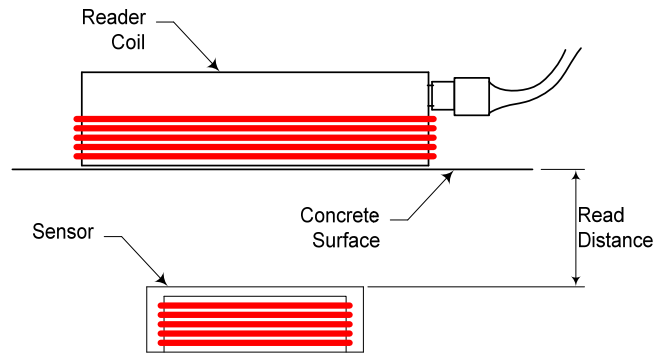
Figure 2.9. A diagram of the scheme of the ESS platform (Dickerson 2005).

2.4 Types of Low-Cost, Resonant Sensors

After several years of effort, researchers at the University of Texas at Austin have developed two types of low-cost, resonant sensors: (a) a threshold corrosion sensor and (b) an analog conductivity sensor. This section explores the design concepts and details of these two sensors.

2.4.1 Threshold Corrosion Sensor

After several generations of improvements and extensive testing, the prototype design concepts for threshold corrosion sensor are discussed in Puryear (2007). Basically, this sensor is a point/isolated sensor that detects the onset of corrosion. Consequently, a large number of these sensors will be required to monitor a large reinforced concrete structure.

The design idea of the threshold corrosion sensor is based on the premise that the

detected object and the sensing components are made of the same material (e.g. steel reinforcement and steel wire) and, therefore, should have the same corrosion rate when they exposed to the same environment. Therefore, if a sensor with a thin steel sensing wire used to monitor a reinforcing bar, the sensor will provide early warning for the corrosion of steel reinforcement. Consequently, this sensor is called the "threshold" corrosion sensor.

Research has shown that this resistance-based sensor is the most appropriate configuration to meet the design objectives. In this sensor, one series RLC circuit and one series LC circuit function as a sensing coil and a reference coil respectively. The sensing coil functions as an indicator to inform engineers of the corrosion of steel reinforcement while the reference coil serves as a locator to locate the position of the sensor. The prototype sensor configuration and its idealized circuit diagram are shown in Figure 2.10.
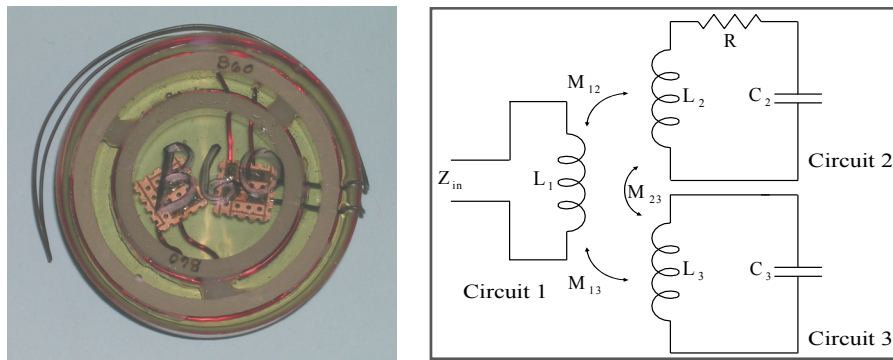
Figure 2.10. The configuration of the threshold corrosion sensor (left) and its idealized circuit diagram (right) (Dickerson 2005).

Figures 2.11 and 2.12 explain the sensor mechanism of the resistance-based threshold corrosion sensor. As shown in Figure 2.11, the impedance of the reader will be affected by the inductive coupling before the sensor reaches the threshold of corrosion. As a result, the phase dip will increase at the resonant frequencies of the sensing circuit and reference circuit. However, this influence will be gradually decreased while the resistance of the sensing circuit increases. Finally, when the resistance of the sensing circuit approaches the infinity or the threshold of the corrosion criterion, the influence of the inductive coupling from the sensor will no longer exist. At this time, the phase dip of the sensing circuit at the resonant frequency will be reduced to zero as shown in Figure 2.12.

This concept is expressed in Eq. 2.7. Andringa (2003) includes the details of the theory in his thesis. In addition to the inductive coupling between the reader and sensor circuits, the reference circuit and the sensing circuit also have their own inductive coupling. Due to the application of both inductive couplings, the reference circuit has less influence than the sensing circuit when the threshold of corrosion is not reached (Figure 2.11). However, once the threshold of corrosion is reached, the phase dip of the reference circuit will increase (Figure 2.12).
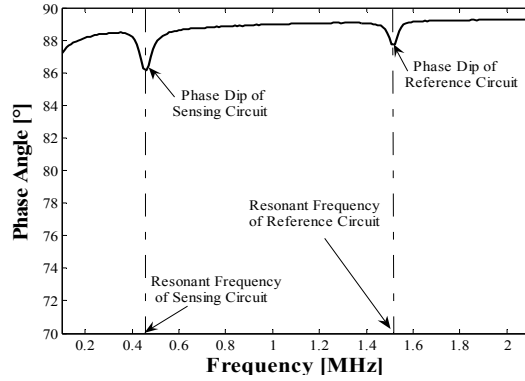
Figure 2.11. Measured phase response of threshold sensor with intact sensing wire (Puryear 2007).
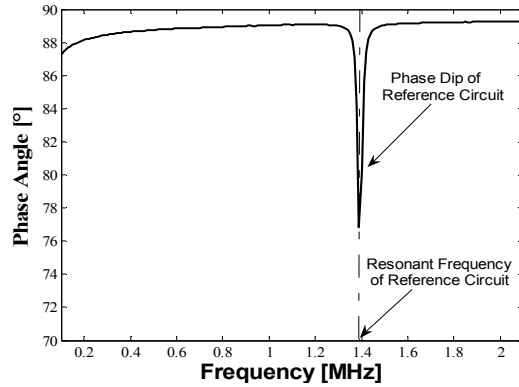
Figure 2.12. Measured phase response of threshold sensor with fractured sensing wire (Puryear 2007).

$$Z_{\text{input}} = Z_{\text{reader}} + \frac{(\omega_0 M)^2}{Z_{\text{sensing circuit}}} \tag{2.7}$$

$$Z_{\text{sensing circuit}} = (R_{\text{sensing circuit}} + R_{\text{sensing wire}}) + jX_{\text{sensing circuit}}$$

$$R_{\text{sensing wire}} \uparrow \implies Z_{\text{sensing circuit}} \uparrow \text{ and } Z_{\text{sensing circuit}} \approx \infty \implies \frac{(\omega_0 M)^2}{Z_{\text{sensing circuit}}} \approx 0$$

Where Z_i is the impedance of a circuit or total input; R_i is the resistance of a circuit; X_i is the reactance of a circuit; index *i* represents the reader, sensing coil or sensing wire; ω_0 is the resonance frequency of the sensing circuit; M is the inductive

26

coupling between the reader and sensing coil (Andringa 2003).

2.4.2 Analog Conductivity Sensor

The resonant conductivity sensor was proposed by Andringa (2006). After a series of preliminary tests in salt water and concrete, this sensor appears to be promising. In general, only a few sensors are required if the sensor is used to detect the conductivity of a liquid medium. However, a large number of sensors are needed if the sensor is used to detect the conductivity in a solid medium (such as concrete). In a solid medium, the conductivity in the entire medium cannot reach equilibrium in a short time even if the electrons can be transported through the four basic mechanisms: (a) capillary suction, (b) permeation, (c) diffusion and (d) migration (Bertolini et al. 2004). As a result, the conductivity sensor is still classified as a point/isolated sensor.

The design idea of the analog conductivity sensor is based on the premise that the presence of moisture and chloride ions will change the electrical conductivity/ resistivity of the concrete. The higher the chloride ions concentration, the higher the conductivity of the concrete. Therefore, the measured conductivity can serve as an indirect indicator of the likelihood of corrosion of the embedded reinforcement.

Although the analog conductivity sensor and the threshold corrosion sensor have different design concepts, both sensors measure the impedance change of the reader caused by the changes in resistance. Therefore, the detailed design of the conductivity

sensor can refer to the previous design of the threshold corrosion sensor. For circuit design, the series circuit is easily implemented to cause a significant increase in the resistance of a circuit. A parallel circuit, however, is adopted in the design of the conductivity sensor to measure higher resistances. The threshold corrosion sensor can successfully use a series RLC circuit due to the fact that its transducer (the sensing wire) has a low resistance. As a result, the phase dip can be sustained in a detectable range. The conductivity sensor, on the other hand, measures relatively high resistance within the concrete. Therefore, it is impossible to maintain a detectable phase dip when the series RLC circuit design is used in the conductivity sensor. To overcome this difficulty, the parallel circuit was selected.

Figure 2.13 (right) shows the transducer placed in parallel with the capacitor of the circuit. This illustrates the circuit diagram of the conductivity sensor. Figure 2.13 (left) shows the photograph of a prototype conductivity sensor with a set of parallel probes.
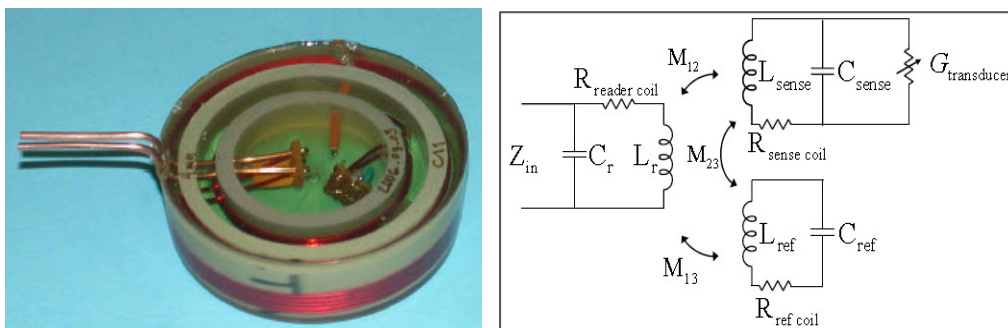
Figure 2.13. The configuration of the conductivity sensor (left) and its idealized circuit diagram (right) (Andringa 2006).

The measured conductivity is calculated from the pseudo-quality factor $\overline{Q}$ for the resonant circuit. Andringa (2006) provides a detailed derivation. This section only lists the final conversion formula (Eq. 2.8).

This formula can only be used to calculate the conductivity for a conductivity sensor with two parallel probes. It is not appropriate for application to other configuration probes.

$$\sigma_m = \frac{\omega_{\theta min}}{\overline{Q}_{medium}} \frac{\cosh^{-1}(d/a)}{l\pi} \tag{2.8}$$

$$\overline{Q}_{medium} = \left[\frac{1}{\overline{Q}_{total}} - \frac{1}{\overline{Q}_{air}}\right]^{-1}$$

Where σ_m is the conductivity of a medium; $\omega_{\theta min}$ is the frequency at the minimum phase in the phase curve (similar to the resonance frequency) obtained from curving fitting results; $\overline{Q}_{air}$ is the pseudo-quality factor obtained from the curving fitting result through the measurement of the phase response in air; $\overline{Q}_{total}$ is the pseudo-quality factor obtained from the curving fitting result through the measurement of the phase response in the objective media; $\overline{Q}_{medium}$ is the pseudo-quality factor of the objective media; d is the distance between the two centers of parallel probes; a is the diameter of the probe; and l is the length of the probe exposed in the medium.

2.5 Response of Resonant Circuits

For RLC circuits, the quality factor (Q factor) represents the influence of the

electrical resistance. For series circuits, such as the threshold corrosion sensor, the Q factor is larger when the circuit resistance is small. In contrast, the Q factor is large if the circuit resistance is high for parallel circuits, such as the analog conductivity sensor (Davis and Agarwal 2001). The quality factor is a key parameter that must be extracted from the sensor response. To obtain analog data from the resonant sensors, the Q factor can be defined in two ways. The most commonly used Q factor is defined as the ratio of the energy stored in the RLC circuit to the energy being lost in one cycle, as shown in Eq. 2.9 (Davis and Agarwal 2001):

$$Q = 2\pi \times \frac{\text{Energy Stored}}{\text{Energy dissipated per cycle}} \tag{2.9}$$

The second definition, on the other hand, is related to the sharpness of the resonance as shown in Eq. 2.10 (Tipler and Mosca 2004).

$$Q = \frac{f_0}{\Delta f} = \frac{\omega_0}{\Delta \omega} \tag{2.10}$$

Where f_0 is the resonant frequency, Δf is the bandwidth, ω_0 is the angular resonant frequency, and $\Delta \omega$ is the angular bandwidth.

Because the resonant sensors are embedded in concrete and interrogated wirelessly, it is not possible to measure the Q factor directly using Eq. 2.9. But an indirect measurement can be used with Eq. 2.10 to extract a factor that is similar in concept to the Q factor. Andringa (2003) proposed the pseudo-quality factor, $\overline{Q}$ factor, as defined in Eq. 2.11. Although an indirect measurement is used to determine

the $\overline{Q}$ factor, it has proved to be sufficient in most situations (Dickerson 2005, Andringa 2006, and Puryear 2007).

$$pseudoQ = \overline{Q} = \frac{\omega_{\theta min}}{\Delta\omega} \qquad\qquad (2.11)$$

$$M \ll \Rightarrow \omega_{\theta min} \cong \omega_0 \Rightarrow \overline{Q} = Q$$

Where $\omega_{\theta min}$ is the angular frequency at the minimum phase in the phase curve; $\Delta\omega$ is the full-width half-max (FWHM) of the phase (Figure 2.14); and M is the inductive coupling.
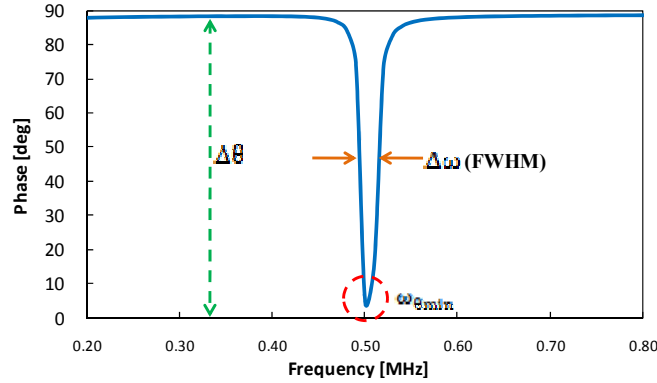
Figure 2.14. The parameters for the pseudo-quality ($\overline{Q}$) factor (Andringa 2006).

When interrogating a resonant sensor in air with a small read range, the phase response away from the resonant frequency is approximately 90 degrees (Figure 2.14). However, when interrogating sensor embedded in concrete, the phase response shown in Figure 2.11 and Figure 2.12 is more representative.

To reduce the sensitivity of the calculated $\overline{Q}$ factor and the baseline values, Andringa (2003) developed a numerical algorithm. The algorithm adjusts for baseline

shifting using a curve-fitting routine to interpolate between the measured data points, and then calculates the critical parameters, phase dip (ΔQ), resonant frequency ($f_{\theta_{min}}$) and $\overline{Q}$ factor.

2.6 Sensitivity of Resonant Circuits to Moisture

2.6.1 Baseline Shifting

Extreme baseline shifting (Figure 2.15) was measured by Puryear (2007) when the surface of the reader coil was not complete dry at the time the measurement was taken. Once the case was identified, it is easy to avid this problem by preventing moisture from accumulating on the reader coil.
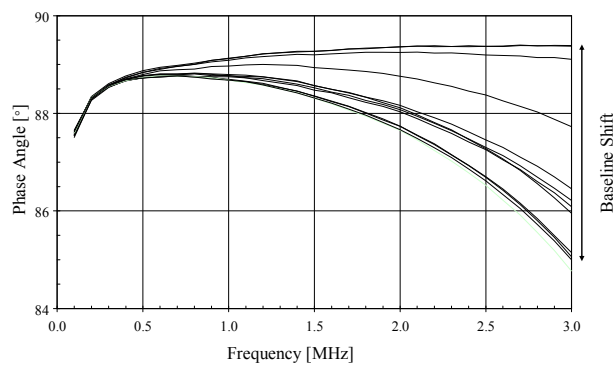
Figure 2.15. Observed baseline shift of reader coil (Puryear 2007).

2.6.2 Environmental Protection for Embedded sensors

Several attempts have been made to protect the resonant circuits from moisture

and corrosive agents within the concrete. However, additional work in this area is required.

Marine epoxy was used to construct a puck-shaped protective sensor housing (Figure 2.16 left) in the first design. Two problems with this design were identified: (a) the flat puck created a large air void in the concrete below the sensor. (b) Contaminants penetrated into the epoxy during the exposure tests. The second design used a hemisphere-shaped, protective sensor housing (Figure 2.16 right). To eliminate the air void, the sensor was potted using fiber-reinforced cement paste except for the capacitors which were potted using PC-11 marine epoxy. However, moisture penetrated into the housing and influenced the characteristics of the inductive coils.
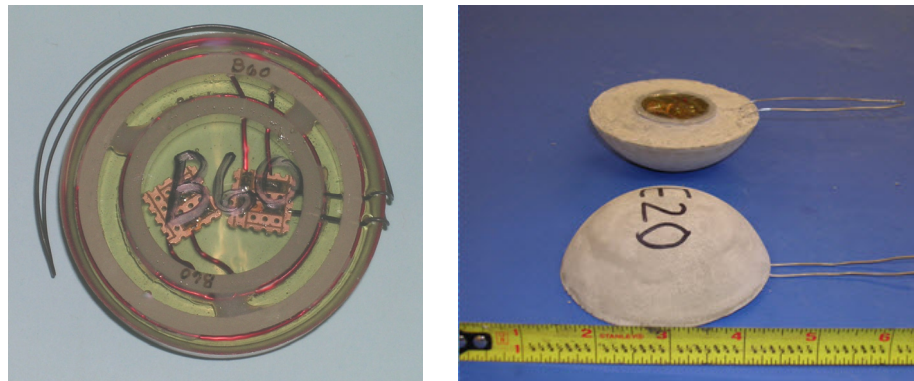
Figure 2.16. Puck-shaped PC-11 marine epoxy housing (left) and hemisphere-shaped cement-paste housing (right) (Puryear 2007).

Neither design was considered to be adequate for the passive sensors. Refinement of the environmental enclosure is discussed in detail in Chapter 4.

CHAPTER 3

Testing Corrosion and Conductivity Sensors in a Section of Reinforced Concrete Slab

3.1 Introduction

In order to test the performance of threshold corrosion sensors embedded in reinforced concrete structures, Dickerson (2005) and Puryear (2007) constructed test specimens that were intended to model section of reinforced concrete bridge decks. The measured responses of the sensors in Slab 3 are reported in this chapter.

The middle portion of the specimen was exposed to salt water periodically for 30 months during an accelerated corrosion test and then dried naturally for 4.5 months until the concrete cover was removed to observe the extent of corrosion on the reinforcement and the condition of the sensors. The design of this experiment is described in Section 3.2. Section 3.3 assesses the extent of corrosion of the steel reinforcement in Slab 3 based on the measured sensor responses. Furthermore, the performance of the conductivity sensor is also discussed. Section 3.4 compares the observed corrosion of steel reinforcement following the autopsy with the measured sensor responses to examine the reliability of the concentric coupled threshold corrosion sensor in corrosion detection. Possible durability issues for the sensors related to the PC-11 marine epoxy used to provide environmental protection are also

discussed. Finally, the conclusions are summarized in Section 3.5. Addition information about the measured response of the sensors in Slab 3 is presented in Appendix A.

3.2 The Design of the Experiment

The design of the accelerated corrosion tests was discussed in Puryear (2007). Section 3.2 summarizes that discussion, and provides some commentary on essential points.

The reinforced concrete slab specimen, labeled Slab 3, measured 120-in long, 18-in wide and 8-in deep. The top and bottom plan views and a typical section of the specimen are shown in Figures 3.1 to 3.3. Eighteen sensors including 14 concentric, coupled, threshold corrosion sensors (B125 to B128 and B134 to B143) and four conductivity sensors (C01 to C04) were embedded in this specimen. The top and bottom layer of reinforcing steel were connected with five, 100-Ohm resistors to assist the development of macrocell corrosion. Type K Thermocouples (T01 to T05) were also installed at the bottom layer of the steel reinforcement to monitor temperature changes in the specimen during the test.
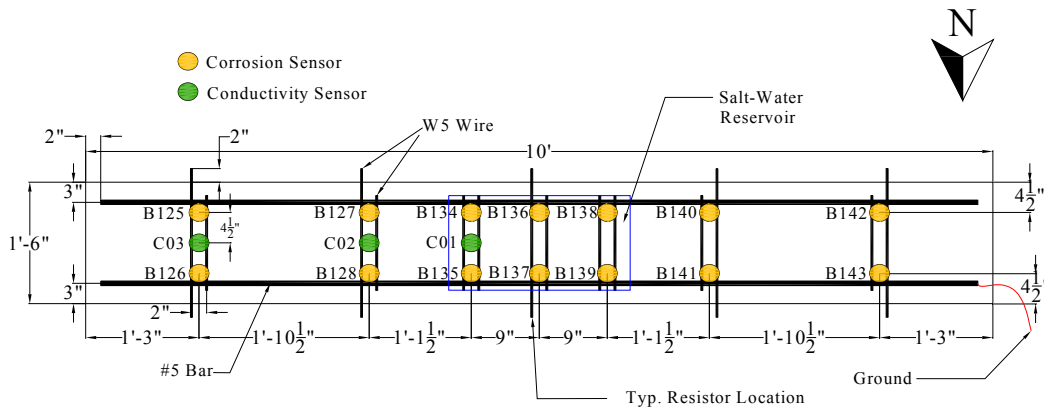
Figure 3.1. Top plan view of Slab 3 (Puryear 2007).
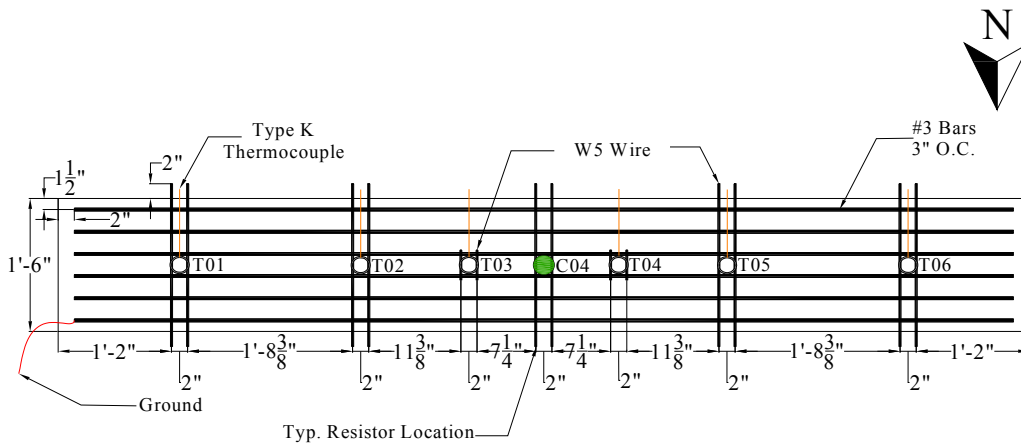
Figure 3.2. Bottom plan view of Slab 3 (Puryear 2007).
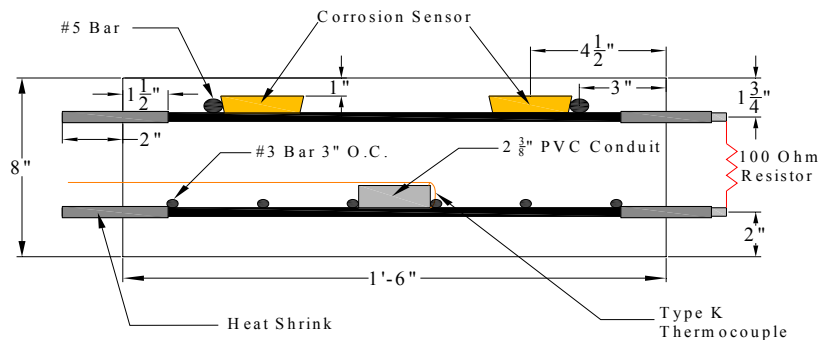
Figure 3.3. Cross-section of Slab 3 (Puryear 2007).

The sensing wires for the seven corrosion sensors located along the north side of Slab 3 were attached to the transverse reinforcement in the top layer of steel. The sensing wires for the seven corrosion sensors located along the south side in Slab 3 were attached to the longitudinal reinforcement. Photographs of both configurations are shown in Figure 3-4. To minimize the time to initiation of corrosion, the longitudinal reinforcement was sprayed with salt-water prior to the placement of the concrete. An overview of all instrumentation is shown in Figure 3-5, where the south side of the specimen in shown on the right of the photograph.
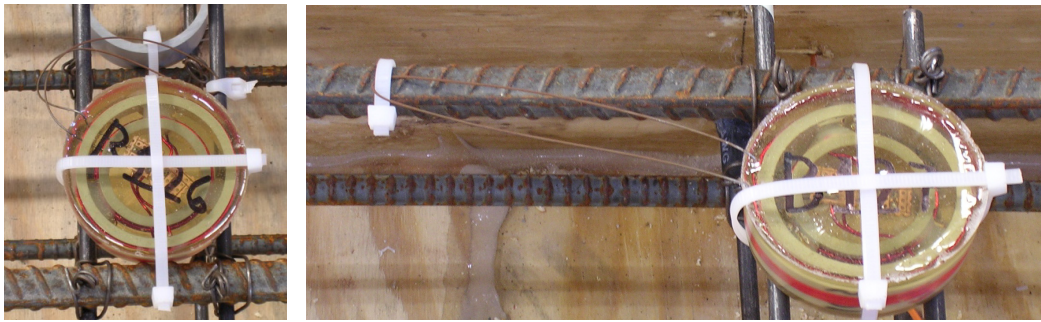
Figure 3.4. Photographs of sensing wires attaches to transverse reinforcement (left) and of sensing wires attaches to longitudinal reinforcement (right) (Puryear 2007).

Figure 3.5. Photograph of the layout of the sensors and steel reinforcement (Puryear 2007).

The slab, as shown in Figure 3.6, was loaded at both ends with concentrated loads such that flexural cracks formed on the top surface in the constant moment region. The maximum crack widths were approximately 0.01 in. A salt-water reservoir was attached at midspan to the top surface of the specimen with a waterproof adhesive Sika 11FC, Figure 3.7. Maps of the cracks observed on the top surface of Slab 3, one day after loading, are shown in Figure 3.8.
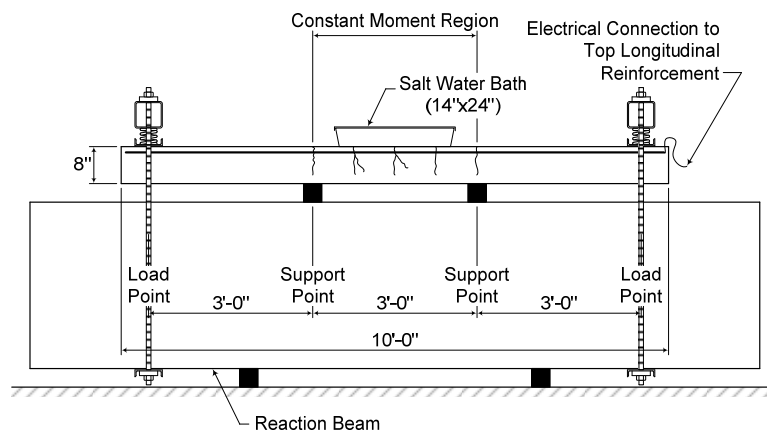
Figure 3.6. Loaded slab with water reservoir in place (Dickerson 2005).

Figure 3.7. Photograph of the salt-water reservoir positioned at the midspan of Slab 3 (Puryear 2007).
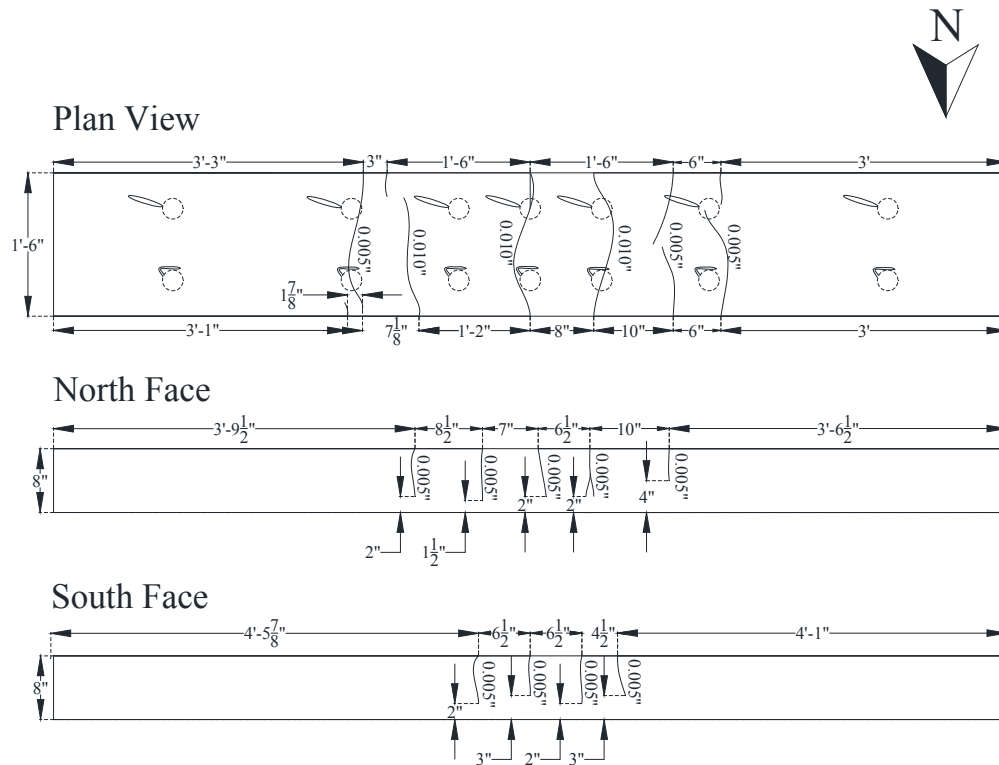
Figure 3.8. The crack map of Slab 3 one day after loading (Puryear 2007).

The sensors were interrogated 49-times during the accelerated corrosion test. The first interrogation took place on 6 April 2006, which was 28 days after placing the concrete. The sensors were interrogated for the last time on 7 February 2009, 1038 days later. During most of this time, the specimen was subjected to alternating wet and dry cycles. The reservoir at midspan was filled with salt water (3.5% by weight) for two weeks, and then emptied for two weeks. Sensors were interrogated after each wet and dry cycle.

However, between 5 November 2007 and 16 June 2008 and between 29 September 2008 and 7 February 2009, the specimen was not subjected to moisture,

and the sensors were interrogated infrequently. The complete timeline for the accelerated corrosion test is given in Table A.1.

The specimen was stored indoors during the accelerated corrosion test in order to control the moisture. However, the building was not heated, and the specimen experienced temperature fluctuations of nearly 60 °F during the test.

As the salt water exposure was restricted to the middle of Slab 3, three distinctive environments developed within the specimen: (a) dry conditions with no exposure to chlorides (b) controlled moisture conditions with high exposure to chlorides and (c) transition region where moisture and chlorides are transported through the concrete. Corresponding to these environments, the sensors were also exposed to three levels of corrosion risk: (a) low, (b) high to severe, and (c) intermediate to high. The conditions to which the sensors were exposed are summarized in Table 3.1.

Table 3.1 The Corrosion Risk Conditions of the Tested Sensors.

Regions/Corrosion Risk Level	Sensor No.
Low Chloride Ions Penetration (Low Corrosion Risk Level)	B125, B126, B142, B143
Beneath Salt-Water Reservoir (High to Severe Corrosion Risk Level)	B134, B135, B136, B137, B138, B139
Transition Regions (Intermediate to High Corrosion Risk Level)	B127, B128, B140, B141

To monitor the extent of corrosion within Slab 3, the sensors were interrogated at the end of each wet/dry cycle using Solartron SI 1260 Impedance/Gain-Phase Analyzer, a 4-in. diameter reader coil, and a 3-ft coaxial cable. The reader coil was

fabricated with five turns of 18 AWG copper magnet wire. Prior to the autopsy of the specimen, ancillary half-cell potential measurements were taken at 76 locations on the top surface of Slab 3 (Figure 3.9) in accordance with ASTM C876 (2009) to estimate the corrosion of the steel reinforcement. Samples of concrete powder were also collected to determine the acid-soluble chloride ion content at locations along the length of the slab in accordance with ASTM C1152/ C1152M (2006).
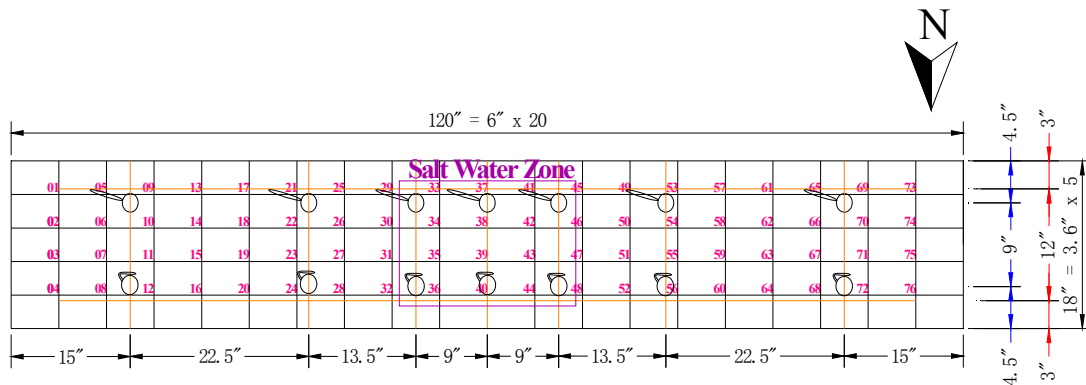
Figure 3.9. Diagram showing the locations where half-cell potential measurements were taken in Slab 3. The locations are marked by pink numbers.

3.3 Detected State of the Sensors at Conclusion of Accelerated Corrosion Test

The sensing wires for all six corrosion sensors placed below the saltwater reservoir fractured during the accelerated corrosion test. The dates corresponding to the first interrogation in which the fractured sensing wire was detected are shown in Figure 3-10. Figure 3.11 shows a plan view of the sensors and identifies the detected states of the sensing wires after the test. Sensors with intact sensing wires are colored yellow and those with fractured sensing wires are colored red.

41
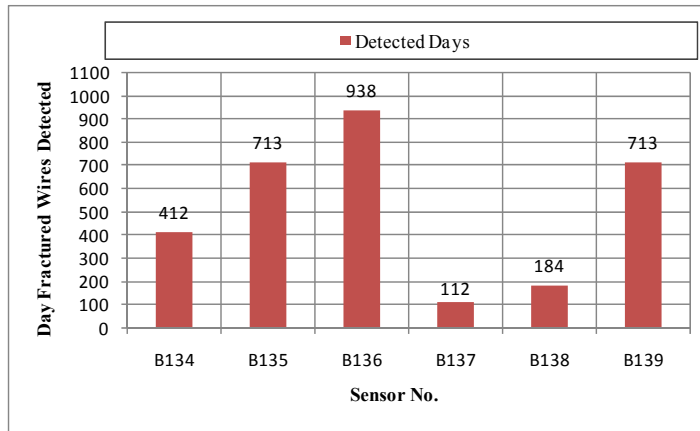
Figure 3.10. Graph showing first date that fractured sensing wire was detected
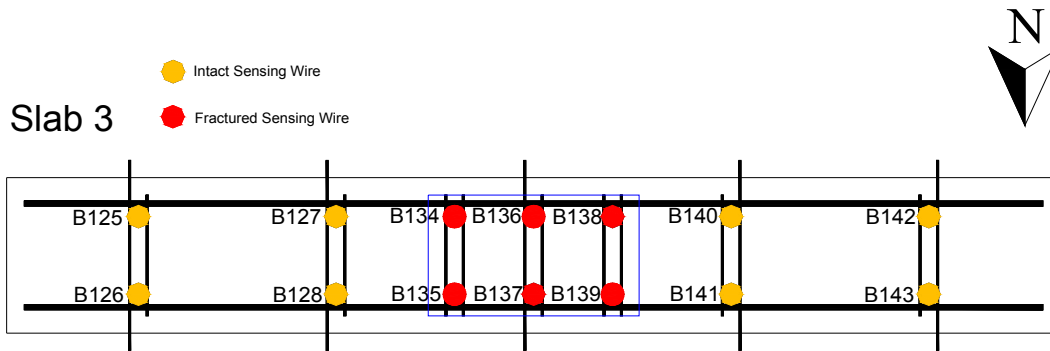
Figure 3.11. The detected states of the sensing wires after a nearly three-year test.

Figure 3.11 clearly reveals that the sensing wires for all corrosion sensors embedded beneath the salt water reservoir are fractured. The sensing wires for all coupled, threshold corrosion sensors located outside the salt water region remained intact. This result was expected as the sensors located in the middle portion of Slab 3 were exposed in the highest moisture and chloride ions environment. For other locations, the corrosion rates are considerably lower because moisture and chloride ions are only transported through the concrete by capillary suction, permeation, diffusion and migration (Section 2.4.2). Consequently, much more time is required for

initiation of corrosion at these locations.

The four conductivity sensors functioned as expected during the corrosion test. Figure 3.12 shows the variation of the pseudo-quality factor for Sensor C01, which is located beneath the salt-water reservoir (Figure 3.1). Changes in the pseudo-quality factor were observed after each wet and dry cycle of the accelerated corrosion test, indicating that the response is very sensitive to the chloride ions and moisture.
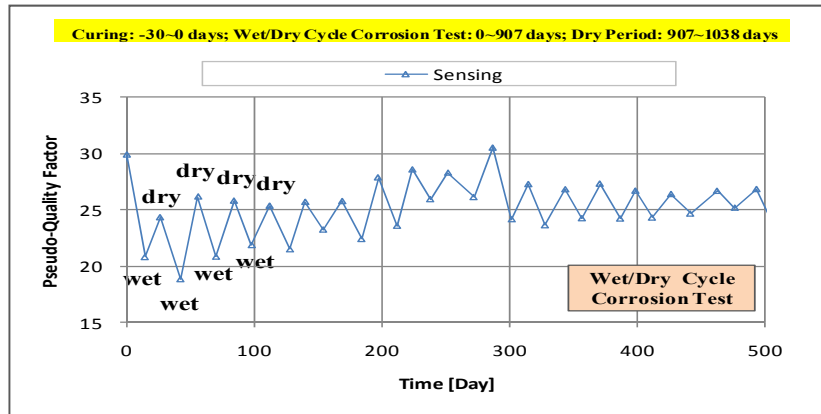
Figure 3.12.Variations of the pseudo-quality factor Sensor C01during the accelerated corrosion test.

Figure 3.13, on the other hand, shows response of Sensor C03, which was located at the end of the slab and not exposed to variations in moisture and chlorides (Figure 3.1). The pseudo-quality factor increased consistently during the first year, indicating that the resistivity of concrete increases with age.

The results from Figure 3.12and 3.13 demonstrate that the relative changes in the sensor reading are consistent with changes in conductivity within the concrete, but

that the absolute values of the pseudo-quality factors from different sensors cannot be compared directly.
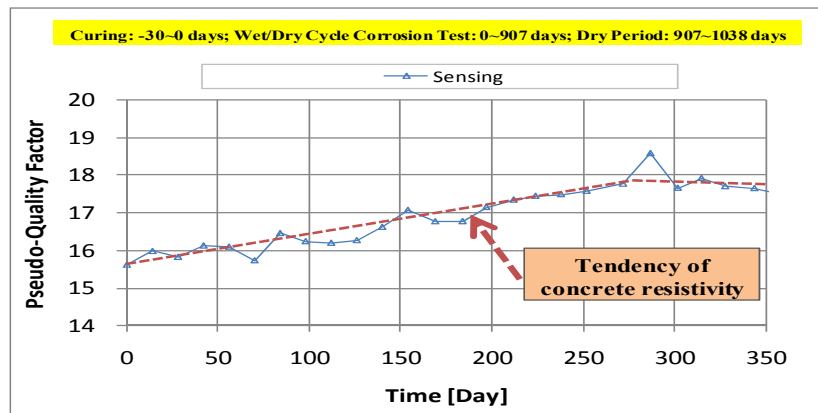
Figure 3.13. Increasing pseudo-quality factors with increasing age of concrete for Sensor C03.

3.4 Comparison between Sensor Responses and Other Indicators of Corrosion

To confirm the reliability of the threshold corrosion sensors, two key events need to occur. The sensing wire of each sensor, according to the design mechanism, must fracture after its sensor detects the initiation of corrosion of the steel reinforcement. Also, the corrosion of steel reinforcement must occur.

Three indicators were used to determine if both events occurred in Slab 3: (a) distribution of half-cell potential measurements, (b) acid-soluble chloride ion levels, and (c) visual observation during a specimen autopsy. Both the half-cell potential measurements and the acid-soluble chloride ions levels are indirect measures of corrosion activity within the reinforced concrete slab. By removing the concrete cover

during the specimen autopsy, the researchers are able to observe the presence of corrosion on the reinforcement and sensing wires.

Sections 3.4.1 and 3.4.2 compare the results obtained from the half-cell potential measurement and the acid-soluble chloride ion tests to the sensor responses respectively. After the autopsy of Slab 3, the states of the corrosion sensors and the condition of the steel reinforcement are documented in Section 3.4.3. They are then compared with the sensor responses measured at the end of the test. Finally, the condition of the sensors at the conclusion of the accelerated corrosion tests is discussed in Section 3.4.4 and recommendations for future improvement will be given.

3.4.1 Measured Half-Cell Potentials

The half-cell potentials for Slab 3 in mV were measured using a standard calomel electrode (SCE). Readings were then converted to the scale for a copper-copper-sulfate electrode (CSE) to assess the risk of corrosion in accordance with ASTM G3 (1989). The conversion algorithm is given in Eq. 3.1. ASTM C876 (2009) groups corrosion risk in three levels: (a) low ($>$ -200 mV), (b) intermediate (-200 to -350 mV), and (c) high ($<$ -350 mV). As the risk of corrosion in Slab 3 decreases with distance from the source of the salt water, the measured values tended to decrease symmetrically from the center toward the two ends of the specimen.

$$CSE = SCE - 60 \text{ (mV)} \hspace{3cm} (3.1)$$

In order to express the changes of the half-cell potentials within the specimen, a contour plot was developed by linear interpolation among the measured values. The contour plot, shown in Figure 3.14, presents the half-cell potential measured nearly three years after the start of the accelerated corrosion tests for Slab 3. 957 days after the start of the test and 51 days after the end of the last wet cycle. Readings within the salt water reservoir area were still considered to be high (-350 to -385 mV). However, in the transition zone and the ends of the slab, the corrosion risk was considered to be low ($>$ -200 mV). The readings indicate that at the end of the accelerated corrosion test, the probability of corrosion activity below the salt-water reservoir was greater than 90%, while the probability of corrosion activity was less than 10% at the locations of the other sensors.
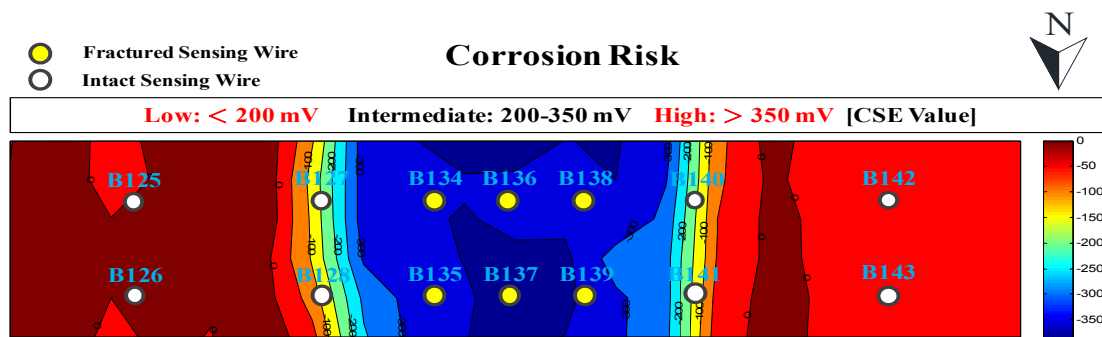
Figure 3.14. Distribution of half-cell potentials for Slab 3 measured on 18 November 2008.

In addition to determining the likelihood of corrosion occurring in Slab 3, observing the half-cell potential changes can help researchers understand some

characteristics of corrosion activities. Figure 3.15 illustrates the half-cell potential distributions in Slab 3 in 3-dimensions. This figure shows that the corrosion activity was higher for the longitudinal reinforcing bar on the south side of slab than the bar on the north side.
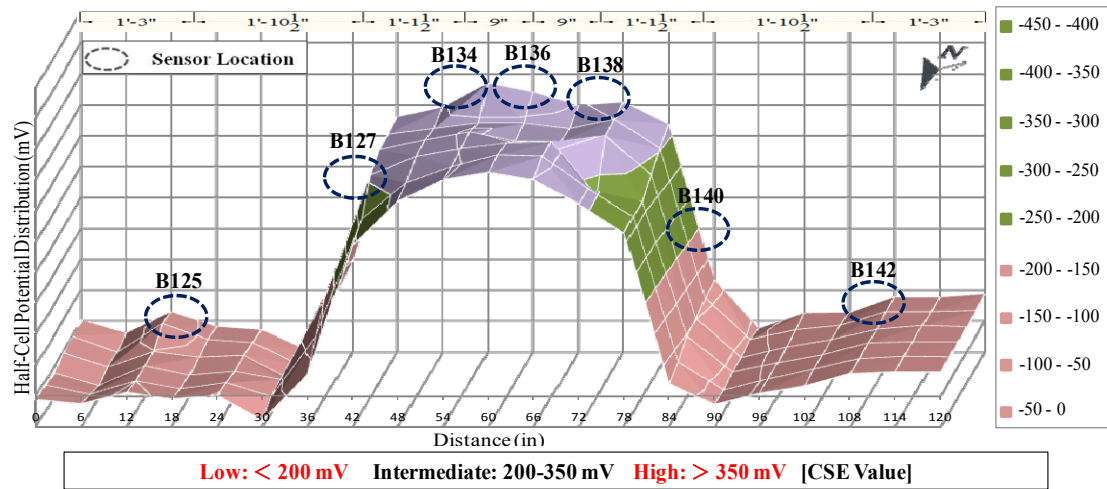
Figure 3.15. 3D distribution of half-cell potentials for Slab 3 measured on 18 November 2008.

3.4.2 Acid-Soluble Chloride Ion Levels

After the conclusion of the accelerated corrosion test, samples of concrete powder were collected to determine the acid-soluble chloride concentration at various locations within Slab 3. A total of 63 holes were drilled into the cover, and the concrete powder was collected at a depth of 1 in. The holes were arranged in groups of three, as shown in Figure 3-16 (bottom) and Figure 3-17, forming 21 groups. Within each group, the three holes were arranged within a 4-in. diameter circle. The

47

crack paths and widths are shown in the top plot in Figure 3-16. The middle plot shows the boundaries of the salt-water reservoir and the region of discolored concrete due to the moisture.

As shown in Figure 3-16 (bottom), groups 09 through 14 were located below the saltwater reservoir. Groups 07, 08, 15, and 16 were located beyond the saltwater reservoir, but within the region that experienced moisture cycles. Groups 04, 05, and 06 were located at visible boundary of the moisture, while groups 01 through 03, and 17 through 21 were located in regions that did not experience moisture fluctuations.

Originally, powder samples from the three holes in each group were mixed and tested in house using AASHTO T-260 test procedure with CL2000 instrument produced by James Instruments Inc. to determine the acid-soluble chloride concentration for each group. However, the results were highly variable and considered to be unreliable. Therefore, six samples were sent to a commercial testing laboratory (Tourney Consulting Group LLC) for evaluation in accordance with ASTM C 1152. Powder samples were combined as indicated in Table 3-5 to form the six samples. It should be noted that samples 001, 002, and 004 contained concrete power that was not exposed to moisture variations, while samples 003, 005, and 006 contained concrete power that was exposed to moisture variations.

The results are summarized in Table 3-2. The acid-soluble chloride levels were extremely low for samples 01, 02, and 04 (less than 45 ppm), while the acid-soluble

chloride levels were above 3000 ppm for the samples that experienced moisture fluctuations. The results are plotted in Figure 3-18. Batch records from the ready-mix plant, the concrete mixture used to cast Slab 3 had a unit weight of 3895 lb/yd^3 and a cement content of 423 lb/yd^3
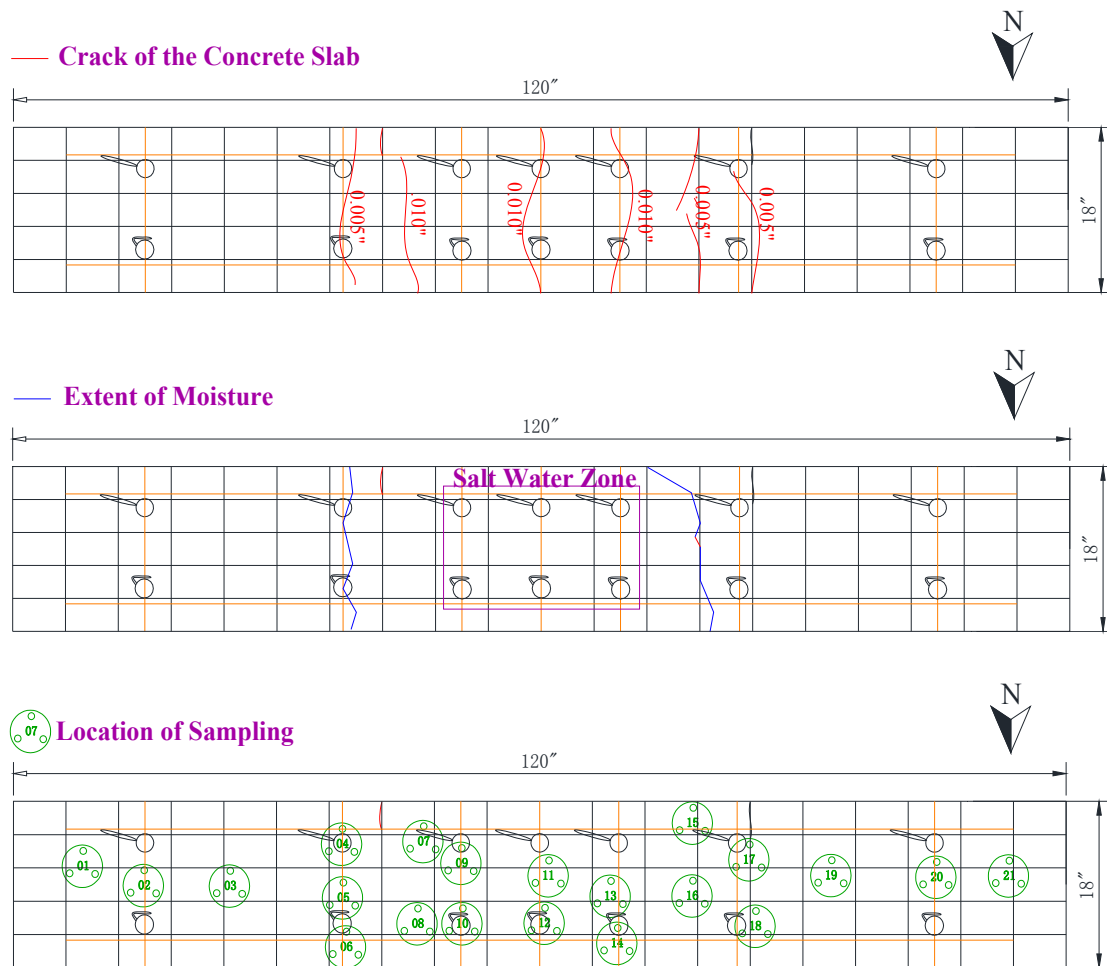
Figure 3.16 Patterns and widths of cracks on top surface of Slab 3 at conclusion of accelerated corrosion test (top); extent of moisture on top surface of Slab 3 (middle); locations where concrete powder samples were collected (bottom).

Table 3.2 Concrete Power Samples Tested at Commercial Laboratory.

Sample No.	Power Samples Combined from Groups	Acid-Soluble Chloride Content, ppm	% Chlorides per Mass Cement
1	01, 03	24	0.02%
2	02	43	0.04%
3	07, 08	3571	3.29%
4	19, 20, 21	29	0.03%
5	09, 10	3152	2.90%
6	12, 13, 14	4367	4.02%

Figure 3.17. Photograph of three holes drilled to collect concrete powder within a 4-in. diameter.
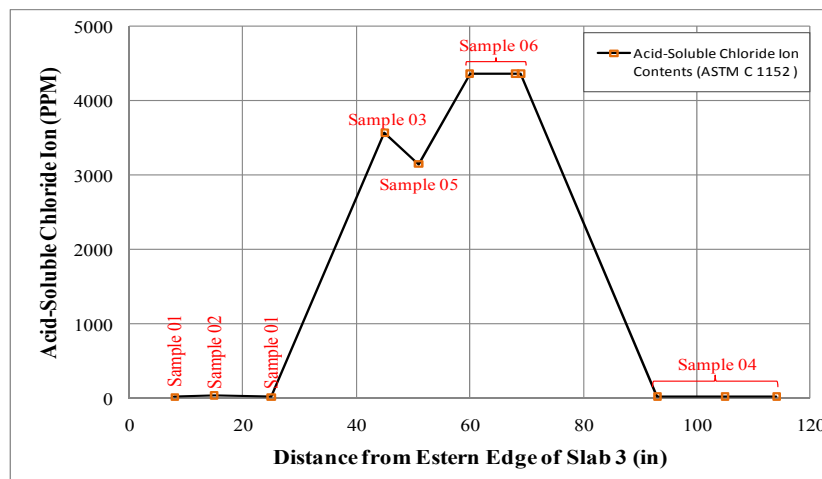
Figure 3.18. The distribution of chloride ions in Slab 3.

3.4.3 The Observed Conditions of Steel Reinforcement

At the conclusion of the accelerated corrosion test, the concrete cover was removed from Slab 3, exposing the sensors and the top layer of reinforcing steel. The extent of observed corrosion is shown in Figure 3-19, where sensors with fractured steel sensing wires are labeled in red and sensors with intact steel sensing wires are labeled in black. Uniform corrosion on the surface of the longitudinal reinforcement is colored in orange and uniform corrosion on the surface of the transverse reinforcement is colored in green. The most severe corrosion occurred at the junction of the longitudinal and transverse reinforcement, and pitting corrosion was frequently observed in these locations.

As discussed in Puryear (2007), air voids tended to form in the concrete directly below the corrosion sensors (Figure 3-20), and black corrosion products were concentrated in these areas.

It is also interesting to note that the longitudinal rebar long the north side of Slab 3 experienced more corrosion than the longitudinal rebar along the south side. Additionally, the south ends of the transverse reinforcement experienced more corrosion than the north ends. These observations were consistent with the locations where the steel sensing wires were attached to the top layer of reinforcement. The chemical composition of the steel sensing wires were comparable to the deformed reinforcement (Puryear 2007), but the cold-rolled wires were more susceptible to

corrosion than the hot-rolled bars, and the corrosion tended to concentrate at the interface between the two materials..
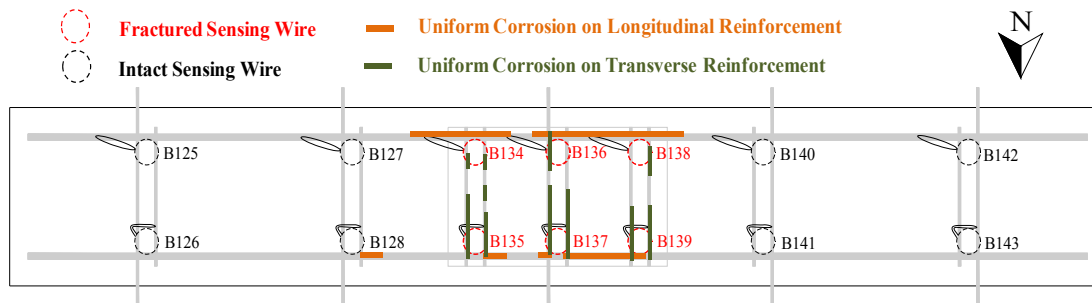
Figure 3.19. Observed corrosion on top layer of steel reinforcement in Slab 3.

Figure 3.20. Photograph of the corrosion directly below Sensor B135.

The observed condition of the steel reinforcement is compared with the measured responses of the sensors in Table 3-3. All sensors provided correct information about the condition of the reinforcement. That is, the sensors themselves demonstrate sufficient reliability and can be applied in practice. However, the coupled the sensing wire to the top layer of reinforcement did not increase the tributary area of the sensors — the passive sensors still behaved as point sensors. In addition, the point of connecting area between the steel sensing wire and reinforcement accelerates

corrosion. Therefore, no advantage to using the coupled sensor was identified, and the isolated threshold corrosion sensor is recommended for future use.

Two different corrosion situations were also discovered in two configurations of sensing wires positioned to the steel reinforcement (Figure 3.4). Figure 3.21 demonstrates the corrosion in vicinity of Sensor B134. As shown, the steel sensing wire of sensor B134 was straight and attached to the longitudinal steel reinforcement. In terms of this photograph, the severe corrosion of the steel reinforcement is mainly along the longitudinal reinforcement and the corrosion of the steel sensing wire seems to start from the connecting point. Figure 3.22, on the other hand, illustrates the observed corrosion situation in vicinity of sensor B137, where the steel sensing wire of Sensor 137 was curved and attached to the transverse reinforcement. In this case, the corrosion of the steel reinforcement appeared to initiate on the transverse steel reinforcement.

Table 3.3 Reliability of Sensors Tested in Slab 3 with Respect to the Observed Condition of the Steel Reinforcement.

| | | Observed State of Reinforcement | |
		No Corrosion	Corrosion
Detected State of Reinforcement	Corrosion	0 (False Positive)	6
	No Corrosion	8	0 (False Negative)
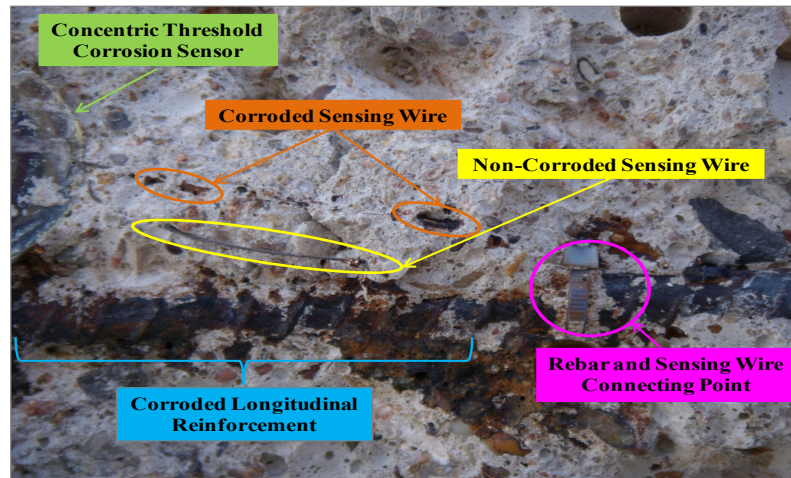
Figure 3.21. Observed corrosion in vicinity of sensor B134.
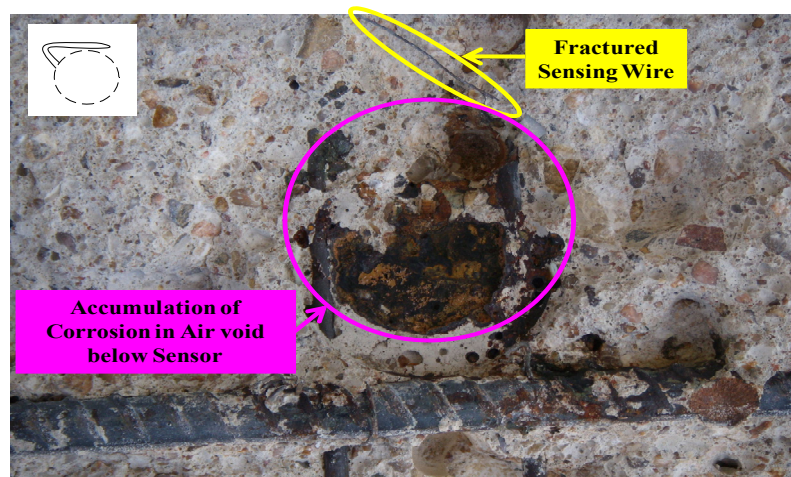
Figure 3.22. Observed corrosion in vicinity of sensor B137.

3.4.4 Observed Conditions of Sensors

Although the reliability of the threshold corrosion sensor has been demonstrated (Table 3.3), issues remain regarding the durability of the sensors. Two representative examples in Figures 3.23 and 3.24 illustrate that the marine epoxy should not be used

protect the electronic circuits from the environment within the concrete. A deep crack was observed in Sensor B139 in Figure 3.23 at the end of the test. The copper wire used to fabricate the inductor coil, exposed to the surrounding concrete. If the inductive coils are exposed to moisture, variations in the measured phase response of the sensors have been observed (Puryear 2007). Sensor B134 illustrates a more serious failure with the epoxy housing (Figure 3.24). The epoxy housing is cracked on top of the reference circuit, and corrosion products have penetrated into the resonant circuits.
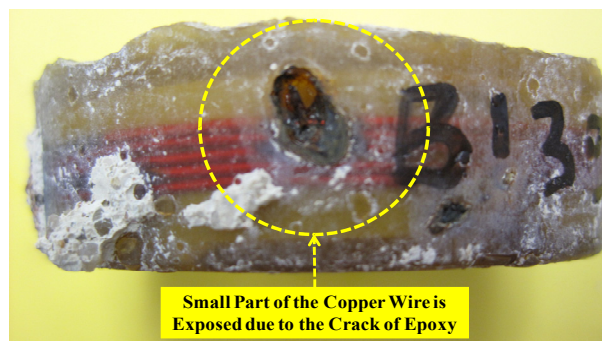
Figure 3.23. Copper wire is exposed to moisture in Sensor B139.
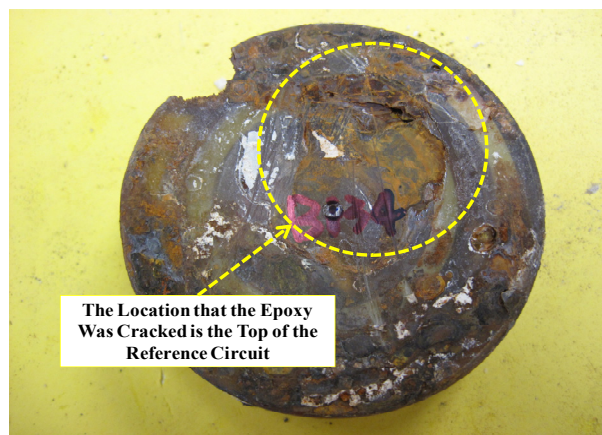
Figure 3.24. Photograph showing cracked epoxy housing for Sensor B134.

In order to understand the possible reasons of the observed response of the marine epoxy housing, the material properties of PC-11 marine epoxy were investigated (Table 3.4). Compared to the average coefficient of linear thermal expansion of steel, 6.5E-6 in/in °F, the coefficient of the linear thermal expansion of PC-11 marine epoxy is ten times larger. As a result, a large amount of moisture and corrosion content can easily penetrate through the PC-11 marine epoxy housing and into the sensor when the temperature increases.

The water absorption property of PC-11 marine epoxy may be another reason behind the unexpected response of Sensor B134. Although moisture and corrosion contents penetrate into the sensor through the steel wire, the marine epoxy housing can keep these contents inside the sensor. This may explain why black corrosion occurs inside the sensor (Figure 3.25).

Table 3.4 Material Properties of PC-11 Marine Epoxy (Protective Coating Company 2010).

Epoxy Property	Test Method	Test Results
Coefficient of Linear Thermal Expansion	Provided by Manufacturer	65E-6 in/in/°F
Water Absorption	ASTM C 413	0.44%
Heat Deflection	ASTM D 648	120°F

Another possibility is that the epoxy housing may have cracked due to development of corrosion within the sensor. As described in Section 2.2.1, the volume of iron corrosion products is six to ten times larger than the volume of the original iron. As a result, when corrosion products start to produce, the sensor epoxy housing

could have been squeezed or bulged by these corrosion products and cracks or small cavities might have appeared on the surface of the epoxy housing.

In addition to the above situations, when the chloride products penetrate into the sensor, the inductive copper coil seems to provide a path for them to enter the circuitry of the sensor. Figure 3.25 shows a possible path that chloride products penetrate from the outer to the inner pipe tube.
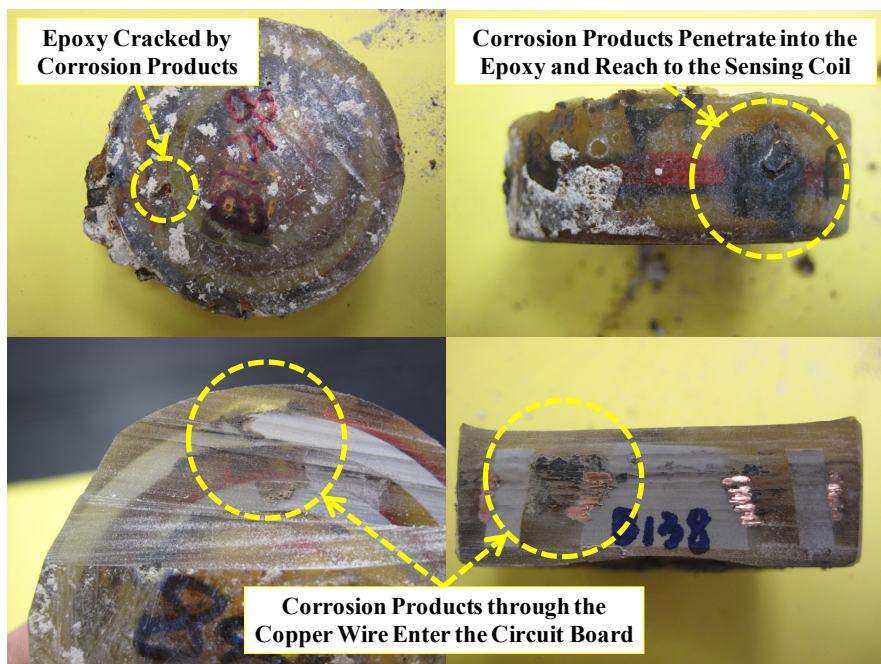
Figure 3.25. Penetration of corrosion products into Sensor B138.

Finally, Figure 3.26 illustrates the state of penetration of corrosion products in conductivity sensor, C01, located beneath the salt water reservoir. As shown, there is no corrosion product within the marine epoxy housing. Though comparing with the situation that the corrosion products penetrate into the epoxy housing in the threshold

corrosion sensor, two possible reasons can be conclude. First, the thermal expansion coefficient of the copper wire is (9.3E-6 in/in °F) larger than the steel sensing wire (6.5E-6 in/in °F). Second, the copper wire is much less likely to corrode than the steel sensing wire. As a result, while the same chloride and moisture contents penetrate into the epoxy housing in the same temperature condition, the steel wire without a passive layer will start to corrode and then the corrosion products will also develop within the epoxy housing.

Figure 3.26. Top (left) and side views (right) of corrosion products in Sensor C01.

3.5 Conclusion

In summary, the nearly three-year corrosion test of Slab 3 proved that the threshold corrosion sensor is sufficiently reliable to reflect real corrosion situations regarding the steel reinforcement embedded in concrete. However, this test revealed that the activation of the sensor mechanism directly comes from the attack of chloride contents on the steel sensing wire of the sensor. Therefore, the threshold corrosion sensor has been identified as a point sensor instead of as a coupled sensor and the hypothesis that Puryear (2007) proposed that the coupled sensor has a larger tributary

area is not true.

Through observations of the tested sensors, PC-11 marine epoxy seems to be an inappropriate material for sensor protection. Because of its low resistance to the corrosion environment, the sensor protection can be easily cracked by the corrosion products. In this circumstance, a large number of moisture and chloride contents can penetrate into the sensor and even damage the electronic circuitries of the sensor.

Suggestions for improving the durability of the sensor are discussed in Chapter 4.

The signals of the sensor interrogate in Slab 3 are also compared with the half-cell potential and chloride concentration of the specimen. According to the testing results, both methods indicate similar conclusions with the signals measured from sensors in the salt water reservoir area.

Finally, the conductivity sensor was also tested in Slab 3. All four conductivity sensors effectively showed relative resistivity changes of the concrete in the wet/dry cycle corrosion test and in the natural drying period. However, as with the threshold corrosion sensor, the sensor housing presents a problem for the conductivity sensor.

CHAPTER 4

Optimization of the Threshold Corrosion Sensor

4.1 Introduction

Researchers in the Department of Civil, Architectural, and Environmental Engineering (Dickerson 2005 and Puryear 2007) and the Department of Electrical and Computer Engineering at the University of Texas at Austin (Andringa 2006 and Pasupathy 2010) developed the basic design framework and completed the relevant laboratory tests for the threshold corrosion sensor. Extending the maximum read distance of this sensor and enhancing the durability of the sensor constitute two unresolved design issues.

One technique to improve the read distance is to increase the inductive coupling of the sensor by adding turns of the copper wire on the sensing circuit and the reader. However, if the geometry of the reader and the sensor are fixed, it will be difficult to achieve a breakthrough regarding the limit of the read distance. Section 4.2 demonstrates how the choice of capacitor can influence the phase response. Optimizing capacitor properties may provide a means by which researchers can improve the maximum read distance.

As discussed in Chapter 3, the test results from Slab 3 revealed that encasing the sensor in marine epoxy is not sufficiently durable for long-term applications. Section

4.3 proposes the detailed design of a new sensor housing for the threshold corrosion sensor. The relevant performance tests of this protection system are presented in Section 4.3. Section 4.4 provides recommendations regarding the sensor protection system and Section 4.5 summarizes the conclusions for this chapter.

4.2 Optimization of the Threshold Sensor Capacitor

The capacitance, physical size, quality of the capacitor and the price constitute four factors that influence the selection of the capacitors used in this study. Dickerson (2005) discussed these issues in Appendix A.7 of his thesis. According to Dickerson (2005), high quality ceramic capacitors labeled either COG or X7R represent the best option for threshold sensors. The capacitors labeled COG are higher in quality than those labeled X7R because they exhibit lower variations in capacitance and lower sensitivity to temperature fluctuations. However, Dickerson (2005) did not discuss in detail the performance of these two types of capacitors. Therefore, Section 4.2.1 of this thesis contains this discussion.

In addition, manufacturers use different techniques to construct capacitors. Therefore, even COG capacitors of the same capacitance will perform differently if they are manufactured by different companies. This difference is discussed in Section 4.2.2 through the comparison between two types of COG capacitors in their sensor responses. The first type of COG capacitor was purchased from the KEMET Company and is used in this thesis. The second type was used by both Dickerson

(2005) and Puryear (2007), but the source is unknown.

4.2.1 Sensitivity of Phase Response to Type of Capacitors

For this research project, thirty-nine sensors were fabricated using COG and X7R capacitors purchased from KEMET. In order to understand the influence of different types of capacitors in the reference and sensing circuits, four capacitor combinations were tested. The combinations and number of sensors are listed in Table 4.1. In all cases, the capacitor in the sensing circuit was 33,000 pF and the capacitor in the reference circuit was 6,800 pF.

Table 4.1 Configurations of Capacitors used in the Sensor Signal Influence Test.

Configuration of Capacitors	Configuration 1	Configuration 2	Configuration 3	Configuration 4
	Sensing: Reference: X7R X7R	Sensing: Reference: X7R COG	Sensing: Reference: COG X7R	Sensing: Reference: COG COG
Number of Sensors Tested	19	5	7	8

The sensors were fabricated with reference and sensing circuits having diameters of 1.25 in. and 2.0 in. respectively, with a 6-in. length of 21-gage steel sensing wire and five turns of 18 AWG copper wire in each resonant circuit. Each sensor was interrogated with a read distance of 0.0 in. in the air using a Solartron SI 1260 Impedance/Gain-Phase Analyzer connected to the reader coil with a 3-ft coaxial cable (Figure 4.1). The reader coil had a diameter of 4 in. and was fabricated using five turns of an 18 AWG copper wire.

62
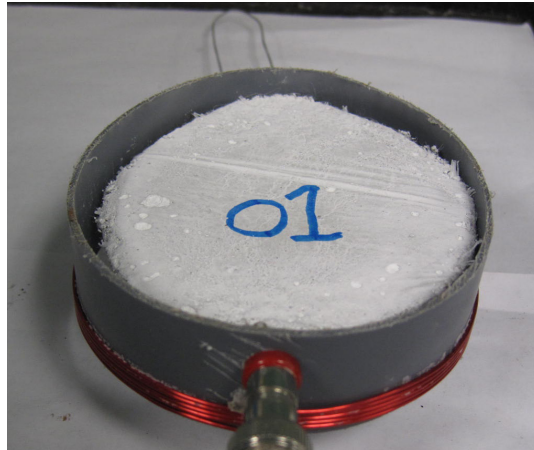
Figure 4.1. Sensor interrogation with read distance of 0.0 in.

The plots in Figures 4.2 summarize the test results for all the sensors. The horizontal axis represents the sensor ID while the vertical axis represents the measured response of the sensor in terms of phase dip, resonant frequency, and pseudo-quality factor. The measured data indicate that the response of the reference circuit can be improved using COG capacitors. Sensors with COG capacitors exhibited phase dips and pseudo-quality factors approximately four times larger than sensors with X7R capacitors. The choice of capacitor did not have as much impact on the measured response of the sensing circuit, however. The phase dips and pseudo-quality factors were approximately 20 to 25% larger for sensors with COG capacitors. The choice of capacitor had a minor influence on the resonant frequencies. In both cases, the resonant frequencies of the COG capacitors were slightly lower than those of the X7R capacitors.
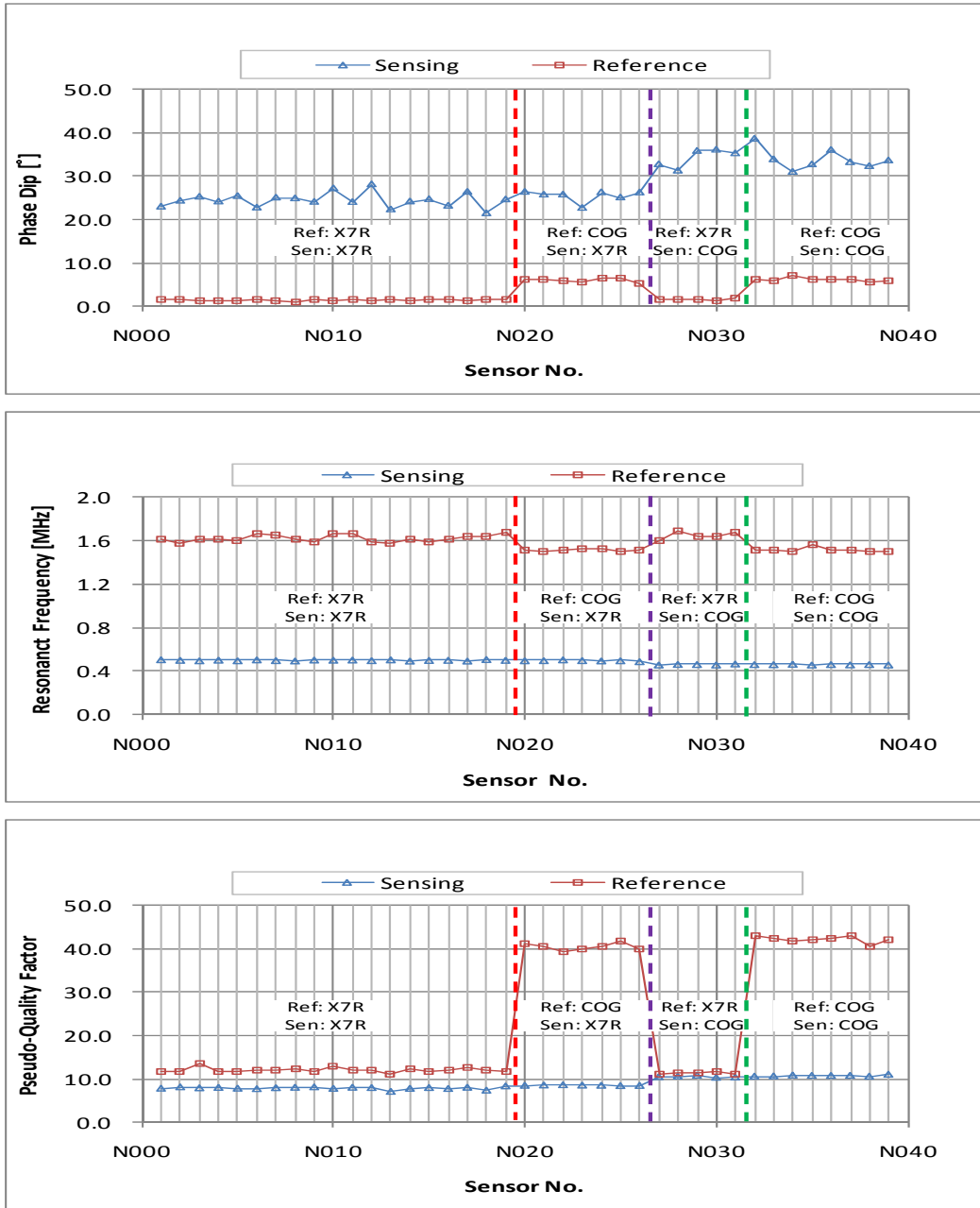
Figure 4.2. Influence of type of capacitor on measured response of threshold corrosion sensors.

64

4.2.2 Sensitivity of Phase Response to Capacitor Manufacturer

Thirteen COG capacitors from two different sources, the KEMET Company and previous research, were tested in this research project. Table 4.2 summarizes the number of sensors used from each source in this project. The specification data sheets for the capacitors are listed in Appendix B.1.

Table 4.2 Source of Capacitors.

Source of Capacitors	KEMET	Previous Research
Number of Sensors Tested	8	5

The configuration of the tested sensors and all test settings and test devices were the same as reported in Section 4.2.1. Figures 4.3 summarize the test results from all of the sensors. Since both are COG, high quality capacitors, their pseudo-quality factors are very similar regardless of the variations in their reference circuit or sensing circuit. The only difference occurs in the phase dip of the sensor response in Figure 4.3. This figure clearly indicates that the phase dip produced in the sensing circuit by the KEMET capacitors is at least ten degrees larger than the phase dip produced by the capacitors used in the previous research projects. Therefore, besides maintaining its high performance as the COG capacitor used by previous researchers, the COG capacitor produced by KEMET provides a larger read distance than the capacitor used in the past. The phase dip diagram of the two capacitors is shown in Figure 4.4.
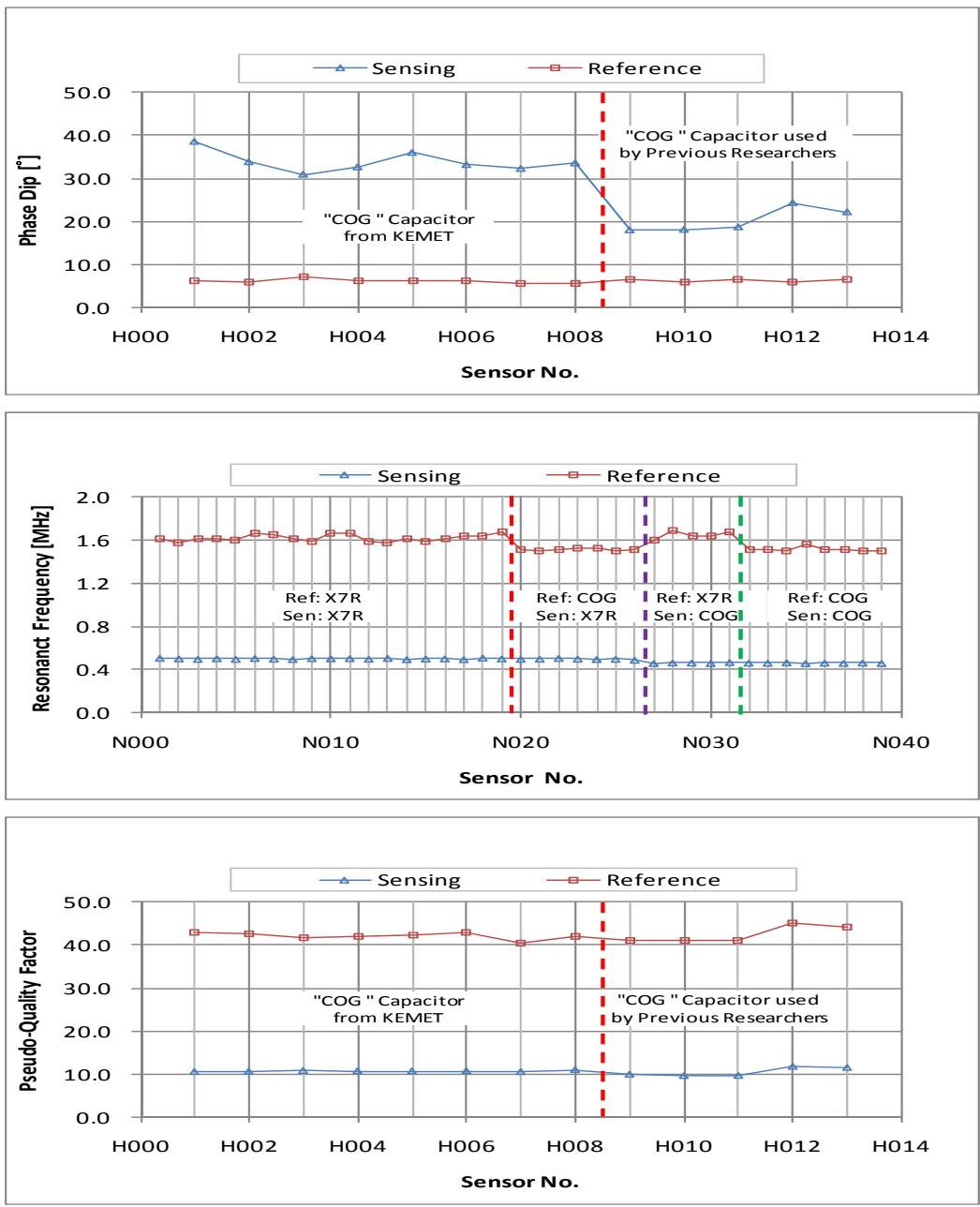
Figure 4.3. Comparison between response of sensors fabricated using capacitors produced by different manufacturers.

66
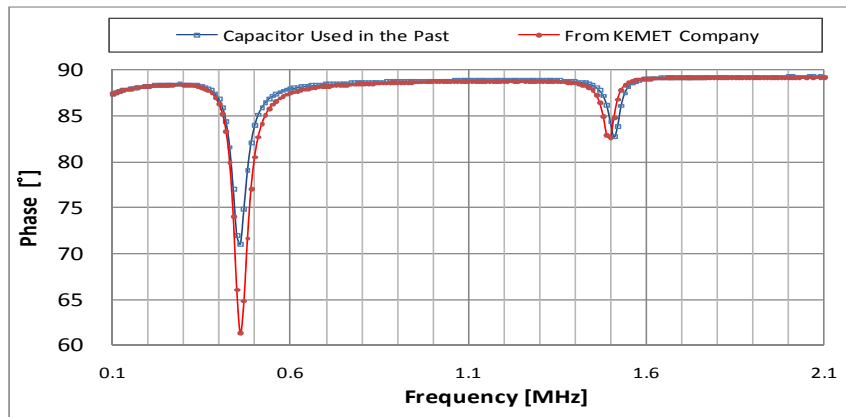
Figure 4.4. Measured phase response of sensors produced by different companies.

4.3 Improving the Durability of Threshold Corrosion Sensors

Based on the observed failure of the epoxy housing for the threshold corrosion sensors in Slab 3 and the failure of the fiber-reinforced cement paste housing (with or without the epoxy core) to protect the circuitry of the sensors in Slabs 5 and 6 (Puryear, 2007), a hybrid method was proposed in order to improve the sensor protection system and increase the performance and durability of the threshold sensor. The unsatisfactory design of the sensor housings/protection systems are summarized in Section 4.3.1. In order to improve the durability of the threshold sensor, two modifications are proposed.

Section 4.3.2 describes how a new epoxy, SHEP-Poxy Tx V, was applied as a substitute for the PC-11 marine epoxy to protect the circuitry of the threshold sensor. This section also explains tests of this new epoxy through accelerated corrosion tests.

Section 4.3.3 discusses the modification of the fiber-reinforced cement paste

67

housing and the other auxiliary protection measures used to enhance the durability of the threshold corrosion sensor.

4.3.1 Environmental Protection Systems Used by Previous Investigators

A housing is required to protect the resonant circuits in the sensors during construction and from environmental contaminants during the service life of the structure. In previous investigations, the sensors were potted in PC-11 marine epoxy (Figure 2.16 left). However, the observed response of the sensors embedded in Slab 3 during the accelerated corrosion tests demonstrated that PC-11 marine epoxy does not protect the sensor circuitry. Black corrosion within the epoxy housing and cracks within the epoxy housing illustrate the inherent deficiencies of using PC-11 marine epoxy for sensor protection.

In view of the insufficient protection of the PC-11 marine epoxy housing for sensors embedded in Slabs 1 and 2, Puryear (2007) proposed using a fiber-reinforced cement paste housing to protect the sensors (Figure 4.5 through Figure 4.8). However, the permeability of cement paste allowed moisture to reach the inductor coils within the sensors and reduced the reliability of the sensor readings. Therefore, additional refinement of the protective housing is required.
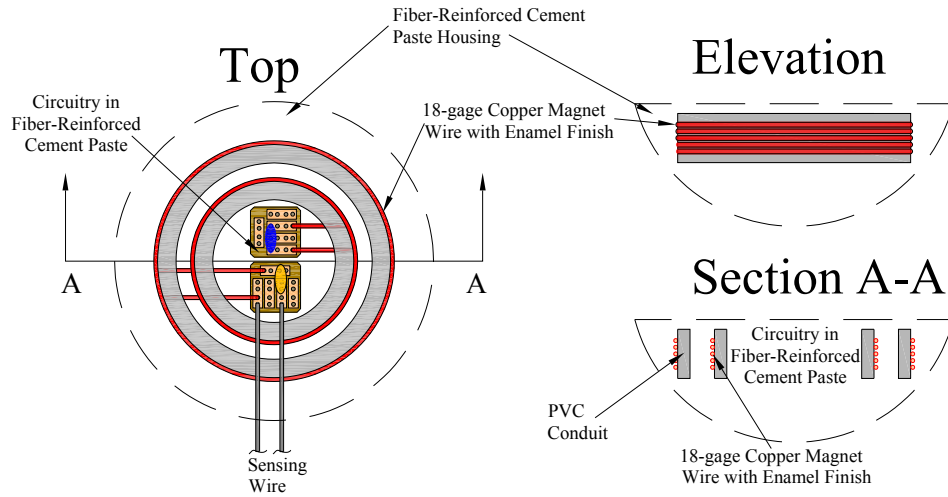
Figure 4.5. Diagram of sensor with fiber-reinforced cement paste housing (Puryear 2007).

Figure 4.6. Photographs of sensor with fiber-reinforced cement paste housing (Puryear 2007).
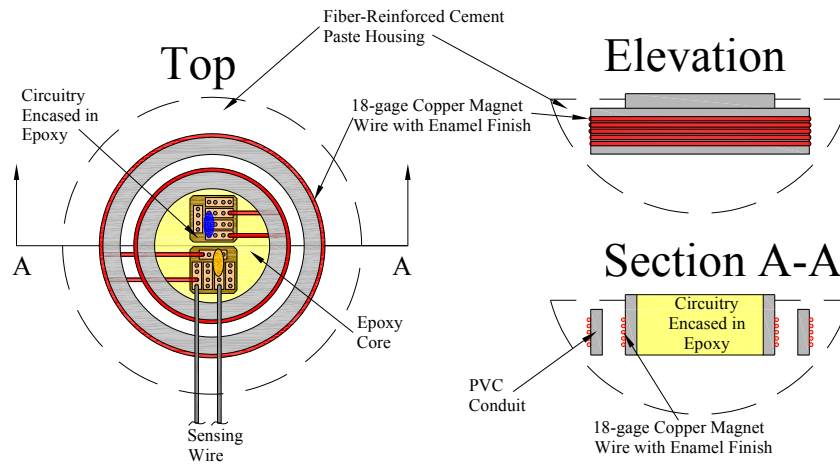
Figure 4.7. Photographs of sensor with fiber-reinforced cement paste housing and epoxy core (Puryear 2007).
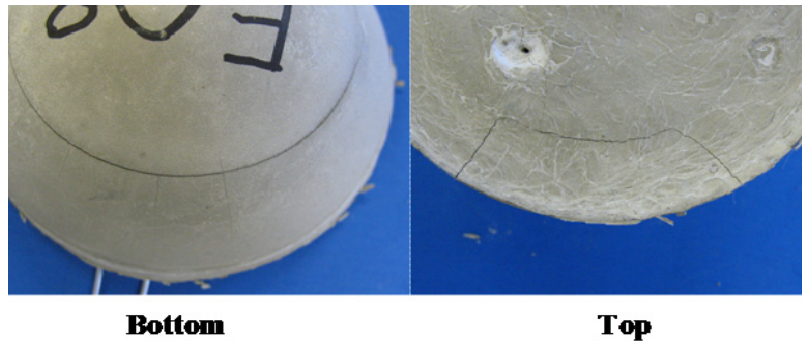
Figure 4.8. Photographs of plastic shrinkage cracks in the housing of Sensor E08 (Puryear 2007).

As described above, neither the PC-11 marine epoxy housing nor the fiber-reinforced cement paste housing satisfactorily protected the threshold corrosion sensor from the environmental conditions within the concrete. However, some of the key components appear to be viable for protecting the sensors. Sensor responses during the accelerated corrosion tests of Slabs 1 through 6 support the following observations:

1. The test results for Slabs 1, 2, 3, and 4 show that PC-11 marine epoxy is an inappropriate potting material for the sensors because water and corrosion products can penetrate the epoxy and significant cracks can occur in the epoxy housing.

2. The test results of Slabs 5 and 6 demonstrate that the sensor circuit components must be protected from moisture to maintain sensor reliability.

Based on the above observations, a hybrid sensor protection system was developed. The configuration is similar to the epoxy-core cement paste housing developed by Puryear (2007), but both the coils and the capacitors are coated with epoxy. A detailed discussion about the new sensor protection system is contained in the next section.

4.3.2 First Modification to the Sensor Protection System

Based on the discussion in the previous section, a key element of the new sensor protection system was using different epoxy to protect the sensor circuitry from moisture and corrosion. For this purpose, SHEP-Poxy Tx V was chosen and used in the following tests: (a) the epoxy performance test in a corrosive environment, and (b) accelerated corrosion tests of sensors. The test results and the discussion regarding this different epoxy are contained in Sections 4.3.2.1 and 4.3.2.2.

In addition to the application of the different epoxy, the cement paste housing is another key component of the new sensor protection system. As a result, the cement paste housing recommended by Puryear (2007) was revised. The relevant performance tests and improvements are discussed in Section 4.3.2.2.

4.3.2.1 Performance Tests of SHEP-Poxy Tx V Epoxy

SHEP-Poxy Tx V epoxy was chosen as the new waterproof material because it does not absorb water (Table 4.3). Due to this property, the moisture influence on the sensor circuitry could be removed if the sensor components were fully sealed by this epoxy. This could also reduce the likelihood of corrosion occurring within the epoxy housing. In order to avoid the accumulation of chlorides in the vicinity of the sensor and to reduce the likelihood of the cracking of the cement paste housing caused by the thermal expansion of the epoxy, the thickness of the epoxy coating was minimized

and only covered the capacitors and coils in the resonant circuits (Figure 4.9).

Table 4.3 Properties of the SHEP-Poxy Tx V Epoxy (CMC Construction Services Company 2010).

Epoxy Property	Test Method	Test Results
Coefficient of Linear Thermal Expansion	ASTM C531	0.0001 in/in°F
Water Absorption	ASTM C413	0%
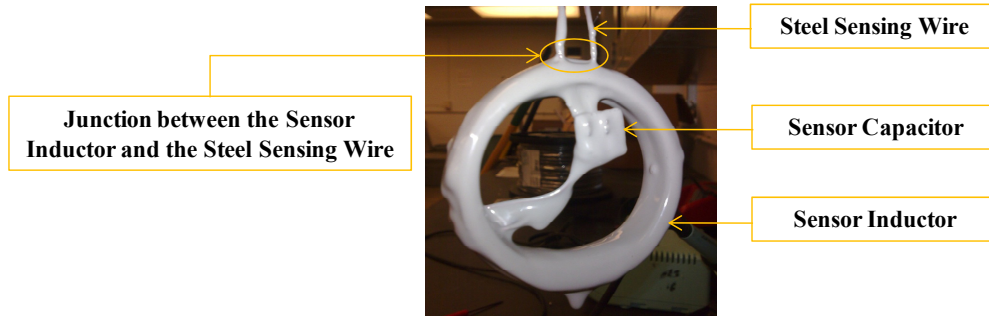
Figure 4.9. Photograph of the thin layer of SHEP-Poxy Tx V covering the coil and capacitor forming the resistant circuit.

To investigate if corrosion will penetrate this new epoxy, ten idealized corrosion sensors were fabricated using a slice of PVC pipe and steel sensing wire. The idealized sensors were coated with thin layers of SHEP-Poxy Tx V epoxy and submerged in a solution of 3.5 % salt water by weight. Since SHEP-Poxy Tx V is a brittle material and the thin coating at the junction between the PVC pipe and steel sensing wire could easily be cracked if the steel sensing wire is bent, the test specimens were divided into two groups before the test. In the first group, the epoxy coating was uncracked. In the second test group, however, intentional cracks were induced in the epoxy at the interface between the PVC pipe and the steel sensing wires.

The experimental setup is shown in the photograph in Figure 4.10. Each specimen was submerged in salt water for four days and then dried in air for three days. The duration of the test was eight, wet/dry cycles. The temperature of the salt water during the test varied from 68˚F to 77˚F.
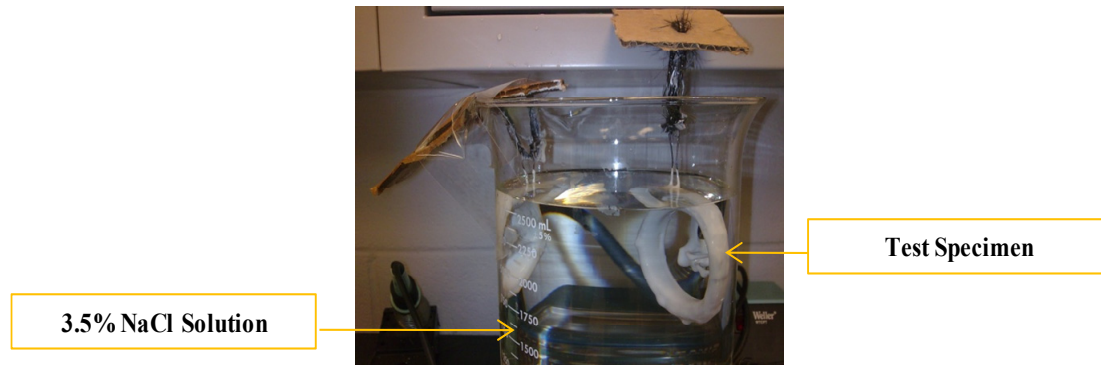
Figure 4.10. Experimental setup used to determine if corrosion products penetrate into the SHEP-Poxy Tx V coating.

After eight weeks, all specimens were checked. Figure 4.11 demonstrates the test results of the first test group in which the epoxy coatings were not cracked. Two characteristics were identified. First, the corrosion reaction only happened on the portions of the steel sensing wires exposed to the salt water (Figure 4.11 left). Second, salt particles were observed on the surface of the epoxy after the test (Figure 4.11) and no cracks or deterioration occurred on the epoxy coating.

Figure 4.12 demonstrates the test results for the second test group in which the epoxy coating of the sensors was cracked intentionally at the junction between the PVC pipe and the steel sensing wire. As in the first test group, salt particles were discovered on the surface of the epoxy after the test and no cracks or deterioration

occurred on the epoxy coating. As for the corrosion of the steel wire, the second group showed corrosion at the intentional crack in addition to corrosion on the exposed steel wires. Therefore, SHEP-Poxy Tx V epoxy, compared with PC-11 marine epoxy, provides a better waterproof environment for the sensor circuitry based on the premise that the epoxy is not cracks.
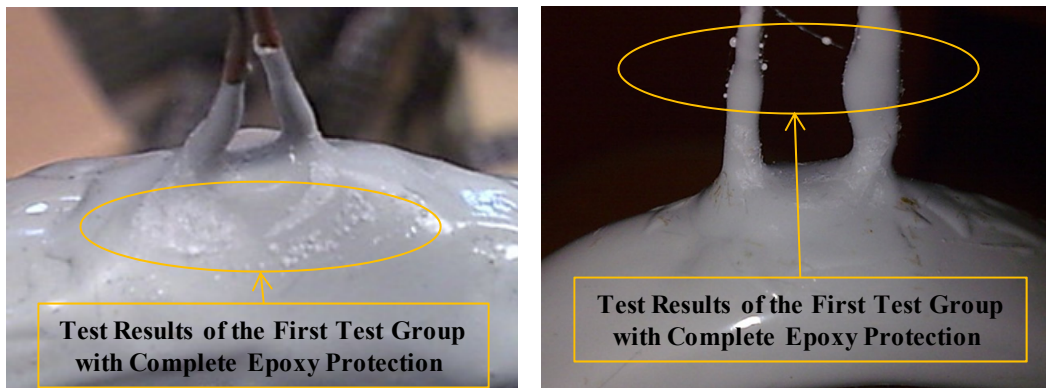
Figure 4.11. Photographs of test results from group with untracked epoxy coating.
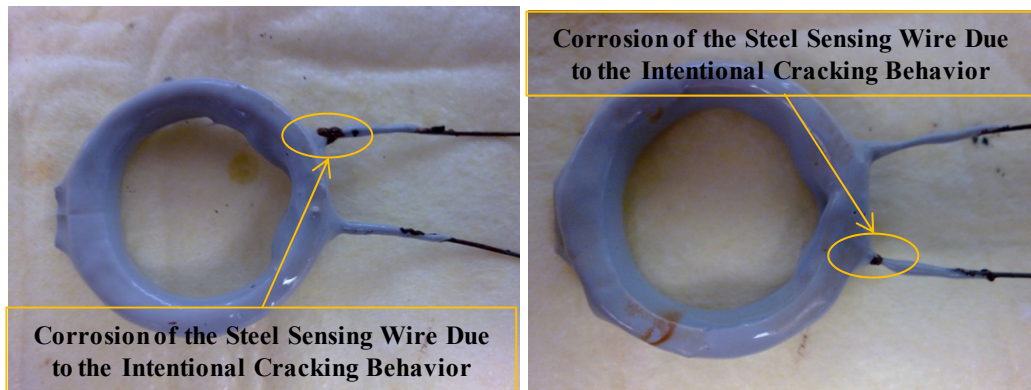
Figure 4.12. Photographs of test results from group with intentional cracks in epoxy coating at the junctions between the steel sensing wires and the PVC pipe.

4.3.2.2 Reduction of Plastic Shrinkage Cracks in the Fiber-Reinforced Cement Paste Housing

In order to understand the performance of the threshold corrosion sensor within the hybrid housing, accelerated corrosion tests were conducted. Section 4.3.2.1 describes this test. Thirty-six threshold corrosion sensors were constructed using the same fiber-reinforced paste housing used by Puryear (2007). The mixture components are listed in Table 4.4 and the molds are shown in Figure 4.13.

The sensors were divided into two groups of 18. The first group contained sensors with fiber-reinforced cement paste housings that covered the epoxy-coated circuit components and the junctions between the steel sensing wire and PVC pipe completely (Figure 4.14 left) completely. The second group contained sensors that were positioned such that the junction between the steel sensing wire and the inductor was not embedded within the cement paste (Figure 4.14 right). The classification of the sensors in terms of the characteristics of the fiber-reinforced cement paste housing is detailed in Table 4.5.

Table 4.4 Mixture Components for Fiber-Reinforced Cement Paste (Puryear 2007).

Component	Amount	Source
Cement	1361 g	
Water	545 g	
Polypropylene Fiber (Fibermesh 500)	5.3 g	Propex Operating Company, LLC
Superplasticizer (product name unknown)	4 ml	Sika Corporation, USA

Figure 4.13. Mold used by Puryear (2007) to fabricate fiber-reinforced cement paste housing (3.5-in. diameter and 1.5-in. high).
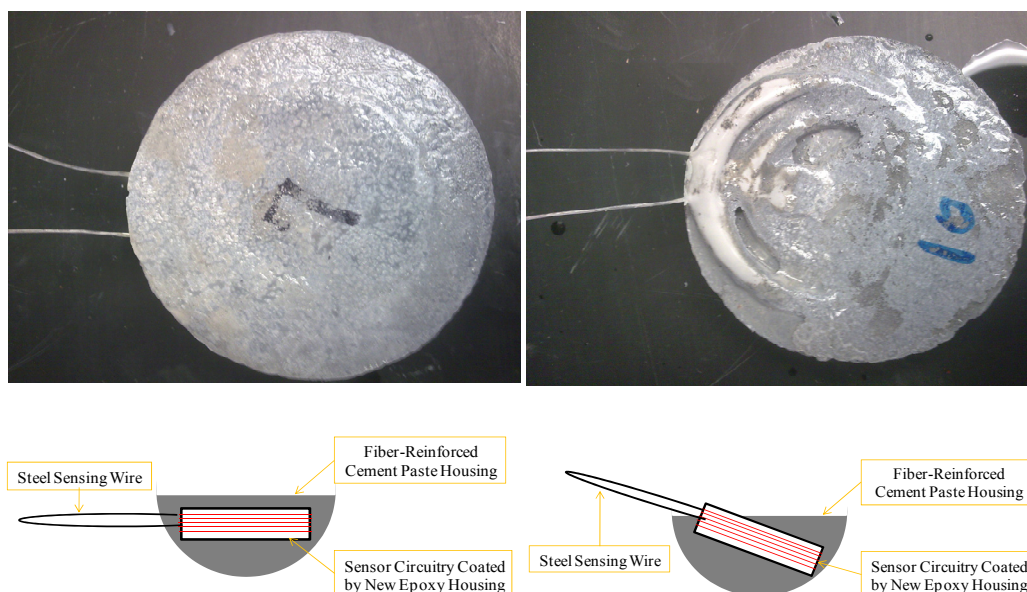
Figure 4.14. Configurations of the two groups of sensors tested to understand the performance of the fiber-reinforced cement paste housing.

Table 4.5 Characteristics of Fiber-Reinforced Cement Paste Housing.

Protection of Steel Wire / Inductor Junction	Sensor No.	Total Quantity
Epoxy and Cement Paste	J001 - J009, J019 - J027	18
Epoxy Only	J010 - J018, J028 - J036	18

According to Puryear (2007), large plastic shrinkage cracks were often observed in the fiber-reinforced cement paste housing. Because the cracks increased the penetration of the chloride ions and moisture into the cement paste housing, it is important to reduce the occurrence of the shrinkage cracks to improve the durability of the sensors.

A common method of reducing the extent of plastic shrinkage cracks is to provide more moisture during curing. In order to develop a recommended curing procedure for the fiber-reinforced cement past housing, the eighteen sensors listed in the first row of Table 4.5 were cured in three different environments: (a) submersion in tap water, (b) submersion in saturated lime water, and (c) storage in an environmental chamber with constant temperature and 100% humidity. Curing times of 7, 14, and 28 days were investigated. The curing conditions for all sensors are listed in Table 4.6.

Table 4.6 Curing conditions for sensors protected by epoxy coating and cement paste housing.

Environmental Conditions during Curing	Duration of Curing		
	7 Days	14 Days	28 Days
Submersion in Tap Water	J005, J006	J003, J004	J001, J002
Submersion in Saturated Lime Water	J026, J027	J009, J025	J007, J008
Environmental Chamber	J019, J020	J021, J022	J023, J024

Table 4.7 summarizes the distribution of widths of the plastic shrinkage cracks observed immediately after the curing period. The widths of the plastic shrinkage cracks were less than 0.02 in. for all sensors with curing times of 14 days or longer. In addition, the widths of plastic shrinkage cracks were less than 0.005 in. for the sensors that were cured in saturated lime water and in the environmental chamber for 28 days. Based on these results, a 28-day curing period was established for the fiber-reinforced cement paste housing designed by Puryear (2007) and 0.005 in. was established as the maximum acceptable width of the plastic shrinkage cracks. Photographs of the shrinkage cracks after 7, 14 and 28 days of curing are shown in Figure 4.15.

Table 4.7 Distribution of widths of plastic shrinkage cracks.

Crack Size	Tap Water			Saturated Lime Water			Environmental Chamber		
	7 days	14 days	28 days	7 days	14 days	28 days	7 days	14 days	28 days
> 0.02 in.	2			1			1		
0.005 ~0.02 in.		1	1	1	1		1	1	
< 0.005 in.		1	1		1	2		1	2
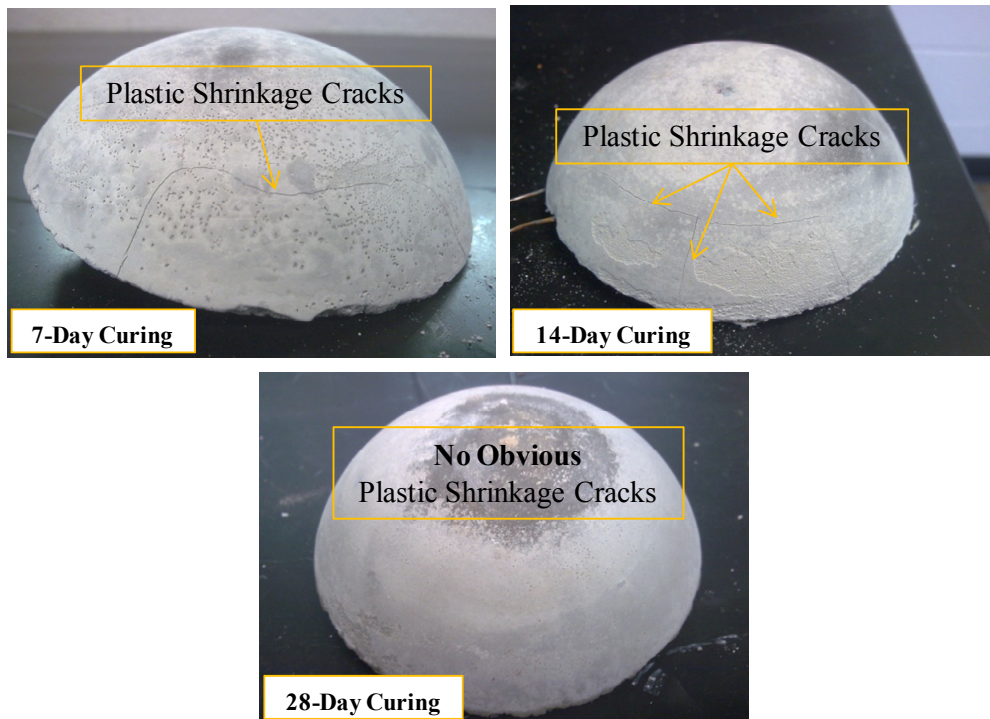
Figure 4.15.Observed plastic shrinkage cracks for Sensors J027 (top-left), J009 (top-right) and J007 (bottom).

Because the entire sensor, including the steel sensing wire, is exposed to moisture during the curing period for the fiber-reinforced cement paste housing, possible corrosion of the steel sensing wire is a concern. The saturated lime water environment was the only curing environment in which the steel sensing wire did not corrode during curing, because a passive layer was formed on the surface of the steel wire in this high pH environment. Corrosion was observed on the surface of the wires for sensors that were submerged in tap water and stored in an environmental chamber. Therefore, saturated lime water is recommended as an appropriate curing environment for the fiber-reinforced cement paste housing.

After curing, the sensors were subjected to an accelerated corrosion test. The duration of the accelerated corrosion test was 106 days. A solution of 3.5% salt by weight was used to simulate the extreme corrosive environment. A three-day dry cycle followed by a four-day wet cycle was implemented in this test. The sensors were interrogated at the beginning of the test and at each end of the wet/dry cycle using a read distance of 0 in. The interrogation process, however, was stopped once each of the sensing wires corroded and fractured. Following the test, the cement paste housings were removed to examine the condition of the steel sensing wire.

The frequency responses of each sensor during the accelerated corrosion tests are summarized in Appendix B. Uniform corrosion was observed on the exposed sensing wires of all sensors (Figure 4.16). For 12 of the 18 sensors, the steel sensing wires fractured at the exterior face of the cement paste housing (Table 4.8 and Figure 4.17). For the remaining six sensors, the steel sensing wires fractured along the free length (Figure 4.18).
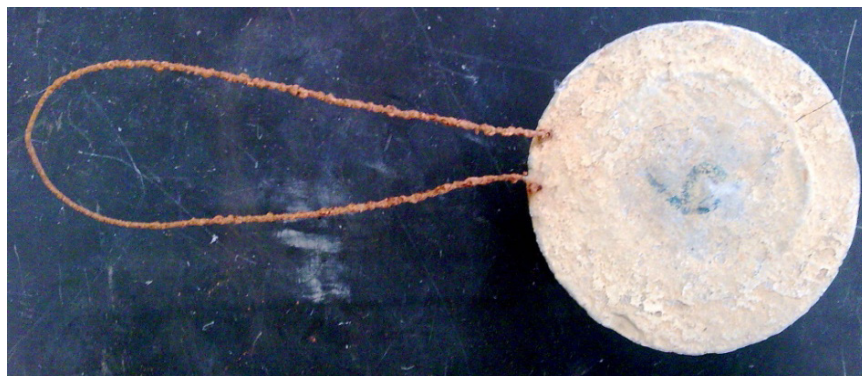
Figure 4.16. Photograph of the uniform corrosion of the steel sensing wire in sensors covered by cement paste housing (Sensor J006).

Table 4.8 Locations of Fractured Sensing Wires.

Location of Sensing Wire Fracture	Sensor No.	Total Quantity
Exterior Face of Cement Paste Housing	J001-J004, J006-J009, J022-J025	12
Other Locations	J005, J019-J021, J026, J027	6

Figure 4.17. Steel sensing wire fractured at the outer face of the cement paste housing for Sensor J002.

Figure 4.18. Steel sensing wire fractured along the free length (Sensor J027).

When the cement paste housing was removed, evidence of corrosion within the cement paste housing was observed. Nine sensors experienced slight corrosion of the steel sensing wire, which did not extend to interface with the epoxy coating (Figure

4.19 left). The corrosion was uniform within the cement paste housing and penetrated to the interface with the epoxy for the other nine sensors (Figure 4.19 right). These results indicate that the cement paste housing provides a level of corrosion protection for the steel sensing wire but only delays the initiation of corrosion rather than preventing it.
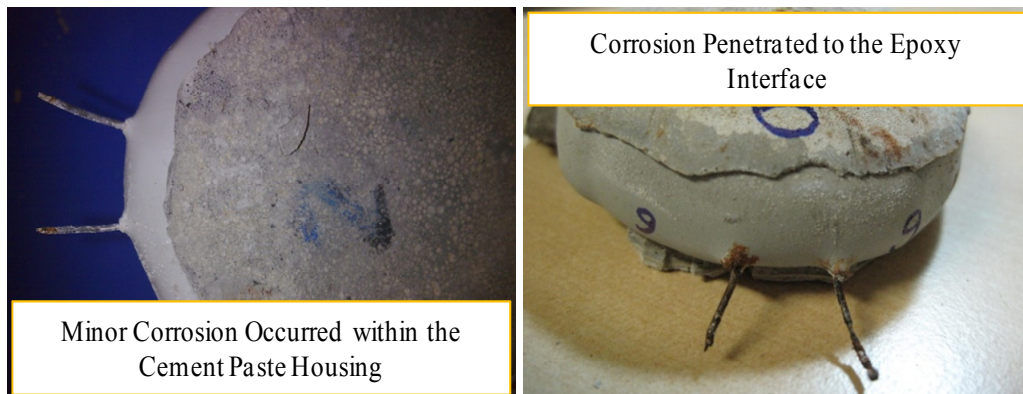
Figure 4.19. Observed corrosion of steel sensing wire within cement paste housing (Sensor J002 (left) and J006 (right)).

Table 4.9 summarizes the observed corrosion within the cement paste housing based on the curing conditions. The sensors that experienced wider plastic shrinkage cracks during curing were more likely to experience penetration of the corrosion to the epoxy interface. Curing in saturated lime water promoted the development of the passive layer on the steel sensing wire, which seemed to delay the onset of corrosion within the cement paste housing.

Table 4.9 Sensitivity of observed corrosion within cement paste housing to curing conditions.

Observed Corrosion	Curing Environments								
	Tap Water			Saturated Lime Water			Environmental Chamber		
	7-day Curing	14-day Curing	28-day Curing	7-day Curing	14-day Curing	28-day Curing	7-day Curing	14-day Curing	28-day Curing
Within the Cement Paste Housing		1	2		2	2			2
Penetration to Epoxy Interface	2	1		2			2	2	

Figure 4.20 illustrates the condition of the cement paste housings after the accelerated corrosion tests. Cracks and spalling of the cement paste housing were observed. Three possible reasons for these observations were identified. First, the cement paste housing was very thin in some places and the cracks were located in these places (Figure 4.21 left). This implies that the size of the mold that Puryear (2007) used is too small. Second, there was no bond between the cement paste housing and the epoxy coating (Figure 4.21 right). Third, some evidence of deterioration of the cement paste housing was observed during the accelerated corrosion test (Figure 4.20 (bottom) and Figure 4.16).

Crack in the Cement Paste Housing

Spall of the Cement Paste Housing

Spall of the Cement Paste Housing

Figure 4.20. Photographs of cement paste housing at conclusion of accelerated corrosion test (Sensors J024 (top-left), J019 (top-right) and J003 (bottom).

Thin Layer of Cement Paste Housing

No Bond between the Cement Paste Housing and Epoxy Coating

Figure 4.21. Photographs of the interface between the cement paste housing and the epoxy coating (Sensors J006 (left) and J027 (right)).

After removing the cement paste housing, another concern was identified. Cracks formed in the epoxy at the interface with the steel sensing wire (Figure 4.22 left). These cracks in the epoxy were discovered in all 18 sensors. During fabrication, the steel wire was bent (Figure 4.22 right), and it is believed that the cracks formed at this time. Although some of the sensing wires did not corrode within the epoxy, these cracks need to be prevented because cracks in the epoxy provide a path for the chlorides and moisture to penetrate into the sensor (see Section 4.3.2.1) and creates the possibility that corrosion will develop within the epoxy coating.
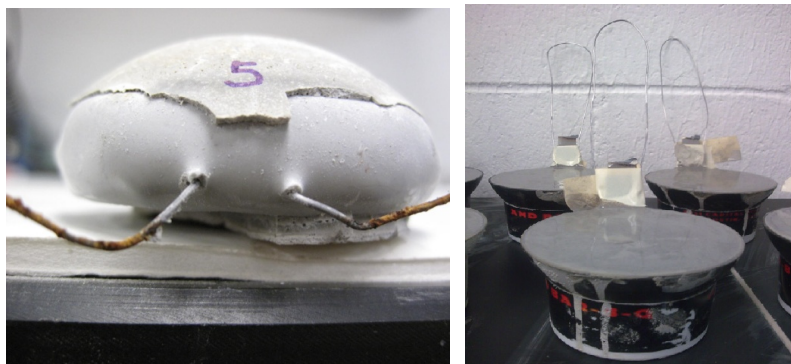
Figure 4.22. Cracks appeared in the epoxy at the interface with the steel sensing wire (left) due to the process used to fabricate the cement paste housing (right).

A second group of sensors, in which the epoxy/steel interface was not embedded within the cement paste housing (Figure 4.14 right and Table 4.5), were also subjected to accelerated corrosion tests. Uniform corrosion developed along the free length of the steel sensing wires, but the fracture occurred at the epoxy/steel interface in all 18 cases (Figure 4.23).

In order to investigate the extent of corrosion within the epoxy coating, part of

the epoxy coating around the steel sensing wire was removed (Figure 4.24 right). It was observed that the corrosion products only appeared on the surface of the epoxy housing, but did not penetrate into epoxy. This finding illustrates that SHEP-Poxy Tx V epoxy prevents moisture from penetrating inside the epoxy coating.

Figure 4.23. Uniform corrosion of the steel sensing wire for sensors that were not completely encased in the cement paste housing (Sensor J012).
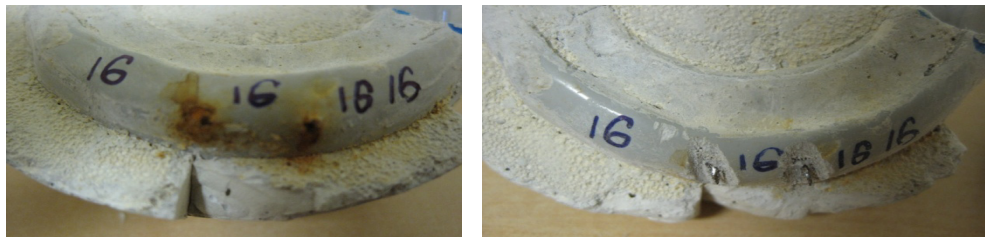
Figure 4.24. Corrosion of the steel sensing wire did not penetrate into the epoxy housing (Sensor J016).

The frequency responses of all 36 sensors tested during the accelerated corrosion test are plotted in Appendix B.2. Because the sensor interrogation process was stopped after fracture of the steel sensing wire, the number of data points collected for each sensor varied. Figure 4.25 demonstrates the variation of the response of Sensor

J003 during the accelerated corrosion test. As shown, the phase dip for the sensing circuit varied during the tests. However, the corresponding pseudo-quality factors were fairly constant.
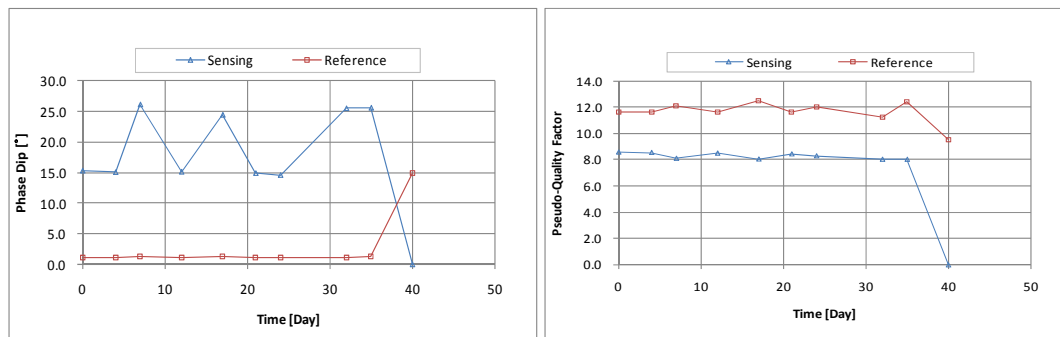
Figure 4.25. Variation of sensor responses in sensor j003 during the first accelerated corrosion test: phase dip (left) and pseudo-quality factor (right).

Based on the results of the first accelerated corrosion test, three significant improvements were made to enhance the durability of the sensor:

1. Cracks did not form on the surface of the SHEP-Poxy Tx V epoxy and there was no evidence of penetration of moisture or corrosion products into the epoxy. The SHEP-Poxy Tx V Epoxy is considered to provide better protection for the circuit components than the PC-11 marine epoxy.

2. Cement paste housing reduces the likelihood that the steel sensing wire will fracture due to corrosion at the epoxy/steel interface.

3. Saturated lime water is the best curing environment for the cement paste housing. A 28-day curing period is recommended to minimize the plastic shrinkage cracks.

88

However, six problems remain and need to be addressed:

1. The fracture of the steel sensing wire due to corrosion usually occurs at the outer surface of the cement paste housing.

2. The cement paste housing delays, but does not prevent, corrosion of the steel sensing wire within the cement paste housing.

3. Cement paste housings fabricated with the mixture proportions recommended by Puryear (2007) deteriorate in a solution of 3.5% salt water by weight.

4. The mold that Puryear (2007) used to fabricate the cement paste housing is too small. Cracking often occurred at locations where thin layers of the cement paste housing existed. It is important to reduce cracking to minimize penetration of moisture and contaminants into the cement paste housing.

5. Due to limitations of the mold, the steel sensing wire needs to be bent during the fabrication of the cement paste housing. This cracks the epoxy at the interface between the steel sensing wires and provides a possible pathway for chlorides and moisture to penetrate into the sensor.

6. The bond between the cement paste housing and the epoxy coating is essentially zero.

4.3.3 Second Modification of the Sensor Protection System

The test results of the first accelerated corrosion test demonstrate the potential of the hybrid system for enhancing the durability of the threshold corrosion sensor. However, the results also identify areas for improvements. Improvements are proposed in Sections 4.3.3.1 and 4.3.2.2 to address the problems discovered in the first accelerated corrosion test. The related performance tests for the proposed design are illustrated in these two sections. Furthermore, to understand the performance of the modified sensor protection system, a second accelerated corrosion test was conducted. Details of those tests are presented in Section 4.3.3.3.

4.3.3.1 Improvements in the Cement Paste Housing

4.3.3.1.1 Mold for Housing

The investigation revealed that plastic shrinkage was not the only cause of the cracks within the cement paste housing. The photographs in Figure 4.5 demonstrate that the diameter of the circular crack on the bottom of the cement paste housing matches the diameter of the outer sensing coil. This implies that the outer sensing coil was in contact with the surface of the cement paste housing (Figure 4.26) and means that Puryear's mold (2007) was too small. In order to improve this, a larger mold was used to fabricate the cement paste housing.

The thickness of the cement paste housing covering the epoxy coating was the key point in determining the size of the mold. Figure 4.27 illustrates that, if the thickness of the cement paste housing is insufficient, spalling of the cement paste housing will occur. To determine the minimum required thickness, six epoxy-coated sensors were fabricated with different thicknesses of cement paste housings. The thicknesses of the housings ranged from 1 mm. to 6 mm. To accelerate the development of cracks on the cement paste housing, after 28 days of curing in saturated lime water, the cement paste housings were exposed to temperature variations. During each seven-day thermal cycle, the sensors were submerged in hot water (approximately 140 $^{\circ}$F) for three days and in ice water (approximately 50 $^{\circ}$F) for four days until cracks occurred. After three thermal cycles, each sensor experienced crack widths of at least 0.005 in. Spalling was also observed in the cement paste housings with minimum thicknesses of 1, 2, and 3 mm (Table 4.10), while the housings with minimum thicknesses of 4 mm or larger remained intact. The potting mold selected for all subsequent sensor tests is shown in Figure 4.28 and provided a minimum thickness of 4 mm. for the cement paste housing.

Slice of PVC Pipe is Contact with the Mold
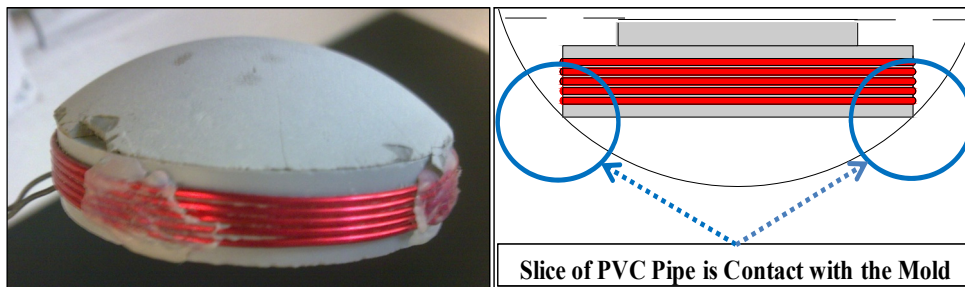
Figure 4.26. Case of circular cracks on the bottom of the cement paste housing.

Figure 4.27. Observed spalling of cement paste cover (Sensor J005).

Table 4.10 Sensitivity of spalling to thickness of cement paste housing.

Thickness of Cement Paste Housing	1 mm	2 mm	3 mm	4 mm	5 mm	6 mm
Condition of Cement Paste	◯	◯	◯	X	X	X

◯: Cement Paste is Spalling   X: Cement Paste is Intact
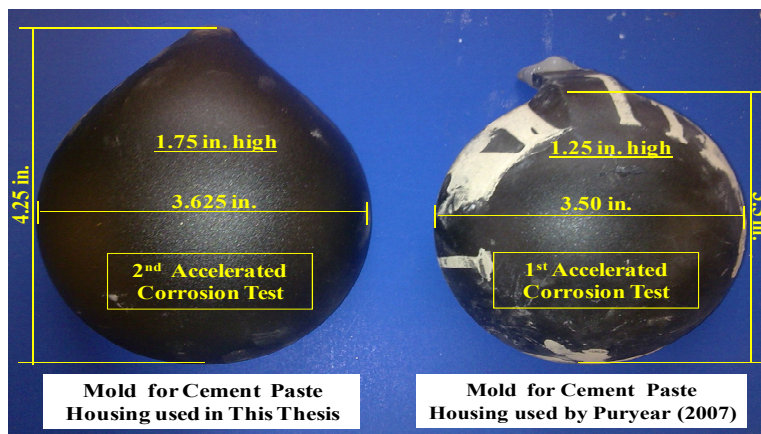
Figure 4.28. Photograph of the molds used in this thesis (left) and by Puryear (2007) (right).

In addition to choosing an appropriate mold for the fabrication of the cement paste housing, it is also important to develop a procedure to fabricate the sensor without bending the steel sensing wire after the epoxy coating has been applied. As shown in Figure 4.22, if the steel wire is bent during potting, the epoxy coating will crack, which provides a pathway for moisture and chloride ions to penetrate into the

sensor. Therefore, the new mold was modified by cutting two grooves to allow the steel sensing wire to pass through the mold without bending the wire (Figure 4.29).

Figure 4.29. Two grooves in the new mold (left) allow the potting to proceed without bending the steel sensing wire (right).

4.3.3.1.2 Enhanced Bond between Epoxy and Cement Paste

Different coefficients of thermal expansion between the cement paste and epoxy can cause cracking within the cement paste housing. Creating an interface that can transfer bond stresses, however, would reduce this problem and reduce the cracks caused by the different coefficients of thermal expansion for these two materials.

Figure 4.30 demonstrates the lack of bond between the cement paste and epoxy in specimens tested during the first accelerated corrosion test. Once cracks formed, the cement paste housing broke into pieces. If bond stresses could be transferred across the interface, the housing would remain intact.

Figure 4.31 illustrates three proposed methods to increase the surface roughness of the epoxy, and thereby increase the bond stress that can be transferred across the interface: (a) modifying the surface of the epoxy by cutting grooves, (b) applying glue to the surface of the epoxy and (c) using sand to cover the surface of the epoxy. Nine sensors were constructed using the three proposed methods. The sensors were subjected to alternating wet and dry cycles in salt water for four months. The cement paste housings were fabricated according to the mixture components (Table 4.4) recommended by Puryear (2007). The results are summarized in Table 4.11 and indicate that spalling did not occur when sand was applied to the surface of the epoxy.

Figure 4.30. Photograph of cement paste housing at the conclusion of the first accelerated corrosion test (Sensor J006).

Modify the Surface of Epoxy Housing	Use Glue to Make the Surface of the Epoxy Housing Uneven	Use Sand to Cover the Surface of Epoxy Housing

Figure 4.31. Three methods used to increase the roughness of the epoxy coating.

Table 4.11 Sensitivity of spalling to surface of epoxy.

Condition of Cement Paste after the Accelerated Corrosion Test	Ways to Modify the Surface of Epoxy Housing		
	Modified Surface	Glue	Sand
Well-bonded	1	1	3
Observed Spalling	2	2	0

4.3.3.1.3 Revised Mixture Proportions for Fiber-Reinforced Cement Paste

The ideal cement paste housing has fine plastic shrinkage cracks, sufficient compressive strength to protect the sensor during construction, and low permeability to minimize the penetration of moisture and contaminants into the sensor housing. These three objectives were achieved by revising the mixture components to reduce the cement content and by adding polypropylene fibers to keep any cracks closed.

One of the goals for this new cement paste housing was to limit the crack widths in the sensor housing to 0.005 in. After several adjustments, the revised mixture components for the fiber-reinforced cement paste housing were selected (Table 4.12).

Table 4.12 Revised mixture components for fiber-reinforced cement paste.

Component	Amount	Source
Cement	140 g	Sika Corporation, USA
Sand	140 g	-
Water	50 g	-
Polypropylene Fiber (Fibermesh 500)	2 g	Propex Operating Company, LLC
Polypropylene Fiber (Fibermesh 150)	1 g	Propex Operating Company, LLC
Superplasticizer (Sika Plastiment)	1 ml	Sika Corporation, USA

To characterize the shrinkage properties of this revised mixture, 28 epoxy-coated sensors embedded within cement paste housings were fabricated and cured for 7 days in air. After curing, the plastic shrinkage cracks in each sensor were measured. The test results are summarized in Table 4.13 and indicate that 24 of the 28 cement paste housings experienced plastic shrinkage cracks with maximum widths of 0.005 in. Comparisons of the plastic shrinkage cracks in the cement paste housings fabricated by Puryear (2007) and using the revised mixture components are shown in Figure 4.32.

Table 4.13 Maximum widths of plastic shrinkage cracks in cement paste housings using revised mixture components after curing for 7 days in air.

Crack size	Number of Sensors
> 0.01 in.	1
0.005 ~0.01 in.	3
< 0.005 in.	24

Mixture Components of the Cement Paste Recommended by Puryear (2007)	**Mixture Components of the Cement Paste Recommended by This Thesis**
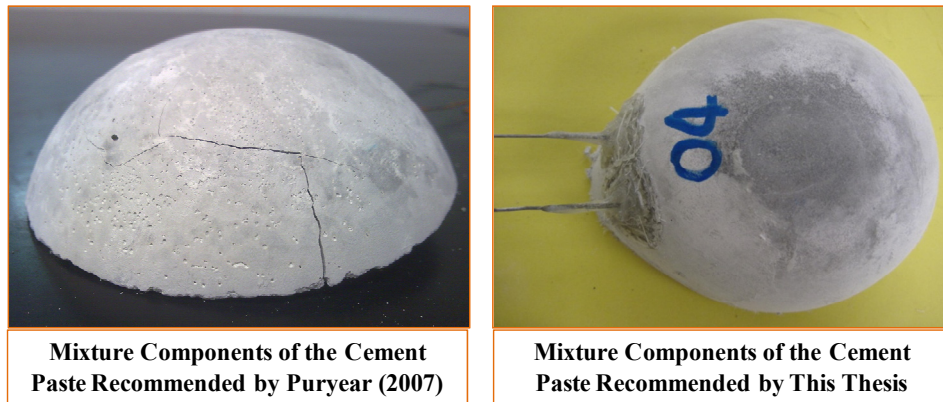
Figure 4.32. Photographs of the plastic shrinkage cracks in the cement paste housings using the mixture proportions recommended by Puryear (2007) (left) and by this thesis (right) after curing for 7 days in air.

In addition to the test described above, the influence of the curing conditions on the revised mixture proportions was also evaluated. For this test, 18 epoxy-coated sensors embedded in cement paste housings were tested. The environmental conditions and testing plan were identical to those described in Section 4.3.2.2. The test results are summarized in Table 4.14 and demonstrate that all 18 sensors achieved the goal of limiting the width of plastic shrinkage cracks to less than 0.005 in. This means that the curing time can be reduced to 7 days.

Table 4.14 Distribution of plastic shrinkage crack widths for varying curing conditions.

Crack Size	Tap Water			Saturated Lime Water			Environmental Chamber		
	7 days	14 days	28 days	7 days	14 days	28 days	7 days	14 days	28 days
> 0.01 in									
0.005 ~0.01 in									
< 0.005 in	2	2	2	2	2	2	2	2	2

The compressive strength of the cement paste was determines testing three, 2 x 4-in. cylinders. The cylinders were cored for 28 days in lime water and then tested in compression. The average compressive strength at 28 days was 2000 psi.

4.3.3.2 Measures to Improve Sensor Performance

Steps were taken to address two other issues that were identified from the first accelerated corrosion test. First, corrosion of the steel sensing wire within the cement paste housing was observed. Second, the steel sensing wire tended to fracture at the

interface with the cement paste housing, which may influence the threshold level of corrosion for the sensor.

In order to correct the first problem, rosin-core silver-bearing solder was applied to the surface of the steel sensing wire within the cement paste housing. The detailed discussion is presented in Section 4.3.3.2.1.

In order to solve the second problem, glue was introduced. Compared to the full protection of the other protection measures, the glue was used to avoid the high concentration of the chlorides around the junction between the cement paste housing and the steel sensing wire. The discussion of the glue is contained in Section 4.3.3.2.2.

4.3.3.2.1 Rosin-Core Silver-Bearing Solder for Corrosion Protection

As discussed in Section 2.2, the design of threshold corrosion sensor is based on the assumption that the steel sensing wire is subjected to the same level of contaminants as the reinforcement in the surrounding concrete. However, the results could be skewed if corrosion also occurs within the cement paste housing. Therefore, in order to reduce the likelihood of corrosion within the cement paste housing, rosin-core silver-bearing solder (62% tin, 36% lead, 2% silver) was used to coat the surface of the steel sensing wire within the cement epoxy housing. A small part of the steel sensing wire exposed in the environment was also coated to reduce the likelihood of corrosion being concentrated at the face of the cement paste housing

(Figure 4.33).

Figure 4.33. Photograph showing the solder coating on the surface of sensing wire.

The reason that rosin-core silver-bearing solder was used as a coating material is because tin forms a stable compound, tin dioxide, which protects the inner metal from being attacked by airborne corrosive agents (Tan 1989). Even in a 3.5% NaCl solution, the outer tin-rich layer provides sufficient protection for the base metal (Li et al. 2008). However, this does not mean that the steel sensing wire will be permanently protected by the solder. Because once the outer tin-rich layer has deteriorated, the inner lead-rich layer will not provide much corrosion protection to the steel wire (Li et al. 2008; Manko 2001).

Furthermore, according to the galvanic compatibility of metals listed in the *Handbook of Corrosion Engineering* (Roberge 2000), when the difference of anodic index between two connected metals is less than or equal to 0.25 V, the combination of these two metal alloys is not susceptible to galvanic corrosion if the alloy is not exposed directly to moisture variations. However, if alloy is stored in a harsh environment, such as exposure to high humidity and salt, the difference of anodic index between two connected metals must not exceed 0.15 V to avoid galvanic

corrosion.

The anodic index of the low-alloy steel is 0.85 V while the anodic index of the lead-tin solder is 0.65 V. Therefore, the difference of the anodic index between the steel sensing wire and the rosin-core silver-bearing solder (lead-tin solder) is 0.2 V which is beyond the critical value for these two metal alloys in the salt water environment.

Two performance tests were conducted in order to evaluate the ability of rosin-core silver-bearing solder to protect the steel sensing wire from corrosion. First, the corrosion response of six bare steel wires coated with the rosin-core silver-bearing solder at their ends (3 cm of coating at each end) were evaluated (Figure 4.34 left). In this test, a solution of 3.5 % salt water concentration by weight was used to simulate the harsh environment. The duration of the test was 168 days with a three-day dry cycle followed by four-day wet cycle. After 168-day test, each of the steel wires was checked. No corrosion was observed within the coating area (Figure 4.34 right). In addition, no significant corrosion behavior or fracture of the steel wire at the junction between the bare steel wire and coating area was found. This indicated that the rosin-core silver-bearing solder could protect the steel wire from corrosion in a solution of 3.5 % salt water concentration by weight.

Second, in order to evaluate the corrosion response of the coated steel sensing wires within the cement paste housing, four PVC slices with coated steel wires were

encased in the cement paste housings and were tested in a solution of 3.5% salt water concentration with a three-day dry cycle followed by four-day wet cycle for 133 days. The cement paste housing was removed at the end of the test to observe the corrosion. Figure 4.35 shows a representative specimen after the autopsy. No corrosion was observed within the cement paste housing where the steel wire was coated with solder. This indicates that, in a high pH environment (i.e. the cement paste housing), the rosin-core silver-bearing solder coating provides a stable corrosion protection for the steel wire.
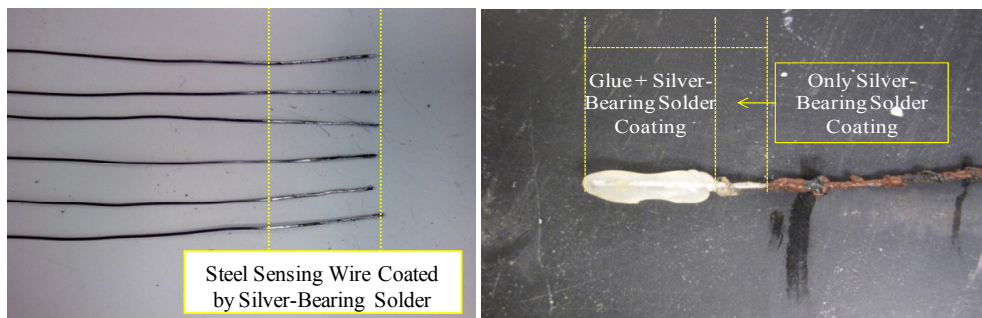
Figure 4.34. The bare steel wire coated with silver-bearing solder at its end (left) and the testing result for its corrosion protection (right).
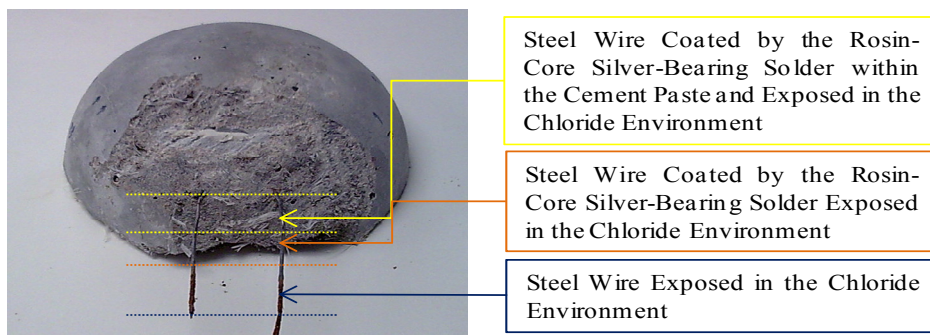
Figure 4.35. Observed the corrosion of steel wires coated with solder within the cement paste housing.

4.3.3.2.2 Use of Glue for Corrosion Protection

Although the rosin-core silver-bearing solder coating protected the steel sensing wire from corrosion within the cement paste housing and with exposed to chlorides, it still could not stop the higher concentration of chloride ions around the interface between the cement paste housing and steel sensing wire. In order to avoid the extreme case that the dense tin-rich layer of the solder coating deteriorated and the steel sensing wire corroded at the interface with the cement paste housing, a small amount of glue was used to coat the steel wire at the interface with the cement paste housing (Figure 4.36).
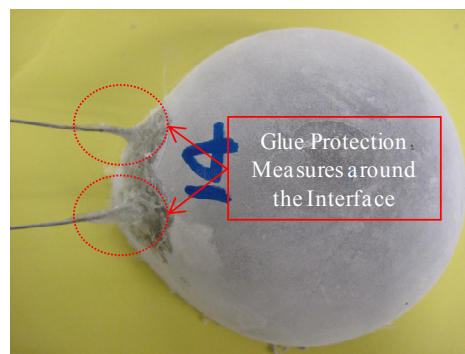
Figure 4.36. Steel sensing wire was coated with glue at the interface with the cement paste housing.

To test the feasibility of this idea, a cement paste block was constructed with a loop of steel wire. Glue was used to coat the wire at the interface with the cement paste. Ten specimens were subjected to four-day wet and three-day dry cycles on 3.5% salt water concentration by weight. The duration of the test was 90 days. Typical test results are shown in Figure 4.37. Corrosion of the steel wire within the

glue was much less than portions of the wire that were directly exposed in the chloride environment. This indicates that applying the glue at the interface between the cement paste housing and steel sensing wire is workable. However, it needs to be noted that the design might cause another interface corrosion problem between the steel wire and the glue.
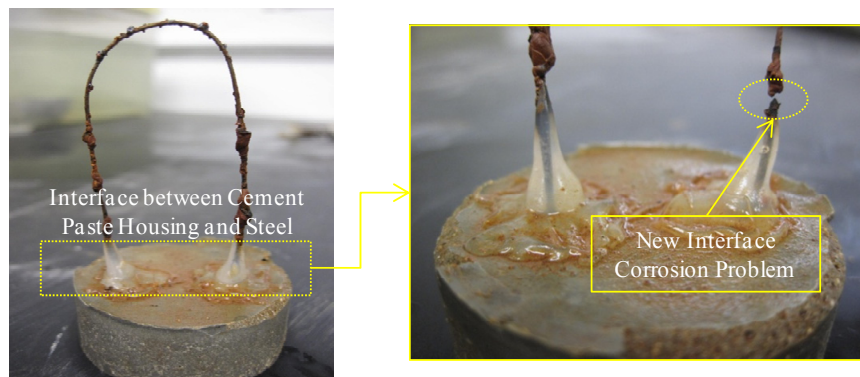
Figure 4.37. Use of glue to avoid fracture of steel sensing wire at interface with cement paste.

4.3.3.3 Second Accelerated Corrosion Test

A second accelerated corrosion test was conducted to evaluate the performance of the revised protection system for the threshold corrosion sensor. Twenty-eight sensors were used in this test and all were constructed using the modifications discussed in this section (Figure 4.38):

- SHEP-Poxy Tx V epoxy coating of circuit components
- Sand coating on surface of epoxy to improve bond characteristics

- Larger mold with slits to avoid bending the steel sensing wire

- Revised mixture of fiber-reinforced cement paste (Table 4.12)

- Silver-bearing solder coating on steel sensing wire within cement paste housing and along the transition to the free length

- Glue coating on steel sensing wire at the interface with the cement paste housing

- 7-day curing in saturated lime water. Widths of plastic shrinkage cracks were less than 0.005 in. at end of curing period

All specimens were subjected to alternating wet and dry cycles in salt water. A three-day dry cycle was followed by a four-day wet cycle. Sensors were interrogated after each cycle until the steel sensing wire fractured due to corrosion. The primary experimental variables are summarized in Table 4.15:

- Four different salt water concentrations, ranging from 2% to 8% by weight, were used.

- Six sensors were fabricated using X7R capacitors, while 22 sensors were fabricated using COG capacitors.

- The epoxy coating at the interface with the steel sensing wire was intentionally cracked for six sensors. The coating was intact for the remaining 22 sensors.

104
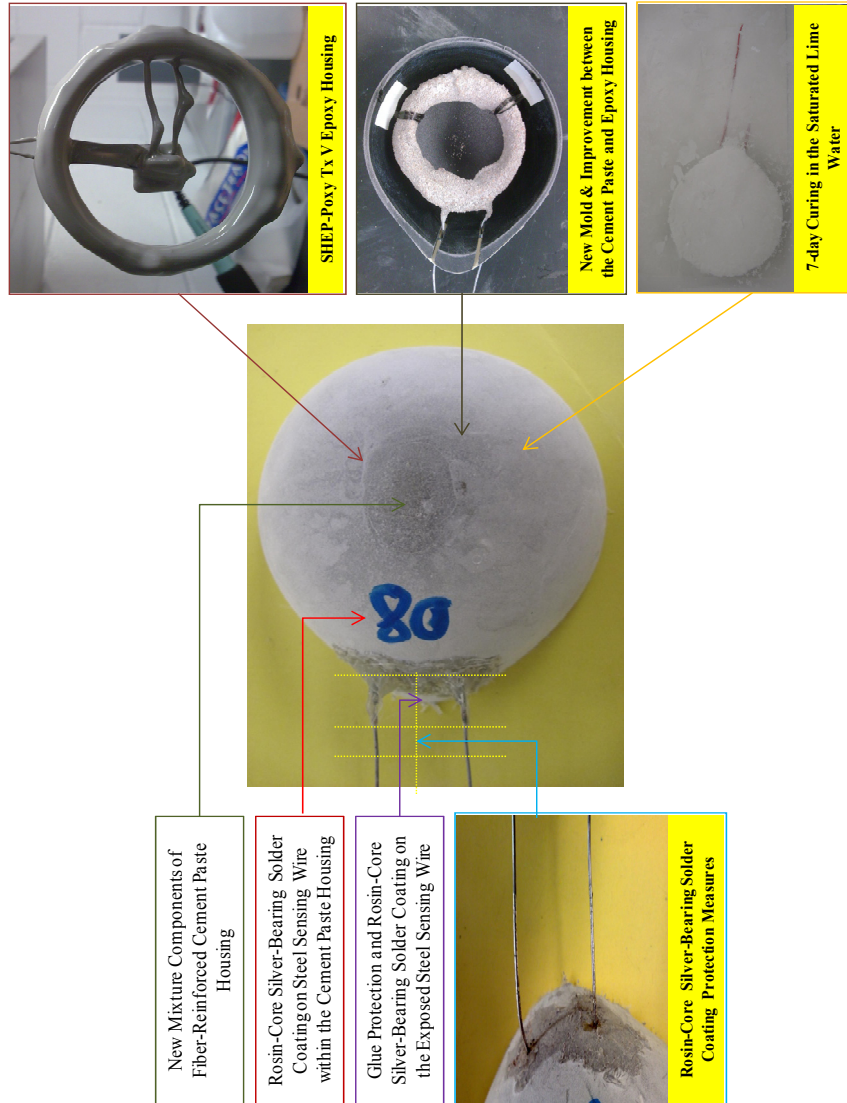
Figure 4.38. Configuration of sensors tested during the second accelerated corrosion test.

Table 4.15. Overview of experimental matrix for second accelerated corrosion test.

Sensor	Type of Capacitors		Salt Water Concentration				Condition of Epoxy	
	COG	X7R	2.00%	3.50%	6.00%	8.00%	Uncracked	Cracked
N001	X			X			X	
N002	X			X			X	
N003	X			X			X	
N004		X		X				X
N005	X			X			X	
N006	X			X			X	
N007	X			X			X	
N008	X			X			X	
N009	X			X			X	
N010	X			X			X	
N011		X		X				X
N012		X		X			X	
N013		X	X					X
N014	X		X					X
N015	X		X				X	
N016	X		X				X	
N017		X			X			X
N018	X				X		X	
N019		X			X			X
N020	X				X		X	
N021	X					X	X	
N022	X					X	X	
N023	X					X	X	
N024	X					X	X	
N025	X			X			X	
N026	X			X			X	
N027	X			X			X	
N028	X			X			X	
Total Quantity	22	6	4	16	4	4	22	6

4.3.3.3.1 Observation from the Second Accelerated Corrosion Test

The second accelerated corrosion test began on October 19, 2009 and concluded 133 days later at the end of February 2010. At this time, the sensing wires in 15 of the 28 sensors had fractured due to corrosion (Table 4.16). Although the sensors were not interrogated beyond this date, the wet/dry cycles conditions until all sensing wires fractured.

Table 4.16 (a). Observed Condition of Steel Sensing Wire at Conclusion of Second Accelerated Corrosion Test.

Sensor	Salt Water Concentration	Location of Fracture			Time to Wire Fracture (Days)
		Along Free Length	Interface with Solder	Interface with Glue	
N001	3.50%	X			94
N002	3.50%	X			73
N003	3.50%	X			73
N004	3.50%	X			73
N005	3.50%		X		151
N006	3.50%	X			76
N007	3.50%	X			63
N008	3.50%	X			138
N009	3.50%	X			125
N010	3.50%	X			143
N011	3.50%	X			63
N012	3.50%	X			69
N013	2.00%	X			178
N014	2.00%	X			167
N015	2.00%	X			182
N016	2.00%	X			190

Table 4.16 (b). Observed Condition of Steel Sensing Wire at Conclusion of Second Accelerated Corrosion Test.

Sensor	Salt Water Concentration	Location of Fracture			Time to Wire Fracture (Days)
		Along Free Length	Interface with Solder	Interface with Glue	
N017	6.00%		X		94
N018	6.00%	X			87
N019	6.00%		X		94
N020	6.00%	X			76
N021	8.00%		X		94
N022	8.00%	X			118
N023	8.00%	X			76
N024	8.00%		X		73
N025	3.50%	X			164
N026	3.50%	X			151
N027	3.50%	X			145
N028	3.50%	X			168
Total Quantity		23	5	0	

A representative example of the condition of the steel sensing wire at the conclusion of the accelerated corrosion test is shown in Figure 4.39. Uniform corrosion was observed on the surface of the exposed steel sensing wire, except for the portion that was covered with the solder. No corrosion was observed at the interface with the cement paste housing. The location of the fracture is also indicated in Table 4.15. It appears that galvanic corrosion between the solder and steel wire was not a factor in the lower concentrations of salt water. However, corrosion did occur at the solder/wire interface for salt water concentrations of 6 and 8%. Close examination of Sensor N019 (Figure 4.40) indicates that corrosion did occur within the region coated by the solder.

In this case, it is likely that initial defects were present in the solder coating.

Following the accelerated corrosion test, the cement paste housings were removed to examine the condition of the steel sensing wire within the housing. No evidence of corrosion was observed within this region (Figure 4.41). However, corrosion was observed at the interface between the solder-coated steel wire and the epoxy coating in for Sensor N019 (Figure 4.42). This was likely caused by the initial cracks in the epoxy housing.

The revised mixture design for the cement paste housing performed well during the accelerated corrosion tests. No spalling of the cement paste housing or additional cracks were observed. Slight discoloration of the surface of the cement paste housing was observed for sensors exposed to the higher concentrations of salt water (Figure 4.43), but no damage was detected for salt water concentrations of 2.0 and 3.5% (Figure 4.44).

Figure 4.45 demonstrates that the sand on the surface of the epoxy coating improved the bond between the epoxy and the cement paste housing. No evidence of relative movement between the two materials was observed.
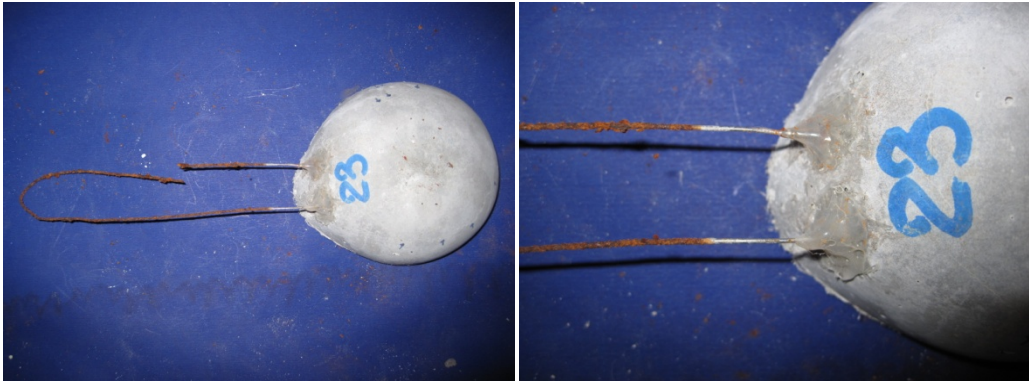
Figure 4.39. Representative example of observed corrosion at conclusion of second accelerated corrosion test — Sensor N023.
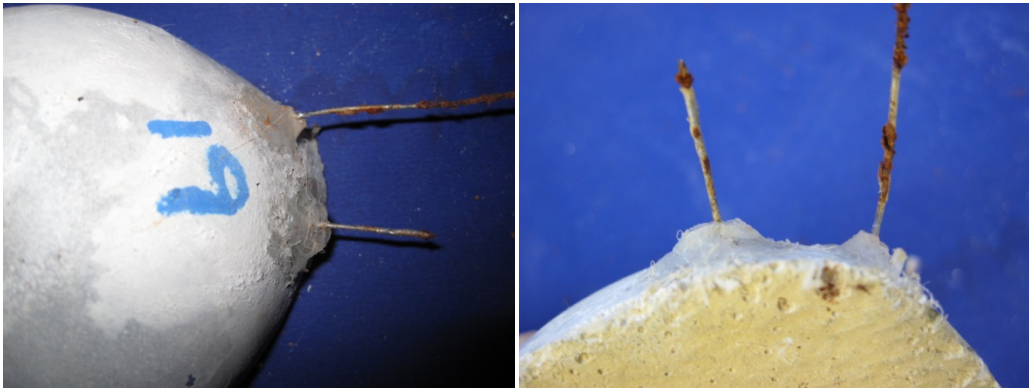
Figure 4.40. Corrosion of the steel sensing wire within the region coated by solder (Sensor N019).

Sensor N007 (3.5% Salt Water)

Sensor N019 (6.0% Salt Water)

Sensor N022 (8.0% Salt Water)
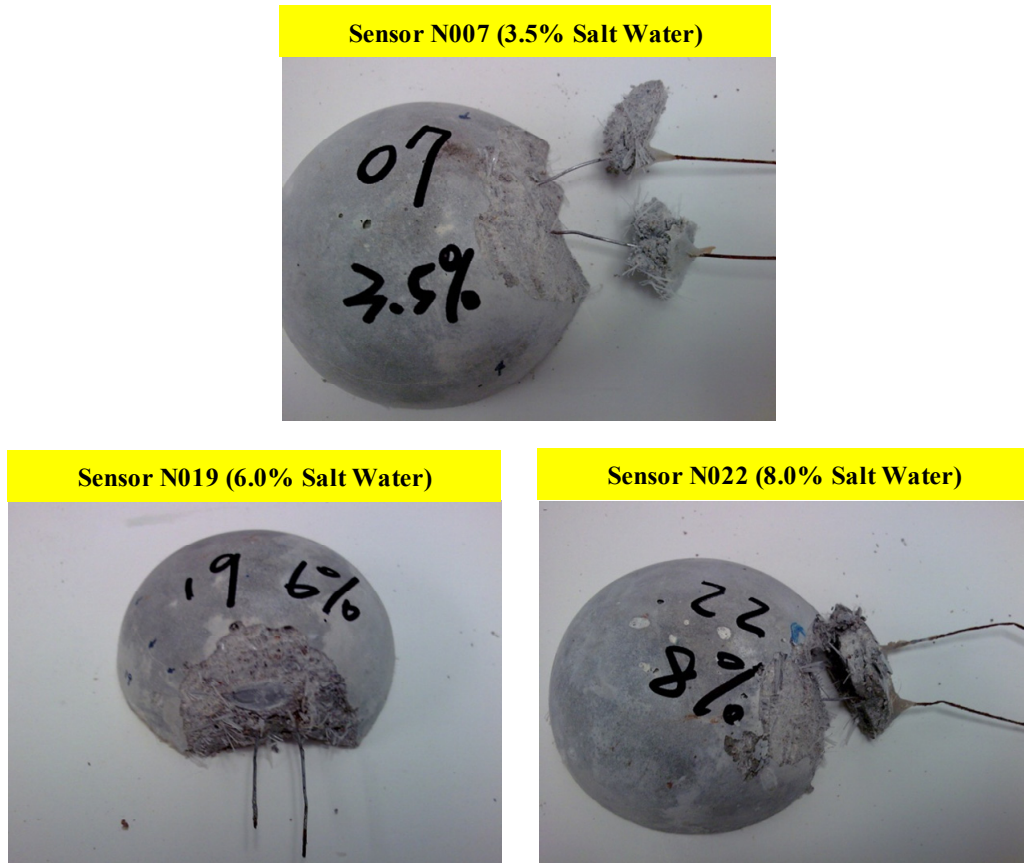
Figure 4.41. Condition of steel sensing wire within cement paste housing.

Epoxy Housing

Corrosion Occurred at the Interface between the Epoxy Housing and Solder-coated Steel Sensing Wire
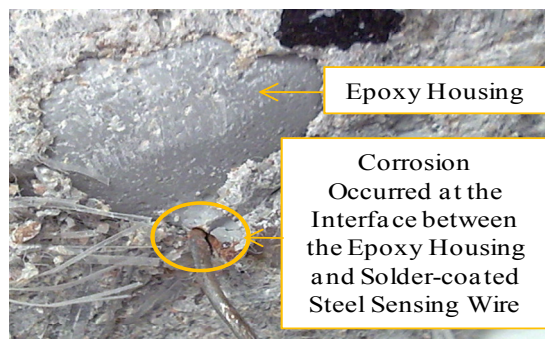
Figure 4.42. Corrosion at interface between solder-coated steel wire and epoxy coating (Sensor N019).

Figure 4.43. Condition of cement paste housing at conclusion of second accelerated corrosion test for Sensor N020 (left, 6% salt water) and N022 (right, 8% salt water)
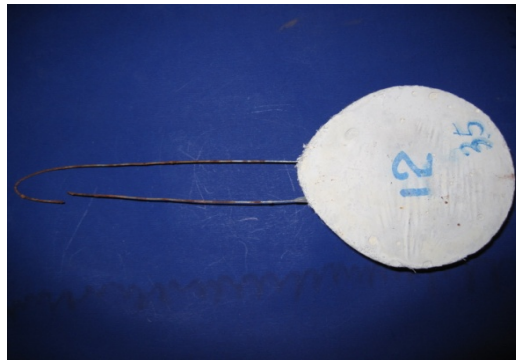
Figure 4.44. Condition of cement paste housing at conclusion of second accelerated corrosion test for Sensor N012 (3.5% salt water).
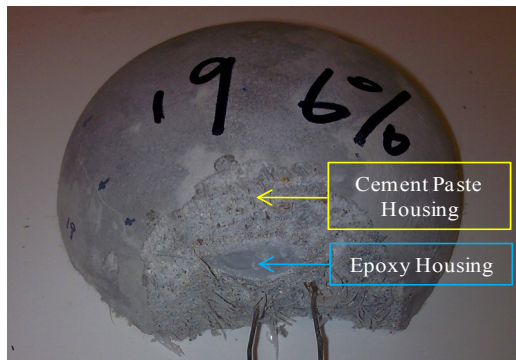
Figure 4.45. Condition of interface between cement paste and epoxy (Sensor N019).

4.3.3.3.2 Measured Frequency Response of the Sensors

The measured frequency responses of the corrosion sensors tested during the second accelerated corrosion test are plotted in Appendix B.3. Other than the amplitude of the pseudo-quality factor for the reference circuit, the response was essentially the same for sensors constructed using COG and X7R capacitors. Figure 4.46 summarizes the time to steel sensing wire fracture in different concentrations of salt water. As shown, after 133 days of the test, all wires in 2% salt water remained intact. All wires in 6% and 8% salt water were fractured. As for the wires in 3.5% salt water environment, the steel sensing wires in 6 of 16 sensors were still intact.

Figure 4.46. Time to steel sensing wire fracture in different concentrations of salt water.

4.3.3.3.3 Summary of Results

The second accelerated corrosion test demonstrated that the revised sensor protection system increased the likelihood that corrosion will occur along the free length of the steel sensing w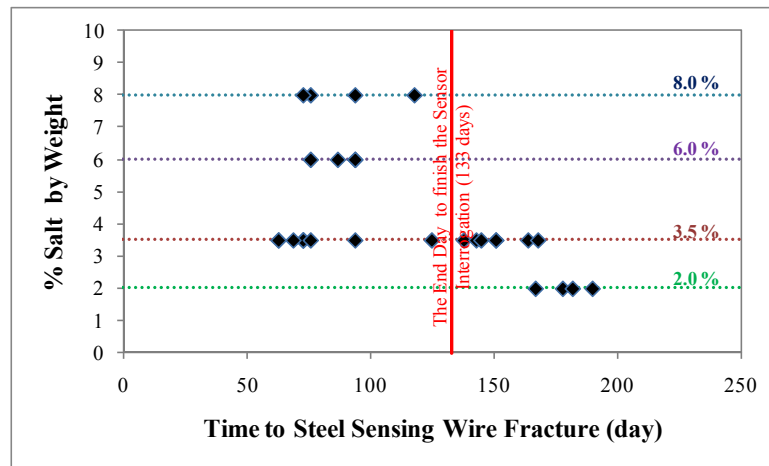ire. However, this sensor protection system still has one imperfection which requires future improvements. Due to the galvanic corrosion of the two different metal alloys, corrosion occurred at the interface between the solder coating and the bare steel wire in salt water concentration above 3.5%. If the sensor is used in environments with higher chloride concentrations, a different coating is required.

4.4 Recommendation of the Sensor Protection System

The revised sensor protection system for the threshold corrosion sensor performed well during the second accelerated corrosion test. Both the reliability and durability of the sensor was improved. Additionally, the cost of materials used to fabricate the protective systems is less than one dollar. The process used to fabricate the sensor is described in Appendix C and summarized in Figure 4.47.
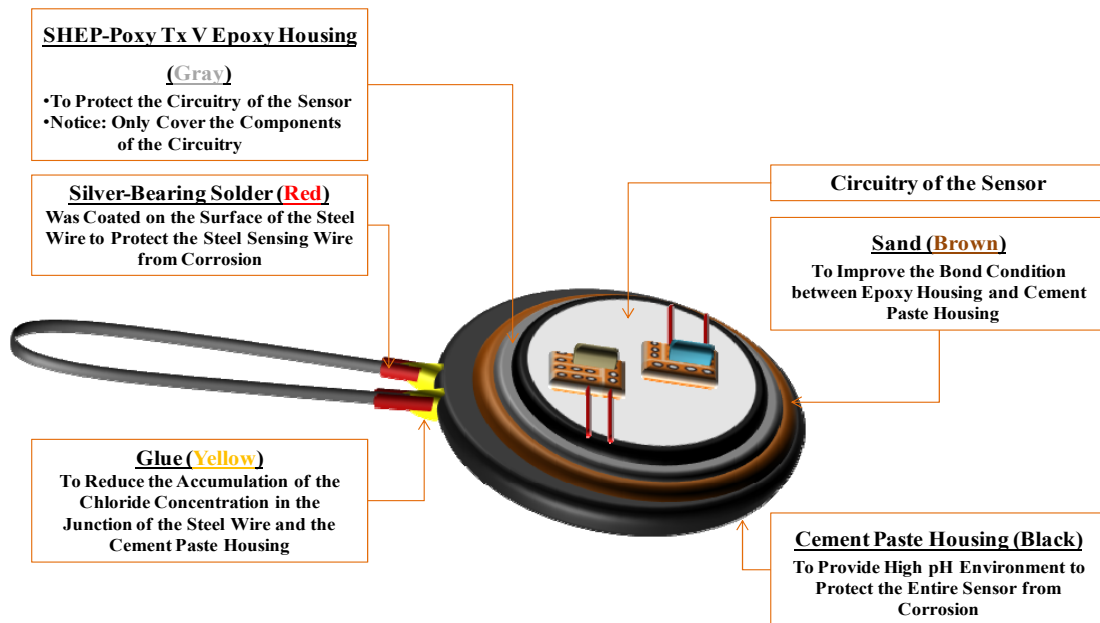
SHEP-Poxy Tx V Epoxy Housing

(Gray)
•To Protect the Circuitry of the Sensor
•Notice: Only Cover the Components
of the Circuitry

Silver-Bearing Solder (Red)
Was Coated on the Surface of the Steel
Wire to Protect the Steel Sensing Wire
from Corrosion

Circuitry of the Sensor

Sand (Brown)
To Improve the Bond Condition
between Epoxy Housing and Cement
Paste Housing

Glue (Yellow)
To Reduce the Accumulation of the
Chloride Concentration in the
Junction of the Steel Wire and the
Cement Paste Housing

Cement Paste Housing (Black)
To Provide High pH Environment to
Protect the Entire Sensor from
Corrosion

Figure 4.47. Recommended configuration of the sensor protection system.

Additional refinement of the epoxy housing and the material used to coat the steel sensing wire are needed, but these tasks can be completed by future researchers.

4.5 Conclusion

Based on the results of the extensive tests described in this chapter, two primary conclusions can be drawn:

The pseudo-quality factors for sensors fabricated using COG capacitors were consistently larger than the pseudo-quality factors for sensors fabricated using X7R capacitors. Differences were more pronounced for the reference circuit than the sensing circuit. However, for the same class of capacitor, the frequency response was different using sensors manufactured by different companies. This variability must be

considered if analog passive sensors are developed.

The sensor protection system was improved significantly by selecting a different epoxy to coat the circuit components, using a different mixture for the cement paste housing, selecting a different mold for the cement paste housing, and selecting a curing environment to minimize plastic shrinkage cracks. These changes have improved both the durability and the reliability of the threshold corrosion sensors.

CHAPTER 5

Optimization of the Conductivity Sensor

5.1 Introduction

Andringa (2006) developed the prototype conductivity sensor and conducted the initial laboratory tests that demonstrated the viability of extracting analog data from this type of passive sensor. Several experiments are discussed in this chapter to investigate the sensitivity of the measured response of the conductivity sensor to design choices and to the environment within the conductive medium.

A simplified conductivity sensor was used in all experiments. The configuration of the simplified sensor is discussed in Section 5.2. The sensitivity of the pseudo-quality factor to the frequency resolution used to interrogate the conductivity sensors is addressed in Section 5.3. The sensitivity of the measured frequency response to the choice of capacitor and configuration of the sensing probe is described in Section 5.4.

The sensitivity of the measured response to temperature is discussed in Section 5.5 and the sensitivity of the measured response to the proximity of reinforcement is described in Section 5.6. The results are summarized in Section 5.7.

117

5.2 Configuration of Simplified Conductivity Sensor

The analog conductivity sensor developed by Andringa (2006) used the same basic configuration as the threshold corrosion sensor developed by Dickerson (2005). Both the conductivity and corrosion sensors included two resonant circuits arranged concentrically. The sensing circuit was constructed using a 6800-pF capacitor and was positioned outside the reference circuit, which was constructed using a 33,000-pF capacitor. As discussed in Section 2.4.2, the primary difference was that the steel sensing wire was positioned in series with the inductor and capacitor in the sensing circuit of the threshold corrosion sensor, while the parallel wires that formed the conductivity probe were in parallel with the capacitor in the sensing circuit of the analog conductivity sensor.

In order to simplify the conductivity sensor for this investigation, the reference circuit was not included (Figure 5.1). The simplified configuration eliminates the parasitic coupling between the two resonant circuits and maximizes the resonant phase response of the sensing circuit. In addition, the range of frequencies over which the sensor must be interrogated can be reduced. A drawback of this configuration, however, is that it may not be possible to detect the presence of the conductivity sensor if the conductivity of the surrounding medium becomes too high. This issue is discussed in Section 5.3.

A photograph of the simplified conductivity sensor is shown in Figure 5.2. The capacitance of the capacitor and the configuration of the parallel probes were varied

in this investigation, but the inductance of the sensing coil was the same in all sensors. All sensing coils were fabricated using five turns of 18-AWG copper wire around a 2.25-in. diameter slice of PVC pipe.

The default configuration of the conductivity probe is shown in Figure 5.2. The parallel copper wires extended 3 cm beyond the epoxy enclosure and the centerline spacing of the wires was 4 mm. Unless otherwise indicated, the default configuration of the conductivity probe was used in all sensors discussed in this chapter.
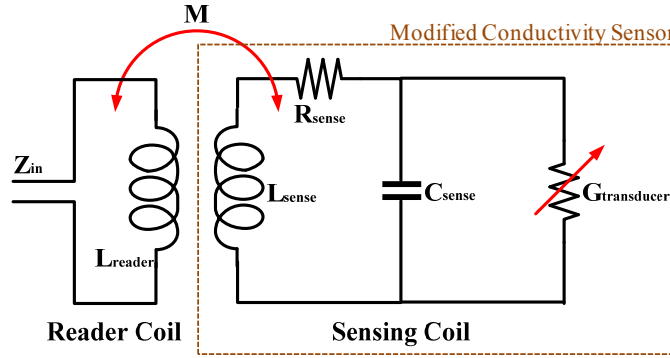
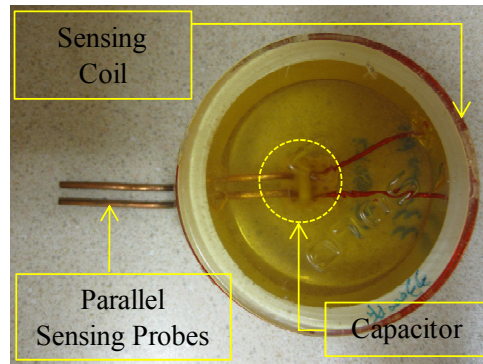*Figure 5.1. Circuit diagram of the simplified conductivity sensor.*

Figure 5.2. Configuration of the simplified conductivity sensor.

5.3 Sensitivity of Pseudo-Quality Factor to Frequency Resolution Used to Interrogate Sensor

Because the prototype conductivity sensor developed by Andringa (2006) included two resonant circuits, it was necessary to interrogate the sensor over a wide frequency range. The resonant frequencies of the sensing and reference circuit were approximately 0.5 MHz and 1.6 MHz, respectively. All interrogations of the corrosion and conductivity sensors embedded in Slabs 3 and 4 (Puryear 2007) were conducted between 0.1 and 2.1 MHz, with a frequency resolution of 10,000 Hz. As a result, 201 data points were collected during each interrogation, and the interrogation cycle lasted approximately 3 min using the Solartron SI 1260 Impedance/Gain-Phase Analyzer.

This frequency resolution was sufficient for the threshold corrosion sensors, because the measured response is only used to detect the presence or absence of the resonant frequencies. However, in order to interpret the response of the analog corrosion sensors, the conductivity of the surrounding medium must be extracted from the pseudo-quality factor, which is calculated from the measured data (Section 2.4.2). Close examination of the data from the conductivity sensors embedded in Slabs 3 and 4 revealed that in many cases, fewer than five data points were captured near the resonant frequency. This observation prompted a more thorough investigation of the sensitivity of the pseudo-quality factor to the frequency resolution used to interrogate the conductivity sensors.

Figure 5.3 illustrates the primary concern. The same sensor was interrogated in air over the same range of frequencies in the three plots. The plot in the upper left corresponds to a fine frequency resolution. More than fifty data points were captured to define the resonant response, and the numerical algorithm developed by Andringa (2006) closely matches the measured data. When the sensor is interrogated using a coarser frequency resolution, errors are introduced because an insufficient number of data points are captured to define the resonant response. As shown in the plot in the upper right, if the amplitude of the resonant response is over-estimated, the corresponding pseudo-quality factor will be over-estimated. As shown in the lower plot, it is also possible for the algorithm to under-estimate the amplitude of the resonant response and the corresponding pseudo-quality factor.

These differences lead to unacceptable levels of error in the pseudo-quality factors, and the conductivity of the surrounding medium (Eq. 2.8). Therefore, it is essential that the frequency resolution be sufficiently fine that the measured response is accurately modeled using the numerical algorithm.
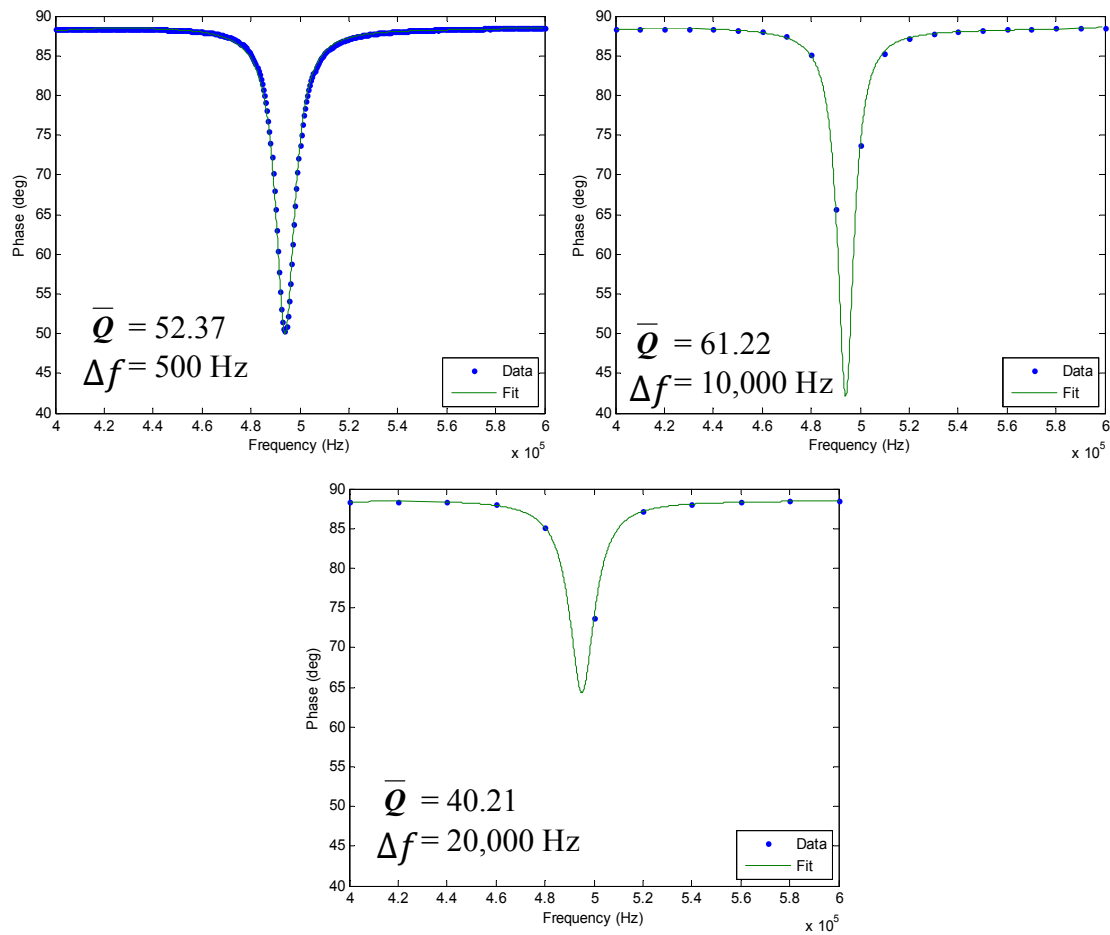
Figure 5.3. Sensitivity of curve-fitting algorithm to frequency resolution.

In order to investigate the sensitivity of the pseudo-quality factor to the frequency resolution, a more detailed series of experiments was conducted. A photograph of the test setup is shown in Figure 5.4. One, simplified conductivity sensor with a 33,000-pF capacitor and the default configuration of the conductivity probe with 18-AWG copper wire was used in all tests. The sensor was supported above the bottom of a plastic container on a 1.25-in. thick slice of PVC pipe. The reader coil was aligned concentrically with the sensor below the plastic container.

122

Data were collected with the plastic container empty, filled with tap water, and filled with salt water. Concentrations of salt water ranged from 0.1% to 0.35% salt by weight. In all cases, the temperature of the water was between 68 and 70 °F. The resonant frequency of the sensing circuit is approximately 0.5 MHz. Therefore, a frequency range of 0.35 to 0.65 MHz was used for all interrogations.
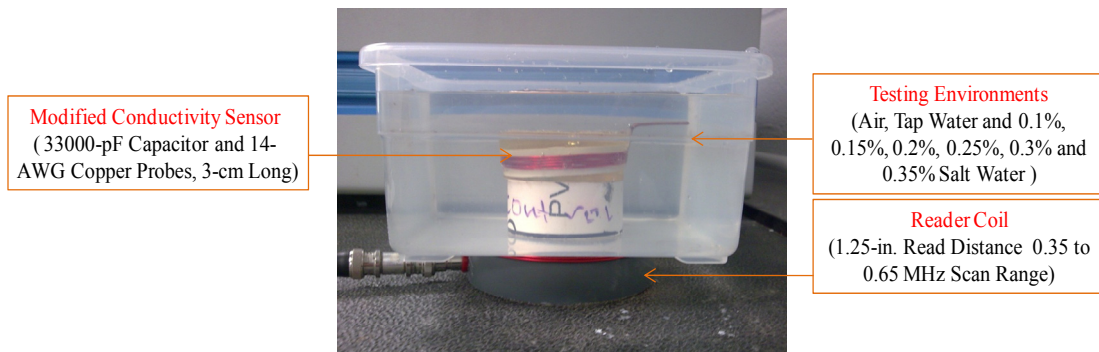
Figure 5.4. Experimental setup for evaluating the influence of the frequency resolution in different environments.

For each environment, the sensor was interrogated six times using frequency increments ranging from 250 to 1500 Hz. As indicated in Table 5.1, 1201 data points were collected for the finest frequency resolution (250 Hz) and 201 data points were collected for the coarsest resolution (1500 Hz). Because the interrogation time is approximately 30 sec for each data point, the duration of the scans ranged from 3 to 18 min.

Table 5.1. Frequency resolutions used to investigate sensitivity of response.

Frequency Increment (Hz)	Total Data Points	Data Points around the Resonant Frequency	Time for Complete Scan (Min)
250	1201	66	18.0
500	601	34	9.0
750	401	23	6.0
1000	301	18	4.5
1500	201	12	3.0

The measured phase responses for each of the eight environments are plotted in Figure 5.5 for a frequency increment of 250 Hz. The amplitude of the phase dip varies from approximately 30 degrees for air to less than 1 degree for 0.35% salt water. As shown in Figure 5.5(b), the resonant frequency is still clearly defined for the highest concentration of salt water, even if it is difficult to see in Figure 5.5(a). The numerical algorithm developed by Andringa (2006) provided an accurate representation of the measured data in all cases. The parameters calculated for each curve are summarized in Table 5.2.
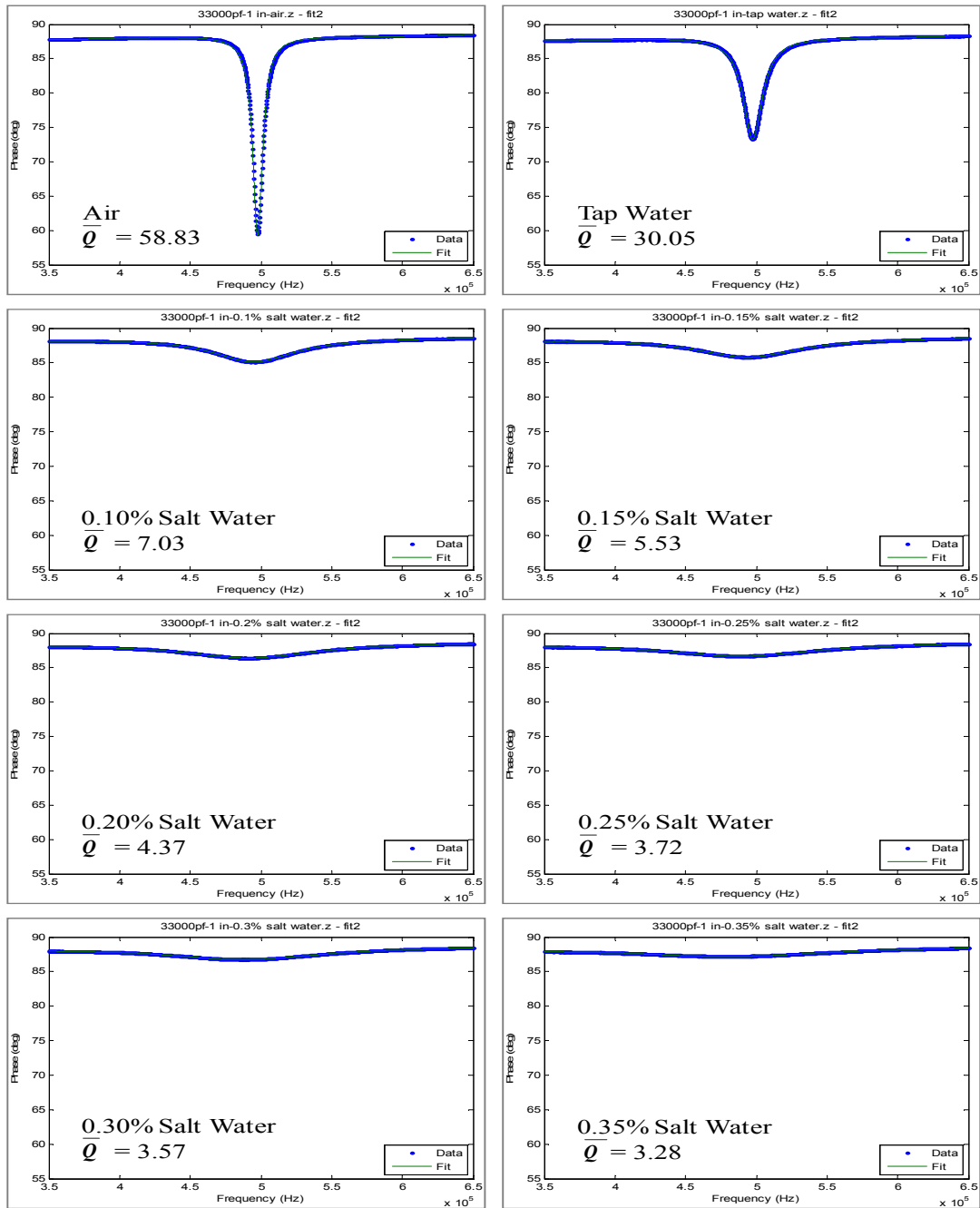
Figure 5.5 (a). Measured phase responses of conductivity sensor measured in different environments (frequency increment: 250 Hz).
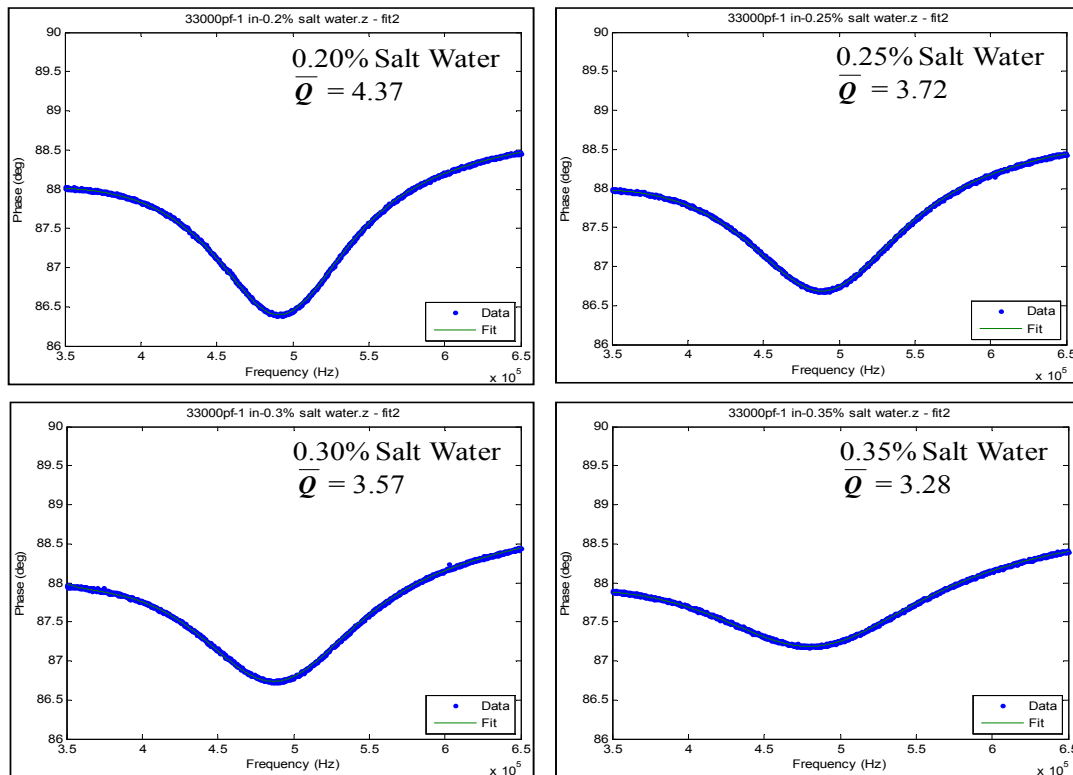
Figure 5.5 (b). Measured phase responses of conductivity sensor measured in different environments (frequency increment: 250 Hz).

Table 5.2. Calculated parameters for interrogations shown in Figure 5.6 (frequency increment: 250 Hz).

Concentration of Salt Water (%)	Resonant Frequency (MHz)	Phase Dip (Degree)	Pseudo-Quality Factor
air	0.498	28.95	58.83
0.00	0.498	14.78	30.05
0.10	0.495	3.44	7.03
0.15	0.494	2.75	5.53
0.20	0.492	2.14	4.37
0.25	0.490	1.87	3.72
0.30	0.489	1.80	3.57
0.35	0.488	0.87	3.28

The sensitivity of the pseudo-quality factor to the frequency resolution is shown in Figure 5.6. For salt water concentrations of 0.25% or less, the calculated values were independent of the frequency increment. However, for the higher salt water concentrations, error was introduced for the coarser frequency resolutions. For example, a 25% error was introduced into the calculated pseudo-quality factor by increasing the frequency resolution from 250 Hz to 1500 Hz for 0.35% salt water. The primary advantage of the coarser frequency resolution is the shorter interrogation time (Table 5.1), but this is offset if error is introduced. It should be noted that Eq. 2.10 is valid only for undamped RLC circuits. Therefore, the lower limit for pseudo-quality factors was taken as 1.0.

Unless otherwise indicated, a frequency resolution of 250 Hz was used for interrogating the conductivity sensors discussed in this chapter.
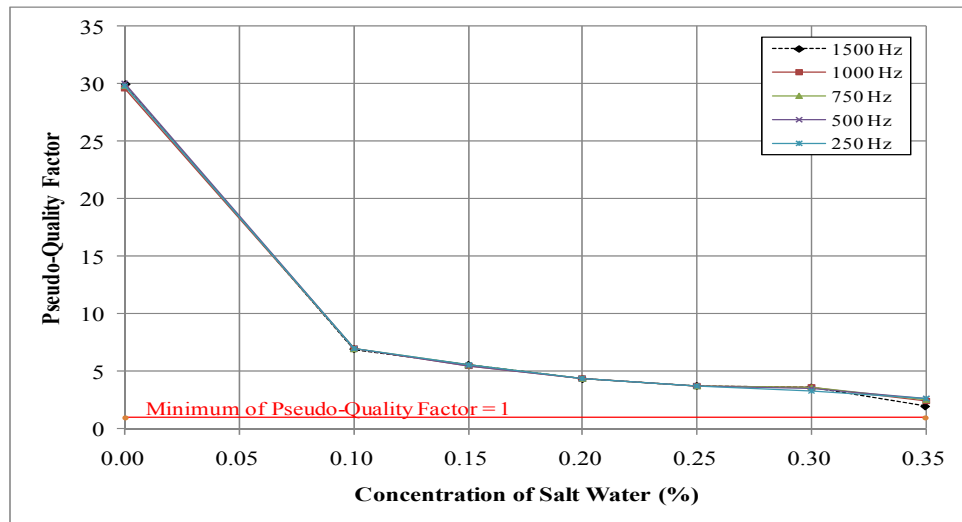
Figure 5.6 (a). Variation of pseudo-quality factor with salt water concentration for different frequency resolutions.

127
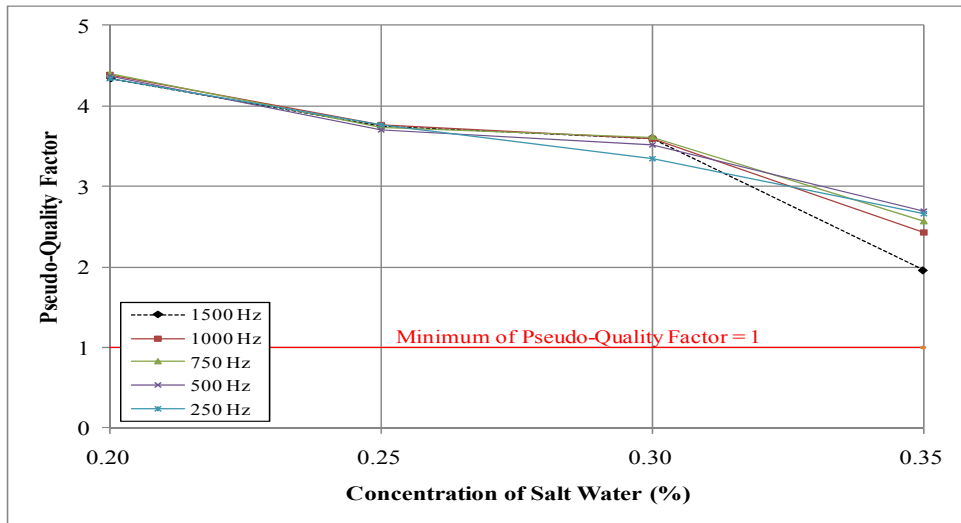
Figure 5.6 (b). Variation of pseudo-quality factor with salt water concentration for different frequency resolutions.

5.4 Optimization of the Simplified Analog Conductivity Sensor Components

The sensitivity of the measured response of the conductivity sensor to the choice of capacitor and the configuration of the sensing probe is investigated in this section. The performance of different capacitors is discussed in Section 5.4.1 and Section 5.4.2 focuses on the sensing probe.

5.4.1 Capacitor Study

All conductivity sensors discussed in this section were fabricated in accordance with Figure 5.2. Capacitors ranging from 33,000 pF to 680,000 pF were considered in the parametric study. All capacitors were purchased from KEMET Company. As indicated in Table 5.3, capacitors between 33,000 pF and 68,000 pF were type COG,

while capacitors between 100,000 pF and 680,000 pF were type X7R. The default configuration of the conductivity probe with 14-AWG wire was used for all sensors.

Sensors were interrogated in air and in salt water. The test setup is shown in Figure 5.7. For sensors interrogated in air, the read distance was 0 in. The reader coil was positioned around the conductivity sensor with no vertical offset. When interrogating sensors submerged in 0.5% salt water, the read distance was 0.25 in. The sensor was positioned on the bottom of a plastic container and the reader coil was directly below the plastic container. Water temperature was between 68 and 70 °F for all experiments discussed in this section. Complete information for all data presented in this section is provided in Appendix D.1.

Table 5.3. Capacitors used in parametric study.

Capacitor	Type of Tested Capacitor	Scan Range (MHz)	Sample Points	Frequency Resolution (Hz)
33,000pF		0.35 ~ 0.65	1201	
47,000pF	COG	0.30 ~ 0.60	1201	250
68,000pF		0.20 ~ 0.45	1001	
100,000pF		0.15 ~ 0.45	1201	
220,000pF		0.10 ~ 0.35	1001	
330,000pF	X7R	0.05 ~ 0.30	1001	250
470,000pF		0.05 ~ 0.30	1001	
680,000pF		0.05 ~ 0.30	1001	
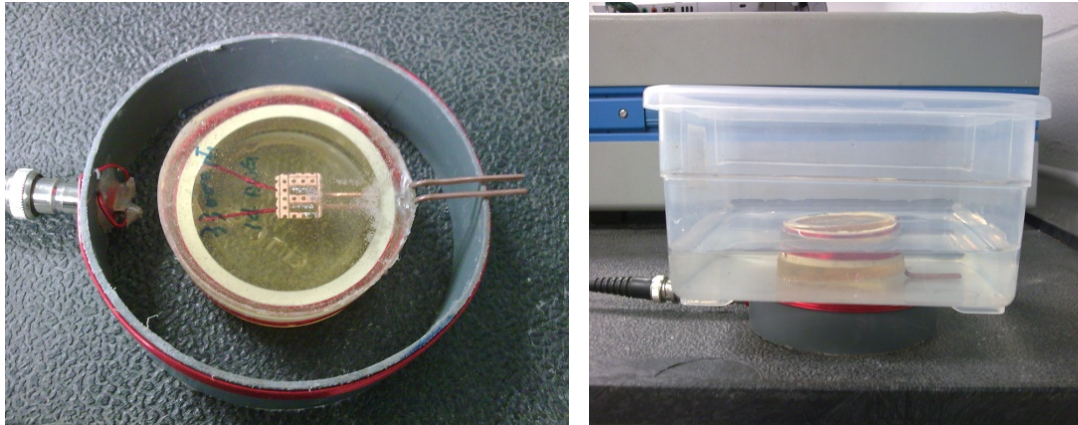
Figure 5.7. Experimental setting for estimating the performance of different capacitors in air (left) and salt water (right).

5.4.1.1 Measured Response of Conductivity Sensors in Air

The measured responses of the eight conductivity sensors in air are shown in Figure 5.8 and summarized in Table 5.4. As expected, the resonant frequency of the sensors decreased as the capacitance of the capacitor increases, when the inductance of the coil remains constant (Eq. 2.6). As with the threshold corrosion sensors, the phase dips and pseudo-quality factors were larger for conductivity sensors constructed using COG capacitors, compared with X7R capacitors (Figure 5.9). The most pronounced response was observed for the conductivity sensor fabricated with the 33,000-pF capacitor.
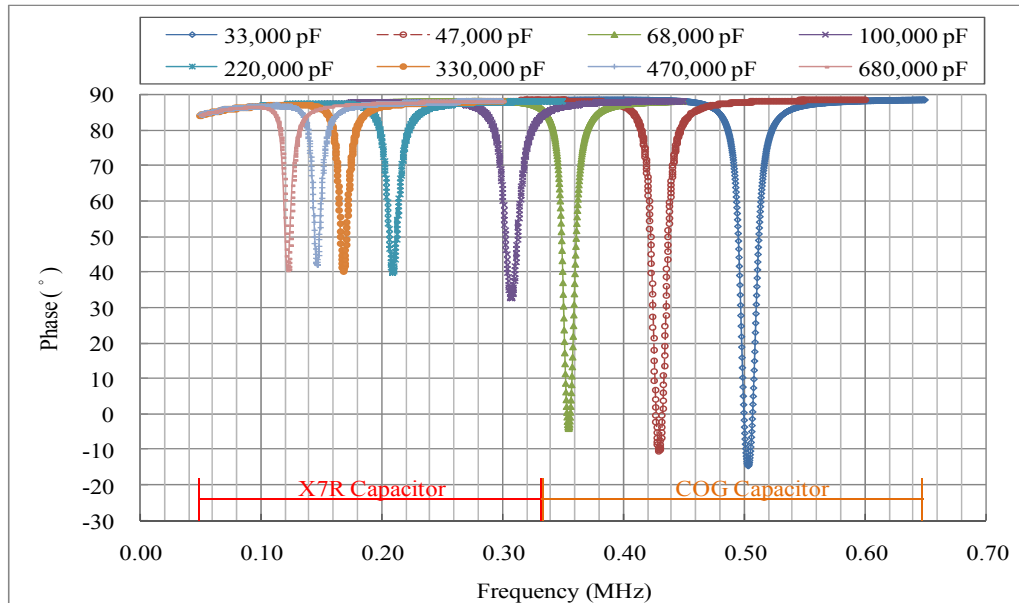
Figure 5.8. Measured phase response for conductivity sensors fabricated with different capacitors and tested in air.

Table 5.4. Calculated parameters for conductivity sensors fabricated with different capacitors (tested in air).

Capacitor Type	Capacitor	Resonant Frequency (MHz)	Phase Dip (degree)	Pseudo-Quality Factor
COG	33,000 pF	0.504	111.3	38.7
	47,000 pF	0.430	106.4	37.0
	68,000 pF	0.355	98.2	35.6
X7R	100,000 pF	0.308	57.2	22.6
	220,000 pF	0.210	49.0	19.2
	330,000 pF	0.169	48.1	19.6
	470,000 pF	0.147	46.3	18.8
	680,000 pF	0.122	47.4	17.6
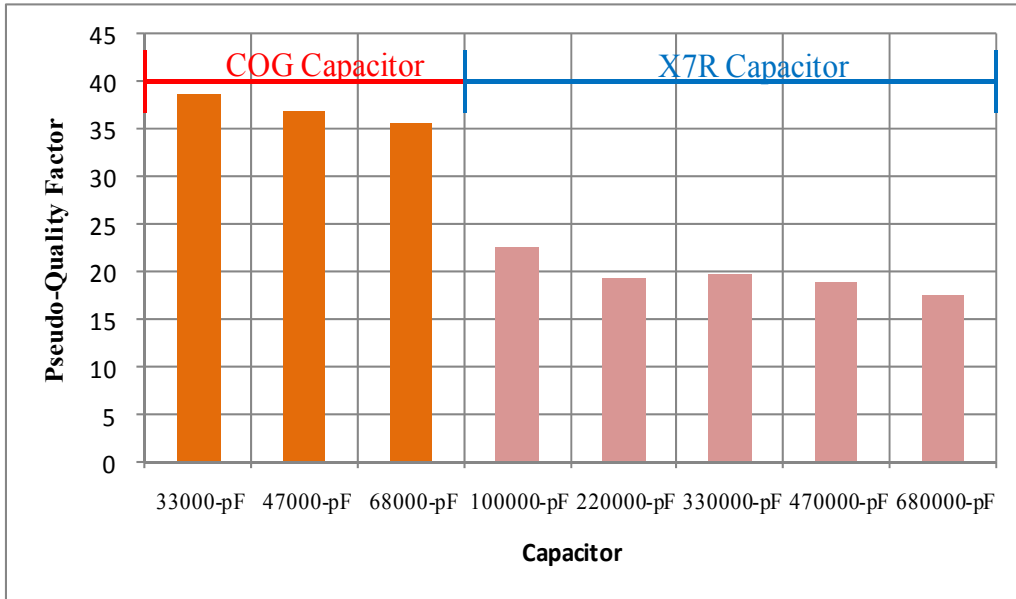
Figure 5.9. Pseudo-quality factors for conductivity sensors interrogated in air.

5.4.1.2 Measured Response of Conductivity Sensors in Salt Water

The measured responses of the eight conductivity sensors in 0.5% salt water are shown in Figure 5.10 and summarized in Table 5.5. As expected, the pseudo-quality factors for each sensor decreased in the higher-conductivity environment, compared with air. However, the largest phase dip and largest pseudo-quality factor (Figure 5.11) were observed for the sensor fabricated with the 680,000-pF capacitor.
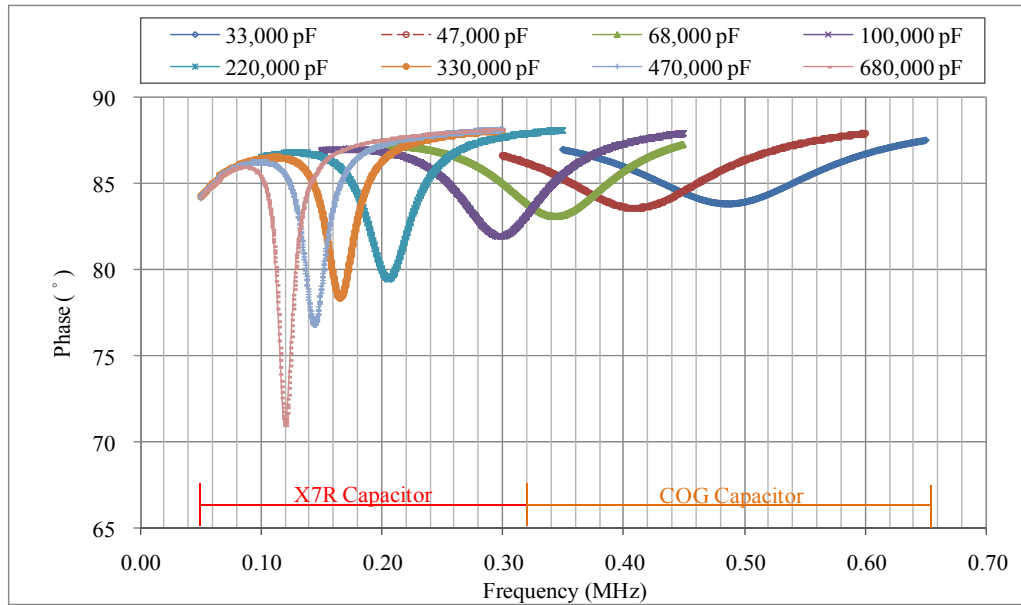
Figure 5.10. Measured phase response for conductivity sensors fabricated with different capacitors and tested in 0.5% salt water.

Table 5.5. Calculated parameters for conductivity sensor fabricated with different capacitors (tested in 0.5% salt water).

Capacitor Type	Capacitor	Resonant Frequency (MHz)	Phase Dip (degree)	Pseudo-Quality Factor
	33,000 pF	0.487	4.7	2.6
COG	47,000 pF	0.410	4.8	2.6
	68,000 pF	0.344	5.2	3.1
	100,000 pF	0.299	6.2	3.4
	220,000 pF	0.206	8.4	4.7
X7R	330,000 pF	0.166	9.2	5.9
	470,000 pF	0.145	10.5	6.5
	680,000 pF	0.120	16.1	8.3

133
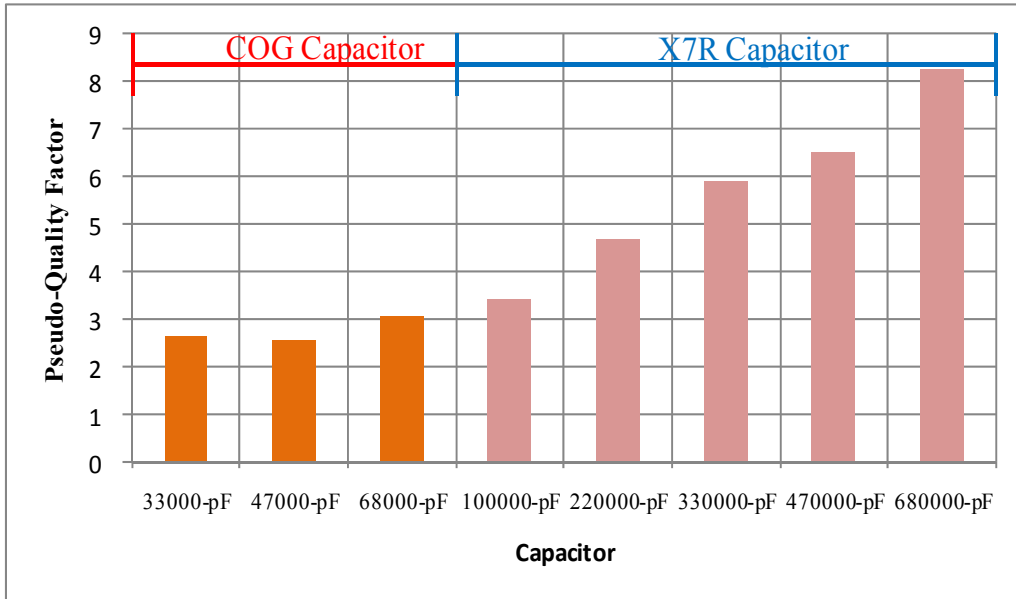
Figure 5.11. Pseudo-quality factors for conductivity sensors interrogated in 0.5% salt water.

5.4.2   Configuration of Conductivity Probe

All conductivity sensors discussed in this section were fabricated in accordance with Figure 5.2. The sensitivity of the measured response to the diameter of the copper wire used for the sensing probe is investigated in 5.4.2.1, the sensitivity of the measured response to the length of the sensing probe is studied in 5.4.2.2, and the inherent variability of the sensor readings due to the formation of copper (II) chloride on the surface of the exposed wires in the conductivity probe is addressed in 5.4.2.3.

134

5.4.2.1 Diameter of Copper Wire in Conductivity Probe

The response of conductivity sensors with the default probe fabricated using 18-AWG (0.0403-in. diameter) and 14-AWG (0.0641-in. diameter) copper wire are discussed in this section. Both sensors were fabricated using 33,000-pF, COG capacitors. The sensors were interrogated in salt water, with concentrations ranging from 0 to 2.0% by weight. The test setup was identical to that shown on the right side of Figure 5.7. Water temperature was between 68 and 70 °F for all experiments discussed in this section.

The measured responses of the two conductivity sensors in varying concentrations of salt water are shown in Figure 5.12 and summarized in Table 5.6. The phase dips were consistently larger for the conductivity probes fabricated using 18-AWG wire. The shift in resonant frequency with increasing salt water concentration was also larger for probes fabricated using 18-AWG wire. However, the pseudo-quality factors were slightly larger for the probes fabricated using 14-AWG wire over the entire range of salt water concentrations tested.
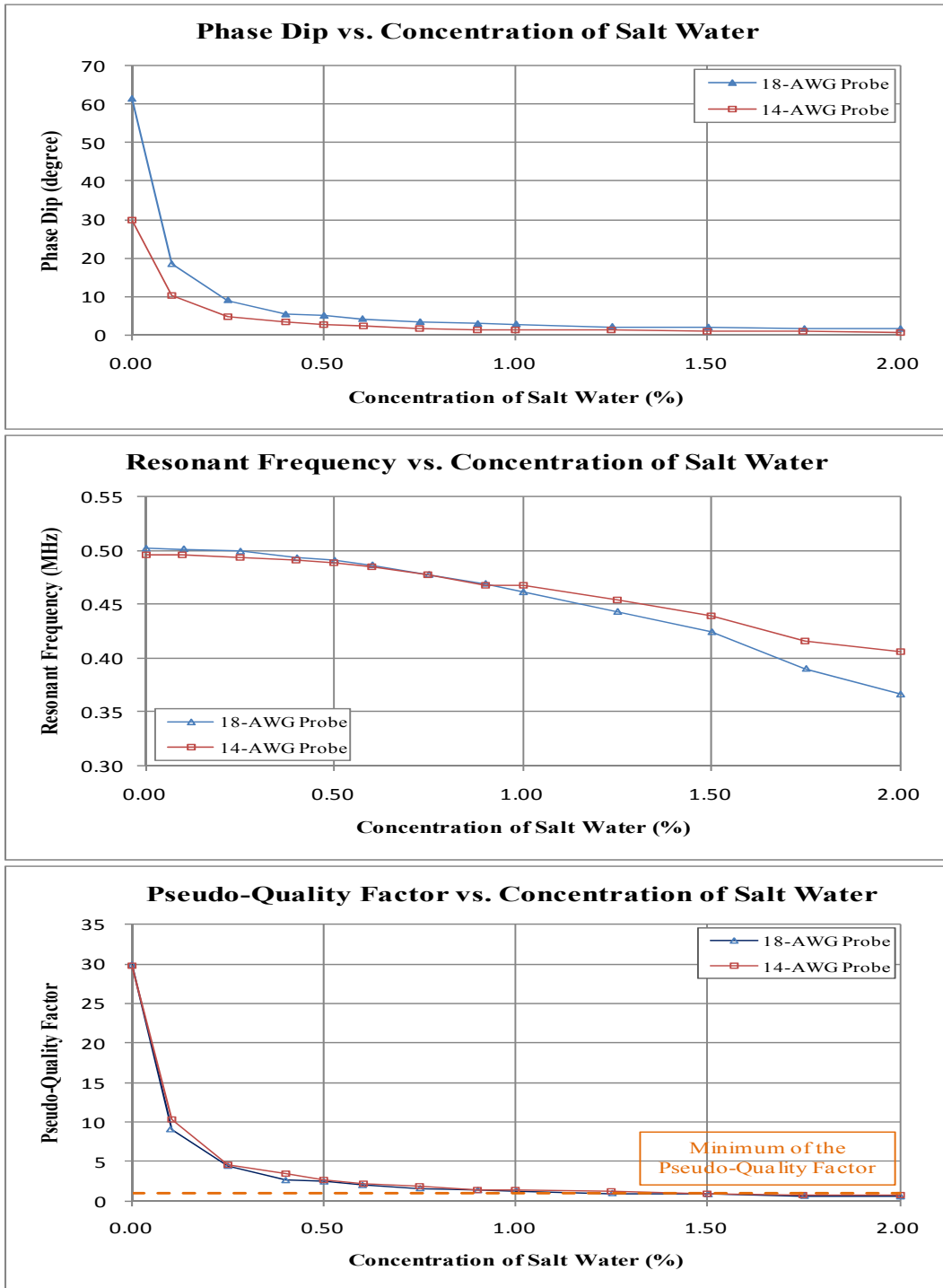
Figure 5.12. Comparison of calculated parameters for conductivity sensors fabricated with different sizes of copper wire in probe.

136

Table 5.6. Calculated parameters for conductivity sensors fabricated with 14- and 18-AWG probes.

	18-AWG Sensing Probe		
Concentration of Tested Salt Water (%)	Resonant Frequency (MHz)	Phase Dips (Degree)	Pseudo-Quality Factor
0.00	0.502	61.6	29.89
0.10	0.501	18.5	9.08
0.25	0.499	9.1	4.46
0.40	0.493	5.3	2.64
0.50	0.491	5.0	2.47
0.60	0.486	4.2	2.03
0.75	0.478	3.4	1.62
0.90	0.469	2.9	1.39
1.00	0.461	2.8	1.31
1.25	0.443	2.1	1.01
1.50	0.424	2.0	0.88
1.75	0.390	1.6	0.67
2.00	0.367	1.6	0.60

	14-AWG Sensing Probe		
Concentration of Tested Salt Water (%)	Resonant Frequency (MHz)	Phase Dips (Degree)	Pseudo-Quality Factor
0.00	0.496	44.8	29.85
0.10	0.496	15.5	10.41
0.25	0.494	6.6	4.61
0.40	0.492	5.0	3.46
0.50	0.488	3.9	2.72
0.60	0.484	3.2	2.24
0.75	0.478	2.7	1.84
0.90	0.468	2.0	1.47
1.00	0.468	2.0	1.44
1.25	0.455	1.7	1.19
1.50	0.439	1.4	1.00
1.75	0.415	1.0	0.82
2.00	0.405	0.8	0.76

5.4.2.2 Length of Parallel Wires in Conductivity Probe

From the perspective of sensor durability, the length of the parallel wires in the conductivity probe is one of the most important design decisions. If the wires are too long, they can be easily bent during placement of the concrete and the sensor results will be compromised.

To understand the influence of the probe length on the response of the conductivity sensor, four sensors were fabricated. The sensing circuit included a 33,000-pF, COG capacitor. The probes were fabricated using 14-AWG copper wire with lengths of 0.5, 1, 2, and 3 cm. The ceneterline spacing between parallel wires was 4 mm for all four sensors. The sensors were interrogated in salt water, with a concentration of 1.0% by weight. The test setup was identical to that shown on the right side of Figure 5.7. Water temperature was between 68 and 70 °F for all experiments discussed in this section.

The measured responses of the four conductivity sensors are summarized in Figure 5.13. Both the phase dip and the pseudo-quality factor were larger for the shorter probes.
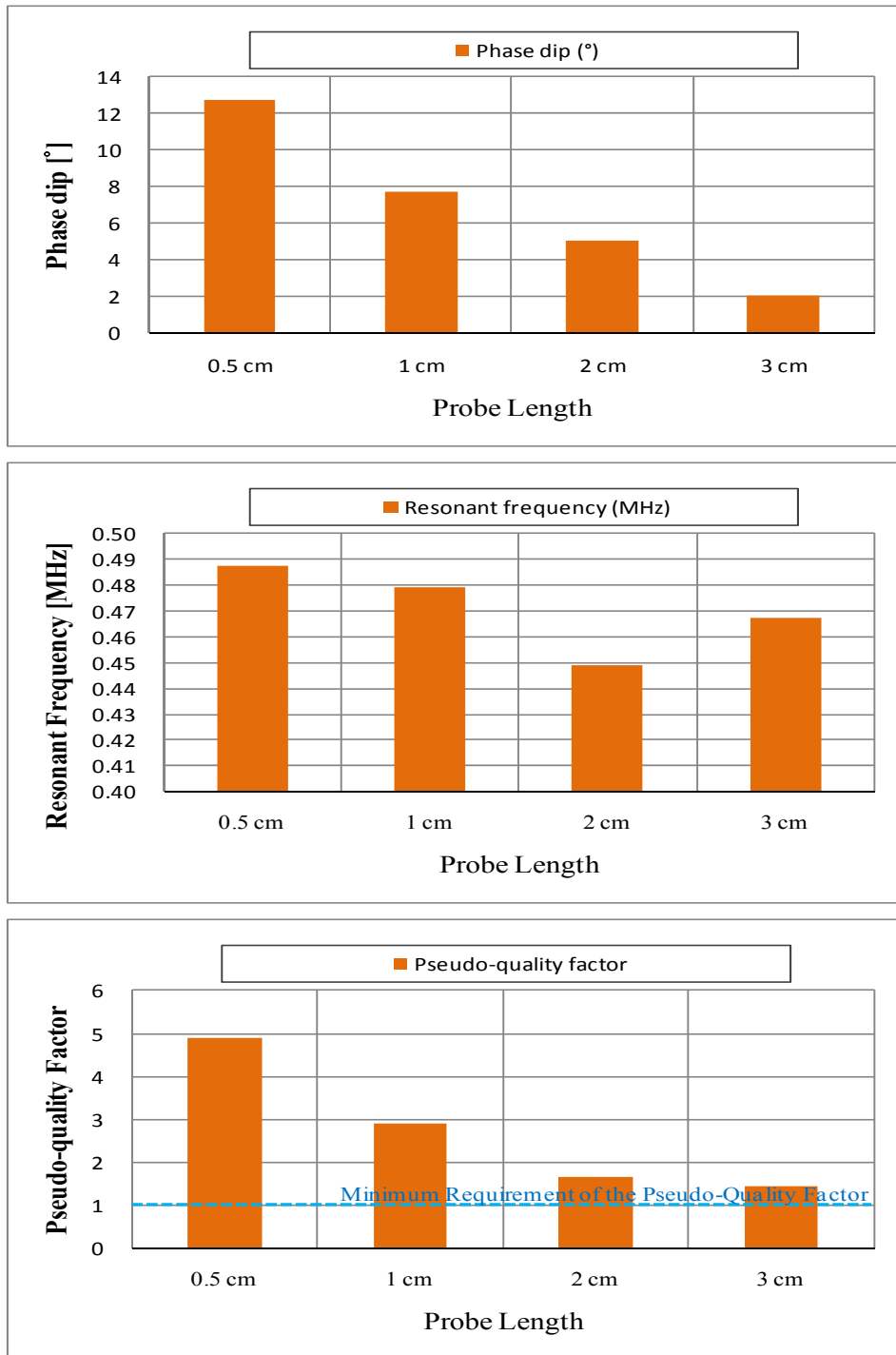
Figure 5.13. Comparison of calculated parameters for conductivity sensors fabricated with probes of different lengths (tested in 1% salt water).

5.4.2.3 Probe Material

When deicing salt is used on concrete structures, the pH of the pore solution can fall below 12 (Bertolini et al 2004). $MgCl_2$-based deicers, for example, can reduce the pore solution pH from 12.6 to 9.0, leading to loss of the passive, iron oxide layer on the surface of the rebar (Newton and Sykes 1987). In terms of the Pourbaix diagram for copper in a chloride solution (Figure 5.14 left), when the potential is larger than -0.25 compared to the standard hydrogen potential (SHE) and the pH value of the solution is lower than 10, green copper chloride compound (e.g. copper (II) chloride) will appear. If a conductivity sensor with a copper sensing probe is embedded in this kind of environment, the probe will be covered with copper (II) chloride shown as Figures 5.14 (right).
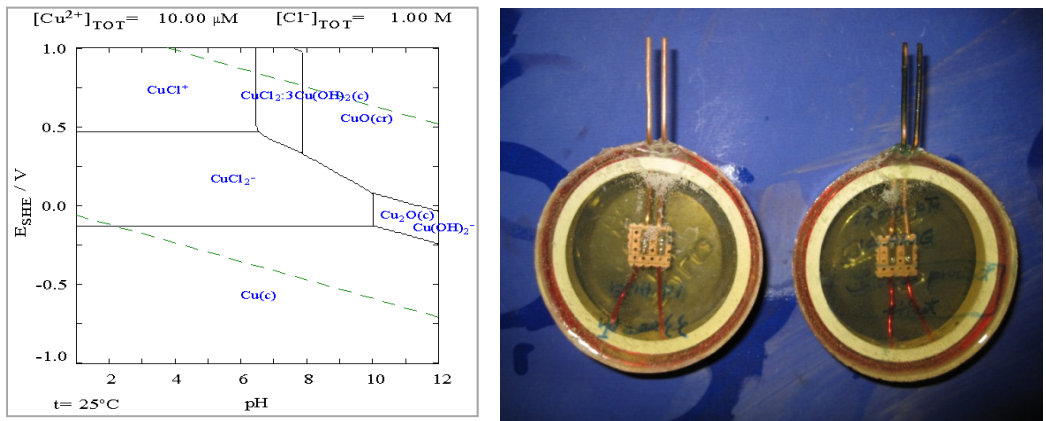
Figure 5.14. Pourbaix diagram for copper in a chloride solution (Pourbaix 1974) (left) and observed condition of copper probes before and after immersion in 3.5% salt water (right).

Although chemical analyses were not conducted, the exposed copper wires from the conductivity probes embedded in Slab 4 were similar in color to those shown in Figure 5.14. The wires were a much darker color for the sensor located beneath the salt-water reservoir compared with the sensors that were not exposed to chlorides and moisture variations.

An experimental program was developed to determine if the presence of the copper (II) chloride layer on the sensing probe influences the measured response of the conductivity sensor. Three conductivity probes were constructed and submerged in a salt water solution (3.5% salt by weight) for 138 days (Figure 5.15). By the conclusion of the test, the copper (II) chloride layer was visible on the surface of all three probes. The sensors were removed from the salt water solution once a week, dried, and interrogated in air.
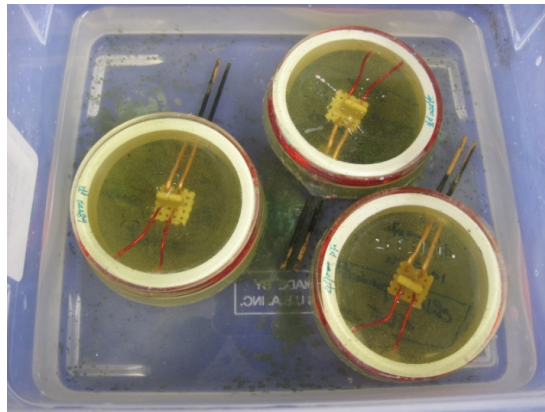
Figure 5.15. Condition of copper sensing probes after 138 days in salt water.

The three conductivity sensors discussed in this section were with 33,000-pF, 47,000-pF, and 68,000-pF, COG capacitors. The default configuration of the

conductivity probe with 14-AWG copper wire was used in all tests. The test setup was identical to that shown on the left side of Figure 5.7. Air temperature was between 68 and 70 °F for all experiments discussed in this section. The frequency resolution was 1000 Hz for all tests. The interrogation process was conducted after 4 hours of natural drying in a temperature controlled room (around 68 ~ 70 °F).

The measured response of the sensor fabricated with a 33,000-pF capacitor is summarized in Figure 5.16. As the copper (II) chloride layer developed, the phase dip and pseudo-quality factors increased; however, the changes were not linear with time. The resonant frequency remained essentially constant.

The data shown in Figure 5.16 illustrate some of the inherent error associated with the passive sensors. Additional testing is required to determine the reliability of the data obtained during long-term monitoring.
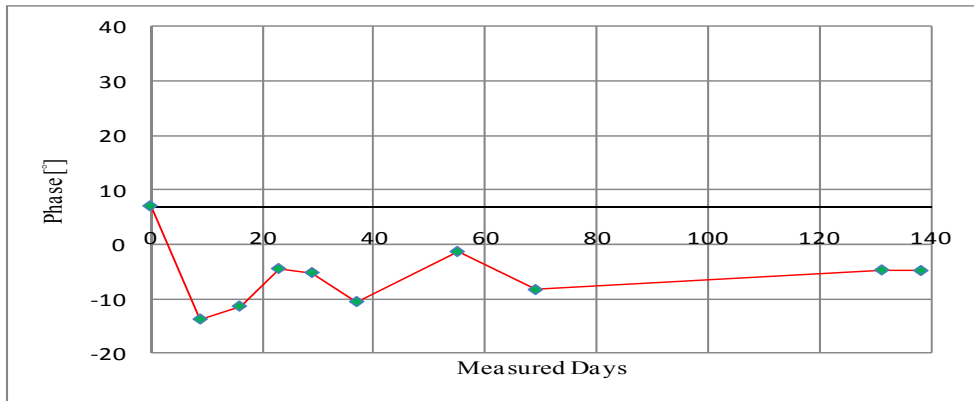
Figure 5.16 (a). Sensitivity of conductivity sensor with 33,000-pF capacitor to copper (II) chloride coating on sensing probes.
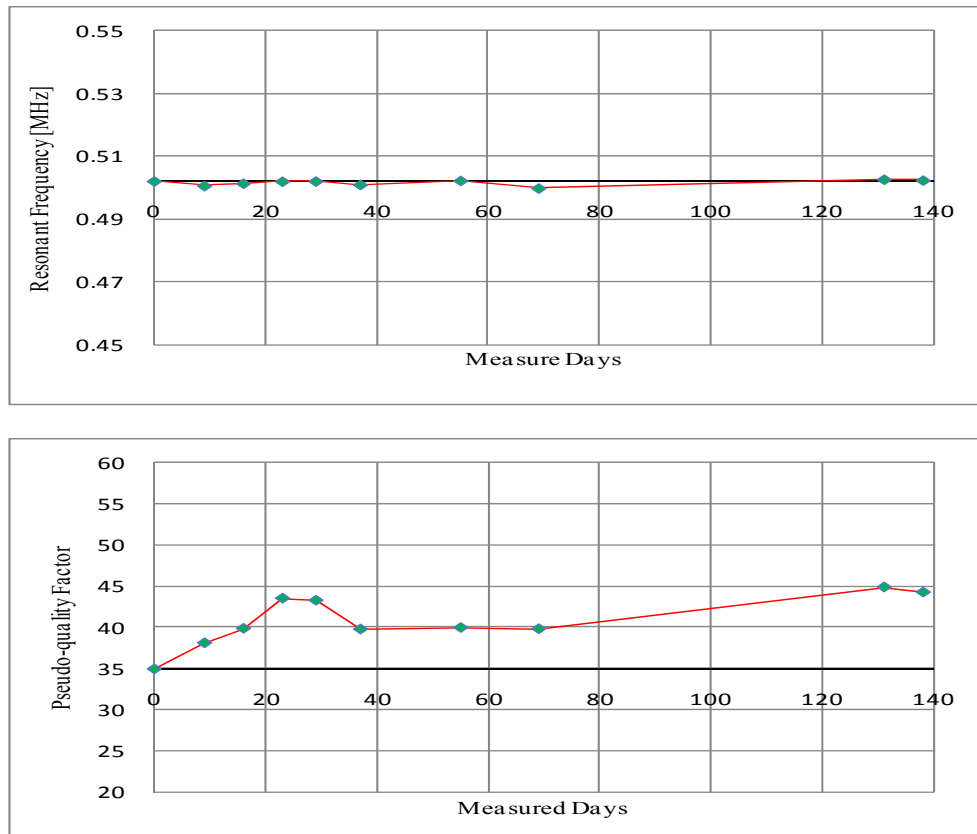
Figure 5.16 (b). Sensitivity of conductivity sensor with 33,000-pF capacitor to copper (II) chloride coating on sensing probes.

5.5 Sensitivity to Temperature

Because the properties of capacitors and copper wire vary with temperature, both the pseudo-quality factor and the calculated conductivity are expected to change with temperature for a given conductive medium. The experiments discussed in this section were conducted to evaluate the sensitivity of the measured response to temperature.

The conductivity sensor tested in this section was fabricated with a 33,000-pF,

COG capacitor. The default configuration of the conductivity probe with 14-AWG copper wire was used in all tests. The experimental setup for the test is shown in Figure 5.17. The sensor was submerged in liquids with different conductivities (tap water and salt water with concentrations between 0.1 and 0.8% by weight). The read distance for all interrogations was 0.25 in.

The inner plastic container shown in Figure 5.17(a) and (b) was filled with the conductive medium. A commercial conductivity probe was used to measure the temperature and conductivity of the conductive medium throughout the test. The initial temperature of the conductive medium was approximately 50 ˚C. In order to minimize the likelihood of appreciable temperature changes during an interrogation, the outer plastic container was filled with tap water with an initial temperature of 50 ˚C, and both plastic containers were placed inside an insulated box (Figure 5.17c). The sensors were interrogated over a frequency range from 0.475 to 0.525 MHz using a frequency resolution of 500 Hz. The interrogation time was approximately 75 sec.

The conductivity of the conductive medium was continuously monitored using the commercial conductivity probe. Each time that the commercial conductivity probe indicated that the conductivity of the medium had changed, the conductivity and temperate were recorded and the sensor was interrogated. The complete test results in the various concentrations of salt water are summarized in Appendix D.3.
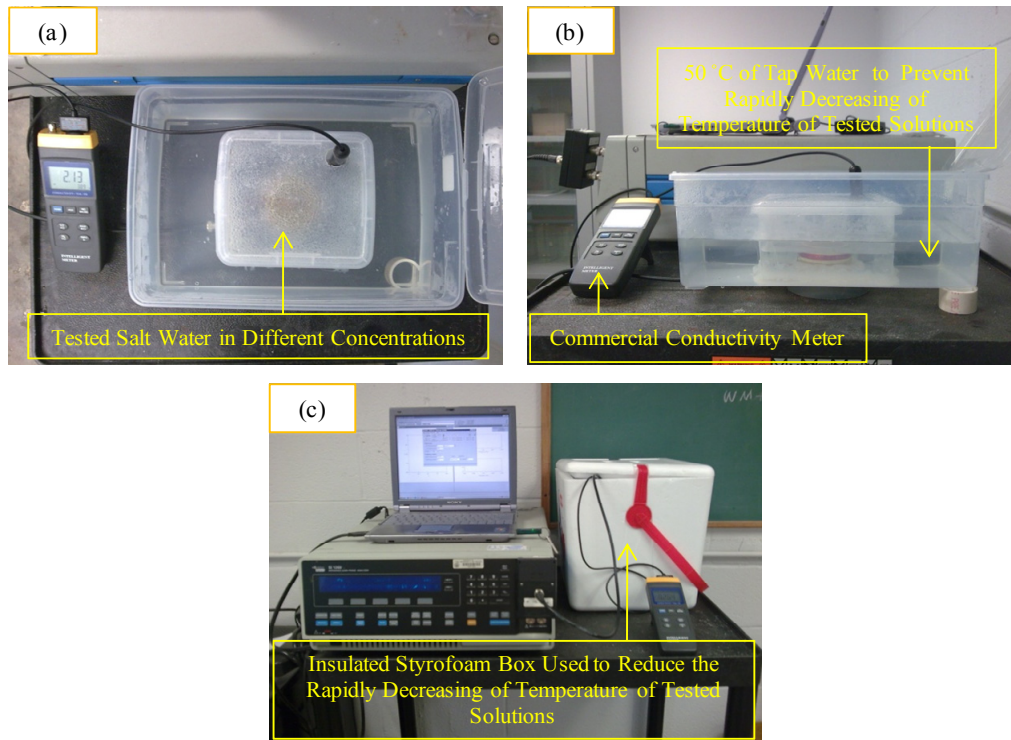
Figure 5.17. Experimental setup for temperature sensitivity test to the analog conductivity sensor

The measured variations in the conductivity of the salt water with temperature, determined using the commercial conductivity probe, are plotted in Figure 5.18. For each conductive environment, the conductivity increased slightly with decreasing temperature.
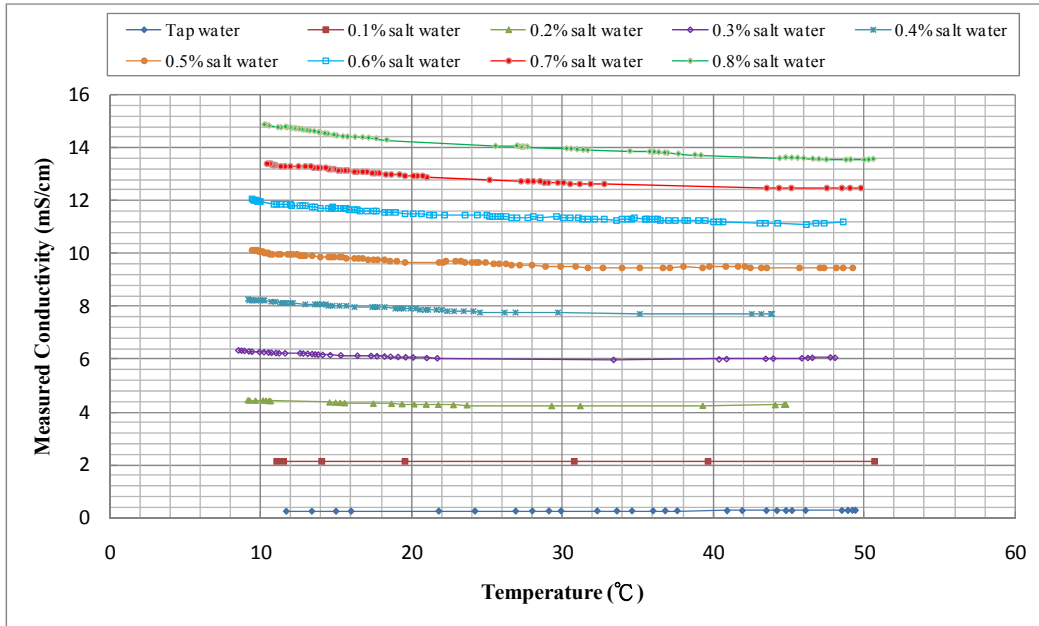
Figure 5.18. Measured relationship between temperature and conductivity for various concentrations of salt water using a commercial conductivity meter.

The pseudo-quality factors ($\overline{Q}_{total}$) extracted from the measured phase response of the conductivity sensor are plotted as a function of temperature in Figure 5.19. As shown in Figure 5.19(a), the pseudo-quality factors were considerably larger when the sensor was submerged in tap water, compared with salt water. Moreover, Figure 5.19 indicates that the pseudo-quality factor increased with decreasing temperatures in all environments and decreased with increasing salt water concentrations for all temperatures.

146
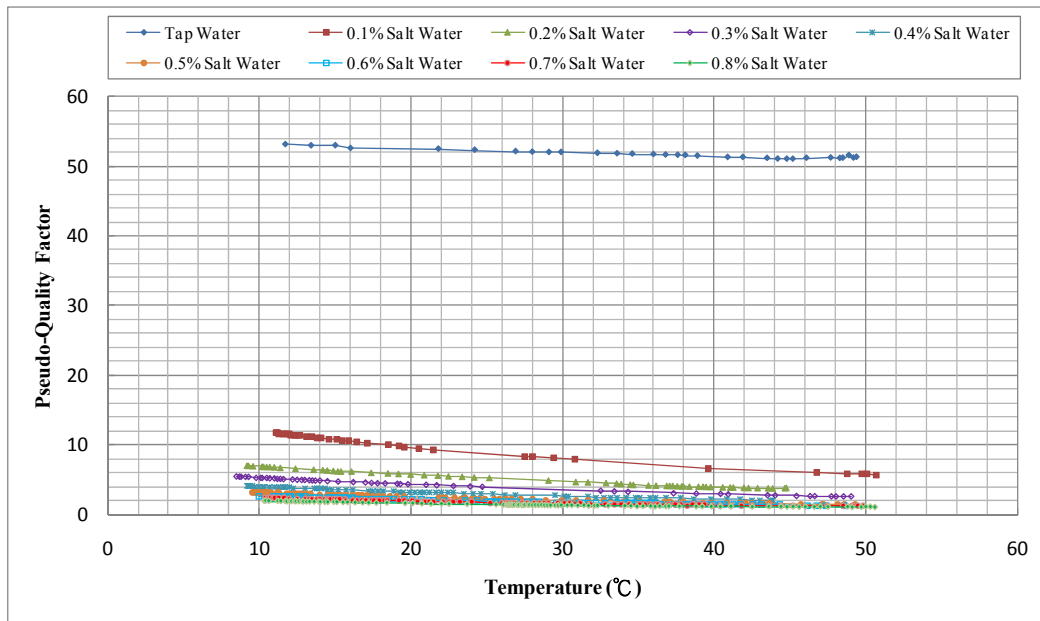
Figure 5.19 (a). Relationship between temperature and total pseudo-quality factor in different salt water concentrations and at different temperatures.
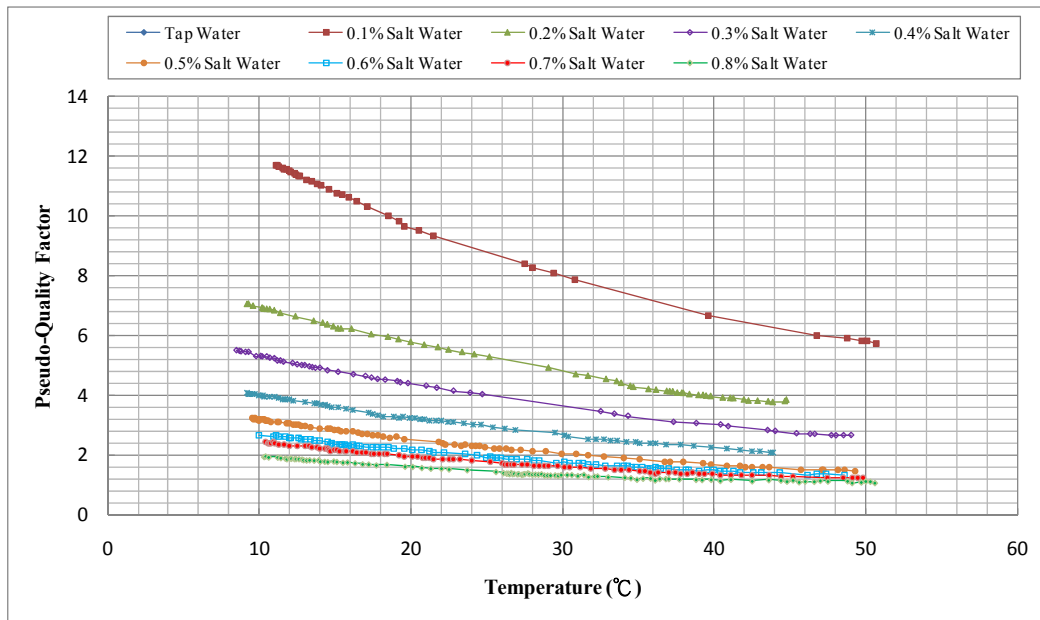
Figure 5.19 (b). Relationship between temperature and total pseudo-quality factor in different salt water concentrations and at different temperatures.

147

To calculate the conductivity of the medium using Eq. 2.8, the total pseudo-quality factor and the pseudo-quality factor in air are required. Because the total pseudo-quality factor was sensitive to temperature (Figure 5.19), the variation of pseudo-quality factor in air at different temperatures was also measured.

Figure 5.20 shows the experimental setup used to determine the pseudo-quality factor in air. The body of the sensor was submerged in water, while the probes were exposed to air (Figure 5.20a). The entire setup was placed inside an insulated box (Figure 5.20b). Initially, the temperature of the water was 50 ˚C, and the sensor was interrogated approximately 30 times at temperatures between 10 and 50 ˚C to determine the variation of $\overline{Q}_{air}$ with temperature. The results are plotted in Figure 5.21.
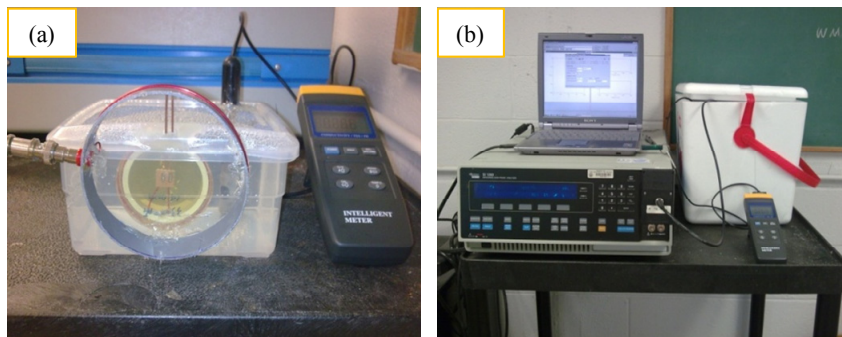
Figure 5.20. Experimental setup used to evaluate temperature sensitivity of body of conductivity sensor.
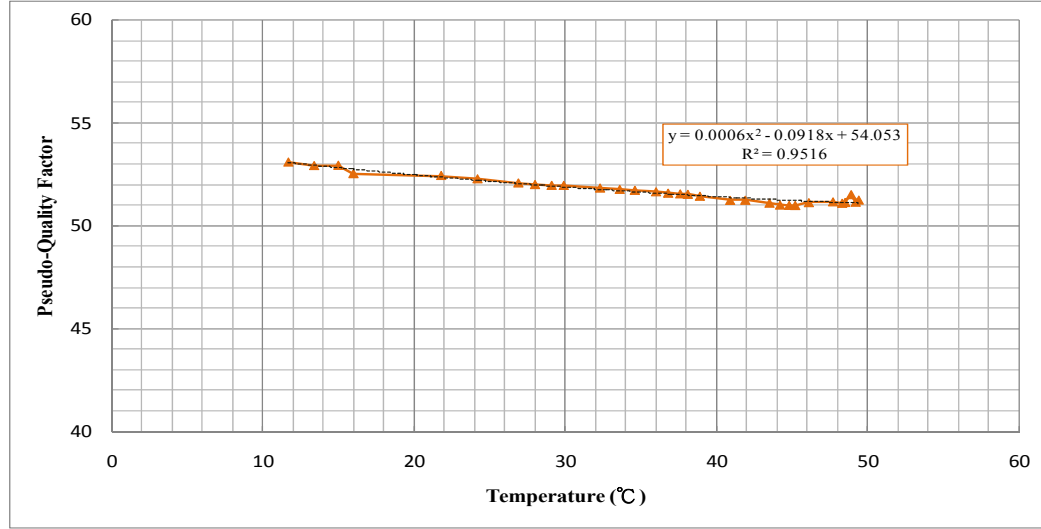
Figure 5.21. Variation of pseudo-quality factor in air with temperature.

At each temperature, the pseudo-quality factor for each conductive medium ($\overline{Q}_{medium}$) was calculated in accordance with Eq. 2.8. Because $\overline{Q}_{total}$ and $\overline{Q}_{air}$ were not necessarily measured at the same temperature, the value of $\overline{Q}_{air}$ corresponding to $\overline{Q}_{total}$ was determined using the quadratic equation shown in Figure 5.21. The values of $\overline{Q}_{medium}$ are plotted in Figure 5.22 as a function of temperature. The observed trends were essentially the same for $\overline{Q}_{total}$ and $\overline{Q}_{medium}$, but the values of $\overline{Q}_{medium}$ were larger.

149
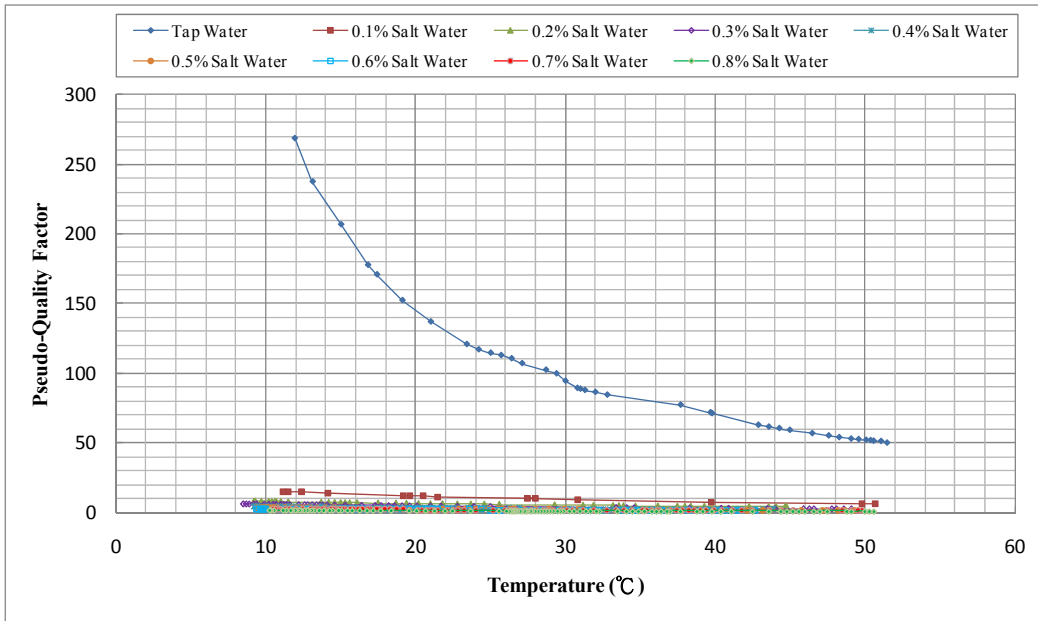
Figure 5.22 (a). Relationship between temperature and pseudo-quality factor in different salt water concentrations and at different temperatures.
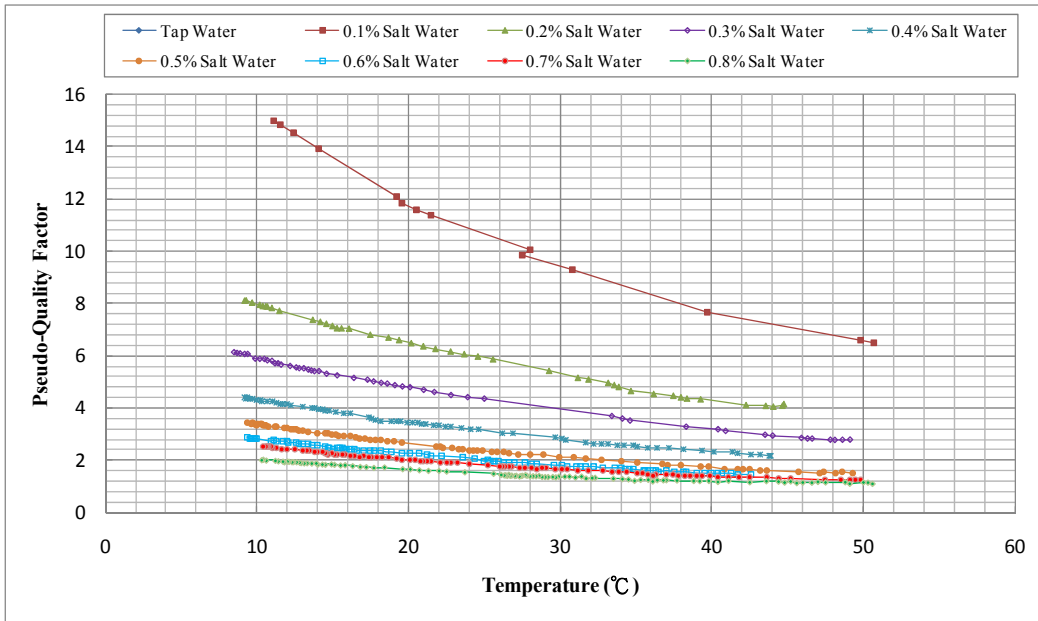
Figure 5.22 (b). Relationship between temperature and pseudo-quality factor in different salt water concentrations and at different temperatures.

150

The conductivities calculated from Eq. 2.8 using $\overline{Q}_{medium}$ are plotted in Figure 5.23. Whereas the conductivities measured using the commercial probe decreased slightly with temperature, the conductivities calculated from the frequency response of the passive conductivity sensor increased with temperature. In addition, calculated conductivities were much more sensitive to temperature and much less sensitive to the concentration of salt water than the measured conductivities.
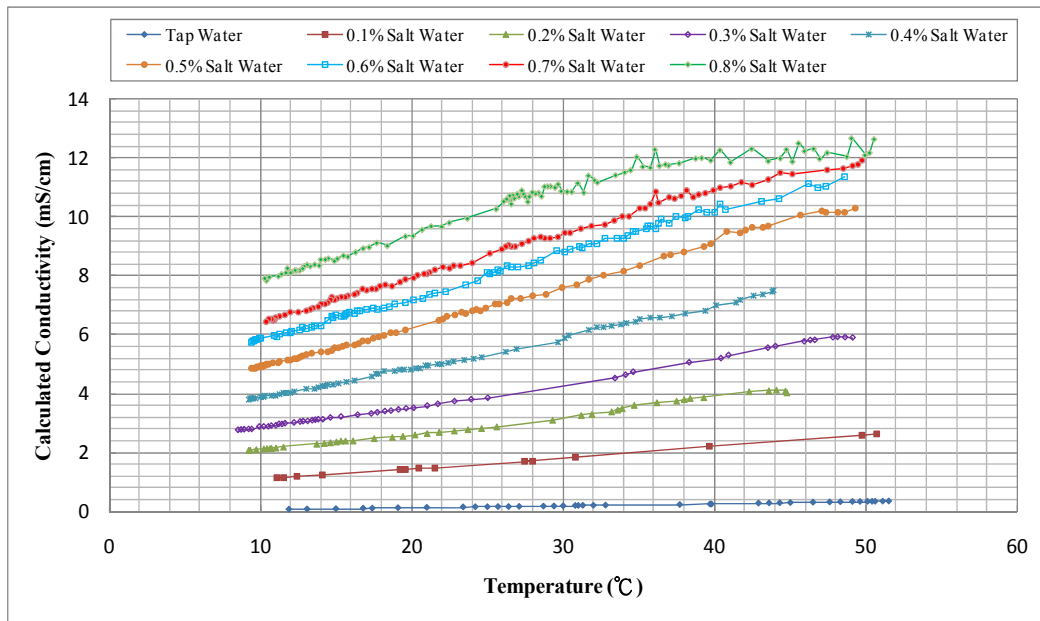
Figure 5.23. Relationship between temperature and conductivity calculated using passive sensor and Eq. 2.8 in different concentration of salt water.

As discussed in the next section, an approach was developed to correlate the conductivity readings from the passive sensor to those from the commercial probe.

151

5.5.1 Temperature Compensation

Conductivity readings are sensitive to temperature. Most commercial conductivity probes include internal algorithms to compensate for temperature. The algorithms used in DC systems is discussed in Section 5.5.1.1. This algorithms is not applicable for AC systems, such as the passive sensors. Therefore, a temperature compensation procedure is proposed in Section 5.5.1.2 for the passive conductivity sensor.

5.5.1.1 Temperature Compensation for DC Systems

Eq. 5.1 lists the formula commonly used for temperature compensation in DC systems. This formula uses the temperature compensation slope of the material, α, to convert the conductivity at temperature T to the conductivity at a common temperature, T'. The complete test results in the different salt water concentration environments are reported in Appendix D.3.

$$\sigma_{T'} = \frac{\sigma_T}{1+\alpha\,(T-T')}$$
(5.1)

Where

$\sigma_{T'}$: Electrical conductivity at a common temperature, T'.

σ_T : Electrical conductivity at a measured temperature, T .

α : Temperature compensation slope of the material.

T　: Measured temperature in degrees Celsius.

T′　: Common temperature in degrees Celsius, generally set at 25˚C.

In order to use Eq. 5.1, α must be known. In general, the temperature compensation slope of a material can be obtained through laboratory testing. Naturally occurring water, for instance, has a temperature compensation slope of about 2% / °C. However, this slope can range from 1 to 3 % / °C due to the variations in the chemical compositions of soluble minerals. In this thesis, the NaCl solution was selected to simulate the pore solution within concrete.

Table 5.7 lists the test results of the temperature compensation slopes for NaCl electrolyte reported by a manufacturer of commercial conductivity probes (Horiba, Ltd, 2010). The temperature compensation slopes for concentrations of salt water used in this thesis can be extrapolated from these data, as shown in Table 5.8.

Table 5.7. Temperature compensation slopes for NaCl electrolytes

Density of NaCl (wt%)	Conductivity (mS/cm)	Temperature Compensation Slope (%/°C)	Source
0	-	3.0	Fitting results to the measurements obtained from the commercial conductivity meter
5	67	2.17	
10	121	2.14	HORIBA, Ltd, 2010
15	164	2.12	

The temperature compensation slopes for tap water in Austin, however, was assumed to be the maximum value of 3.0 %/°C. This value was obtained by fitting the results with the slope of the measurements from the commercial conductivity meter.

Table 5.8. Extrapolated temperature compensation slopes for different concentrations of NaCl.

Concentration of NaCl (wt%)	Temperature Compensation Slope (%/°C)
0.1	2.1994
0.2	2.1988
0.3	2.1982
0.4	2.1976
0.5	2.1970
0.6	2.1964

5.5.1.2 Temperature Compensation for Passive Sensors

The data shown in Figure 5.23 were used to investigate the influence of temperature on the conductivities calculated from the frequency response of the passive conductivity sensors. Because the pseudo-quality factors obtained from the 0.7 and 0.8% concentrations of salt water were very small, and the conductivities calculated from these readings appeared to have more inherent error, only test results obtained from tap water and 0.1 to 0.6% concentrations of salt water were used.

Figure 5.24 illustrates the variations in conductivities using the commercial and passive sensors for 0.1% concentration of salt water. The slopes of the two curves are clearly different. If Eq. 5.1 is used to compensate for temperature, along with $\alpha = 2.1994$, the two curves become parallel (Figure 5.25). However, the calculated conductivity readings are considerably lower than the measured values.

154
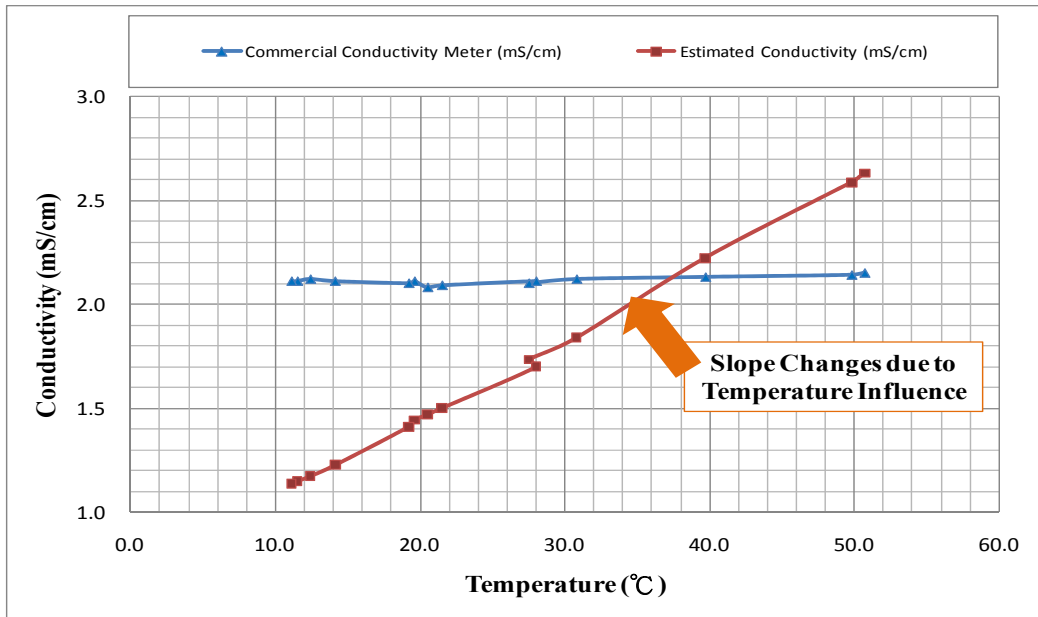
Figure 5.24. Variation of measured and calculated conductivity with temperature for 0.1% concentration of salt water.
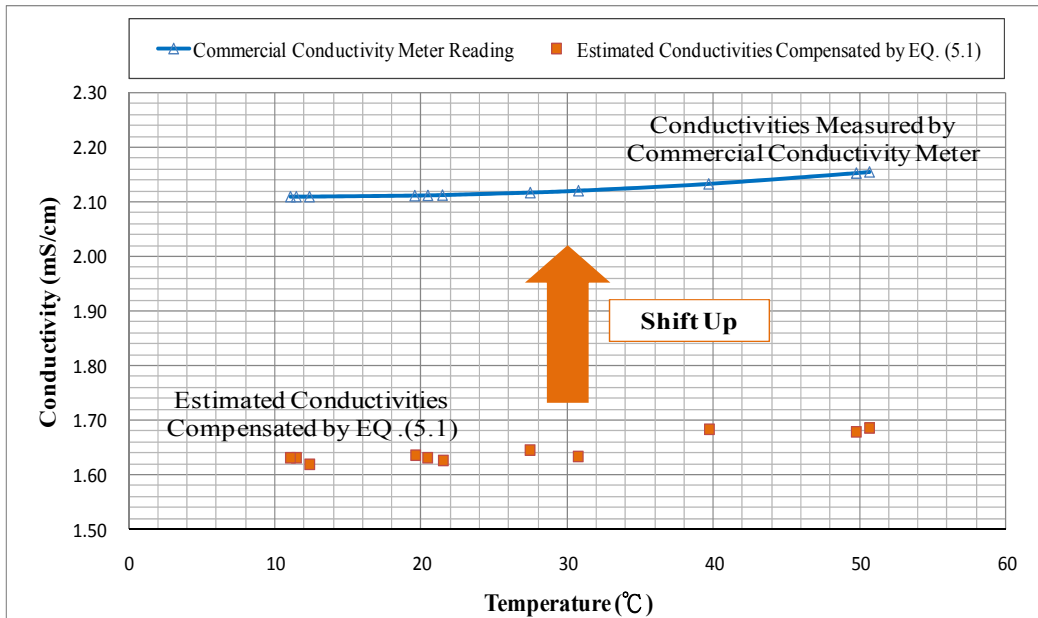
Figure 5.25. Use of Eq. 5.1 to compensate calculated conductivity for temperature variations (0.1% concentration of salt water).

Based on the data shown in Figure 5.25, the algorithm for temperature compensation for the passive conductivity sensor (AC system) was modified to include a constant, C, as shown in Eq. 5.2. The complete temperature compensation process for conductivities calculated from the frequency response of the passive sensor is illustrated in Figure 5.26.

$$\sigma_{T'} = \frac{\sigma_T}{1+\alpha\,(T-T')} + C \tag{5.2}$$

In the first step, Eq. 5.1 was applied to adjust the slope of the estimated conductivity-temperature curve (Figure 5.26 top). The temperature compensation slopes listed in Table 5.8 were used. In the second step, a linear or quadratic equation was fit to the compensated data (Figure 5.26 middle). The step was included to minimize errors associated with small variations in the measured data and is discussed in more detail in Appendix D.4. In the third step, the constant, C, needed to match the measured data using the commercial conductivity probe and the polynomial equation was determined (Figure 5.26 bottom).
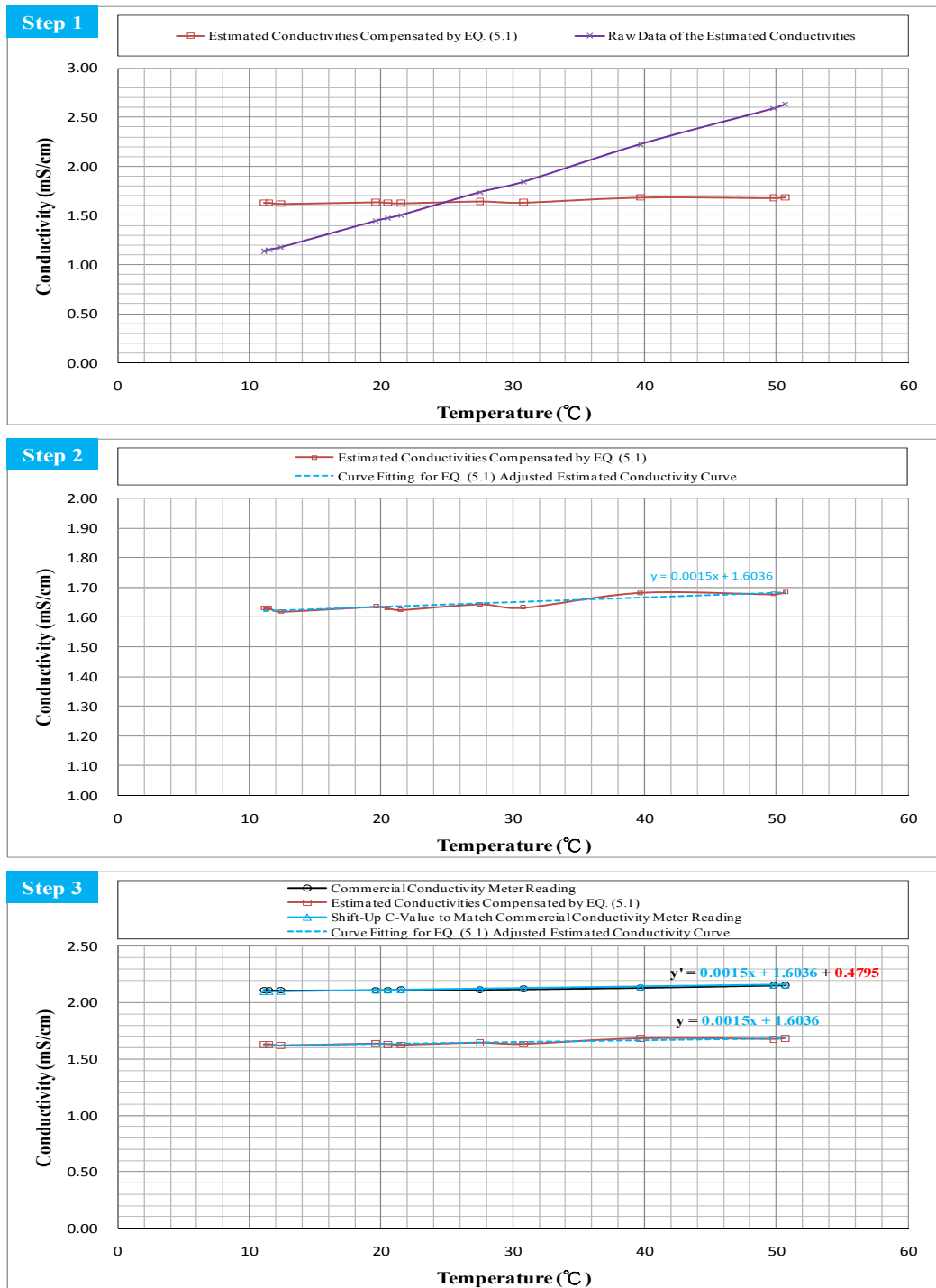
Figure 5.26. Three steps used to compensate the calculated conductivity from the passive conductivity sensor for temperature.

Table 5.9 lists the values of C corresponding to different concentrations of salt water. The value of C increases with the concentration of salt water (Figure 5.27). However, this relationship is not linear.

Table 5.9. Values of C used in Eq. 5.2 for different concentrations of salt water.

Salt Water Concentration (%)	C (mS/cm)
Tap Water	0.106
0.10	0.480
0.20	1.335
0.30	2.056
0.40	2.480
0.50	2.705
0.60	3.342
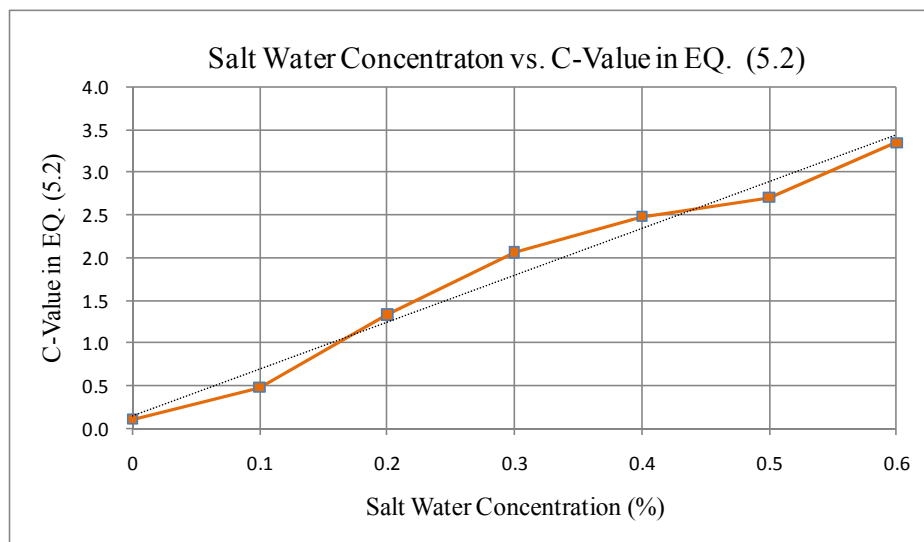
Figure 5.27. Relationship between the salt water concentration and value of C in Eq. 5.2.

5.6 Sensitivity to Proximity of Reinforcement

During construction, the passive conductivity sensor will be tied to the

158

reinforcement cage before placement of the concrete. When the sensor is interrogated within the reinforced concrete member, the steel reinforcement is expected to influence the magnetic field that develops between the reader coil and the sensor. To understand the sensitivity of the measured response to the proximity of steel reinforcement, a set of tests was conducted in air (Figure 5.28). The total read distance between the reader coil and the sensor was 1.25 in. in all experiments discussed in this section.
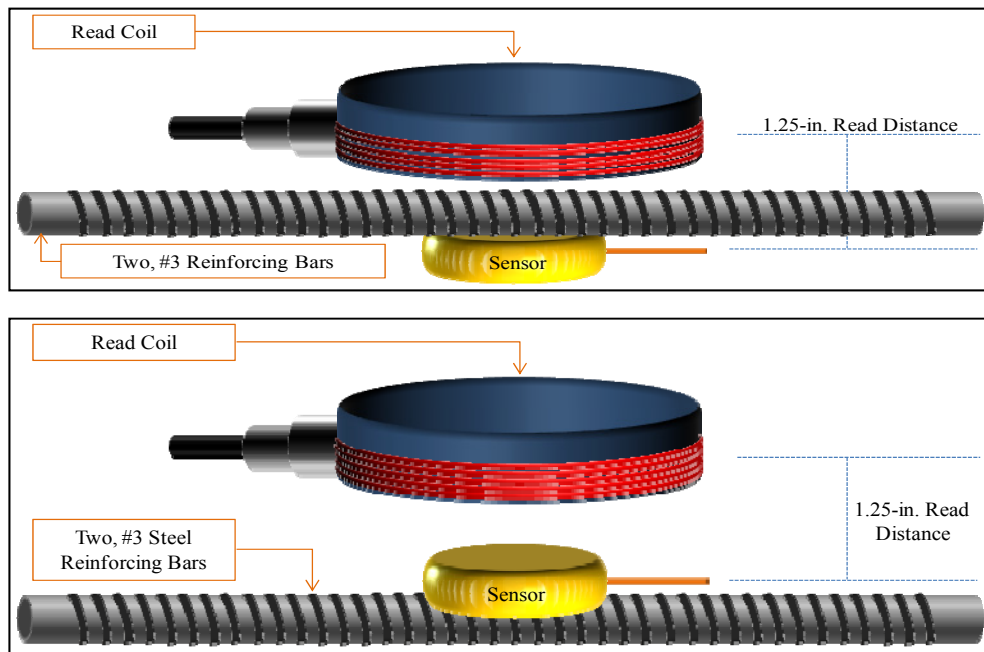
Figure 5.28. Experimental setup to determine sensitivity of sensor response to proximity of reinforcement: case 1 (top) for the sensor below the reinforcement and case 2 (bottom) for sensor above the reinforcement.

The sensor was interrogated between 0.35 and 0.65 MHz using a frequency resolution of 500 Hz. The primary experimental variables are shown in Figure 5.29

and Figure 5.30, for a total of 12 configurations. The sensor was positioned above the rebar in six configurations and below the rebar in the other six configurations. The size of the gap between the sensing probes and the rebar, and the orientation of the probes relative to the rebar were also varied.
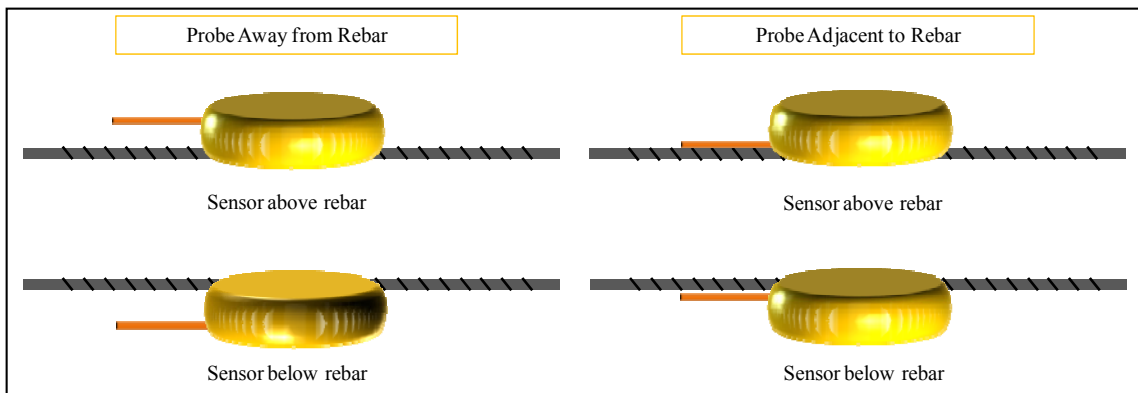
Figure 5.29. Relative positions of sensor probe, and rebar.
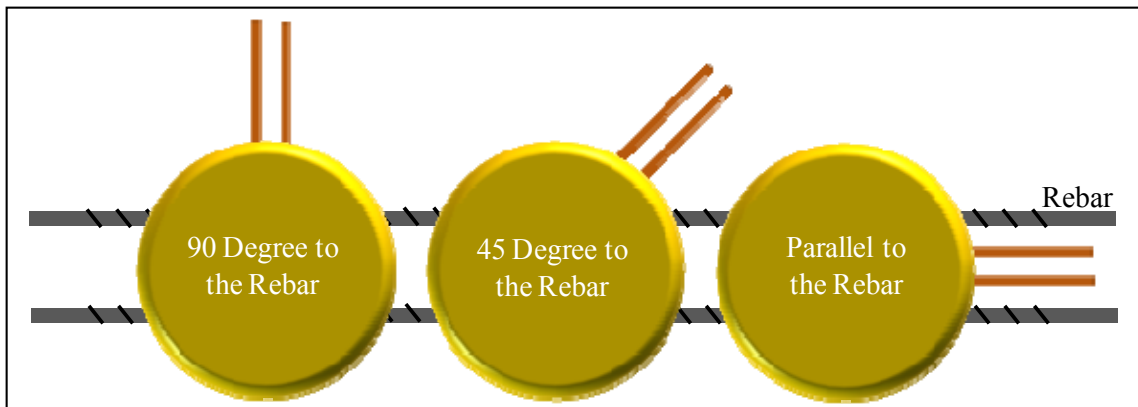
Figure 5.30. Angle between sensing probes and rebar.

Table 5.10 summarizes the configurations tested and results from all the tests. The resonant frequency was not sensitive to the proximity of the reinforcement. The pseudo-quality factors decreased when the conductivity sensor was placed near the

steel reinforcement, while the phase dip increased for configurations with the sensor above the rebar and decreased for configurations with the sensor below the rebar. The pseudo-quality factors and phase dips were sensitive to each of the three parameters investigated.

The pseudo-quality factors were least sensitive to the orientation of the probe, relative to the rebar (Figure 5.30). For cases where the sensing probes were adjacent to the rebar, the pseudo-quality factors were largest when the probes were oriented $45°$ from the reinforcement. However, when the sensing probes were away from the rebar, the pseudo-quality factors were largest when the probes were aligned with the reinforcement.

The pseudo-quality factors were consistently larger when the copper probes were positioned adjacent to the rebar than when the probes were away from the rebar (Figure 5.29). If the other conditions were held constant, the pseudo-quality factor was consistently larger when the sensor was positioned below the steel reinforcement, compared with above the steel reinforcement (Figure 5.31).

Table 5.10. Sensor Responses of the Conductivity Sensor due to the Rebar Influence

Test Case	Relative Sensor Location	Relative Position of Sensing Probes	Angle between Sensing Probes and Rebar (degree)	Resonant Frequency (MHz)	Phase Dip (degree)	Pseudo-Quality Factor
00	No Rebar			0.498	27.4	58.83
01	Above Rebar	Away from Rebar	0	0.501	32.9	33.53
02	Above Rebar	Away from Rebar	45	0.501	31.1	32.50
03	Above Rebar	Away from Rebar	90	0.501	32.0	33.21
04	Above Rebar	Adjacent to the Rebar	0	0.501	48.2	37.50
05	Above Rebar	Adjacent to the Rebar	45	0.500	45.6	39.25
06	Above Rebar	Adjacent to the Rebar	90	0.501	46.6	37.05
07	Below Rebar	Away from Rebar	0	0.500	17.6	37.76
08	Below Rebar	Away from Rebar	45	0.501	16.5	34.54
09	Below Rebar	Away from Rebar	90	0.501	16.1	34.43
10	Below Rebar	Adjacent to the Rebar	0	0.500	16.2	42.43
11	Below Rebar	Adjacent to the Rebar	45	0.499	15.9	42.61
12	Below Rebar	Adjacent to the Rebar	90	0.499	15.2	42.37
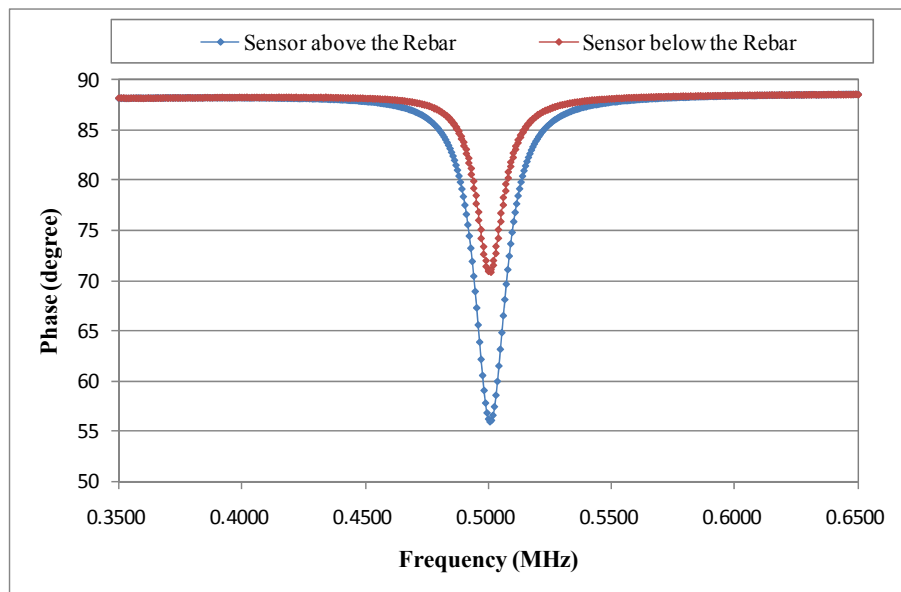
Figure 5.31. Comparison of measured frequency response for configurations 01 and 07.

The trends in phase dip were not consistent with those for pseudo-quality factor. The phase dip was much larger for the configurations where the sensor was placed above the rebar, compared with below the rebar (Figure 5.31). At first glance, the different trends between the pseudo-quality factor and phase dip appear to be contradictory. However, as shown in Figure 5.31, the resonant response is wider and deeper when the sensor is located above the rebar. Because the pseudo-quality factor depends on the width of the resonance curve, rather than the depth, the lower pseudo-quality factor corresponds to the resonant response with the larger phase dip.

The phase dips were consistently larger when the sensing probes were aligned with the reinforcement. If the sensor was located above the rebar, the phase dips were larger when the probes were adjacent to the rebar. In contrast, the phase dips were larger when the probes were away from the rebar if the sensor was located below the rebar.

The results of these experiments demonstrate that both the phase dip and the pseudo-quality factor change when the conductivity sensor is positioned near reinforcing bars. This means that the baseline response of each sensor must be determined after the sensor has been attached to the reinforcing cage. However, this does not limit the applicability of the passive conductivity sensor.

5.7 Conclusion

The results of extensive experimental tests were reported in this chapter. The

goal was to evaluate the sensitivity of the measured frequency response of the passive conductivity sensor to design choices and to the environment. The primary findings are summarized below.

- The analog conductivity sensor must be interrogated using a much finer frequency resolution than the threshold corrosion sensor. The numerical algorithm used to extract the pseudo-quality factor is unreliable if fewer than 20 to 30 readings are captured to define the resonant response.

- For the range of capacitors considered, the maximum resonant response in air was measured using the lowest capacitance while the maximum resonant response in 0.5% salt water was measured suing the highest capacitance.

- As the concentration of salt water increases, the resonant response of the conductivity sensor decreases. The range of conductivities can be increased by decreasing the length of the parallel copper wires in the probe.

- The resonant response of the conductivity sensors is sensitive to both the conductivity and temperature of the medium. While it was possible to correlate the conductivities calculated from the resonant response of the passive conductivity sensor with those measured using a commercial conductivity probe in the laboratory tests, the calibration algorithm requires two constants (α and C) that are extremely sensitive to the conductivity of the medium. Because the chemical composition of the pore solution in

164

concrete is not known a priori, the calculation of these two constants may limit the overall applicability of the passive conductivity sensor.

CHAPTER 6

Summary and Conclusions

Previous researchers at the University of Texas at Austin (Dickerson 2005; Andringa 2006; Puryear 2007) developed prototype, wireless, passive sensors for evaluating conditions within reinforced concrete members. The threshold corrosion sensor was designed to detect the initiation of corrosion and the analog conductivity sensor was designed to monitor environmental conditions within the concrete. Accelerated corrosion tests were used to evaluate the durability and reliability of the sensors.

The research described in this thesis was divided into three parts. Chapter 3 addressed the behavior of the corrosion and conductivity sensors in Slab 3. Puryear (2007) constructed this slab, but the accelerated corrosion tests were ongoing at the time that he completed his graduate studies. The measured response of the sensors and complete autopsy results are presented. Although the sensors behaved as expected, the epoxy housings were not sufficiently durable. Cracking of the epoxy was observed and corrosion products penetrated into the epoxy housing.

Chapter 4 discusses the development of a hybrid housing to protect the corrosion sensors. The circuits were coated with epoxy and then potted using a fiber-reinforced cement paste. This hybrid system addressed the primary durability issues identified in Chapter 3. Some corrosion of the steel sensing wire was observed within the cement

166

paste housing, however. Coating the steel sensing wire with silver solder delayed the onset of corrosion, but is not likely to be a permanent solution. Additional tests of corrosion sensors embedded in concrete are required to determine if corrosion of the steel sensing wire within the cement paste housing limits the applicability of the sensors.

The analog conductivity sensor was investigated in Chapter 5. The analog data extracted from the resonant response of the sensor was found to be extremely sensitive to the frequency resolution used in the interrogation. A much finer resolution is required to obtain reliable data from the analog conductivity sensor than the threshold corrosion sensor. The response of the conductivity sensor was also extremely sensitive to temperature. Although a procedure was developed to compensate for temperature, this procedure is only valid if the environmental conditions within the concrete are known. This sensitivity may limit the overall applicability of the analog conductivity sensor.

APPENDIX A

Measured Response of Sensors in Slab 3

A.1 Timeline of the Wet/Dry Cycle Corrosion Test in Slab 3

Table A.1(a) The timeline of the wet/dry cycle corrosion test in Slab 3

Interrogation	Date	Change in Days	Days	Condition
3	2006/4/6	0	0	Start Test
4	2006/4/20	14	14	End Wet Cycle
5	2006/5/4	14	28	End Dry Cycle
6	2006/5/18	14	42	End Wet Cycle
7	2006/6/1	14	56	End Dry Cycle
8	2006/6/15	14	70	End Wet Cycle
9	2006/6/29	14	84	End Dry Cycle
10	2006/7/13	14	98	End Wet Cycle
11	2006/7/27	14	112	End Dry Cycle
12	2006/8/10	14	126	End Wet Cycle
13	2006/8/24	14	140	End Dry Cycle
14	2006/9/7	14	154	End Wet Cycle
15	2006/9/22	15	169	End Dry Cycle
16	2006/10/7	15	184	End Wet Cycle
17	2006/10/20	13	197	End Dry Cycle
18	2006/11/4	15	212	End Wet Cycle
19	2006/11/16	12	224	End Dry Cycle
20	2006/11/30	14	238	End Wet Cycle
21	2006/12/14	14	252	End Dry Cycle
22	2007/1/3	20	272	End Wet Cycle
23	2007/1/18	15	287	End Dry Cycle
24	2007/2/2	15	302	End Wet Cycle
25	2007/2/15	13	315	End Dry Cycle

Table A.1(b) The timeline of the wet/dry cycle corrosion test in Slab 3

Interrogation	Date	Change in Days	Days	Condition
26	2007/2/28	13	328	End Wet Cycle
27	2007/3/16	16	344	End Dry Cycle
28	2007/3/29	13	357	End Wet Cycle
29	2007/4/12	14	371	End Dry Cycle
30	2007/4/28	16	387	End Wet Cycle
31	2007/5/10	12	399	End Dry Cycle
32	2007/5/23	13	412	End Wet Cycle
33	2007/6/7	15	427	End Dry Cycle
34	2007/6/22	15	442	End Wet Cycle
35	2007/7/13	21	463	End Dry Cycle
36	2007/7/27	14	477	End Wet Cycle
37	2007/8/13	17	494	End Dry Cycle
38	2007/8/24	11	505	End Wet Cycle
39	2007/9/25	32	537	End Dry Cycle
40	2007/10/9	14	551	End Wet Cycle
41	2007/10/23	14	565	End Dry Cycle
42	2007/11/5	13	578	End Wet Cycle
43	2008/3/19	135	713	Continued Dry Cycle
44	2008/6/16	89	802	Continued Dry Cycle
45	2008/7/2	16	818	End Wet Cycle
46	2008/7/15	13	831	End Dry Cycle
-	2008/7/28	13	844	End Wet Cycle
-	2008/8/11	14	858	End Dry Cycle
-	2008/8/24	13	871	End Wet Cycle
-	2008/9/6	13	884	End Dry Cycle
-	2008/9/29	23	907	End Wet Cycle
47	2008/10/30	31	938	Continued Dry Cycle
48	2008/11/11	12	950	Continued Dry Cycle
49	2009/2/7	88	1038	Continued Dry Cycle

A.2 Response of Sensors in Slab 3
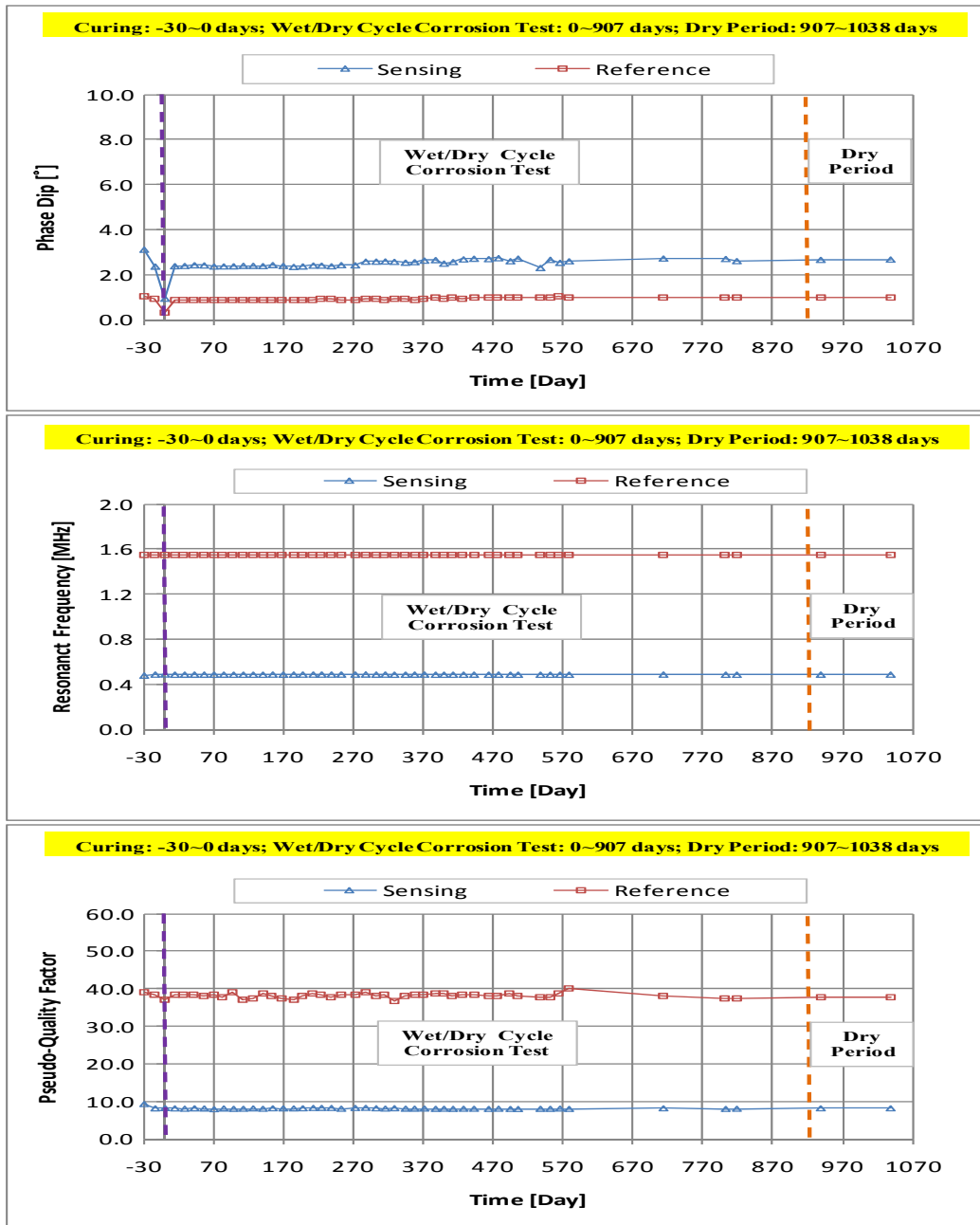
Figure A.2.1. The response of Sensor B125.
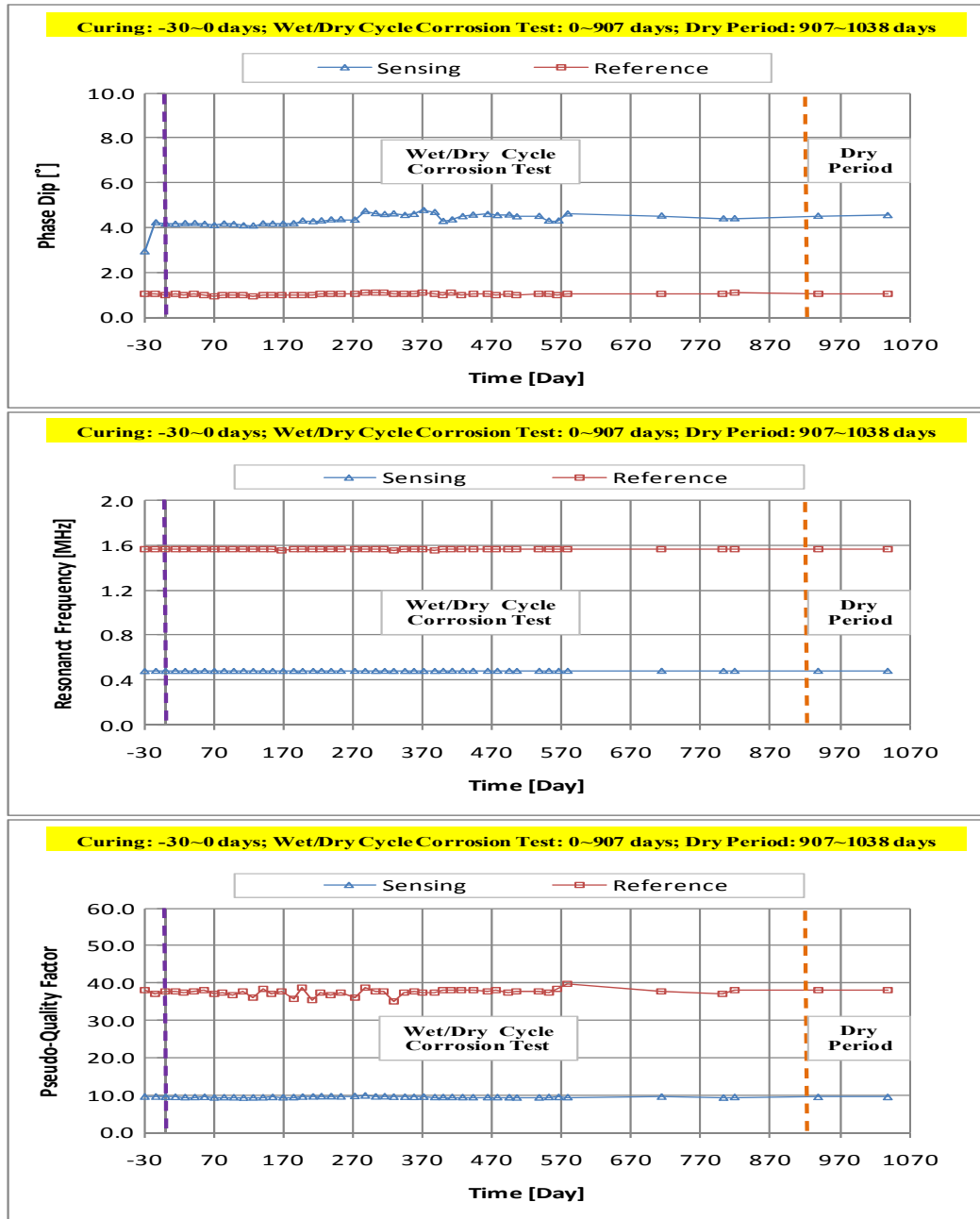
Figure A.2.2. The response of Sensor B126.
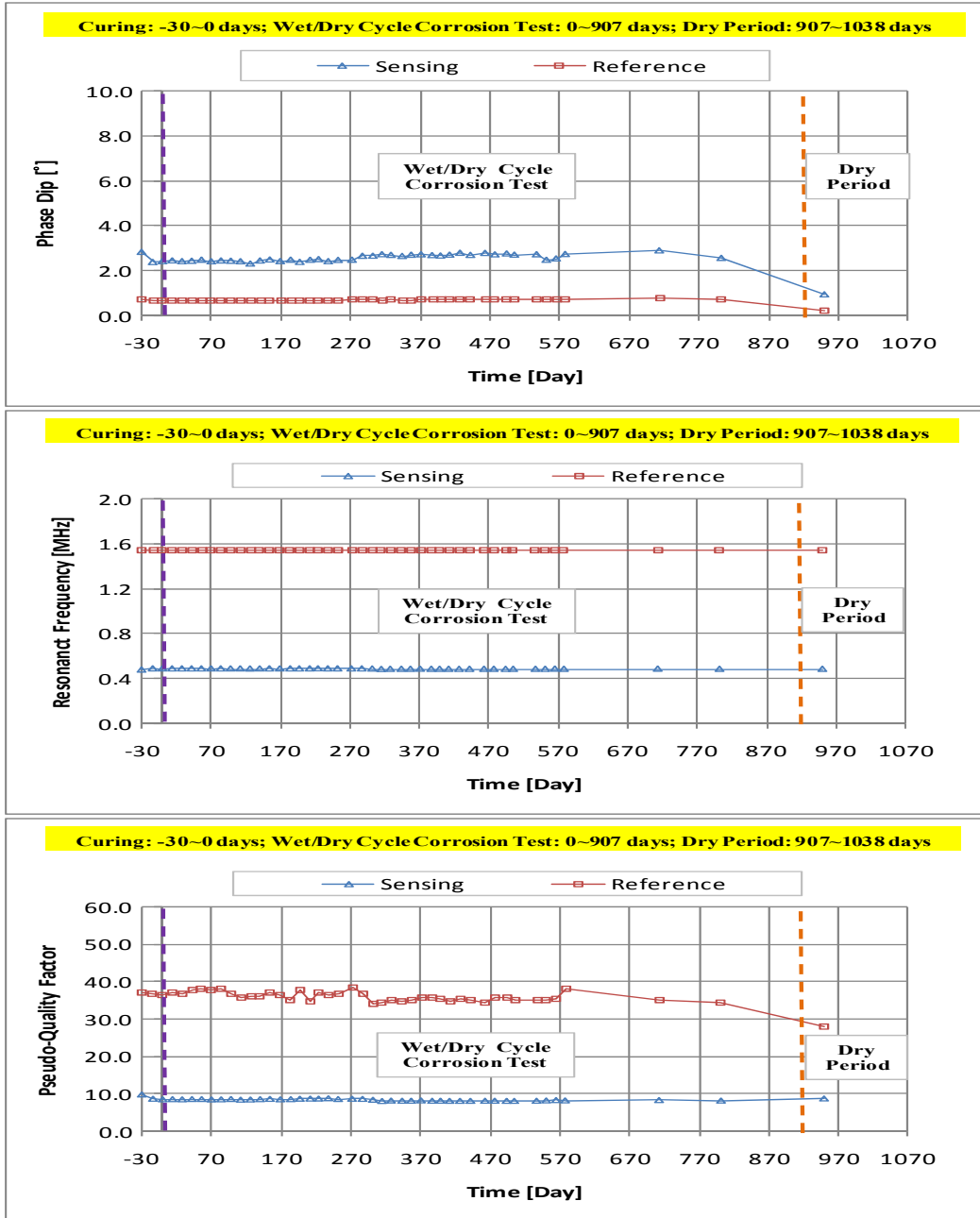
Figure A.2.3. The response of Sensor B127.

172
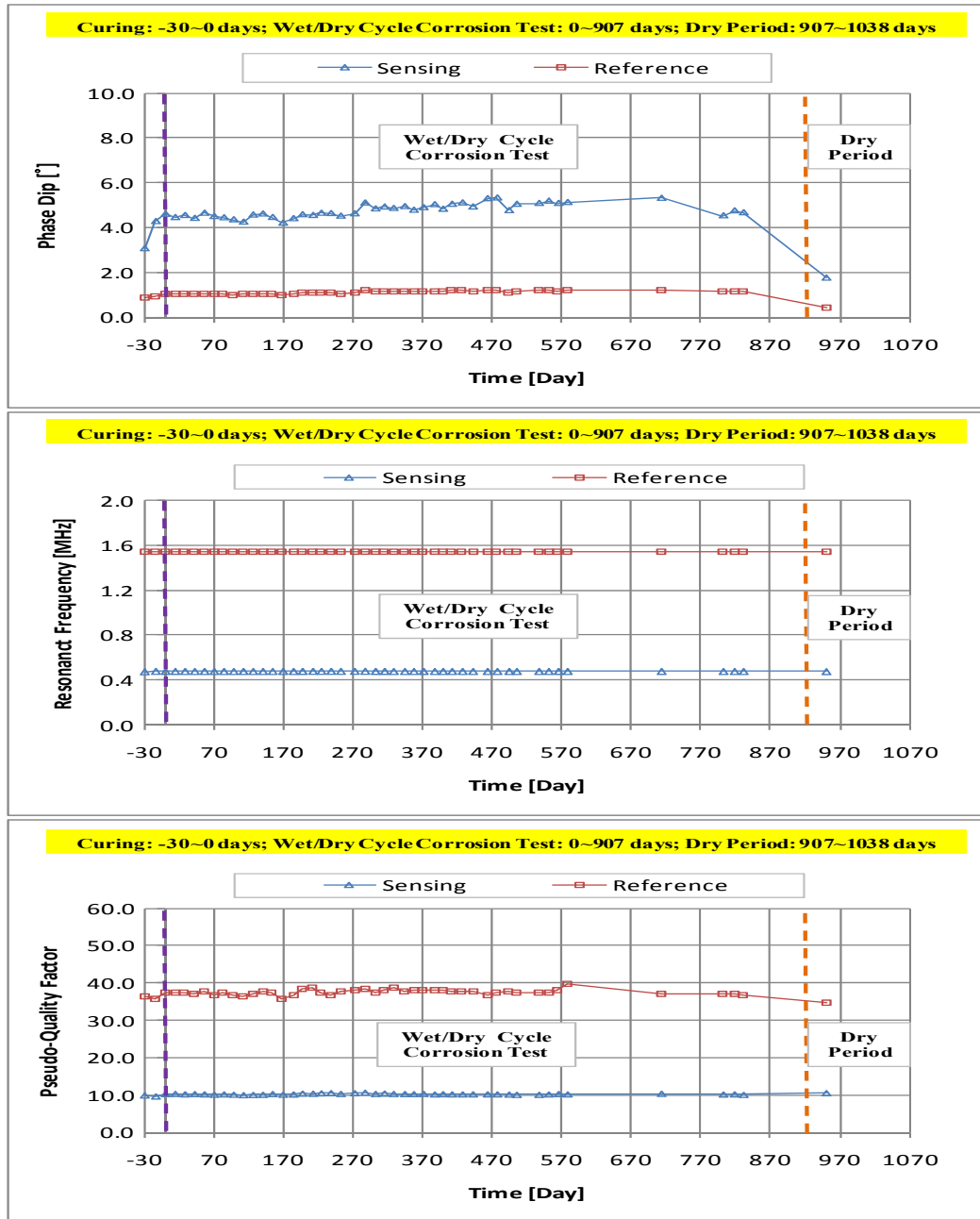
Figure A.2.4. The response of Sensor B128.

173
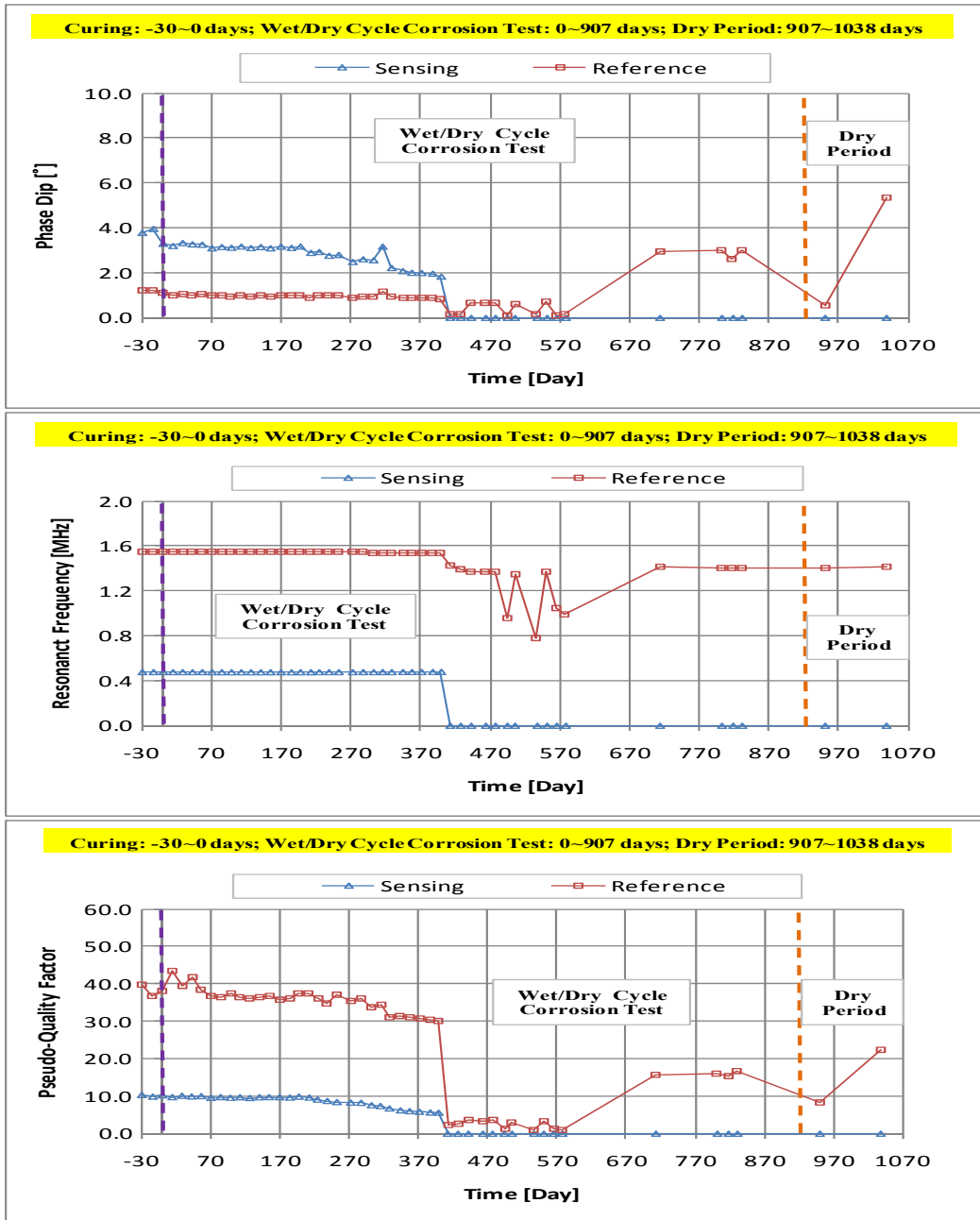
Figure A.2.5. The response of Sensor B134.

174
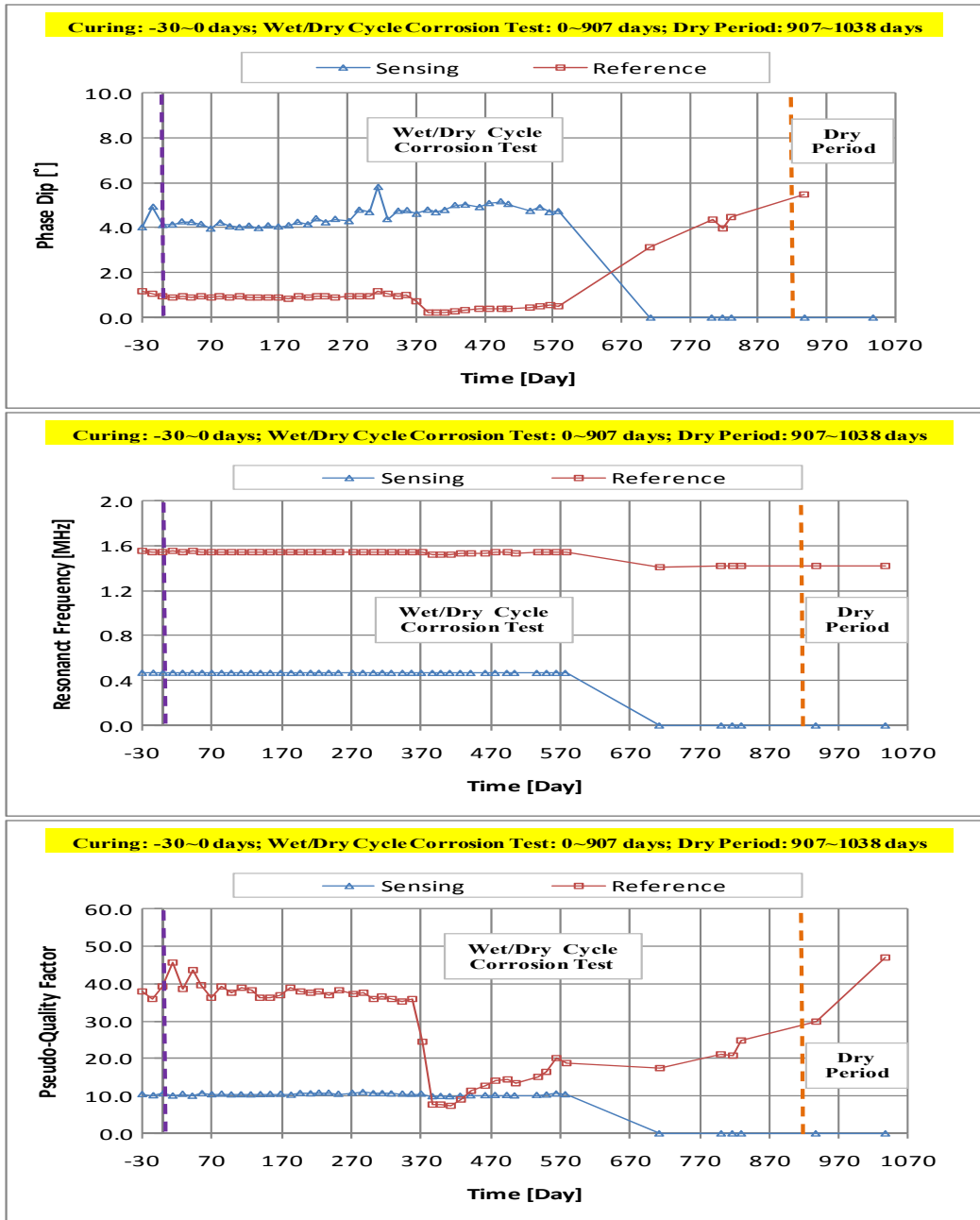
Figure A.2.6. The response of Sensor B135.

175
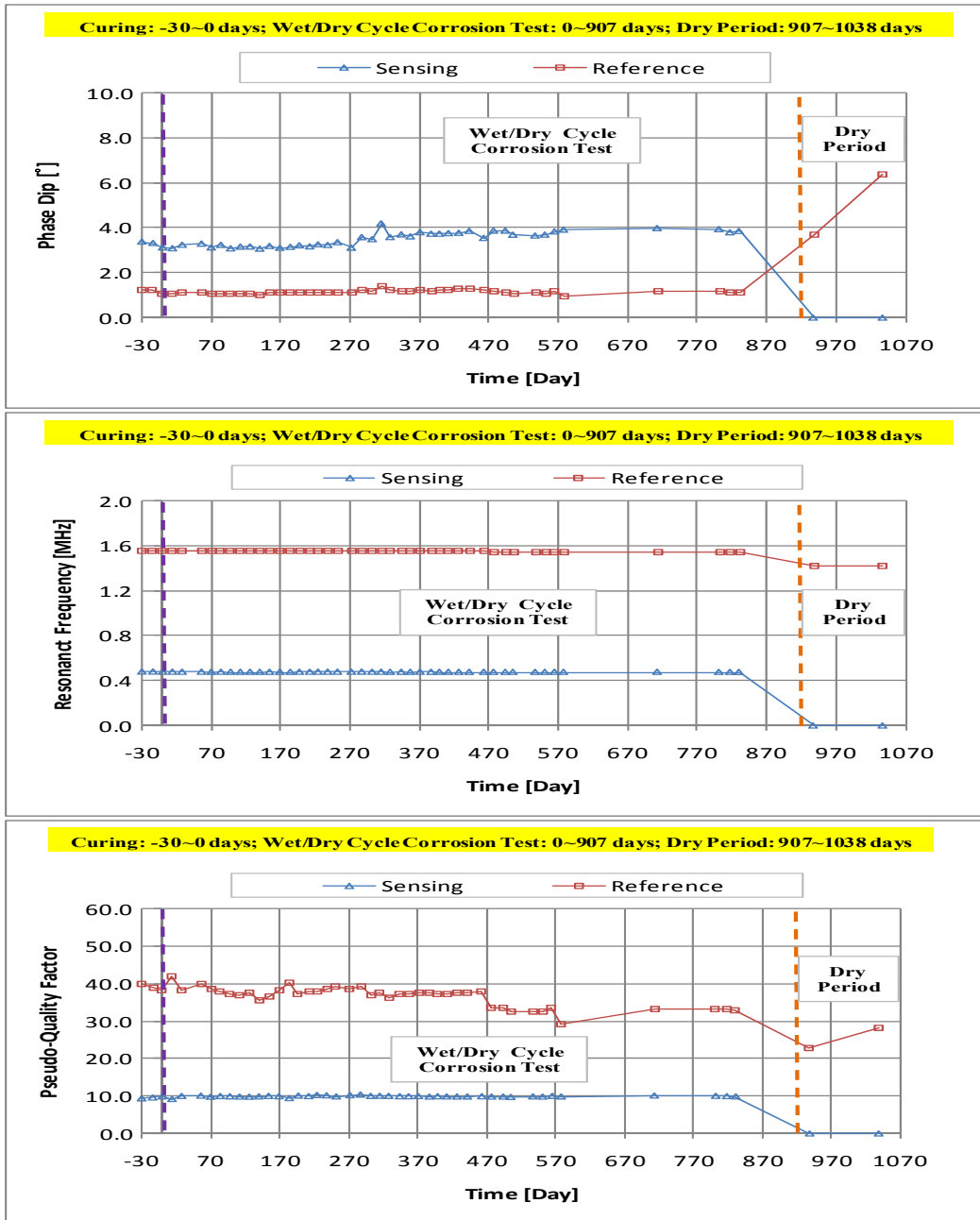
Figure A.2.7. The response of Sensor B136.

176
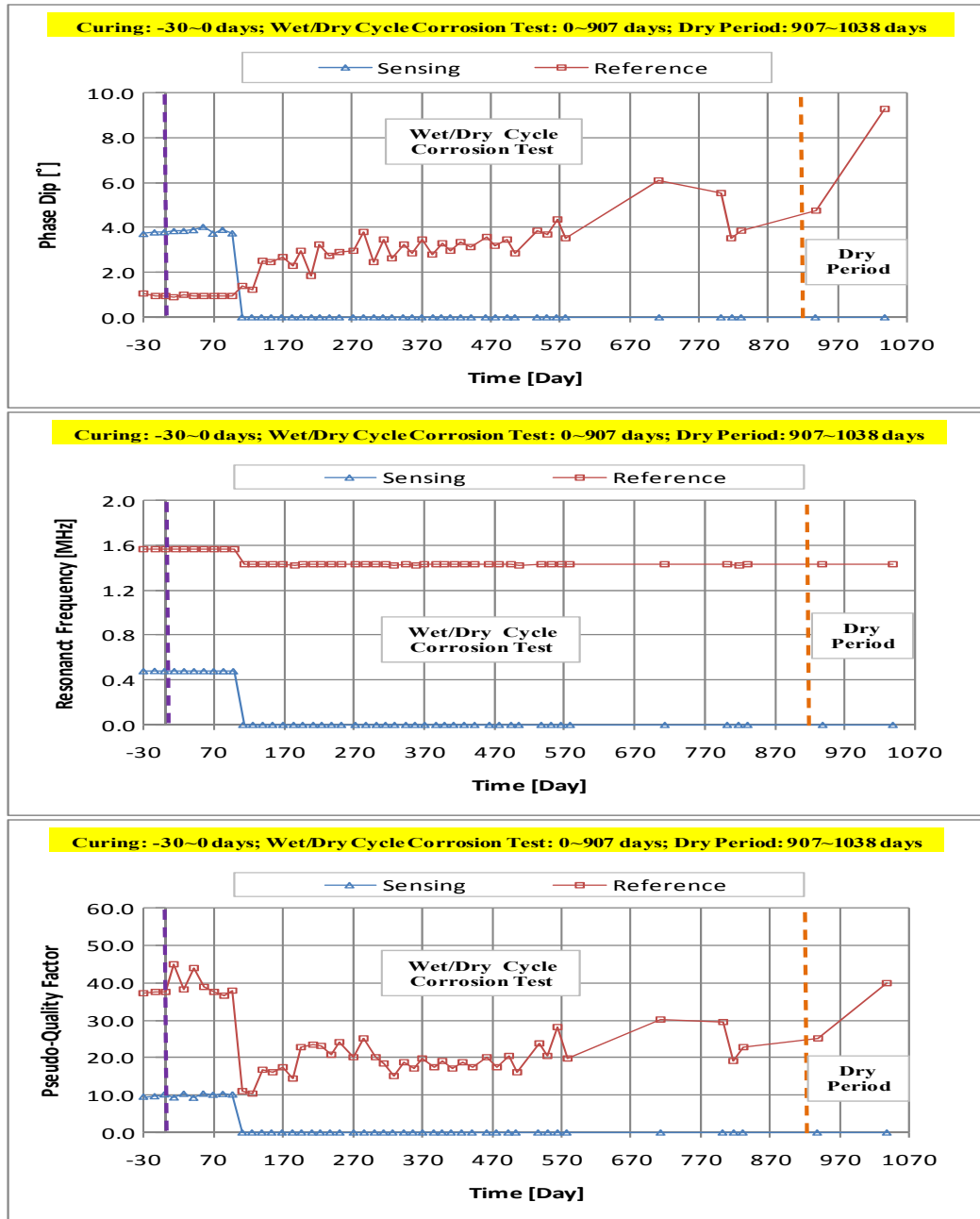
Figure A.2.8. The response of Sensor B137.

177
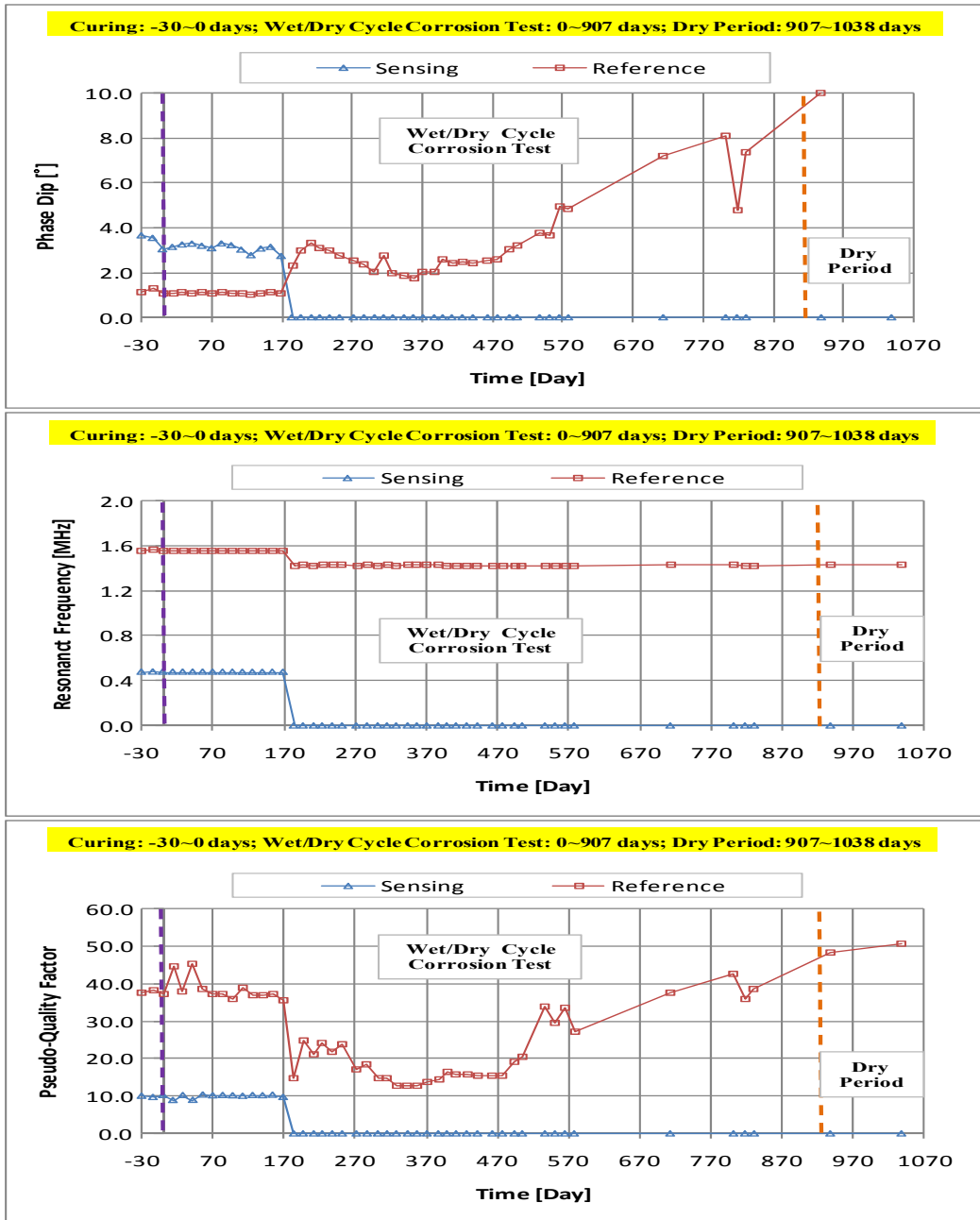
Figure A.2.9. The response of Sensor B138.

178
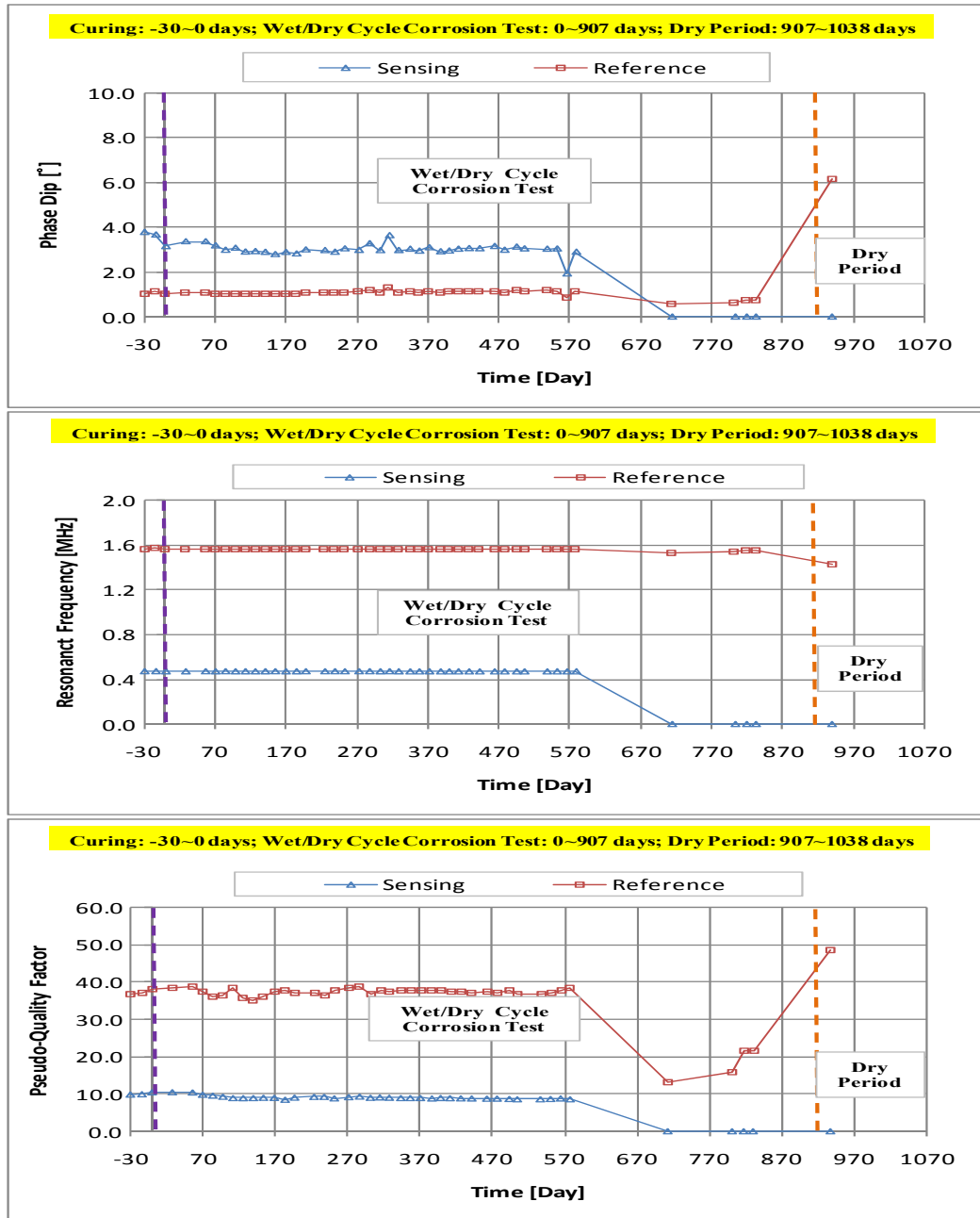
Figure A.2.10. The response of Sensor B139.

179
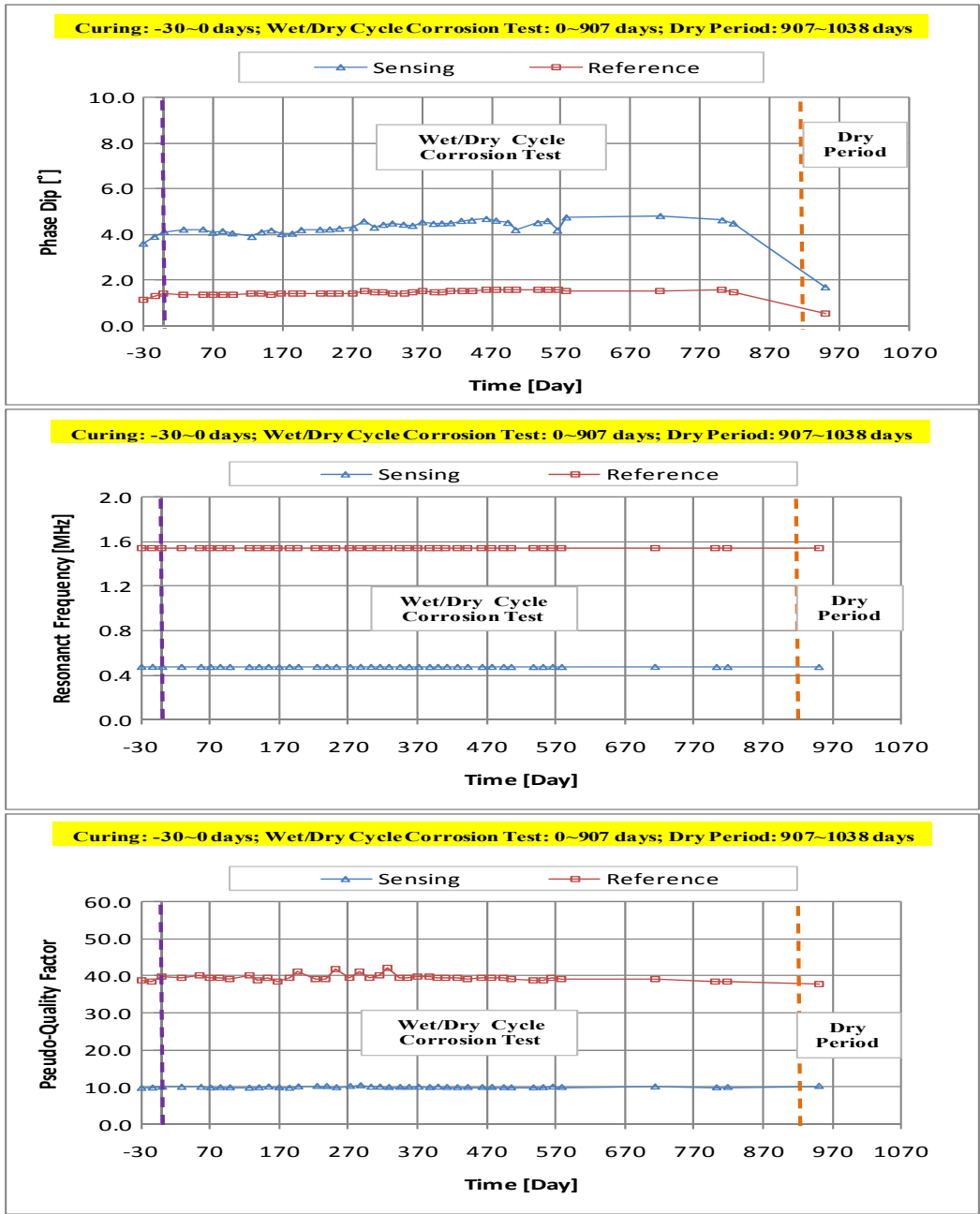
Figure A.2.11. The response of Sensor B140.
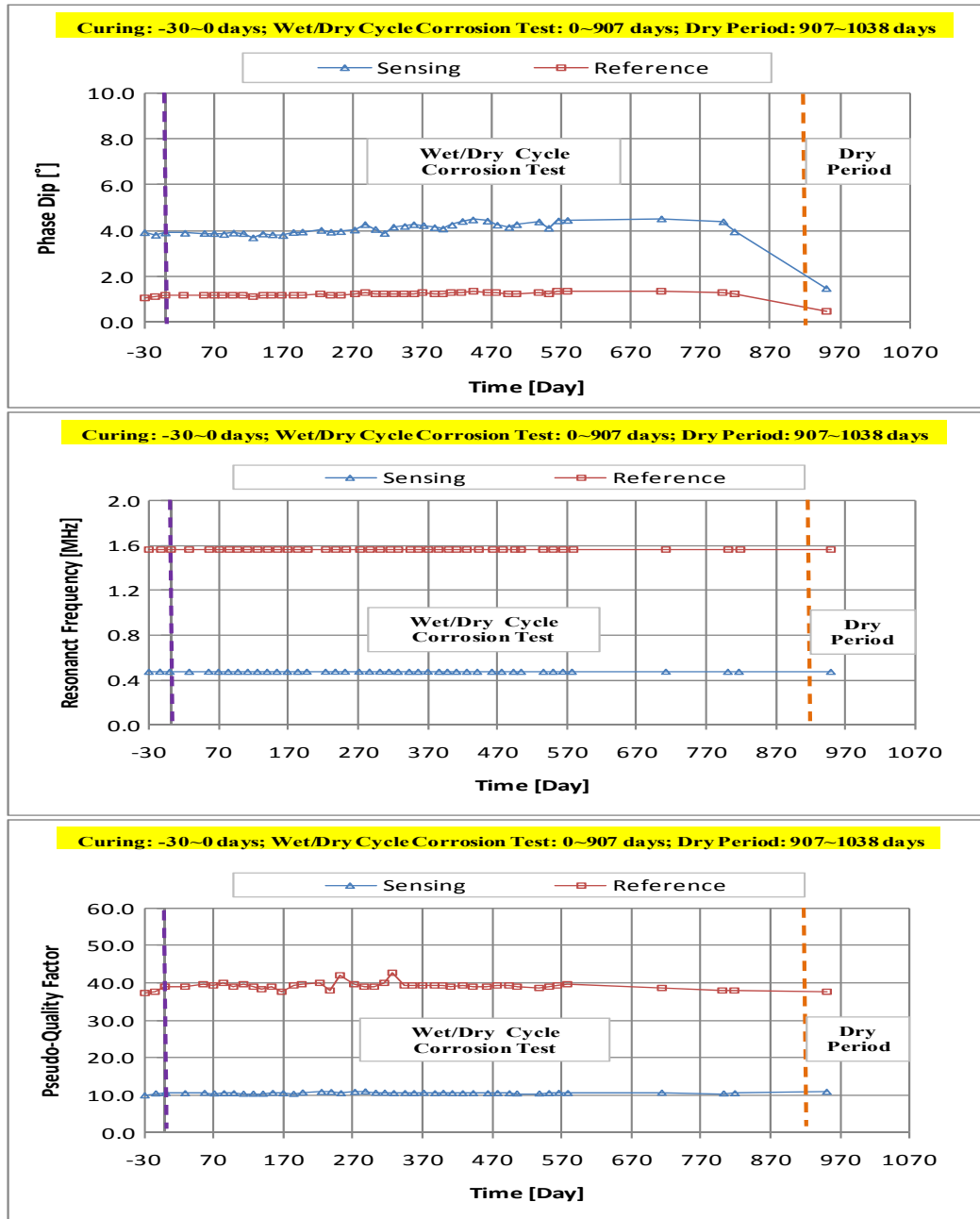
Figure A.2.12. The response of Sensor B141.
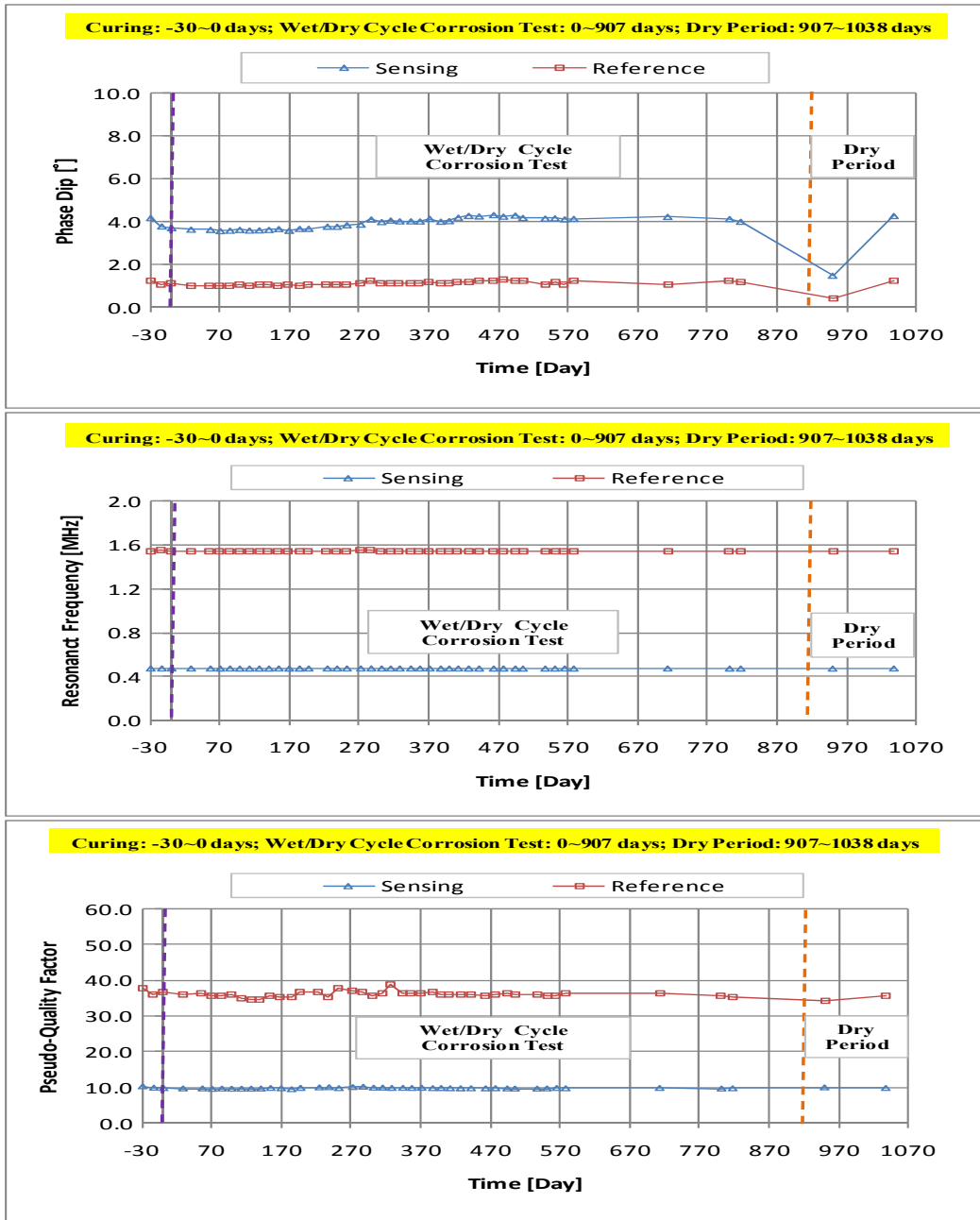
Figure A.2.13. The response of Sensor B142.

182
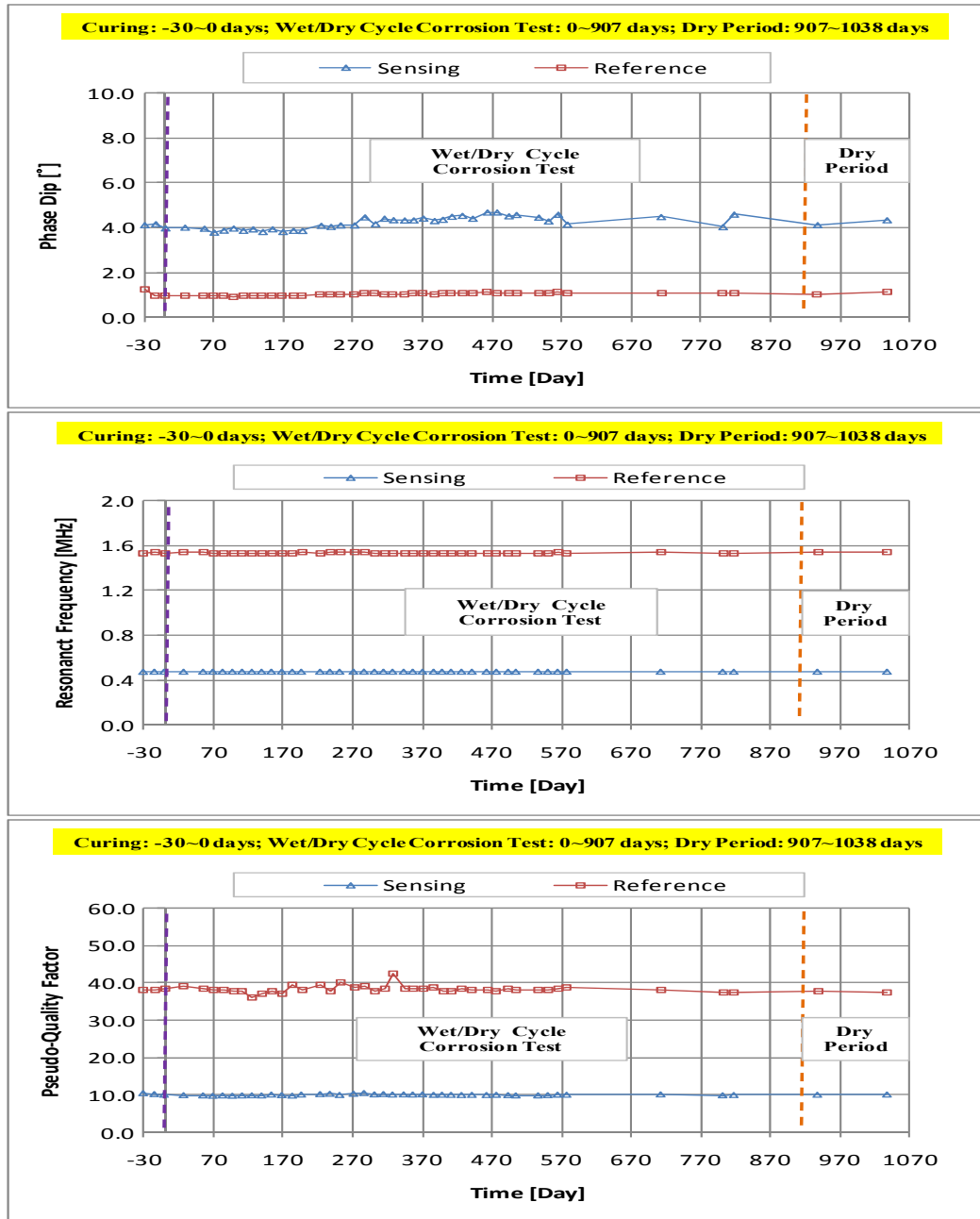
Figure A.2.14. The response of Sensor B143.
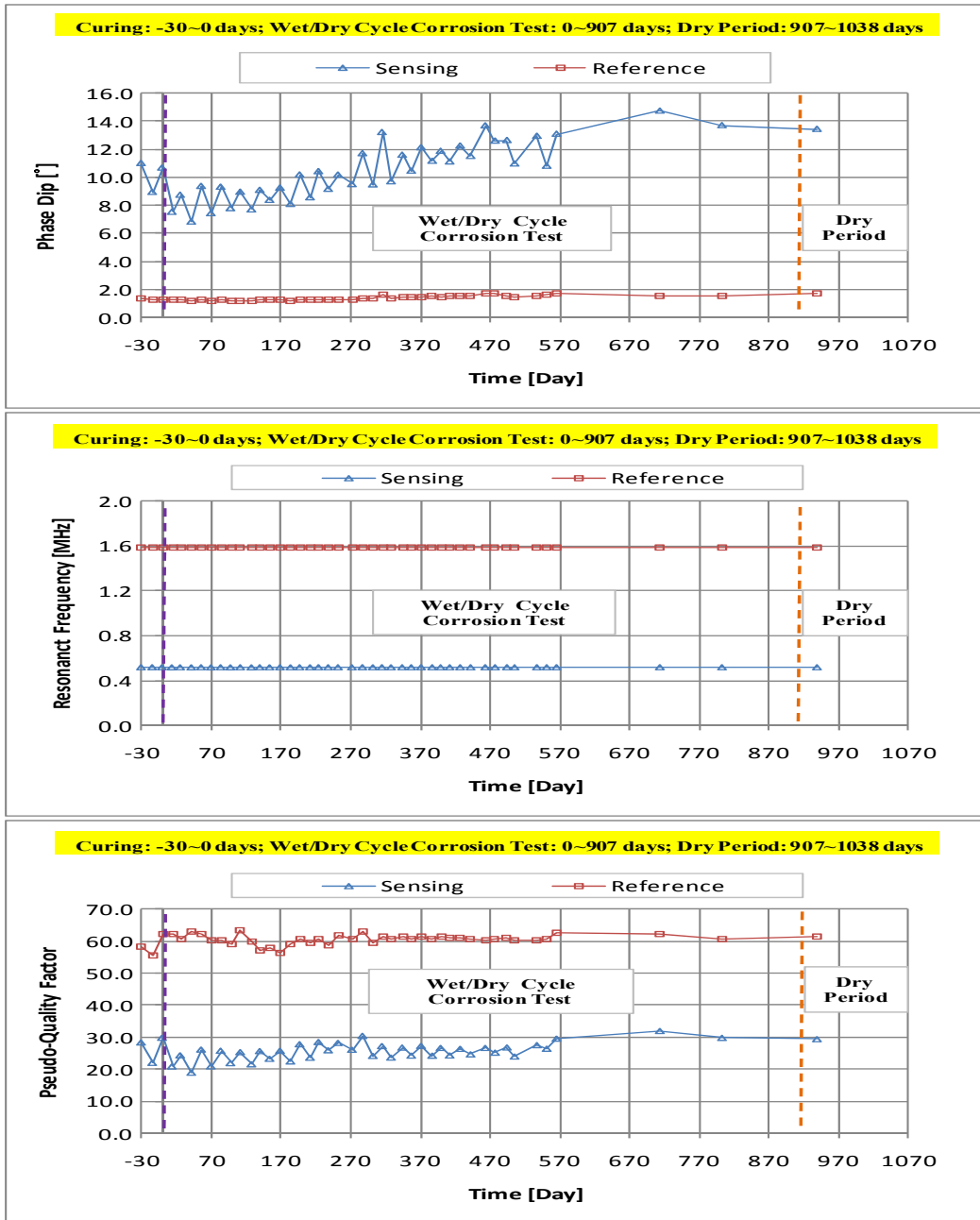
Figure A.2.15. The response of Sensor C01.
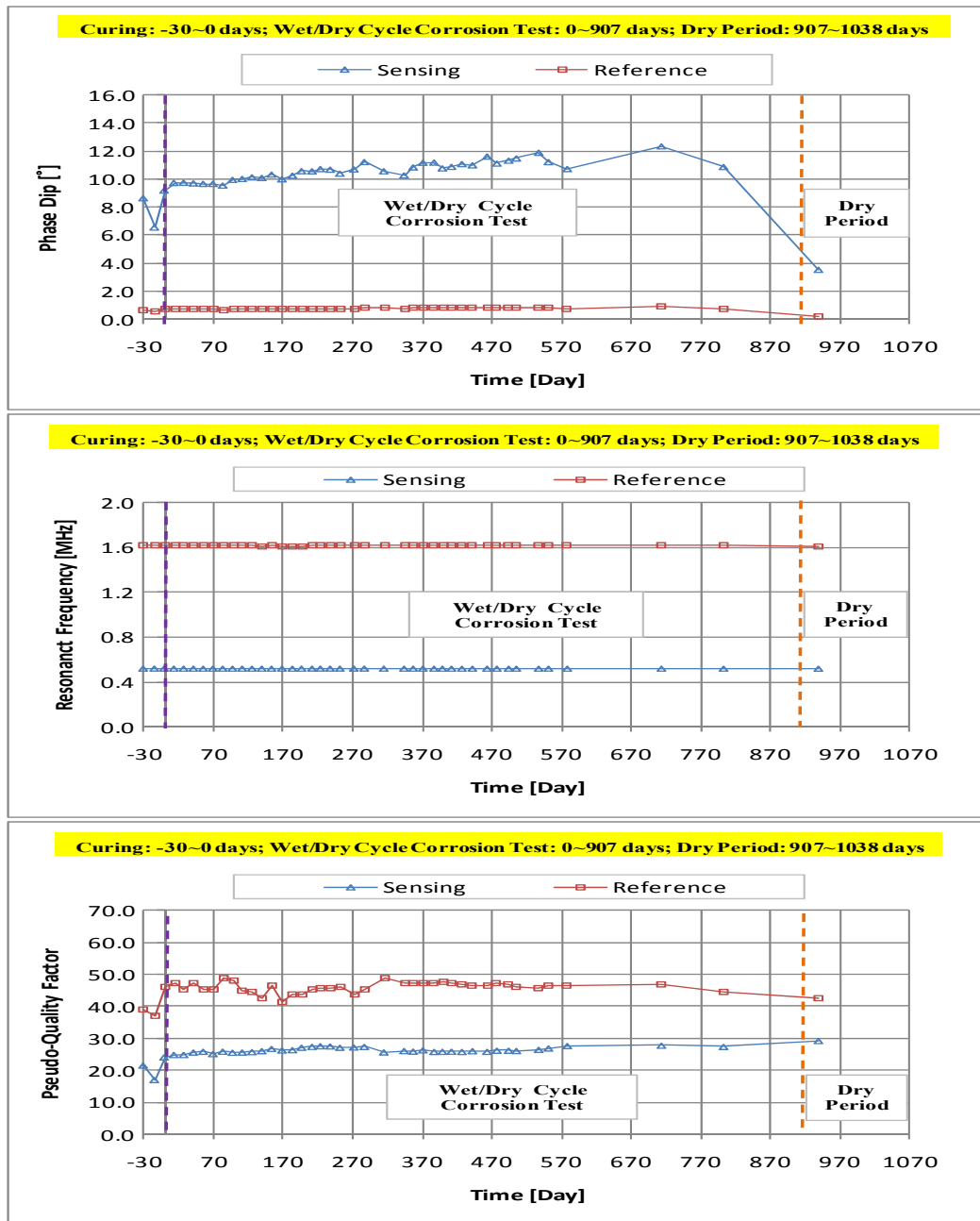
Figure A.2.16. The response of Sensor C02.
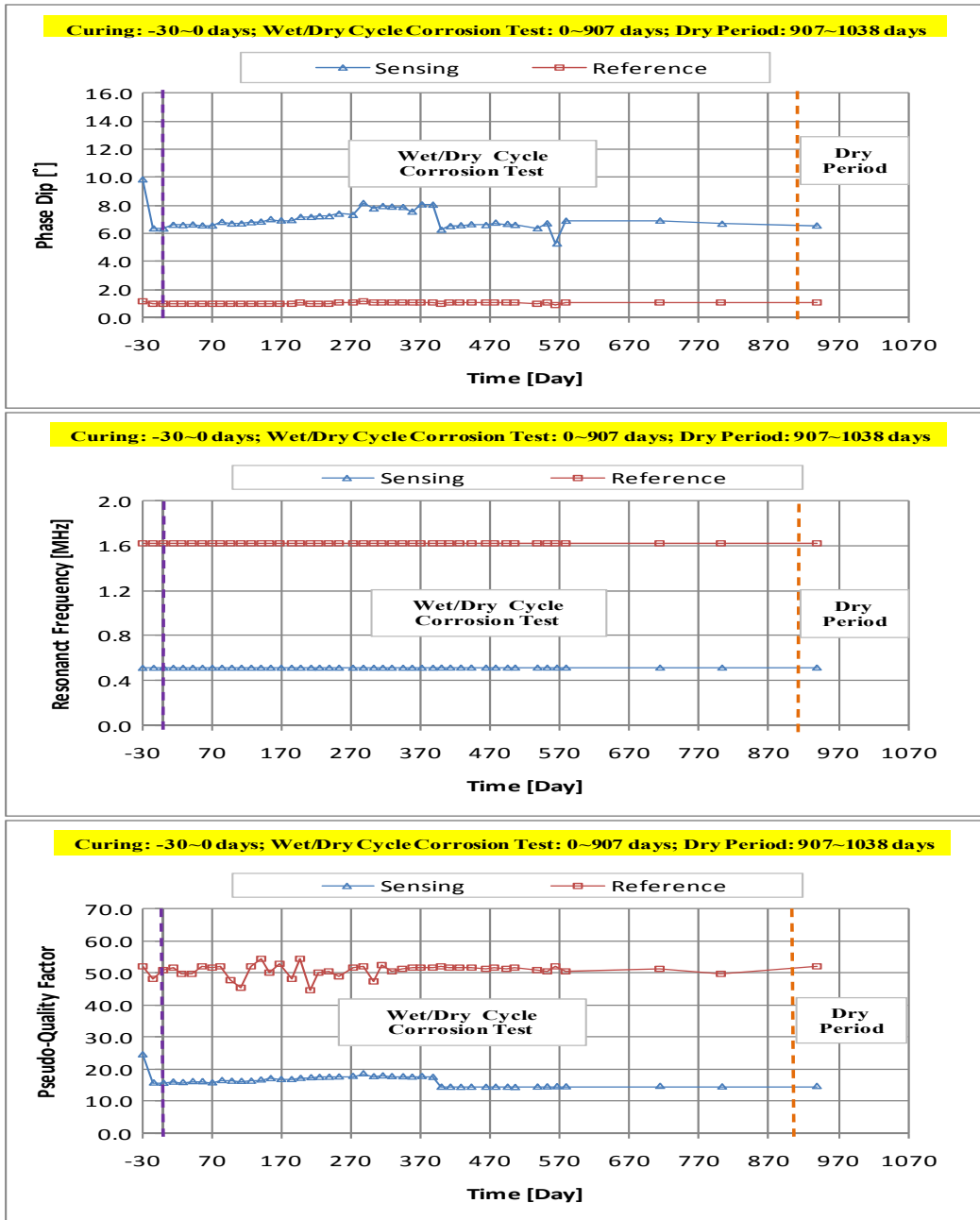
Figure A.2.17. The response of Sensor C03.

APPENDIX B

Testing Results for the Accelerated Corrosion Tests

B.1 Data Sheets for KEMET Capacitors

MULTILAYER CERAMIC CAPACITORS/AXIAL & RADIAL LEADED **KEMET**

Multilayer ceramic capacitors are available in a variety of physical sizes and configurations, including leaded devices and surface mounted chips. Leaded styles include molded and conformally coated parts with axial and radial leads. However, the basic capacitor element is similar for all styles. It is called a chip and consists of formulated dielectric materials which have been cast into thin layers, interspersed with metal electrodes alternately exposed on opposite edges of the laminated structure. The entire structure is fired at high temperature to produce a monolithic block which provides high capacitance values in a small physical volume. After firing, conductive terminations are applied to opposite ends of the chip to make contact with the exposed electrodes. Termination materials and methods vary depending on the intended use.

TEMPERATURE CHARACTERISTICS

Ceramic dielectric materials can be formulated with a wide range of characteristics. The EIA standard for ceramic dielectric capacitors (RS-198) divides ceramic dielectrics into the following classes:

Class I: Temperature compensating capacitors, suitable for resonant circuit application or other applications where high Q and stability of capacitance characteristics are required. Class I capacitors have predictable temperature coefficients and are not effected by voltage, frequency or time. They are made from materials which are not ferro-electric, yielding superior stability but low volumetric efficiency. Class I capacitors are the most stable type available, but have the lowest volumetric efficiency.

Class II: Stable capacitors, suitable for bypass or coupling applications or frequency discriminating circuits where Q and stability of capacitance characteristics are not of major importance. Class II capacitors have temperature characteristics of ± 15% or less. They are made from materials which are ferro-electric, yielding higher volumetric efficiency but less stability. Class II capacitors are affected by temperature, voltage, frequency and time.

Class III: General purpose capacitors, suitable for by-pass coupling or other applications in which dielectric losses, high insulation resistance and stability of capacitance characteristics are of little or no importance. Class III capacitors are similar to Class II capacitors except for temperature characteristics, which are greater than ± 15%. Class III capacitors have the highest volumetric efficiency and poorest stability of any type.

KEMET leaded ceramic capacitors are offered in the three most popular temperature characteristics:
C0G: Class I, with a temperature coefficient of 0 ± 30 ppm per degree C over an operating temperature range of - 55°C to + 125°C (Also known as "NP0").
X7R: Class II, with a maximum capacitance change of ± 15% over an operating temperature range of - 55°C to + 125°C.
Z5U: Class III, with a maximum capacitance change of + 22% - 56% over an operating temperature range of + 10°C to + 85°C.

Specified electrical limits for these three temperature characteristics are shown in Table 1.

SPECIFIED ELECTRICAL LIMITS

PARAMETER	TEMPERATURE CHARACTERISTICS		
	C0G	X7R	Z5U
Dissipation Factor: Measured at following conditions: C0G — 1 kHz and 1 vrms if capacitance > 1000 pF 1 MHz and 1 vrms if capacitance ≤ 1000 pF X7R — 1 kHz and 1 vrms* or if extended cap range 0.5 vrms Z5U — 1 kHz and 0.5 vrms	0.15%	2.5%	4.0%
Dielectric Strength: 2.5 times rated DC voltage.	Pass Subsequent IR Test		
Insulation Resistance (IR): At rated DC voltage, whichever of the two is smaller	1,000 MΩ-µF or 100 GΩ	1,000 MΩ-µF or 100 GΩ	1,000 MΩ-µF or 10 GΩ
Temperature Characteristics: Range, °C Capacitance Change without DC voltage	-55 to +125 0 ± 30 ppm/°C	-55 to +125 ±15%	+10 to +85 +22%, -56%

* 1 MHz and 1 vrms if capacitance ≤ 100 pF on military product.

Table I

GENERAL SPECIFICATIONS

Working Voltage:

Axial (WVDC)	Radial (WVDC)
C0G – 50 & 100	50, 100, 200, 500, 1k, 1.5k, 2k, 2.5k, 3k
X7R – 50 & 100	50, 100, 200, 500, 1k, 1.5k, 2k, 2.5k, 3k
Z5U – 50 & 100	50 & 100

Temperature Characteristics:
C0G – 0 ± 30 PPM / °C from - 55°C to + 125°C (1)
X7R – ± 15% from - 55°C to + 125°C
Z5U – + 22% / -56% from + 10°C to + 85°C

Capacitance Tolerance:
C0G – ±0.5pF, ±1%, ±2%, ±5%, ±10%
X7R – ±10%, ±20%, +80% / -20%, +100% / -0%
Z5U – ±20%, +80% / -20%

Construction:
Epoxy encapsulated - meets flame test requirements of UL Standard 94V-0.
High-temperature solder - meets EIA RS-198, Method 302, Condition B (260°C for 10 seconds)

Lead Material:
100% matte tin (Sn) with nickel (Ni) underplate and steel core.

Solderability:
EIA RS-198, Method 301, Solder Temperature: 230°C ±5°C.
Dwell time in solder = 7 ± ½ seconds.

Terminal Strength:
EIA RS-198, Method 303, Condition A (2.2kg)

ELECTRICAL

Capacitance @ 25°C:
Within specified tolerance and following test conditions.
C0G – > 1000pF with 1.0 vrms @ 1 kHz
     ≤ 1000pF with 1.0 vrms @ 1 MHz
X7R – with 1.0 vrms @ 1 kHz
Z5U – with 1.0 vrms @ 1 kHz

Dissipation Factor @ 25°C:
Same test conditions as capacitance.
 C0G – 0.15% maximum
 X7R – 2.5% maximum
 Z5U – 4.0% maximum

Insulation Resistance @ 25°C:
EIA RS-198, Method 104, Condition A <1kV
C0G – 100k Megohm or 1000 Megohm x µF, whichever is less.
 ≤500V test @ rated voltage, ≥1kV test @ 500V
X7R – 100k Megohm or 1000 Megohm x µF, whichever is less.
 ≤500V test @ rated voltage, ≥1kV test @ 500V
Z5U – 10k Megohm or 1000 Megohm x µF, whichever is less.

Dielectric Withstanding Voltage:
EIA RS-198, Method 103
≤200V test @ 250% of rated voltage for 5 seconds with current limited to 50mA.
500V test @ 150% of rated voltage for 5 seconds with current limited to 50mA.
≥1000V test @ 120% of rated voltage for 5 seconds with current limited to 50mA.

ENVIRONMENTAL

Vibration:
EIA RS-198, Method 304, Condition D (10-2000Hz; 20g)
Shock:
EIA RS-198, Method 305, Condition I (100g)

Life Test:
EIA RS-198, Method 201, Condition D.
≤ 200V
 C0G – 200% of rated voltage @ +125°C
 X7R – 200% of rated voltage @ +125°C
 Z5U – 200% of rated voltage @ +85°C
≥ 500V
 C0G – rated voltage @ +125°C
 X7R – rated voltage @ +125°C

Post Test Limits @ 25°C are:
Capacitance Change:
C0G (≤ 200V) – +3% or 0.25pF, whichever is greater.
C0G (≥ 500V) – +3% or 0.50pF, whichever is greater.
X7R – + 20% of initial value (2)
Z5U – + 30% of initial value (2)
Dissipation Factor:
C0G – 0.15% maximum
X7R – 2.5% maximum
Z5U – 4.0% maximum
Insulation Resistance:
C0G – 10k Megohm or 100 Megohm x µF, whichever is less.
 ≥1kV tested @ 500V.
X7R – 10k Megohm or 100 Megohm x µF, whichever is less.
 ≥1kV tested @ 500V.
Z5U – 1k Megohm or 100 Megohm x µF, whichever is less.

 Moisture Resistance:
EIA RS-198, Method 204, Condition A (10 cycles without applied voltage.)
Post Test Limits @ 25°C are:
Capacitance Change:
C0G (≤ 200V) – +3% or 0.25pF, whichever is greater.
C0G (≥ 500V) – +3% or 0.50pF, whichever is greater.
X7R – + 20% of initial value (2)
Z5U – + 30% of initial value (2)
Dissipation Factor:
C0G – 0.25% maximum
X7R – 3.0% maximum
Z5U – 4.0% maximum
Insulation Resistance:
C0G – 10k Megohm or 100 Megohm x µF, whichever is less.
 ≤500V test @ rated voltage, ≥1kV test @ 500V.
X7R – 10k Megohm or 100 Megohm x µF, whichever is less.
 ≥500V test @ rated voltage, >1kV test @ 500V.
Z5U – 1k Megohm or 100 Megohm x µF, whichever is less.

Thermal Shock:
EIA RS-198, Method 202, Condition B (C0G & X7R: -55°C to +125°C); Condition A (Z5U: -55°C to 85°C)

(1) +53 PPM -30 PPM/ °C from +25°C to -55°C, + 60 PPM below 10pF.
(2) X7R and Z5U dielectrics exhibit aging characteristics; therefore, it is highly recommended that capacitors be deaged for 2 hours at 150°C and stabilized at room temperature for 48 hours before capacitance measurements are made.

CERAMIC CONFORMALLY COATED/RADIAL
"STANDARD & HIGH VOLTAGE GOLDEN MAX"

KEMET

STANDARD LEAD CONFIGURATION — OUTLINE DRAWINGS

*.276 (7.00) MIN.

C317 C322 C330   C323   C333   .060 (1.52) MAX.   C315 C320 C330 C340 C350
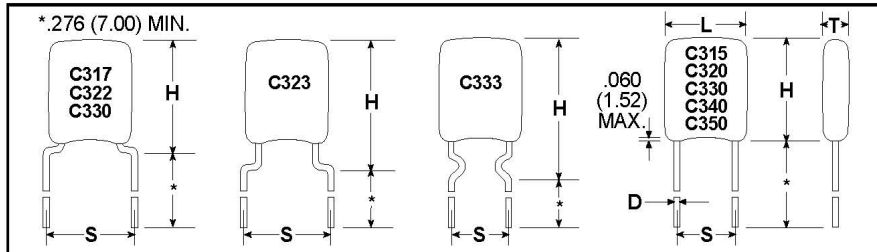
Drawings are not to scale. See table below for dimensions.
See page 10 for optional lead configurations.

DIMENSIONS — INCHES & MILLIMETERS

Case Size	L Max.	H. Max	Standard T Max.	High Voltage T Max.	S(1) ±.030 (.78)	D +.004(.10) -.001(.025)
C315	0.150 (3.81)	0.210 (5.33)	0.100	0.150	0.100 (2.54)	0.020 (.51)
C317	0.150 (3.81)	0.230 (5.84)	0.100	0.150	0.200 (5.08)	0.020 (.51)
C320	0.200 (5.08)	0.260 (6.60)	0.125	0.200	0.100 (2.54)	0.020 (.51)
C322	0.200 (5.08)	0.260 (6.60)	0.125	0.200	0.200 (5.08)	0.020 (.51)
C323	0.200 (5.08)	0.320 (8.13)	0.125	0.200	0.200 (5.08)	0.020 (.51)
C330	0.300 (7.62)	0.360 (9.14)	0.150	0.250	0.200 (5.08)	0.020 (.51)
C333	0.300 (7.62)	0.390 (9.91)	0.150	0.250	0.200 (5.08)	0.020 (.51)
C340	0.400 (10.16)	0.460 (11.68)	0.150	0.270	0.200 (5.08)	0.020 (.51)
C350	0.500 (12.70)	0.560 (14.22)	0.200	0.270	0.400 (10.16)	0.025 (.64)

NOTE: 1 inch = 25.4 mm.
NOTE: (1) Measured at seating plane.

ORDERING INFORMATION

C 320 C 102 M 1 R 5 T A*

CERAMIC

CASE SIZE
(See Table Above)

SPECIFICATION
C — Standard

CAPACITANCE, CODE
Expressed in Picofarads (pF)
First Two Digits — Significant Figures
Third Digit — Number of Zeros (Use 9 for 1.0 thru 9.9 pF. Example: 2.2pF — 229)

CAPACITANCE TOLERANCE
D — ±0.5 pF   K — ±10%
F — ±1%   M — ±20%
G — ±2%   P — 0%, +100%
J — ±5%   Z — -20, +80%

*Part Number Example: C320C102M1R5CA (14 digits – no spaces)

FAILURE RATE
A — Not Applicable

TERMINATION MATERIAL
T — 100% Tin
H — SnPb
C — 100% Sn
(Not recommended for new design)

INTERNAL CONSTRUCTION
5 — Standard

DIELECTRIC
EIA Designation
G — C0G (NP0) — Ultra-Stable
R — X7R — Stable
U — Z5U — General Purpose

RATED VOLTAGE
2 — 200   F — 1500
1 — 100   G — 2000
5 — 50   Z — 2500
C — 500   H — 3000
D — 1000

Golden Max

For packaging information, see pages 40, and 41.

9

B.2 The testing Results of the First Corrosion Test
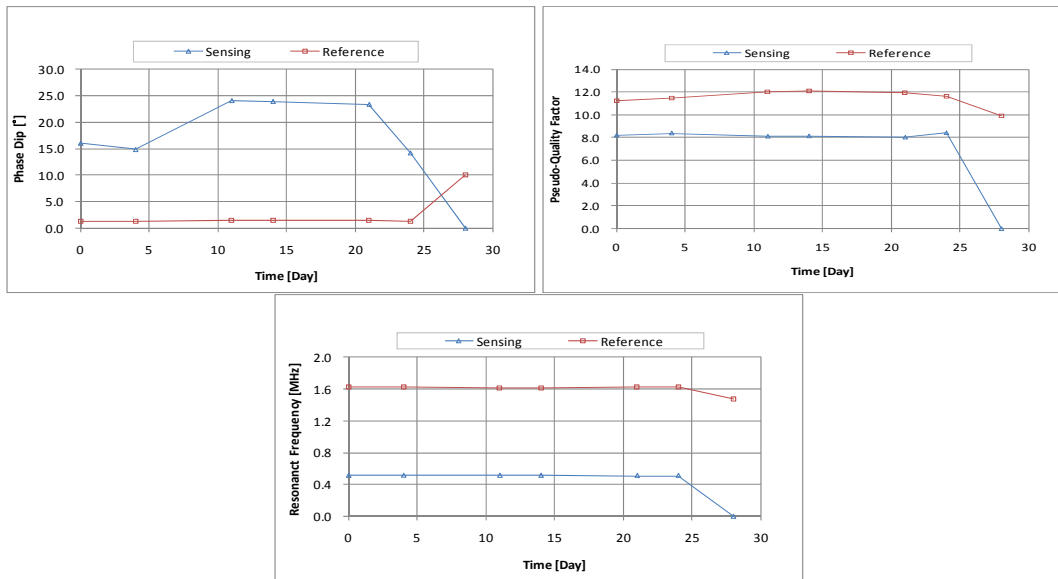
Figure B.2.1. The response of Sensor J001.
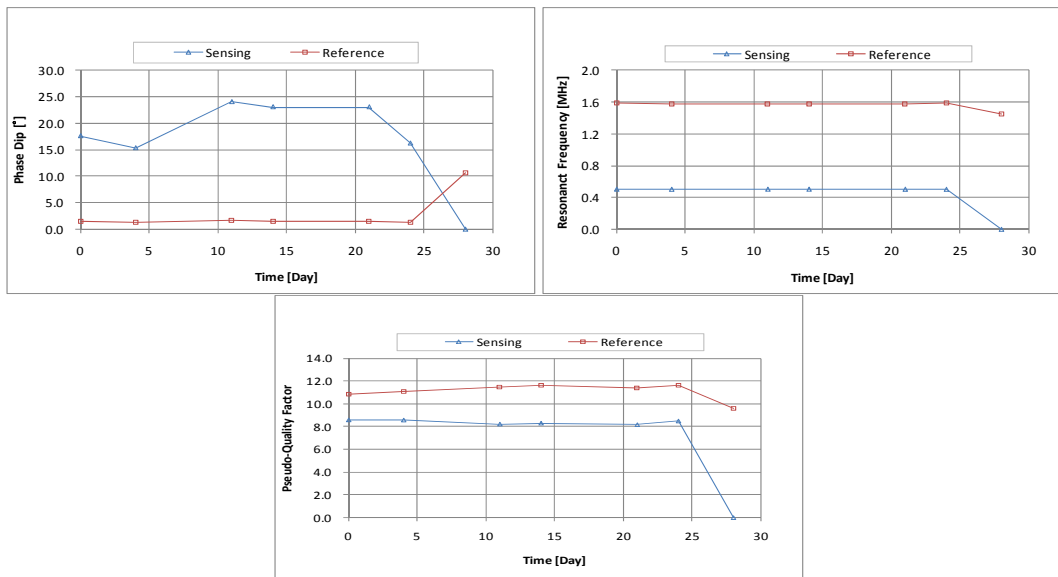
Figure B.2.2. The response of Sensor J002.
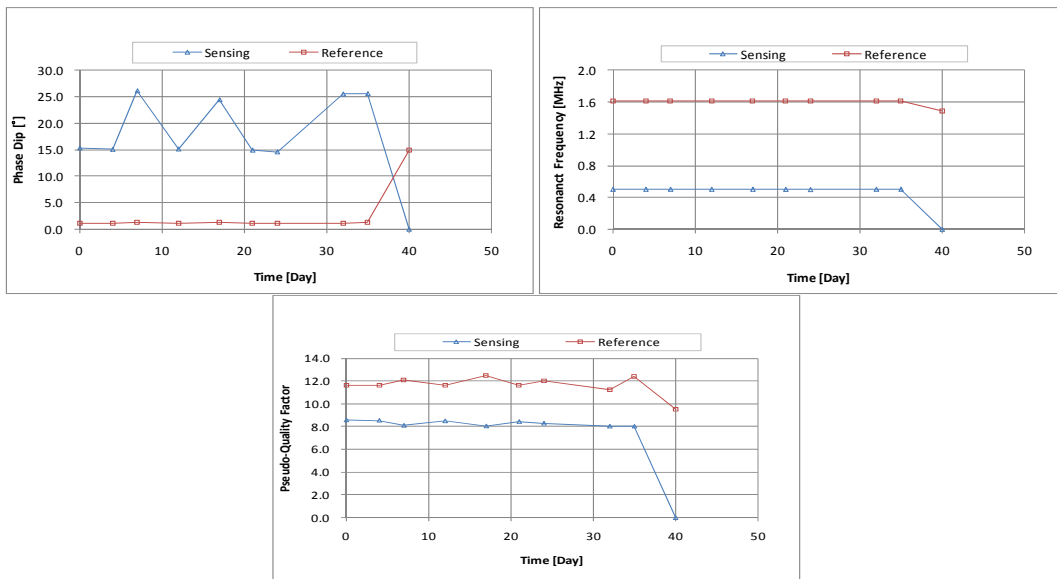
Figure B.2.3. The response of Sensor J003.
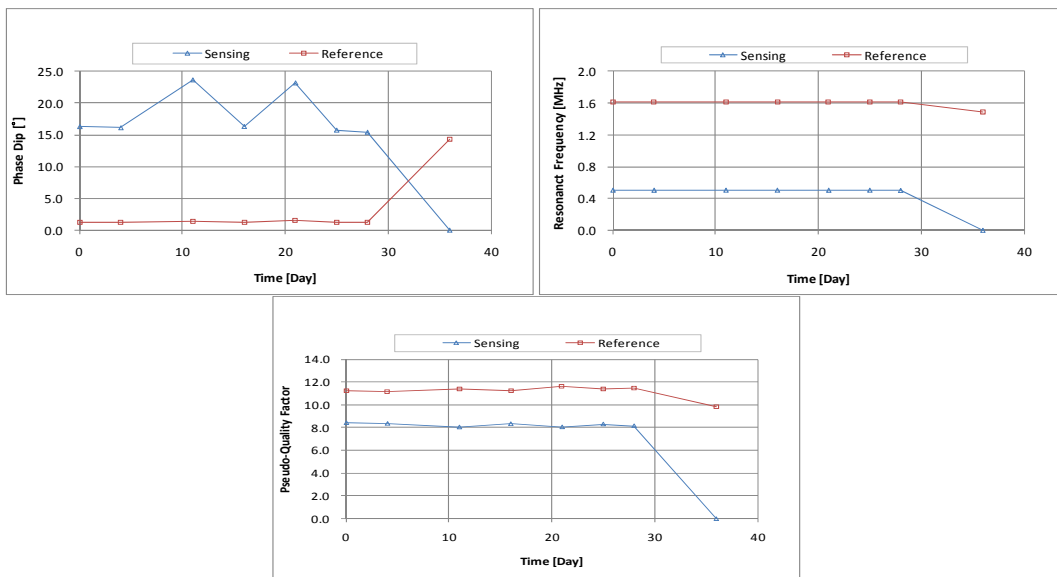
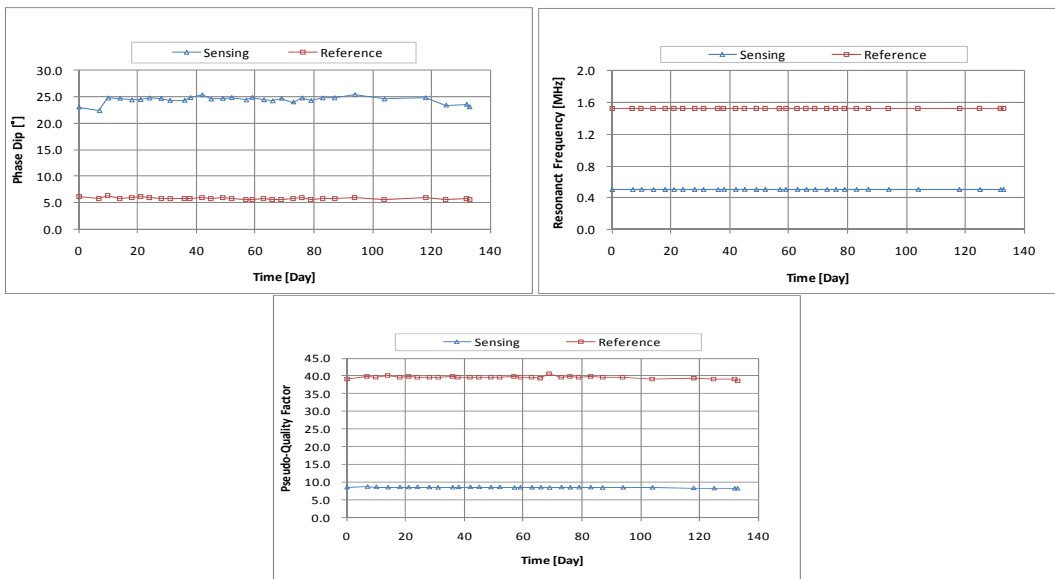*Figure B.2.4. The response of Sensor J004.*

191
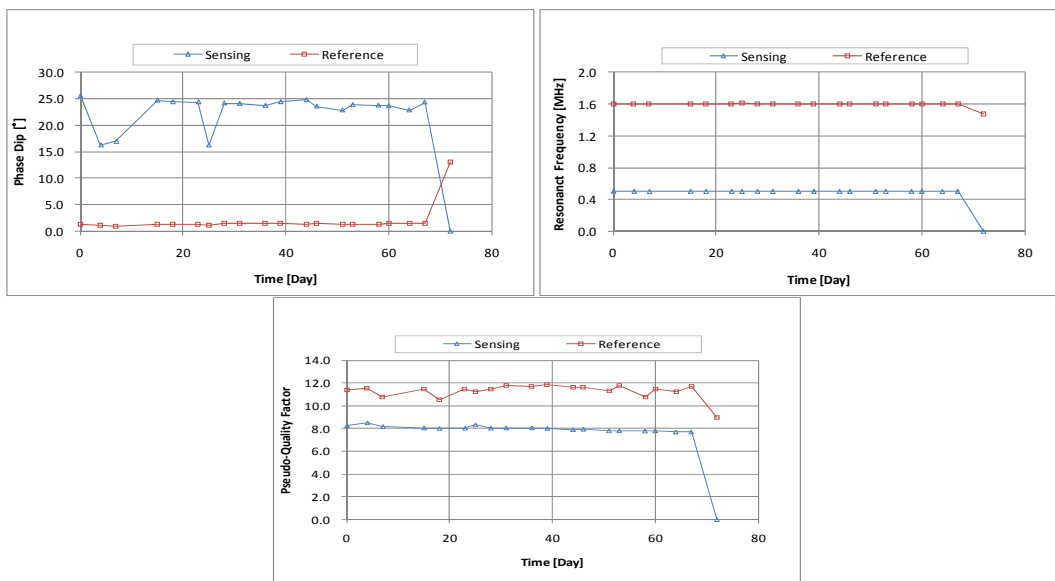
Figure B.2.5. The response of Sensor J005.
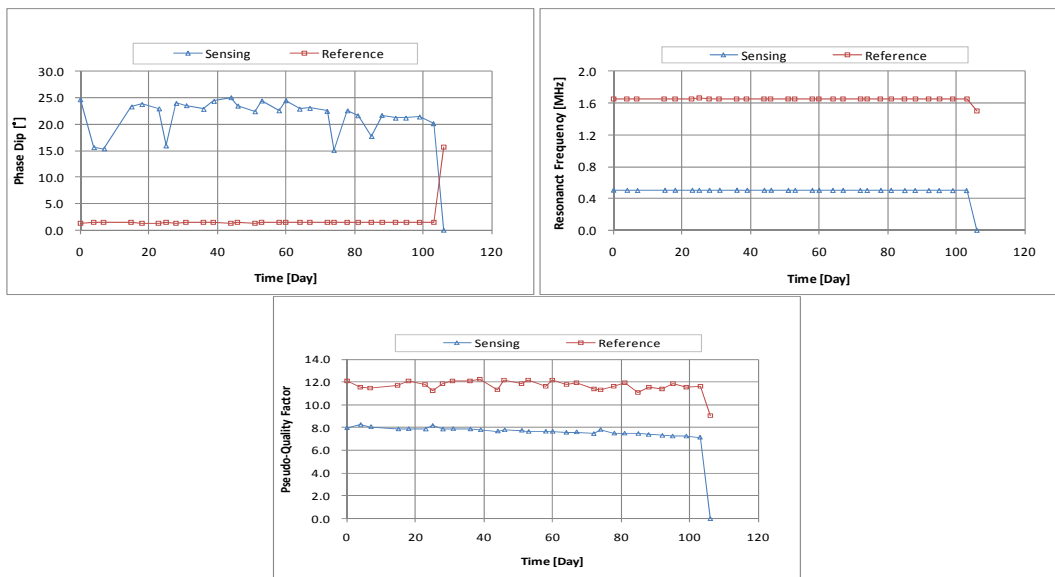
Figure B.2.6. The response of Sensor J006.
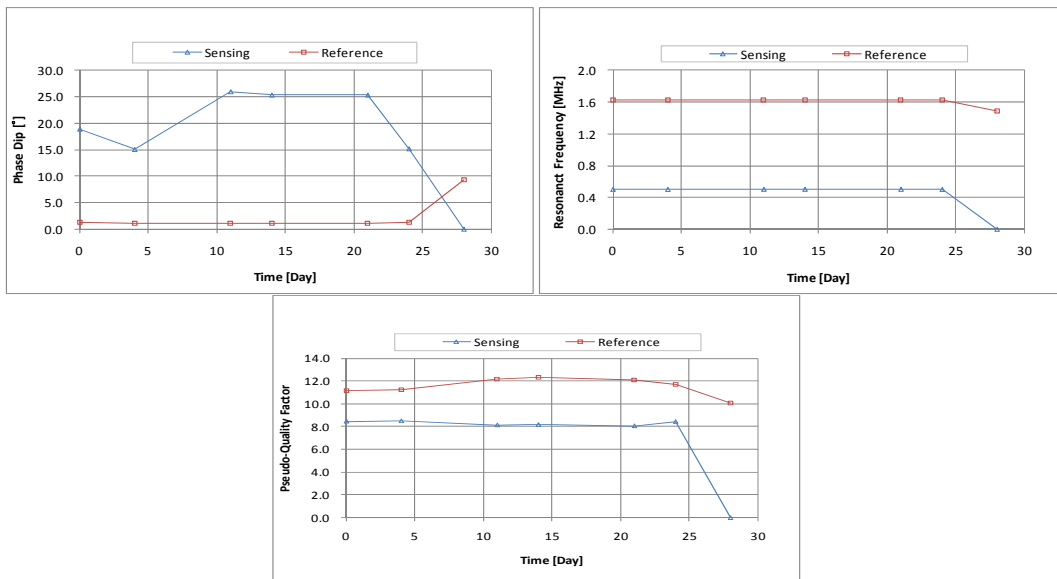
Figure B.2.7. The response of Sensor J007.
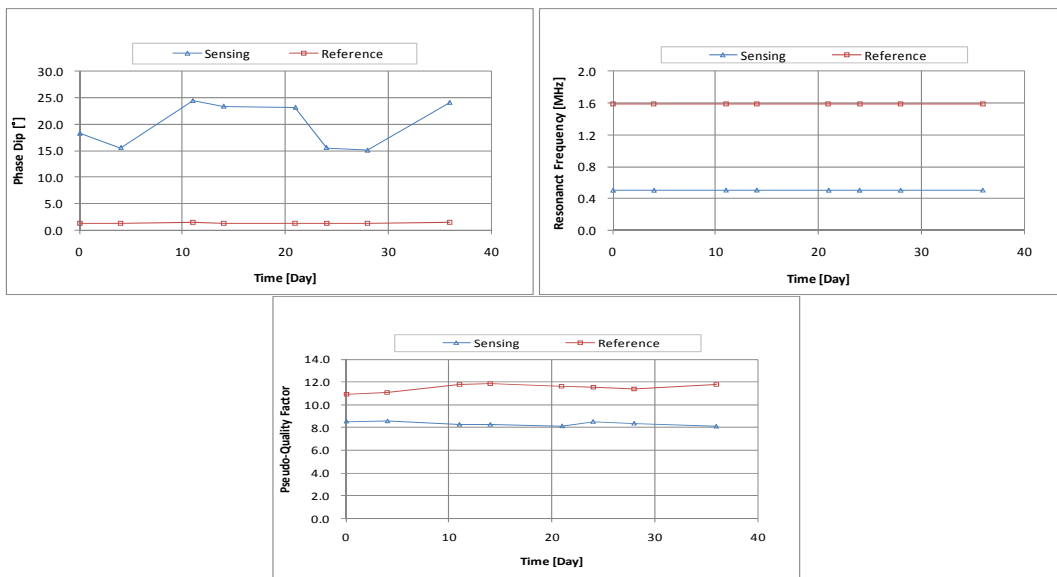
Figure B.2.8. The response of Sensor J008.
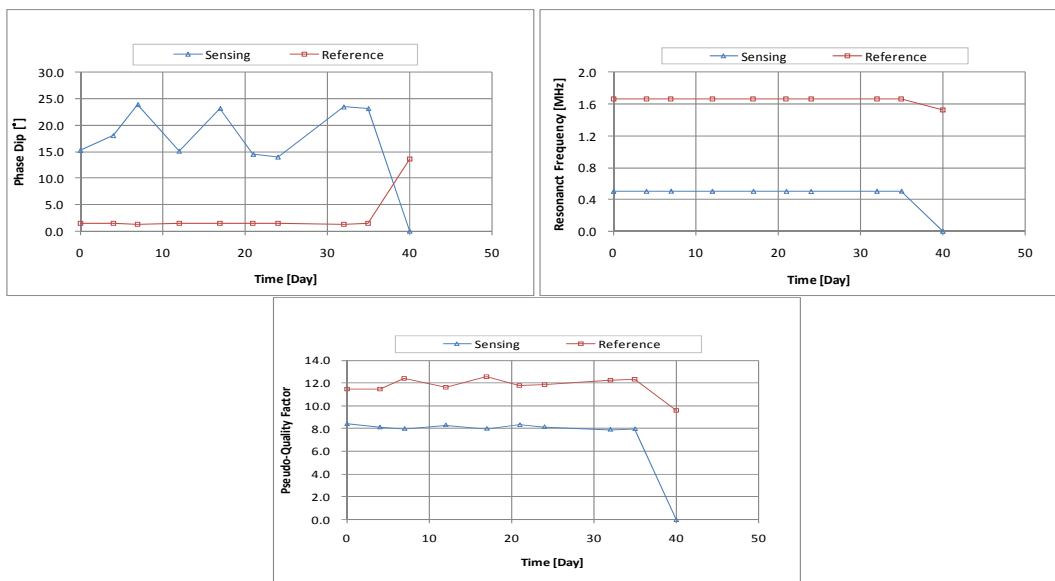
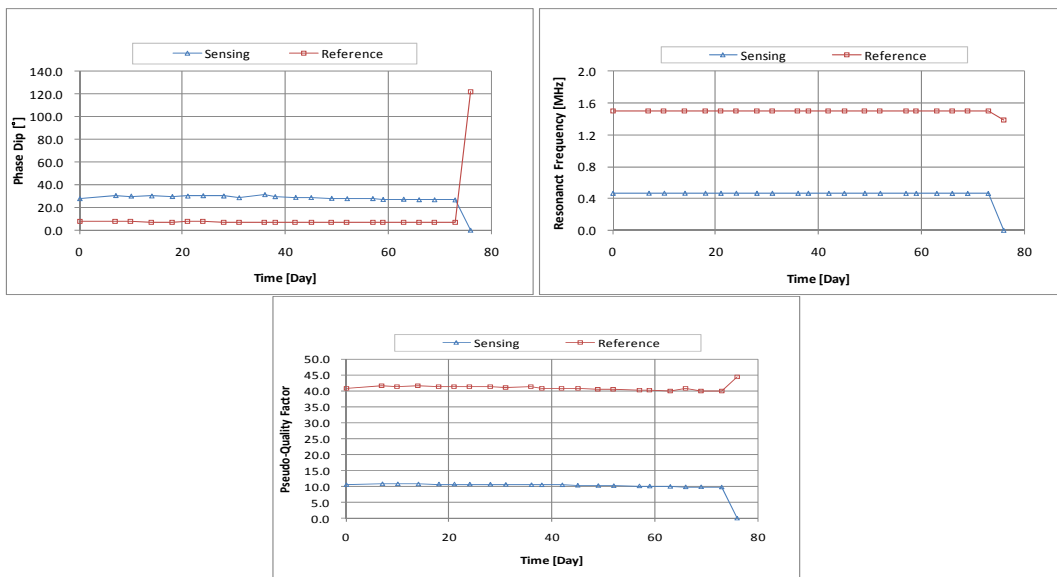*Figure B.2.9. The response of Sensor J009.*
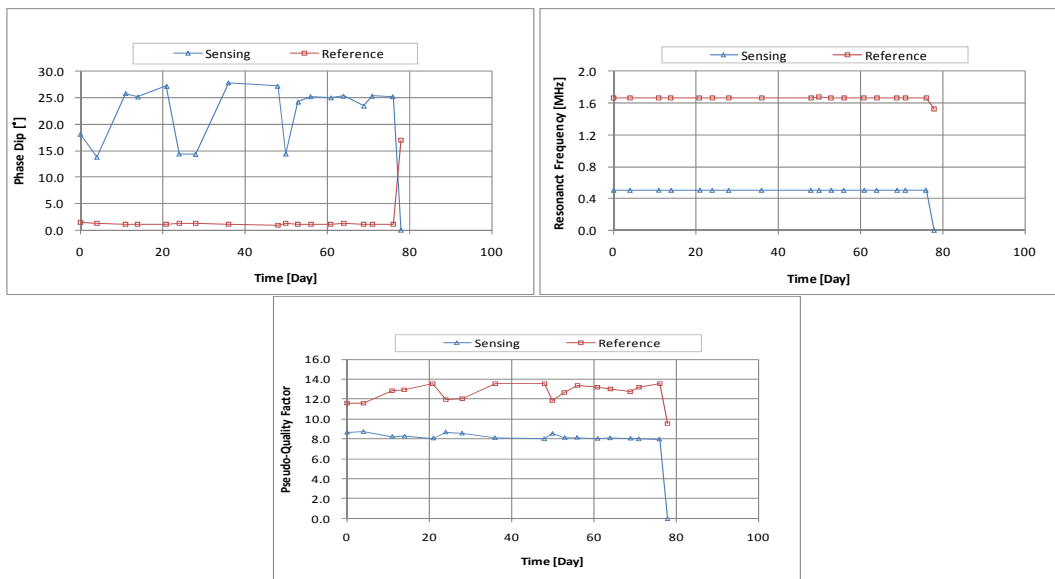
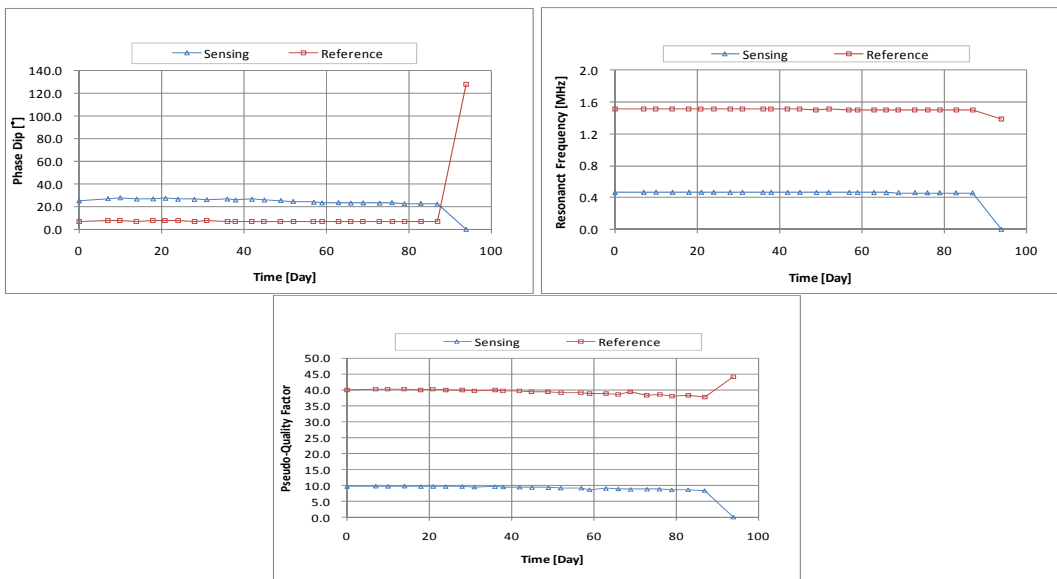
Figure B.2.10. The response of Sensor J010.
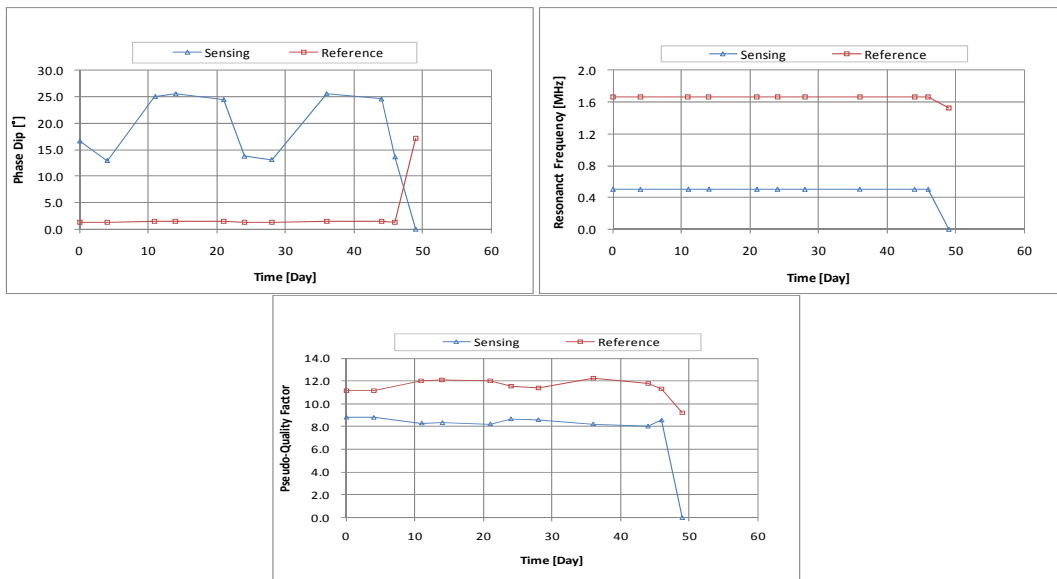
Figure B.2.11. The response of Sensor J011.
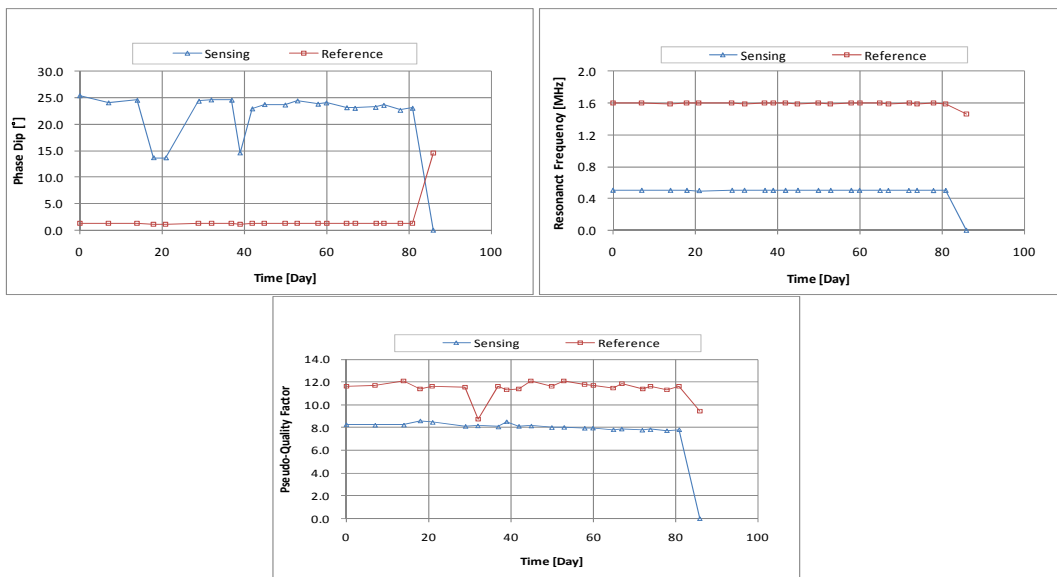
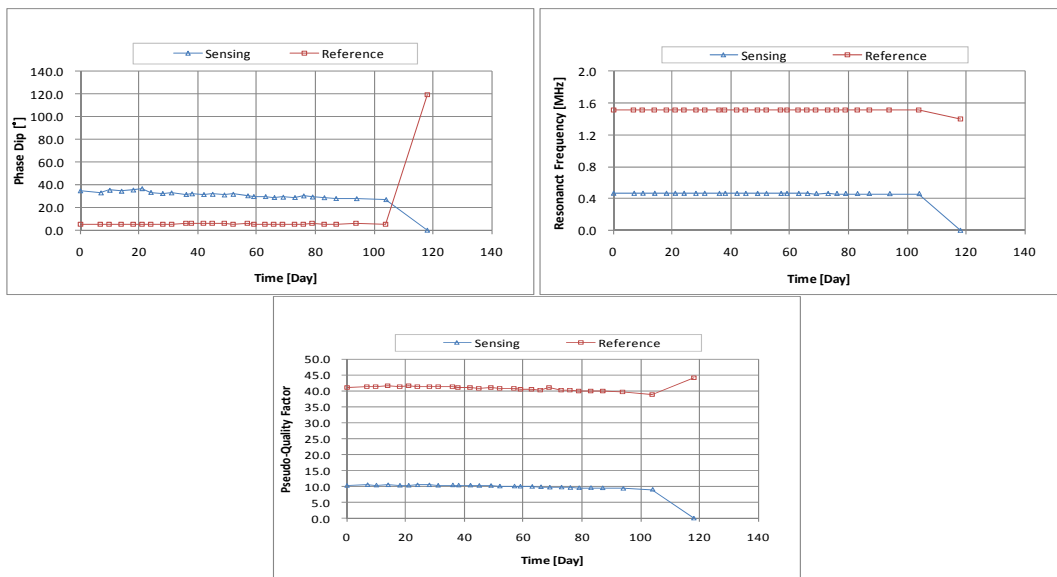*Figure B.2.12. The response of Sensor J012.*
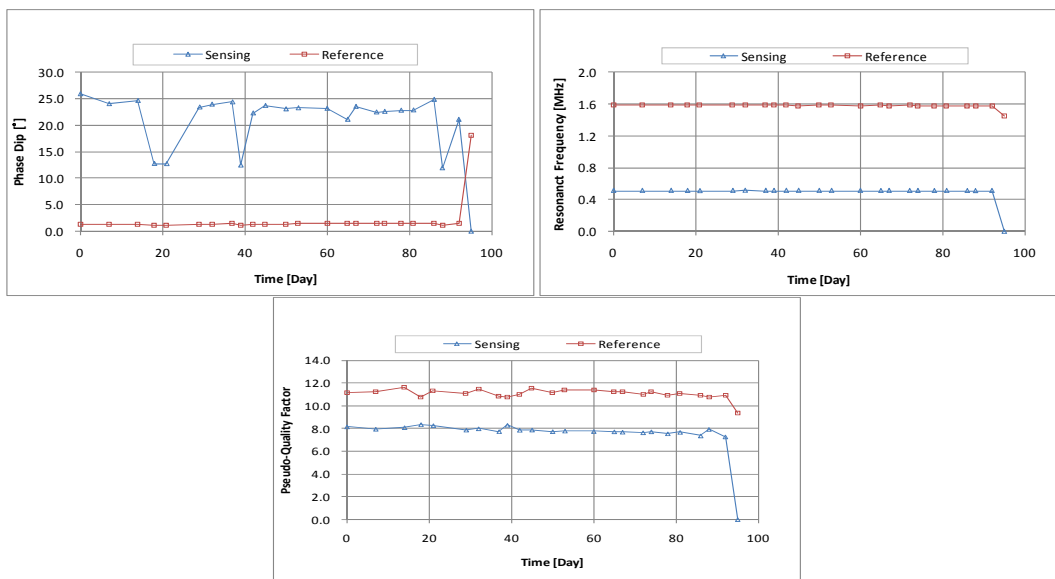
Figure B.2.13. The response of Sensor J013.
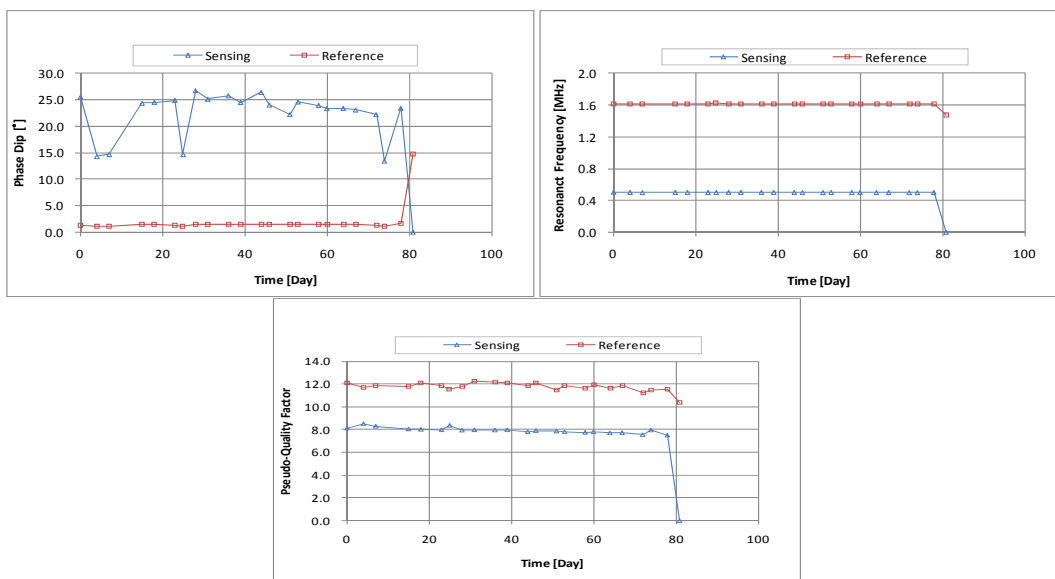
Figure B.2.14. The response of Sensor J014.

196
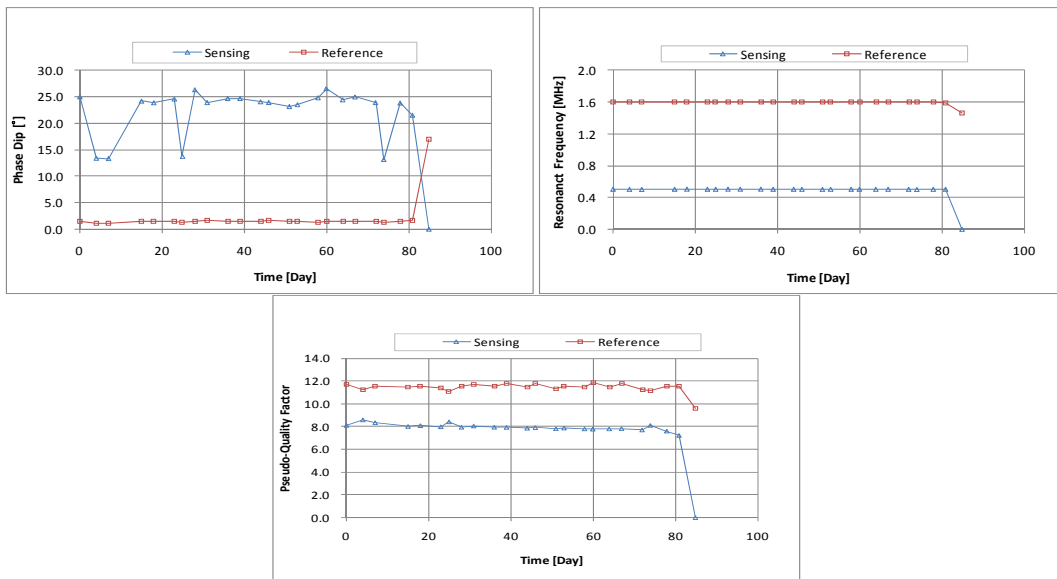
Figure B.2.15. The response of Sensor J015.
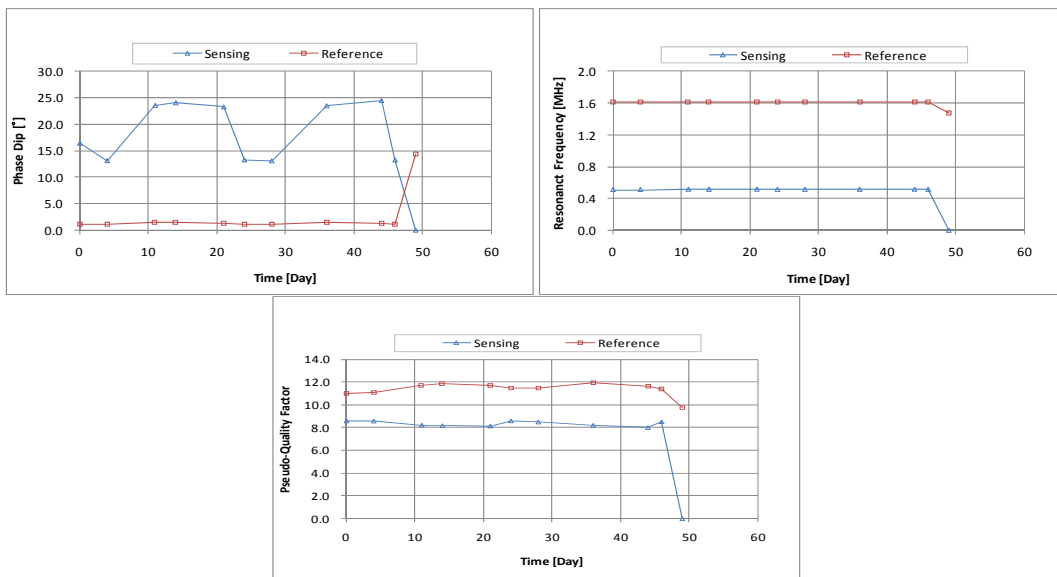
Figure B.2.16. The response of Sensor J016.
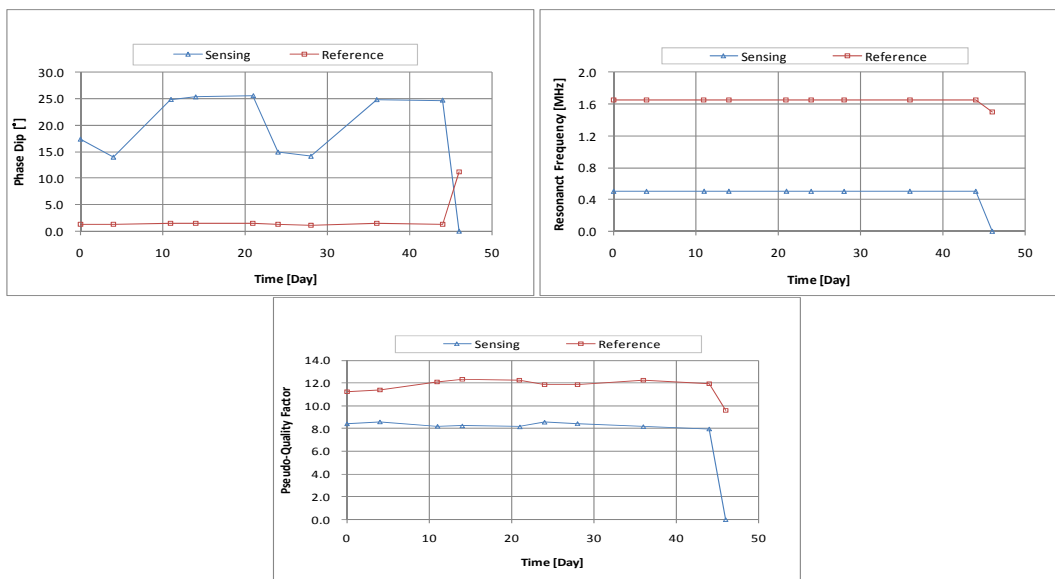
Figure B.2.17. The response of Sensor J017.
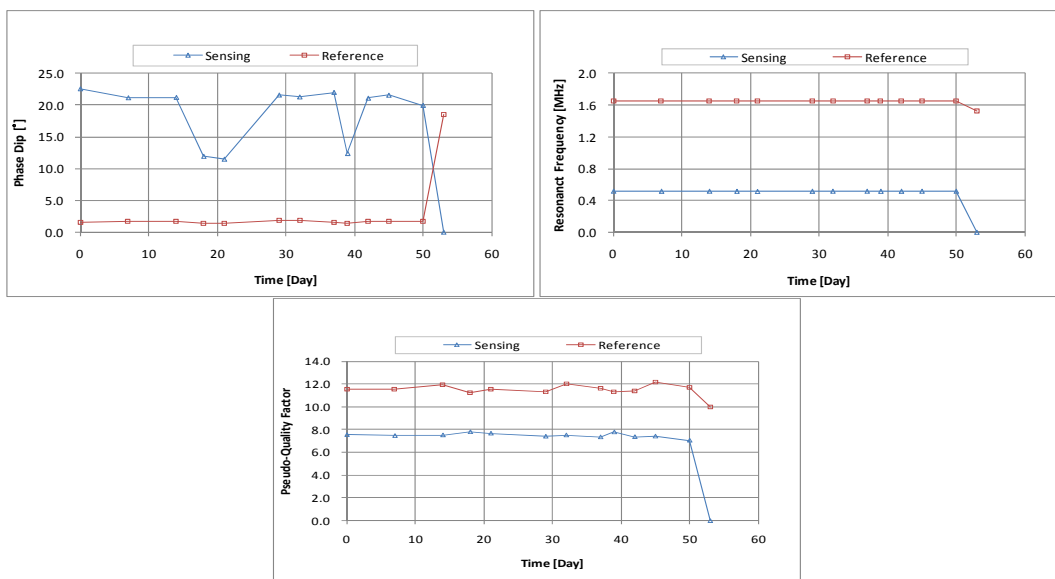
Figure B.2.18. The response of Sensor J018.
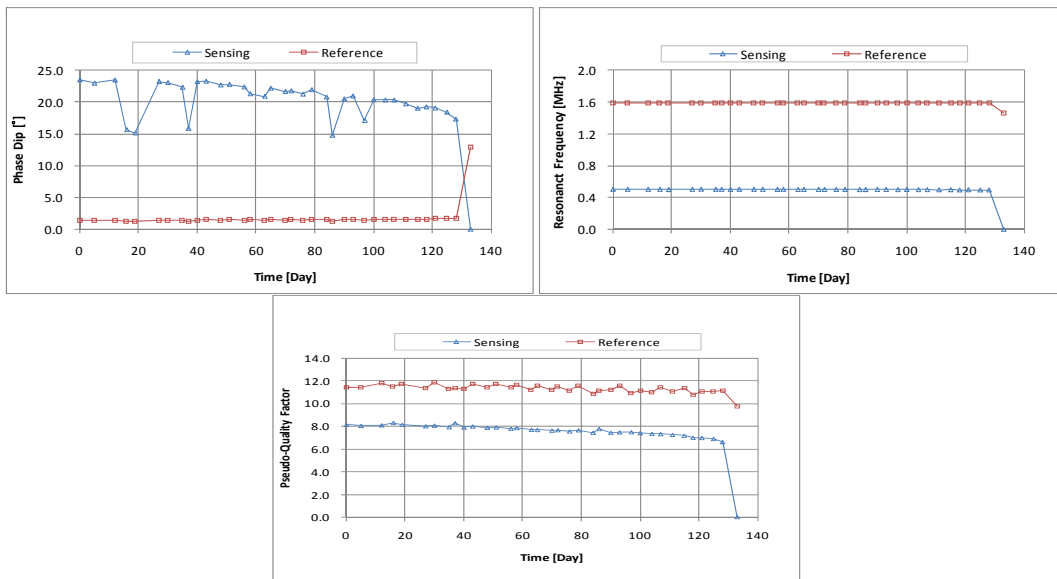
Figure B.2.19. The response of Sensor J019.
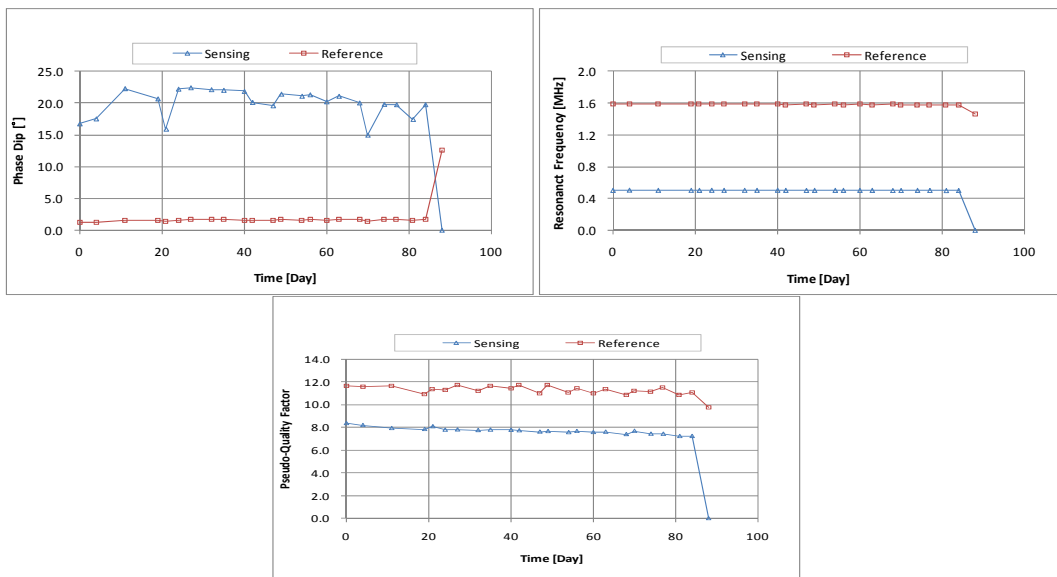
Figure B.2.20. The response of Sensor J020.
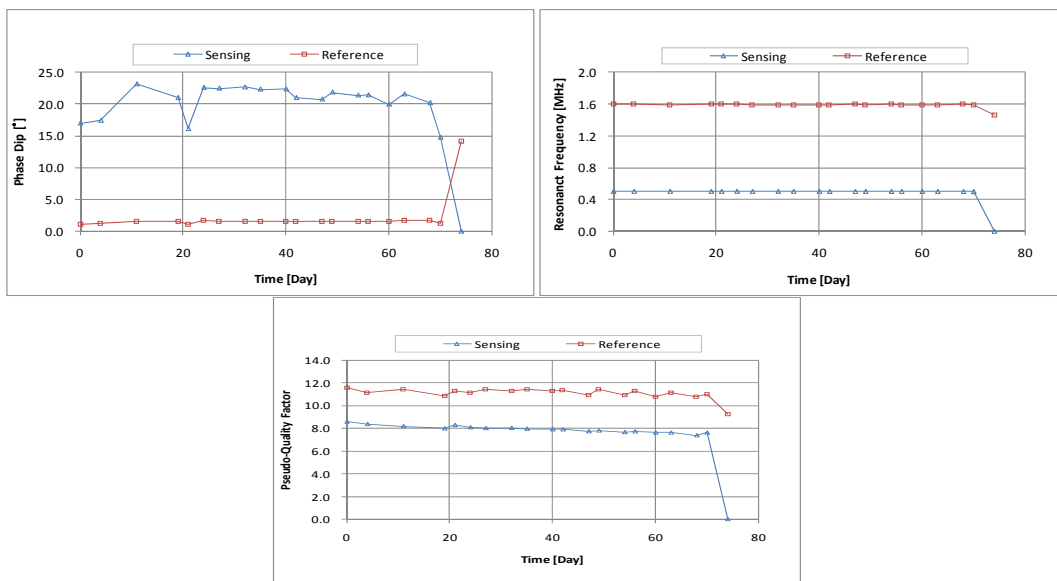
Figure B.2.21. The response of Sensor J021.
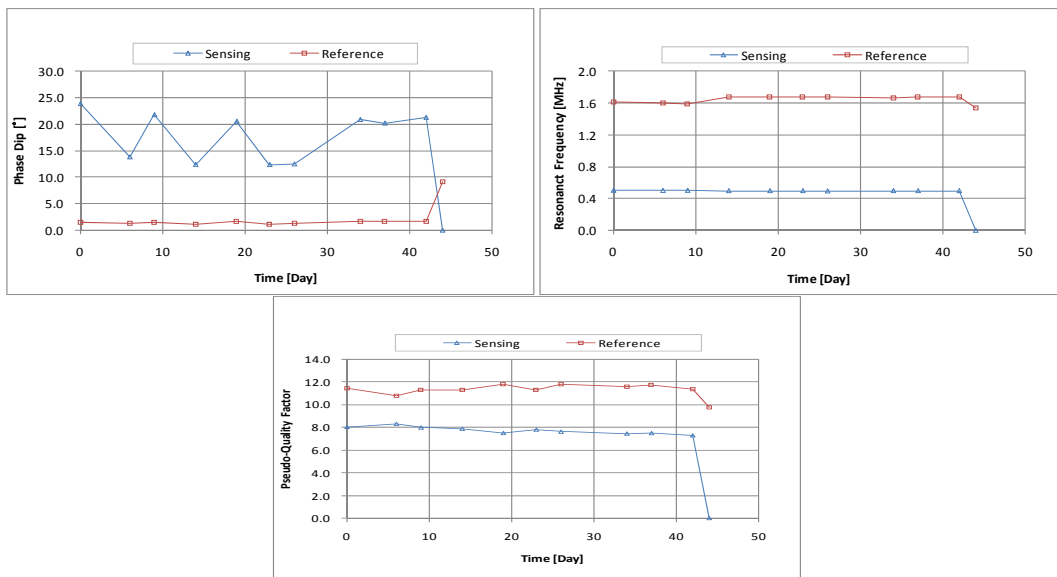
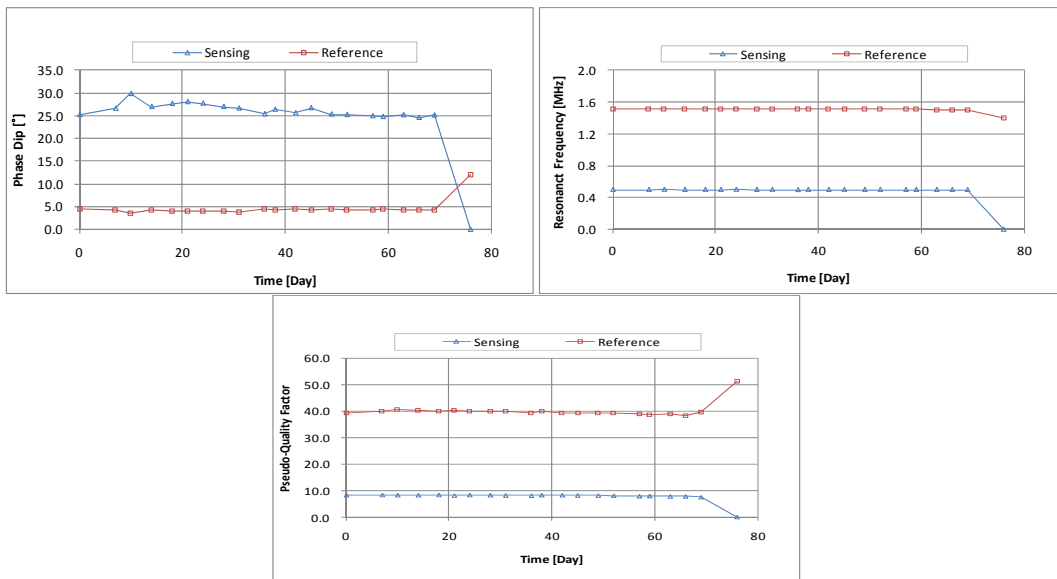*Figure B.2.22. The response of Sensor J022.*
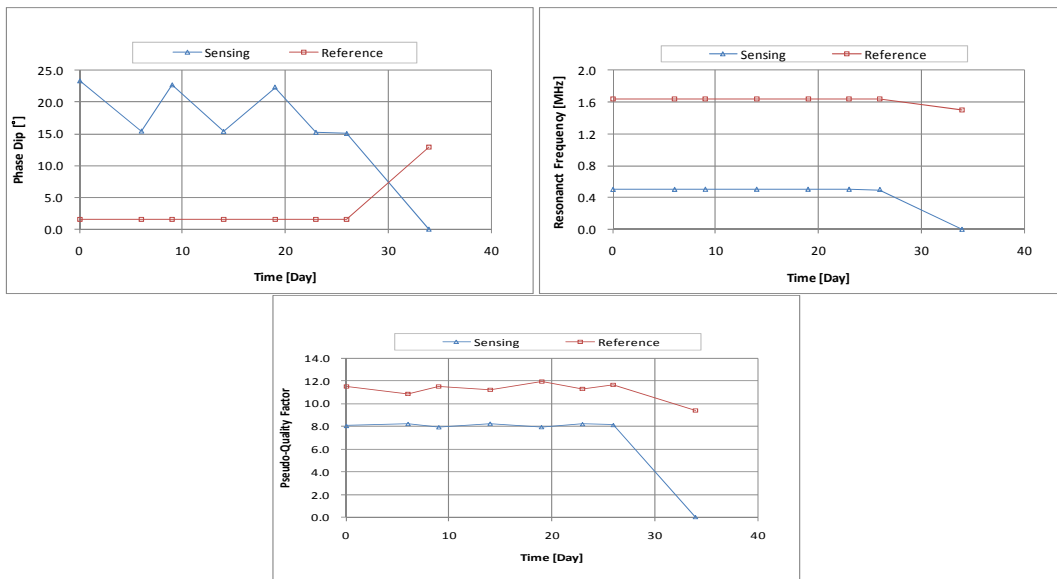
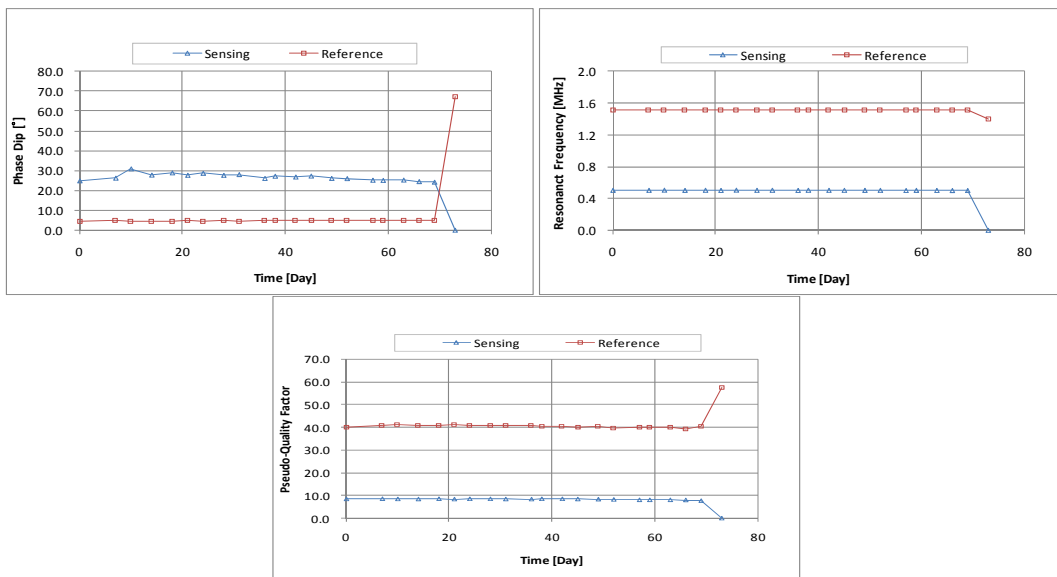*Figure B.2.23. The response of Sensor J023.*
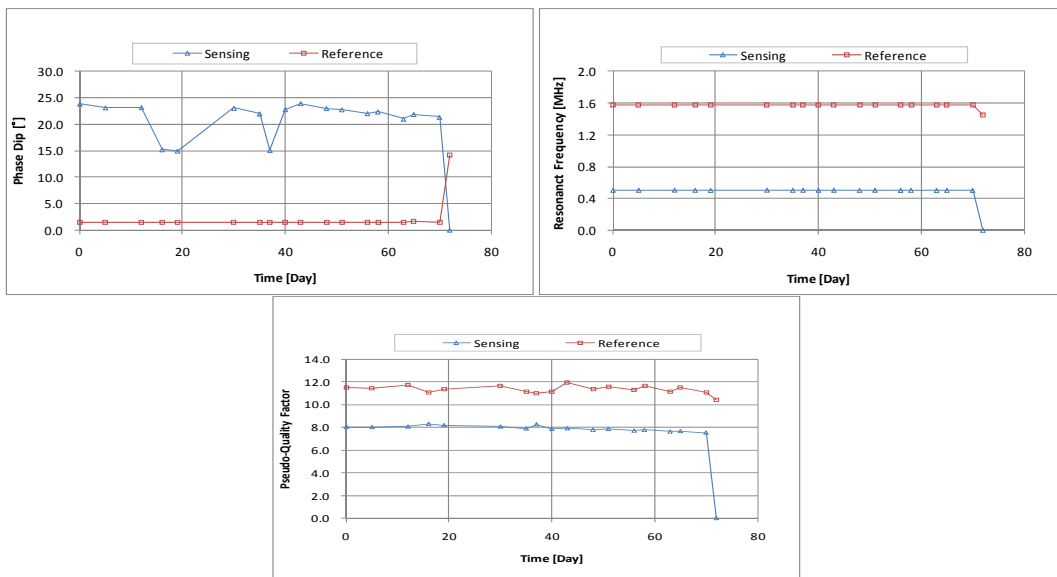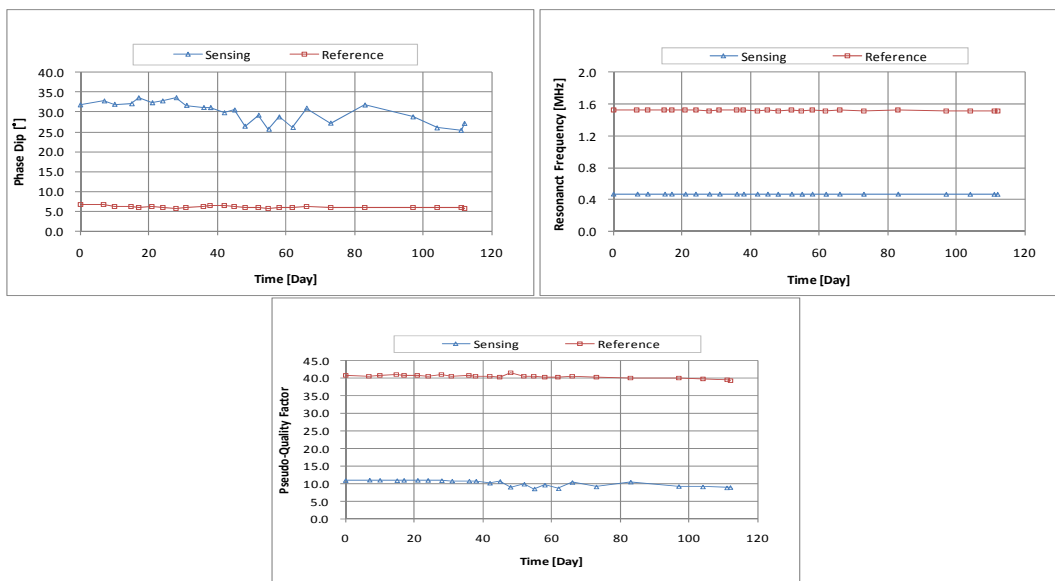

Figure B.2.24. The response of Sensor J024.
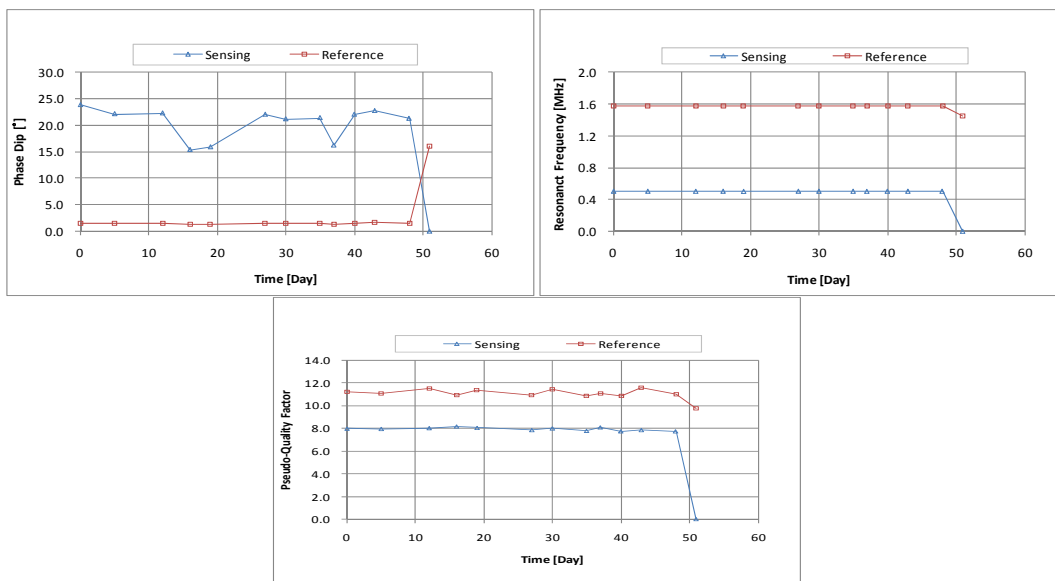
Figure B.2.25. The response of sensor J025.
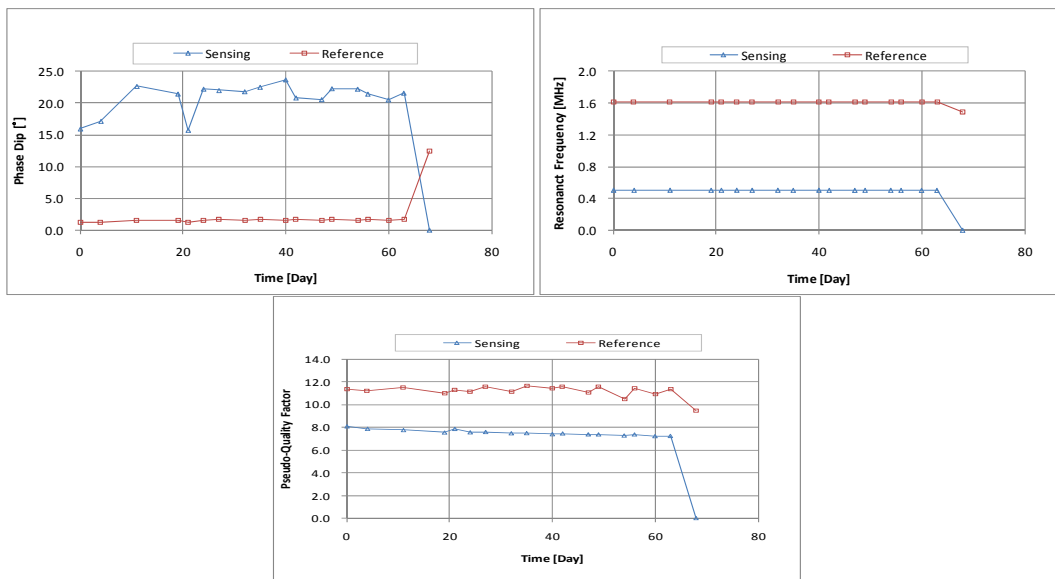
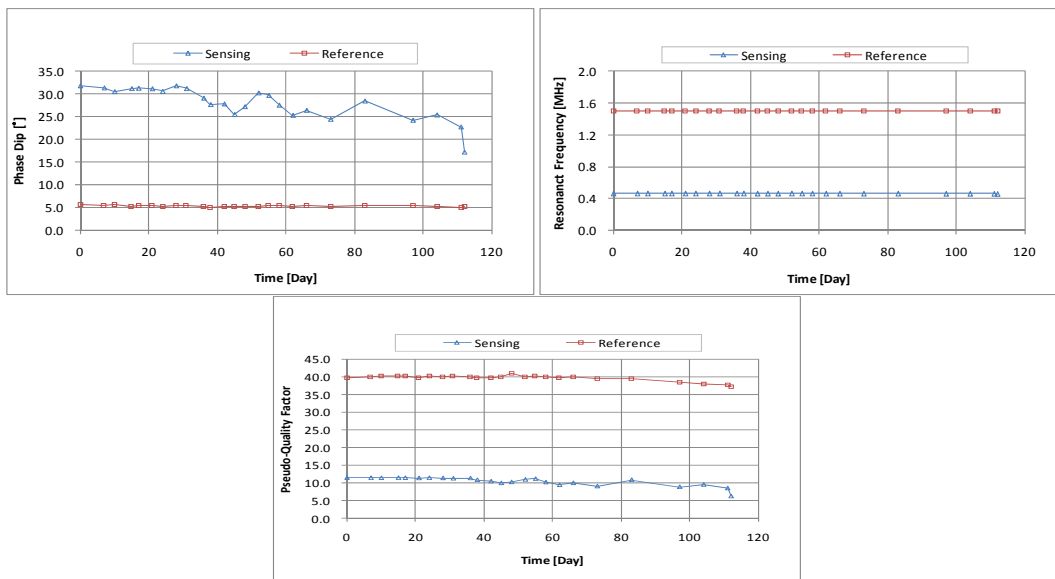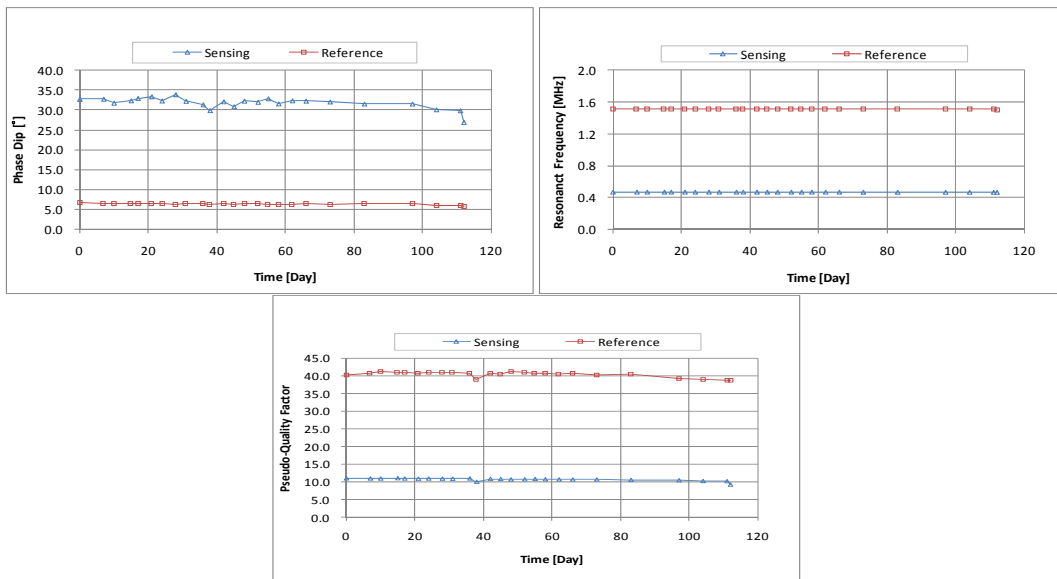
Figure B.2.26. The response of Sensor J026.
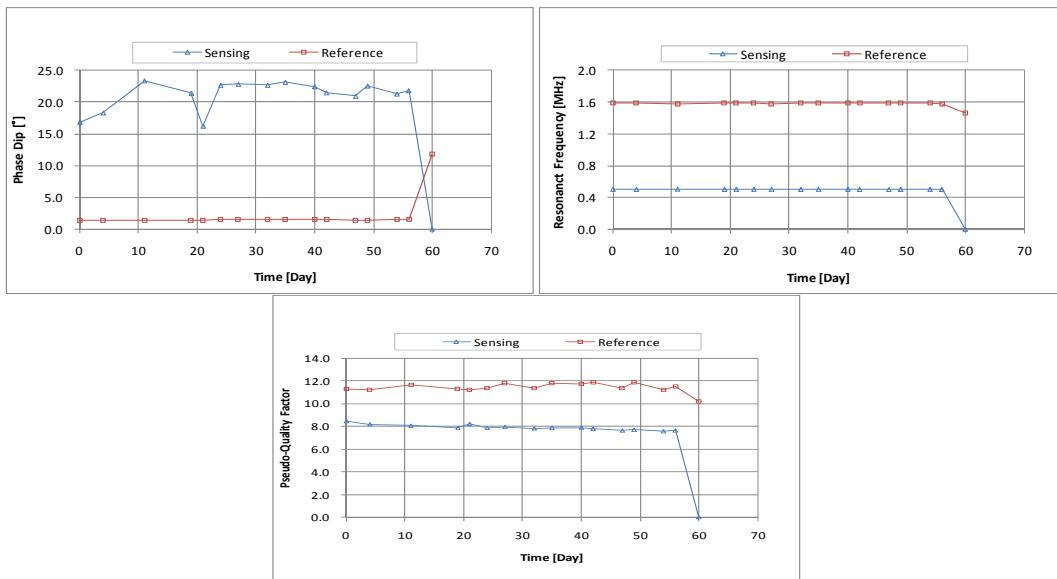
Figure B.2.27. The response of Sensor J027.
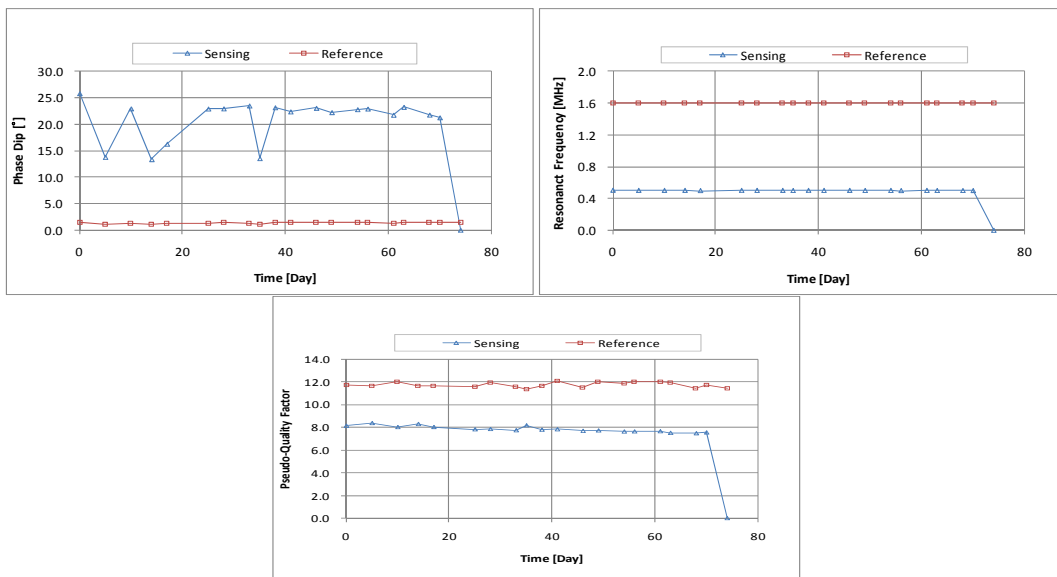
Figure B.2.28. The response of Sensor J028.
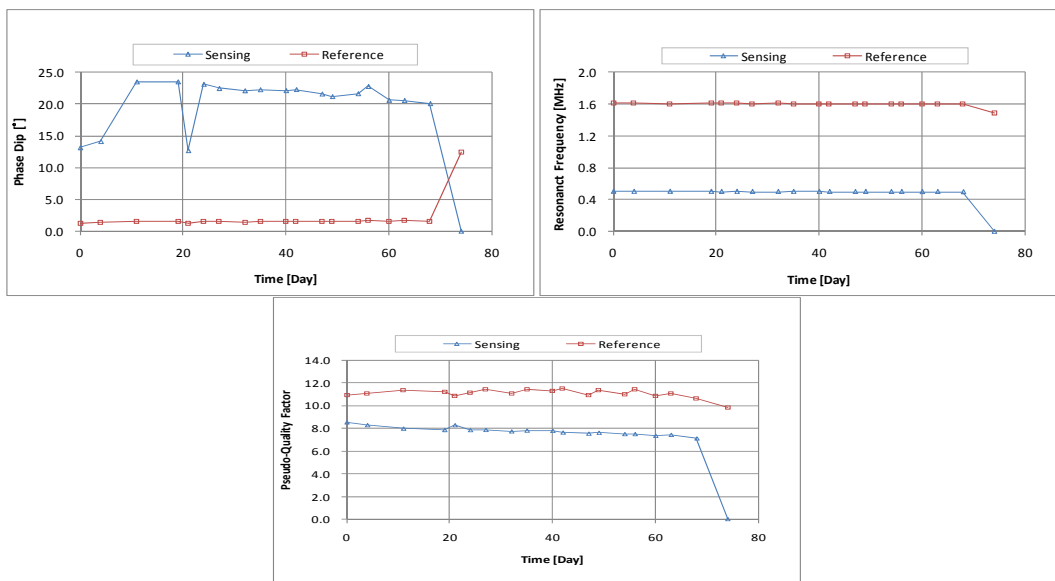
Figure B.2.29. The response of Sensor J029.
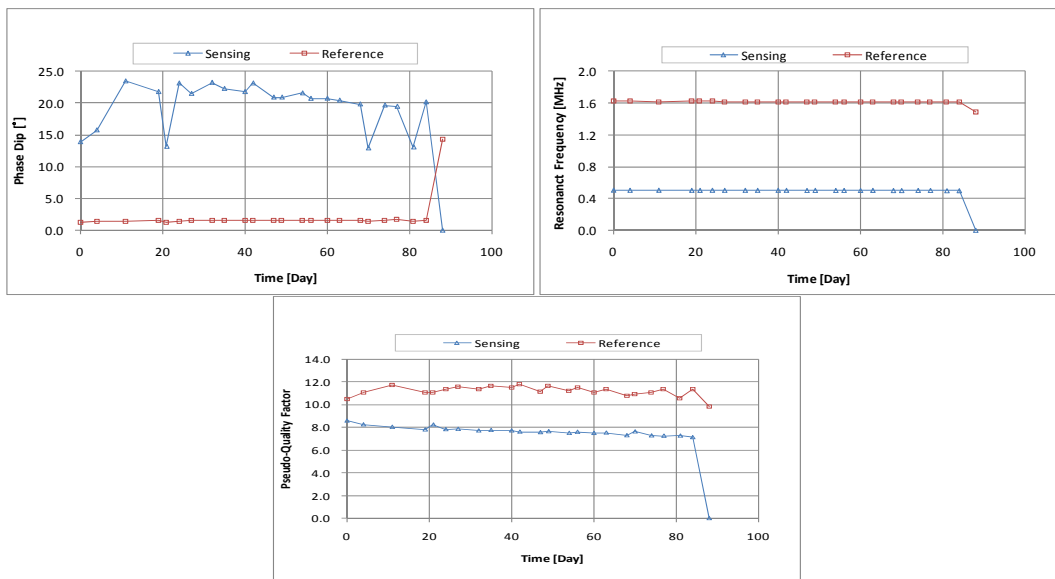
Figure B.2.30. The response of Sensor J030.
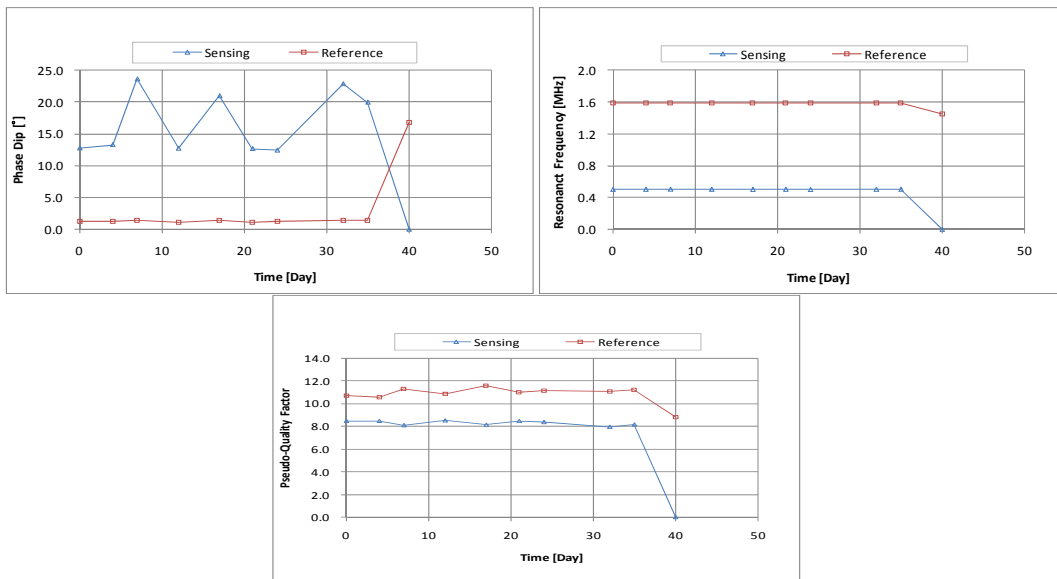
Figure B.2.31. The response of Sensor J031.
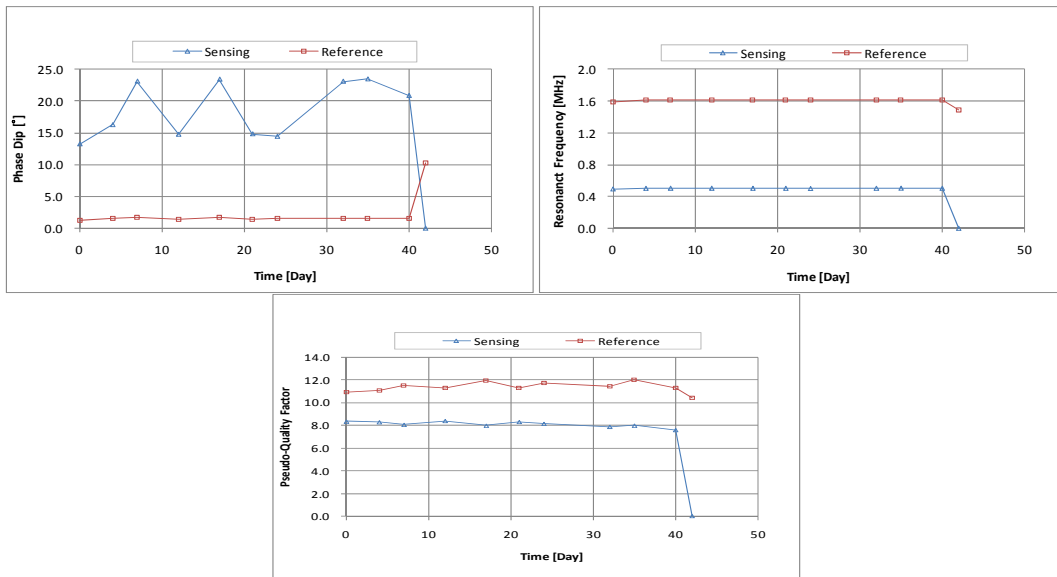
Figure B.2.32. The response of Sensor J032.
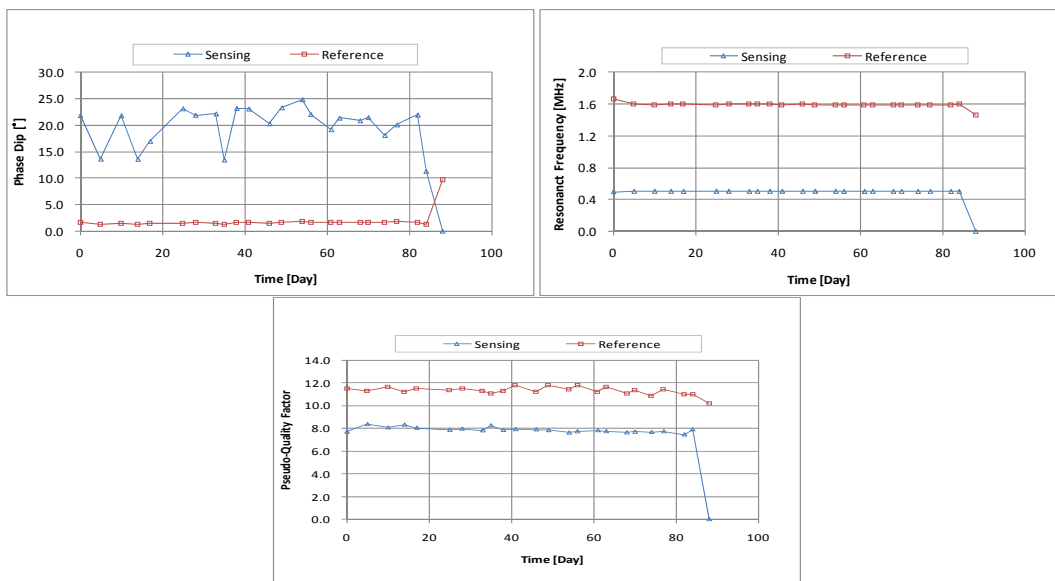
Figure B.2.33. The response of Sensor J033.
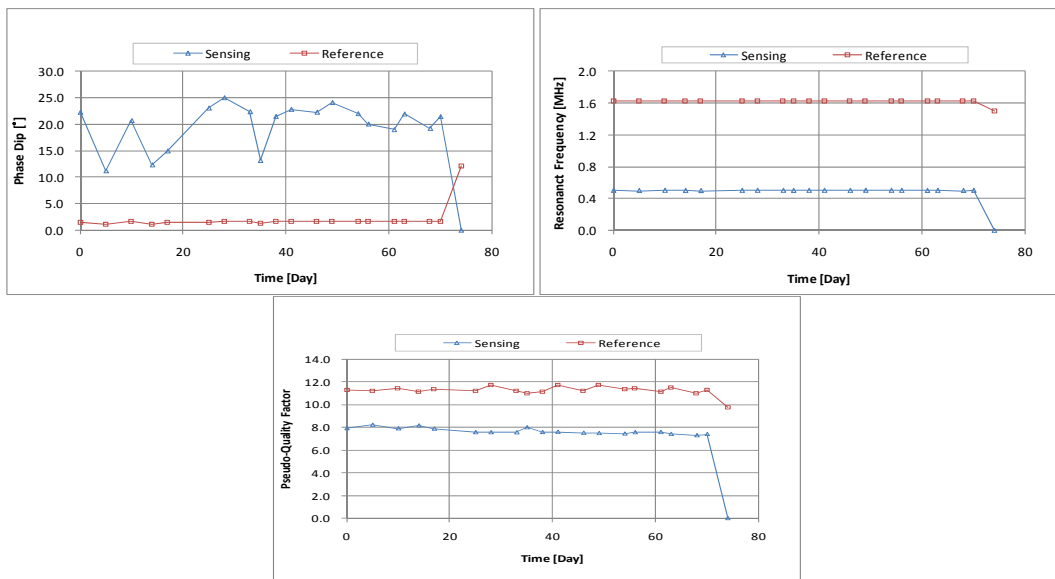
Figure B.2.34. The response of Sensor J034.

206
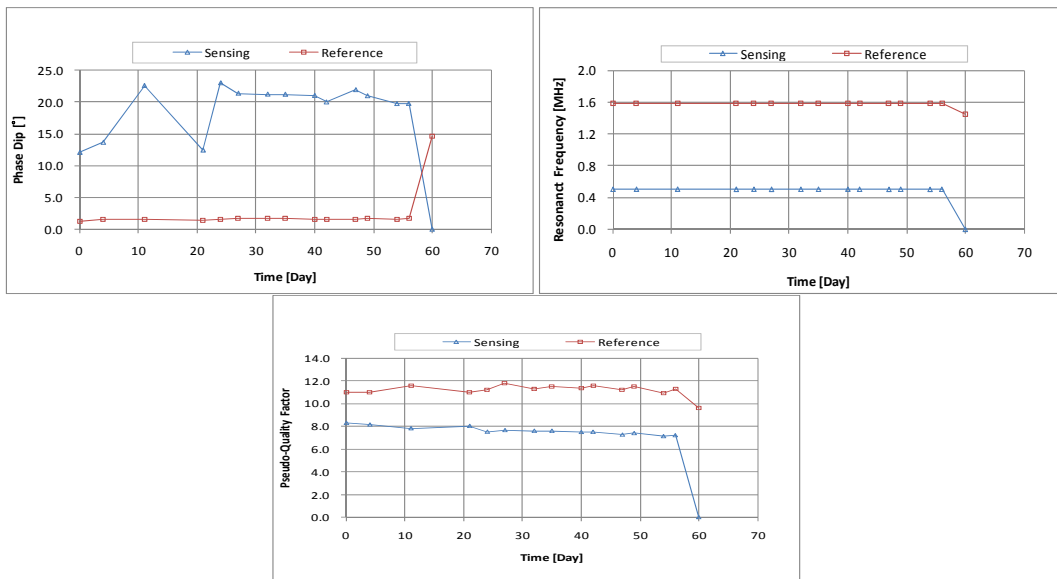
Figure B.2.35. The response of Sensor J035.
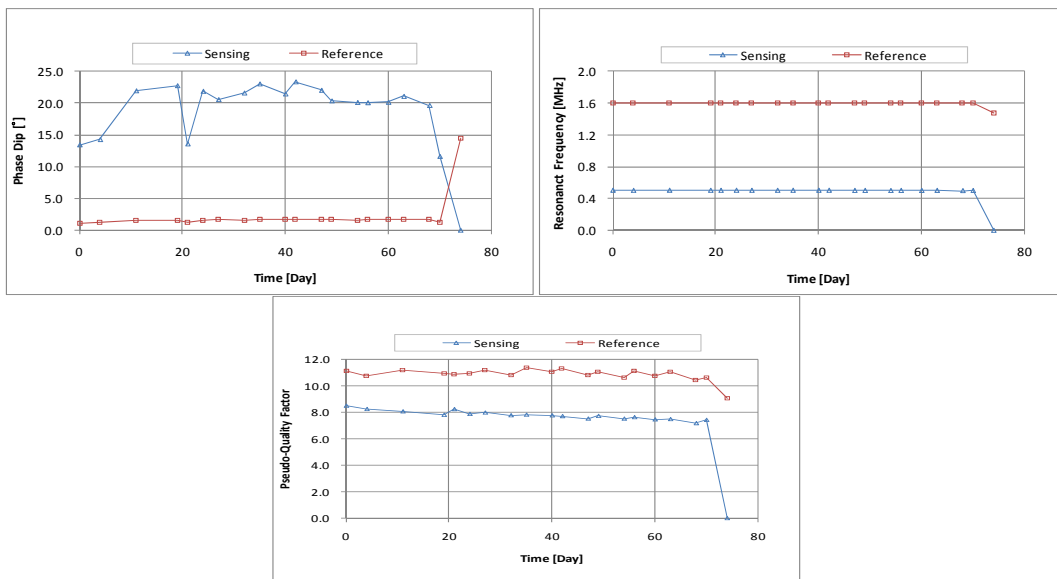
Figure B.2.36. The response of Sensor J036.

B.3 The Testing Results of the Second Corrosion Test
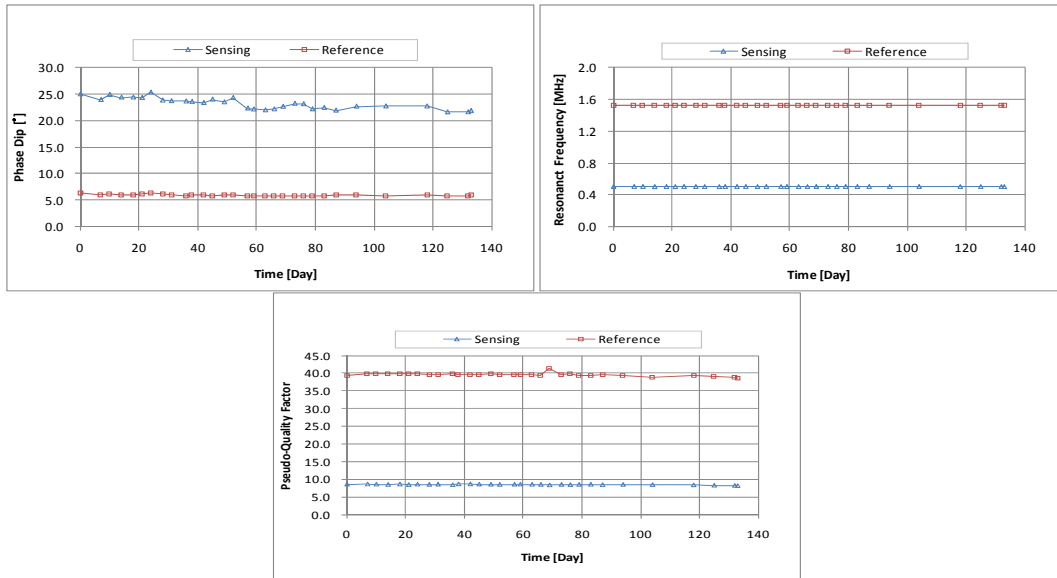
Figure B.3.1. The response of Sensor N001.
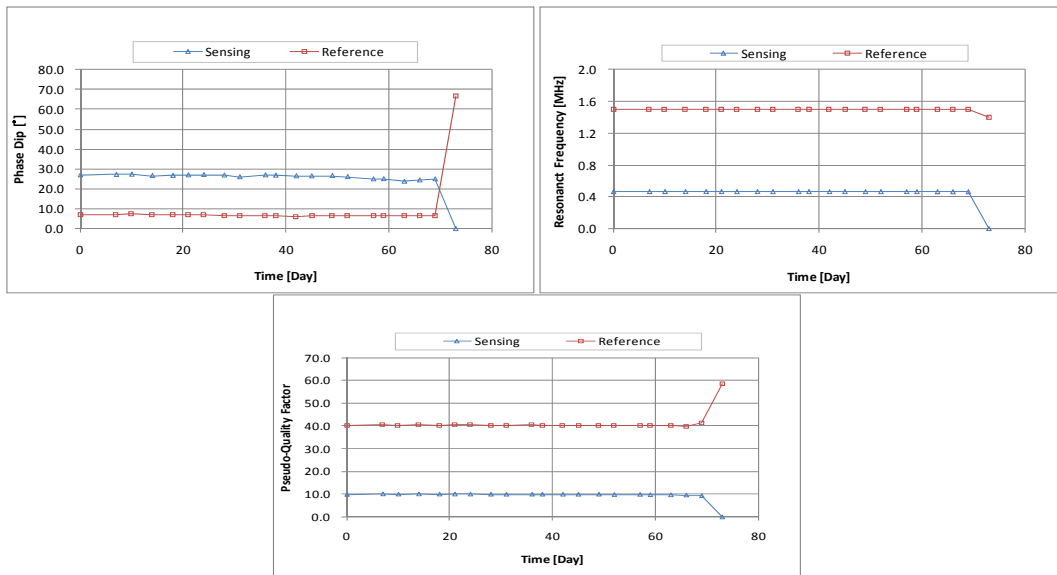
Figure B.3.2. The response of Sensor N002.
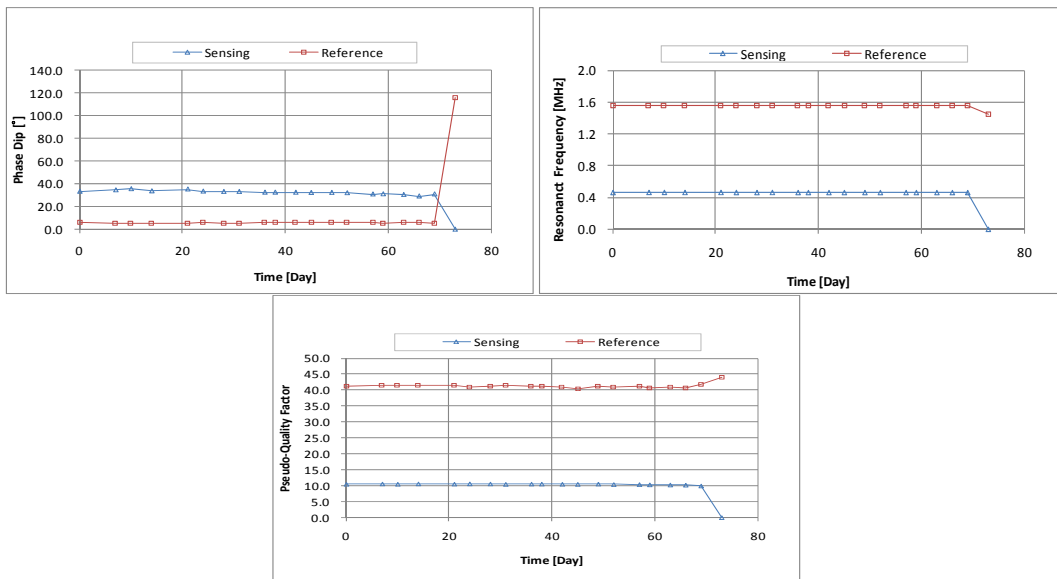
Figure B.3.3. The response of Sensor N003.
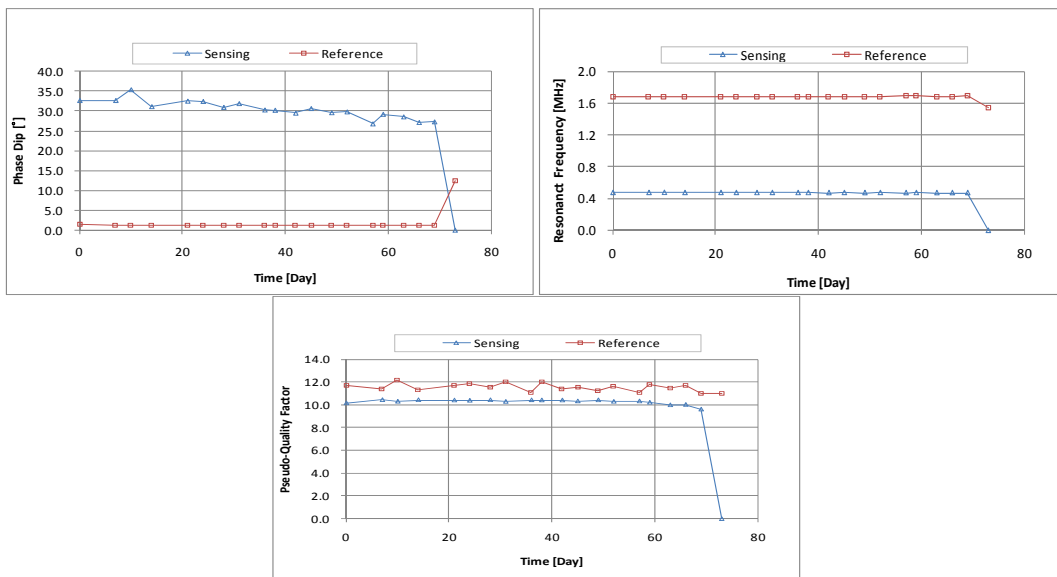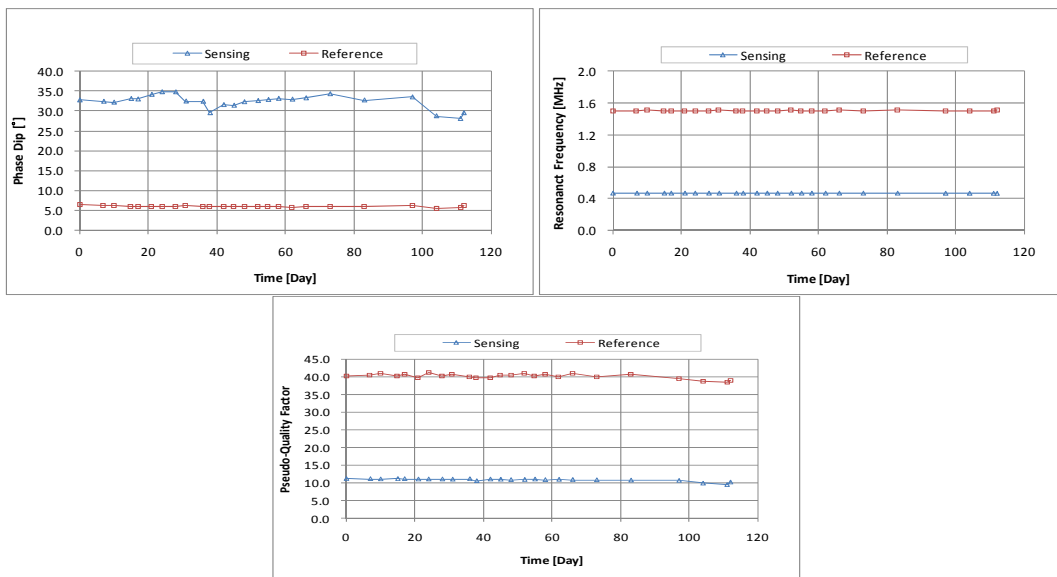

Figure B.3.4. The response of Sensor N004.

Figure B.3.5. The response of Sensor N005.
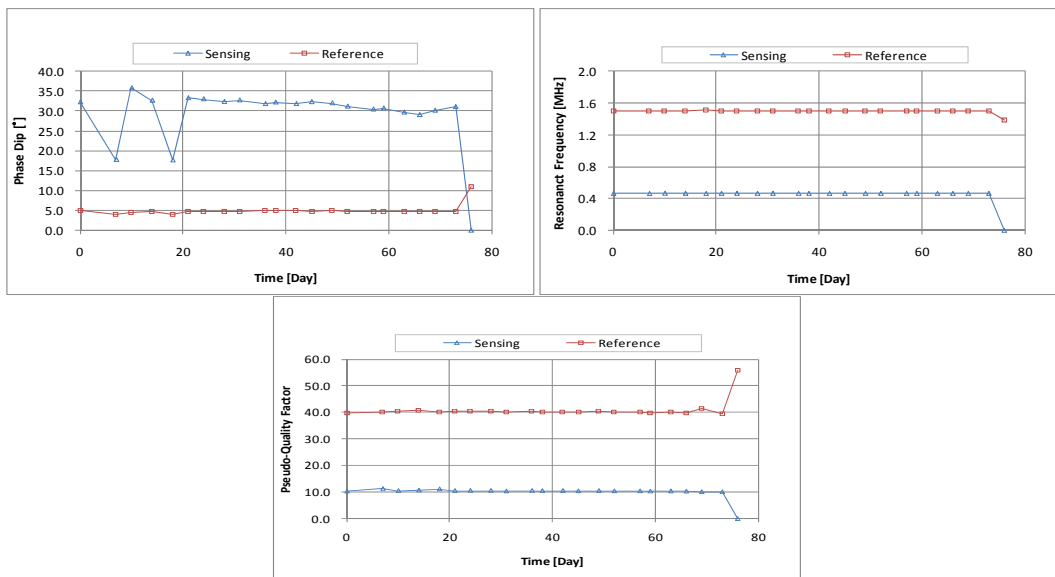
Figure B.3.6. The response of Sensor N006.
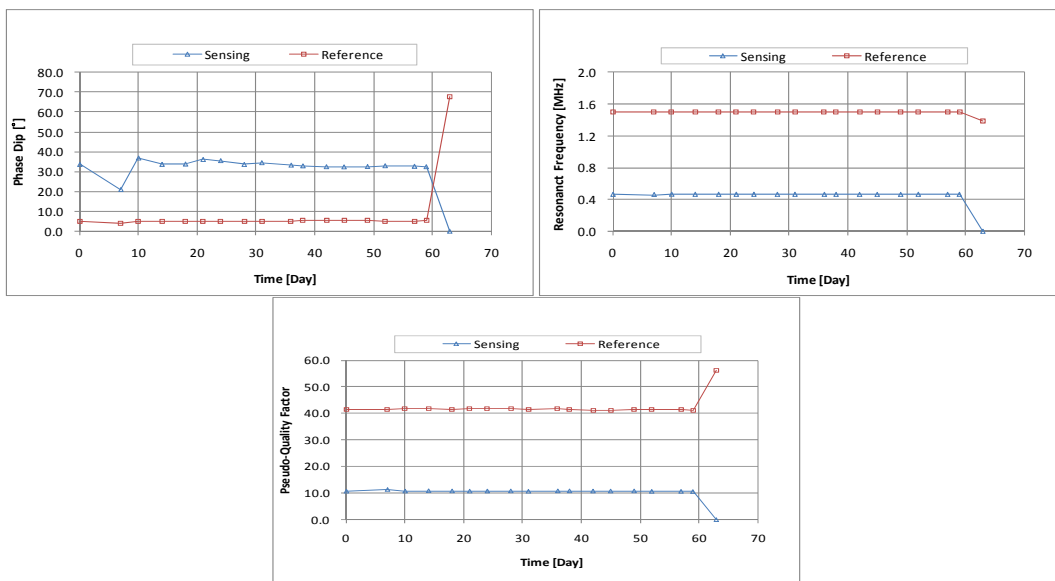
Figure B.3.7. The response of Sensor N007.
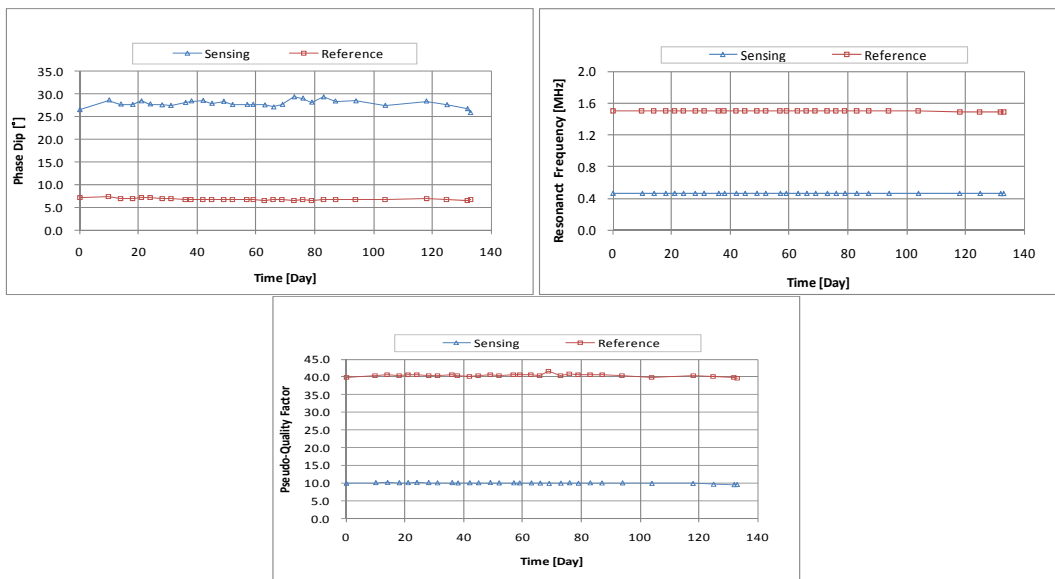
Figure B.3.8. The response of Sensor N008.

211
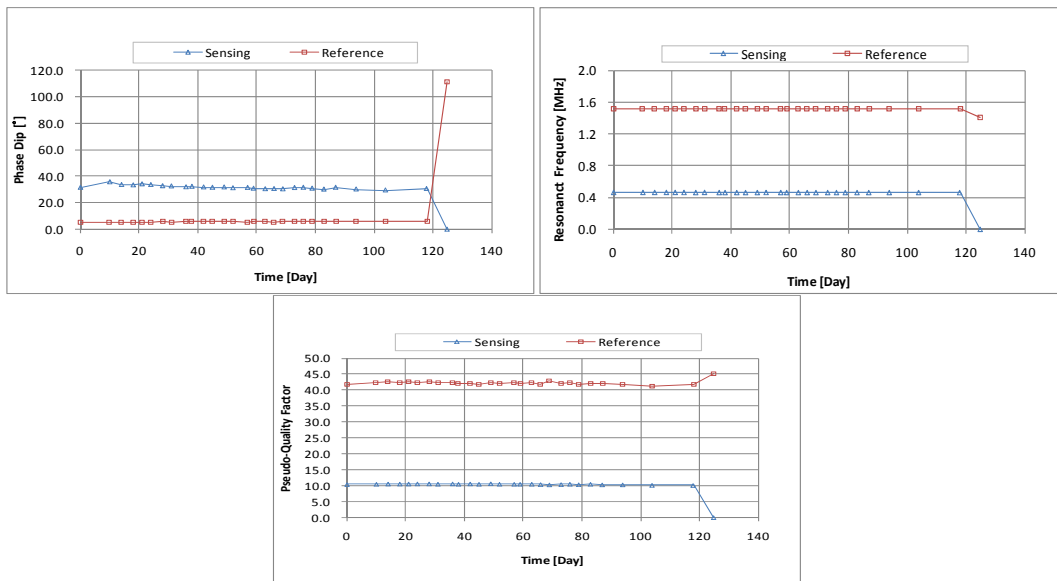
Figure B.3.9. The response of Sensor N009.
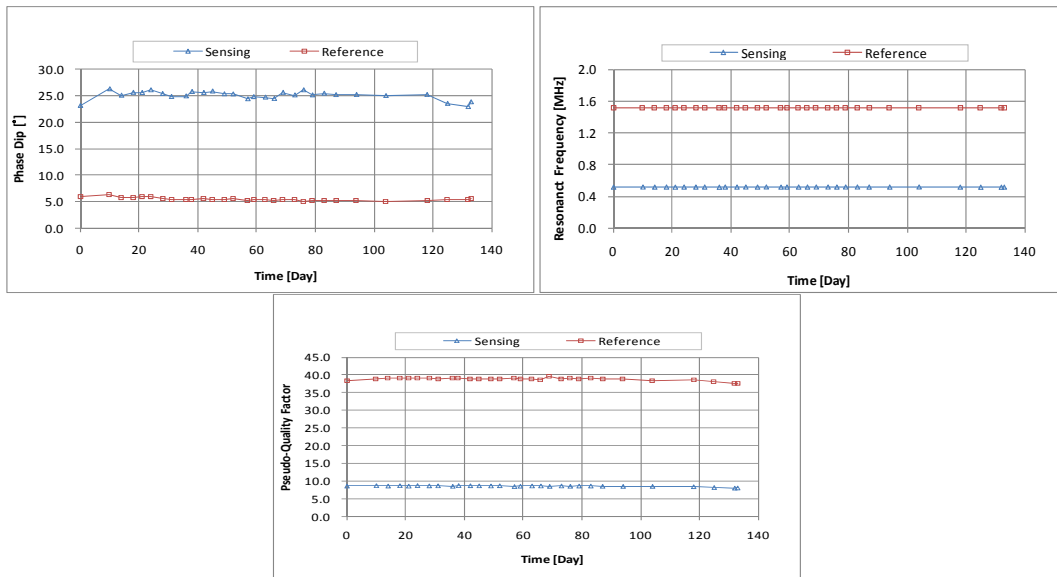
Figure B.3.10. The response of Sensor N010.
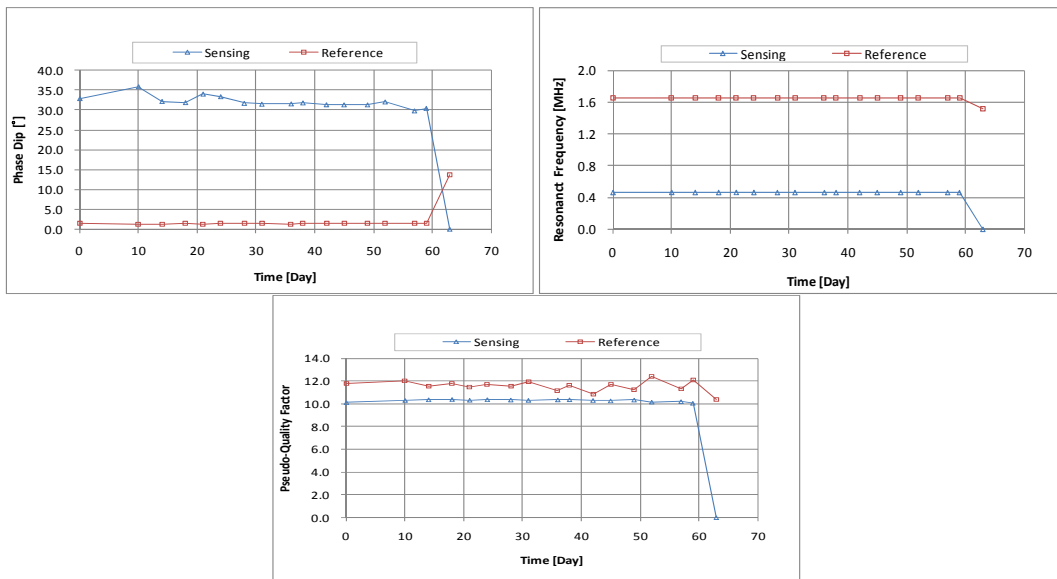
Figure B.3.11. The response of Sensor N011.
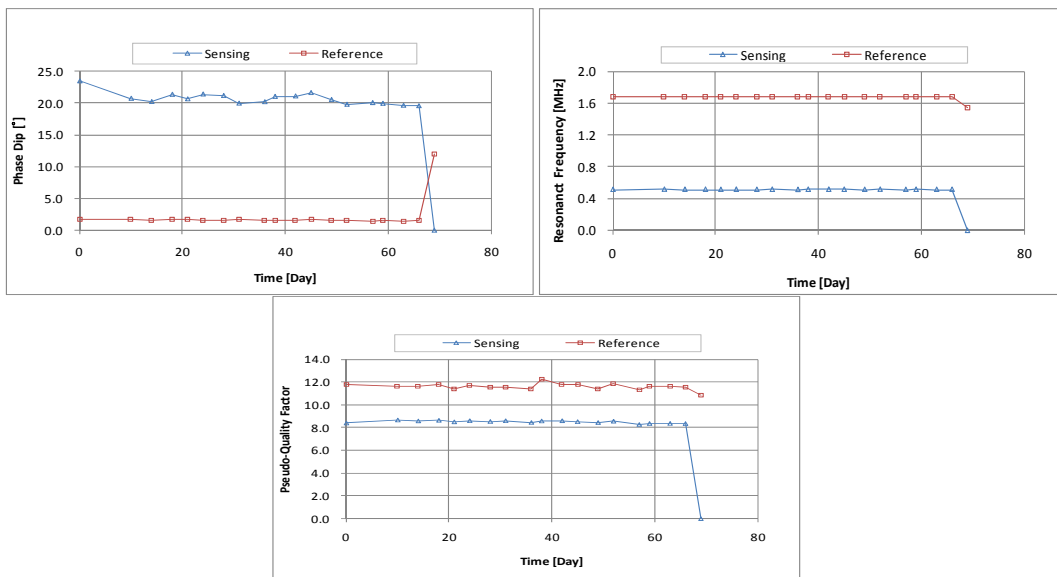
Figure B.3.12. The response of Sensor N012.
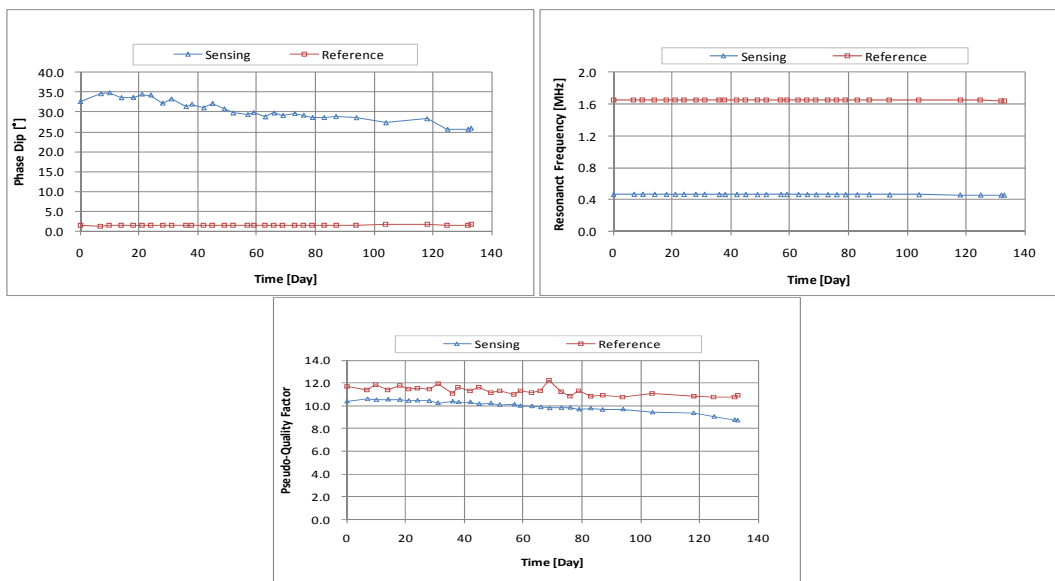
Figure B.3.13. The response of Sensor N013.
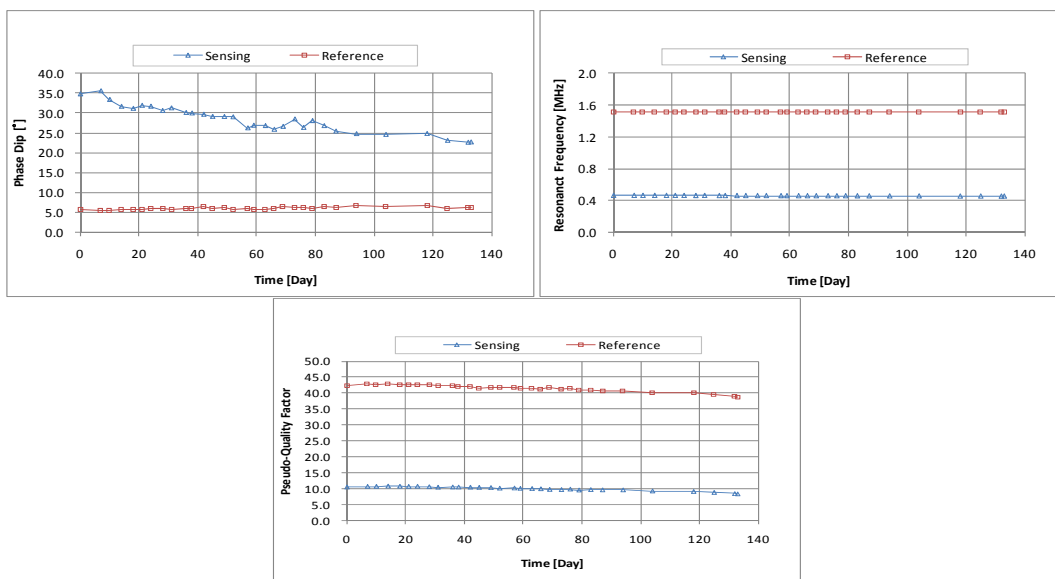
Figure B.3.14. The response of Sensor N014.
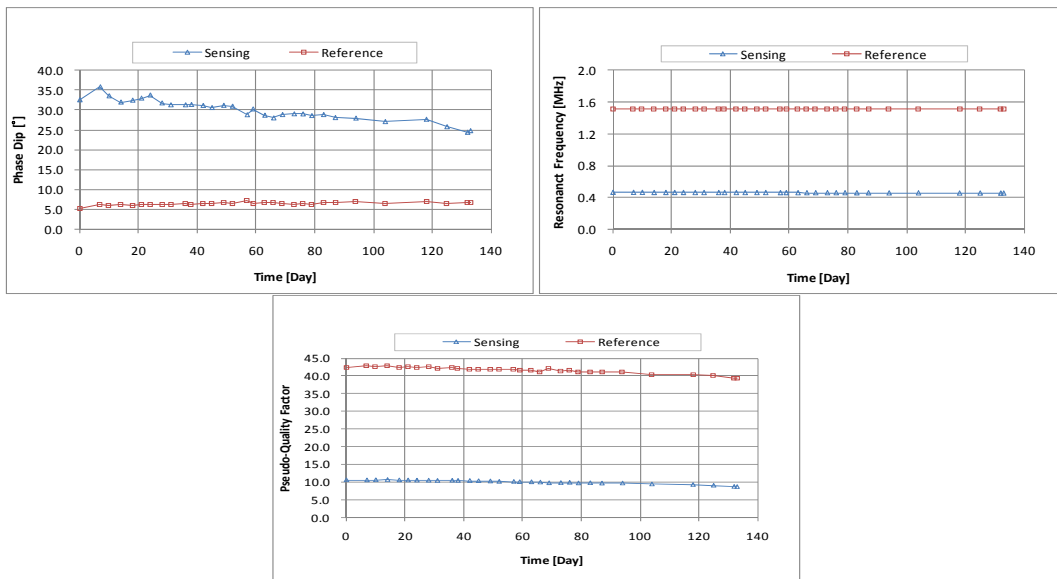
Figure B.3.15. The response of Sensor N015.
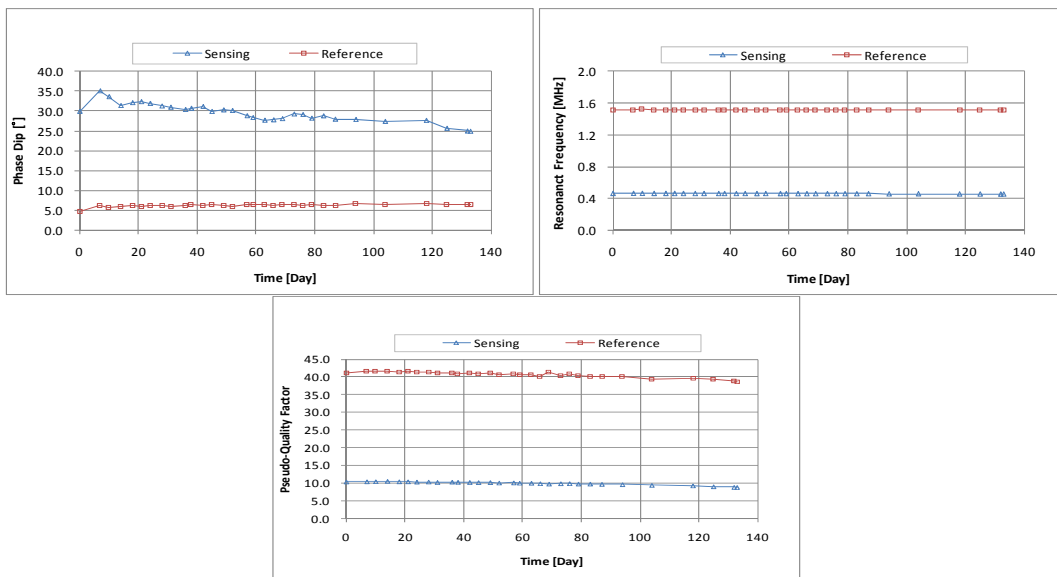
Figure B.3.16. The response of Sensor N016.
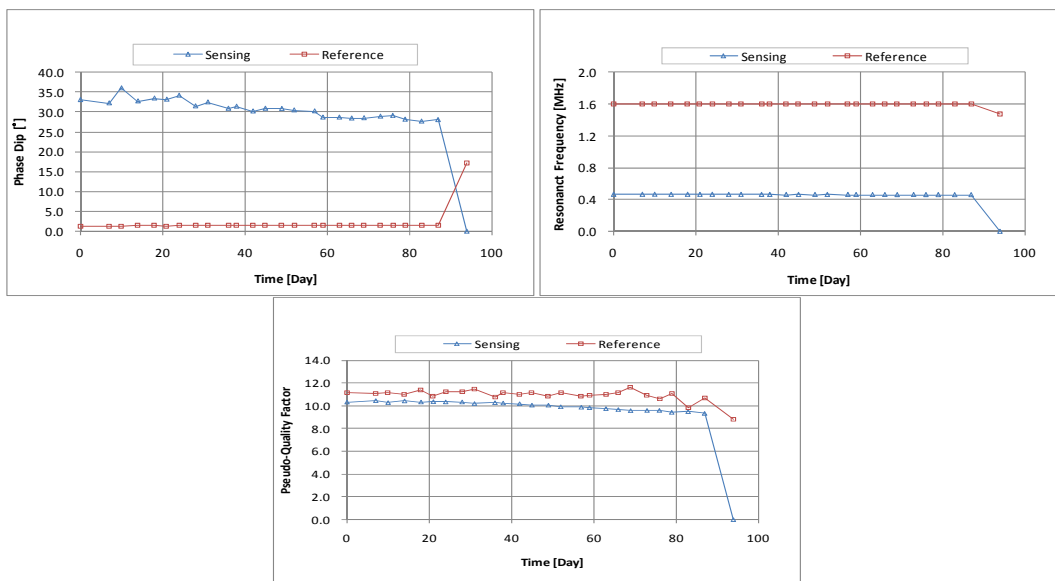
Figure B.3.17. The response of Sensor N017.
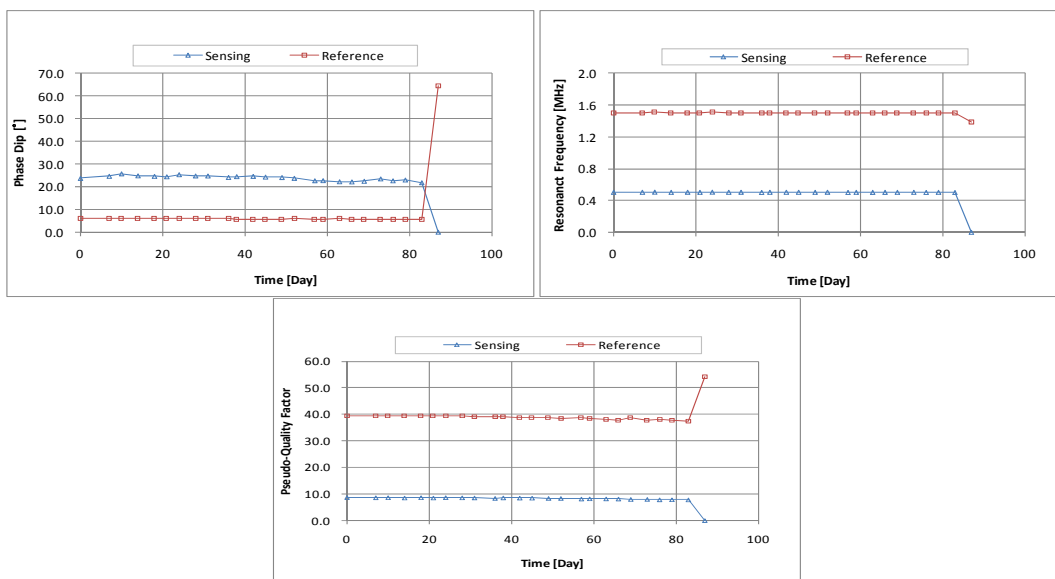
Figure B.3.18. The response of Sensor N018.

216
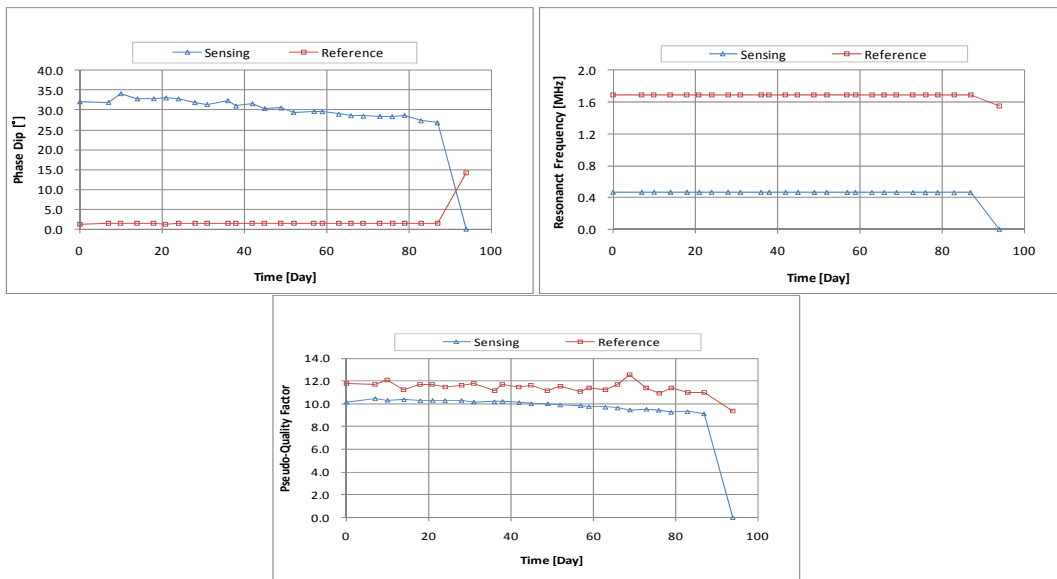
Figure B.3.19. The response of Sensor N019.

Figure B.3.20. The response of Sensor N020.

Figure B.3.21. The response of Sensor N021.

Figure B.3.22. The response of Sensor N022.

Figure B.3.23. The response of Sensor N023.

Figure B.3.24. The response of Sensor N024.

Figure B.3.25. The response of Sensor N025.

Figure B.3.26. The response of Sensor N026.

Figure B.3.27. The response of Sensor N027.

Figure B.3.28. The response of Sensor N028.

APPENDIX C

Fabrication of Protective Housing for Threshold

Corrosion Sensor

In order to provide environmental protection for threshold corrosion sensors, four steps need to be finished. These are: (a) solder coating on steel sensing wire, (b) epoxy coating of all circuit components, (c) cement paste housing, and (d) application of glue. Figure C.1 demonstrates the location where sensing wire should be coated by silver-bearing solder in order to provide the first line of defense to prevent the corrosion of the sensing wire within the cement paste housing.
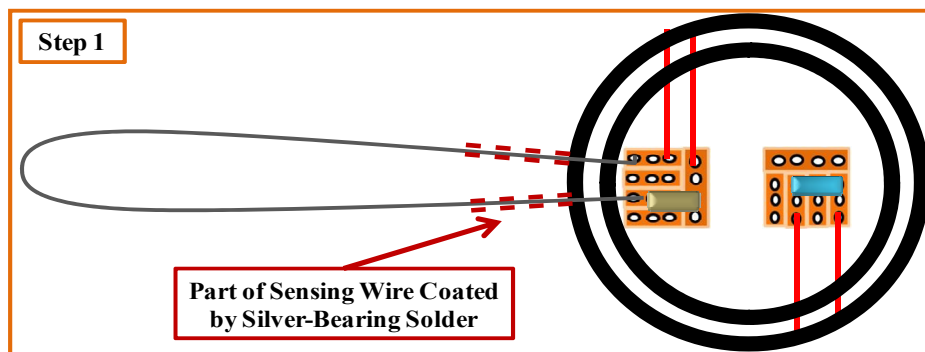
Figure C.1. The coating location of the sensing wire after finishing the circuitry of the sensor.

In the second step, the circuitry and the coils of the sensor need to be covered by epoxy (Figure C.2). The only caution here is to avoid breaking the epoxy around the junction of the steel wire and the outer coil (Figure C.3). If the epoxy housing is broken in that region, a clear void will be produced and will provide a path for

chloride content to penetrate the sensor housing.
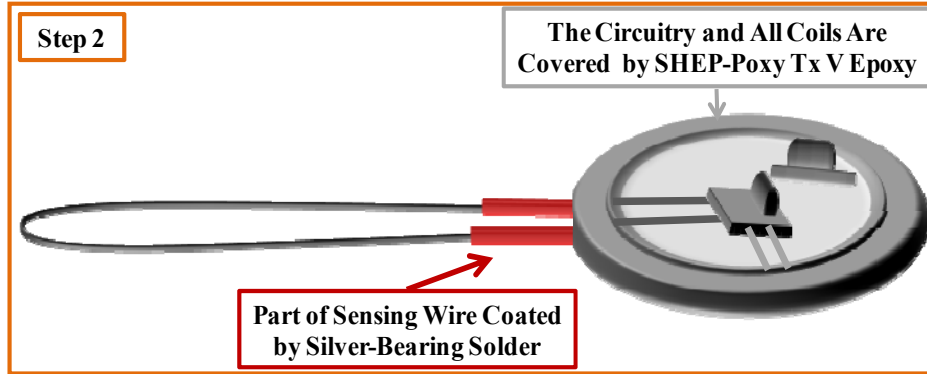
Figure C.2. The circuitry of the sensor covered by epoxy housing in the second step.
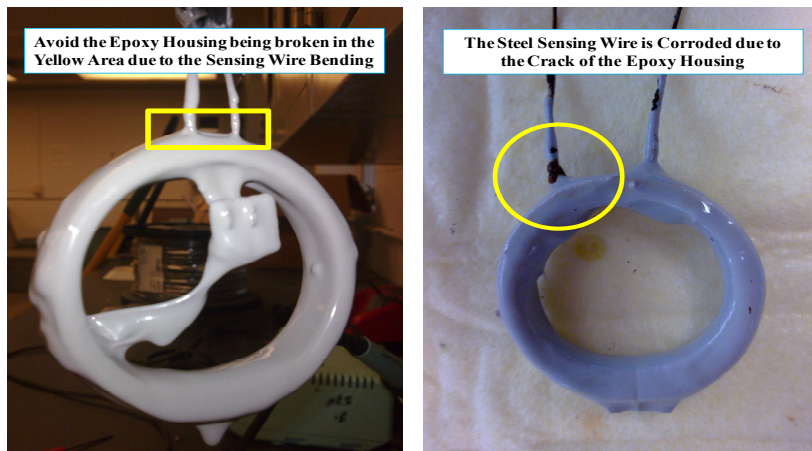
Figure C.3. Possible failure of the epoxy housing protection.

Before starting the third step, the surface of the epoxy housing needs to be covered by sand in order to prevent cracks of the cement paste housing occurring due to the poor bond condition between the epoxy housing and the cement paste housing. As shown in Figure C.4, the sand cover needs to be applied before the epoxy housing completely dries. The only caution here is to ensure that the sand completely covers the whole epoxy housing.

Figure C.4. The process to increase the roughness of the epoxy housing surface.

During the third step, the new mold discussed in Section 4.3.3.1.1 will be used to pot the cement paste housing with the mixture proportions in Table 4.12. The left side of Figure C.5 shows that the sensor will float during the potting process if it is not restrained. From this, many following problems arise (e.g. the phase dip will be influenced resulting from the tilt of the sensor). In order to avoid these unexpected situations impacting the performance of the sensor in the future, two threads wind the epoxy coated sensor with the angle approximate 120 degree and fix at the same level of the new mold surface to prevent the situation of the floating of the sensor during the cement paste housing potting process (Figure C.5). The other caution, as concluded in Section 4.3.3.1.1, regards the thickness of the cement paste housing. The thickness must be at least 4 mm to avoid the cracking or spalling of the cement paste housing.
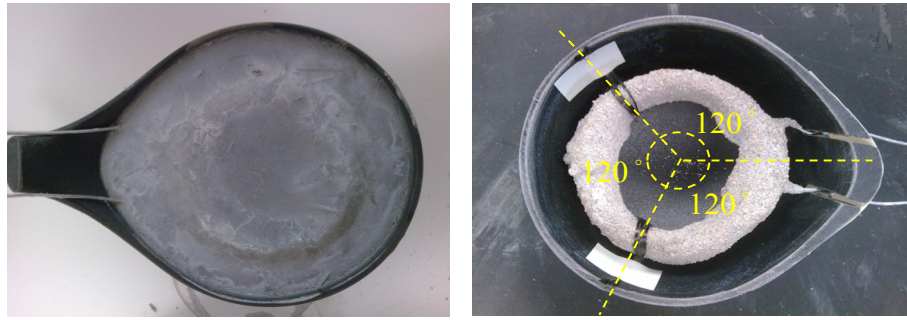
Figure C.5. Floating of circuit components during the potting process (left) and restraint system (right).

After construction of the cement paste housing is completed, the last step is to use glue to cover a small region of the sensor wire around the cement paste housing. This will prevent the accumulation of the chloride content in the junction of the sensing wire and cement paste housing (Figure C.6).
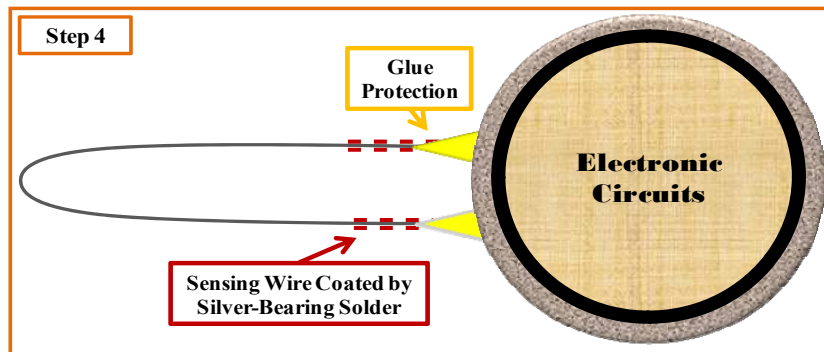
Figure C.6. Glue applied to surface of wire at interface of cement paste housing.

Once the previous step is completed, all the protection measures of the threshold corrosion sensor are also basically completed. However, if more time is required for the cement paste housing to provide a high pH environment, the mold attached with tape, as shown at the bottom of Figure C.7, improved finish of cement

paste housing. The significant improvement can be observed in Figure C.7.
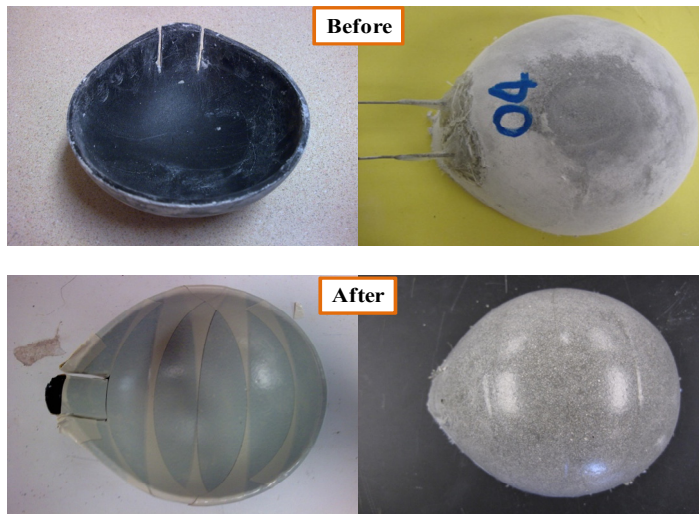
Figure C.7. The before and after modification of the surface of the cement paste housing.

APPENDIX D

Parameter Study of the Conductivity Sensor
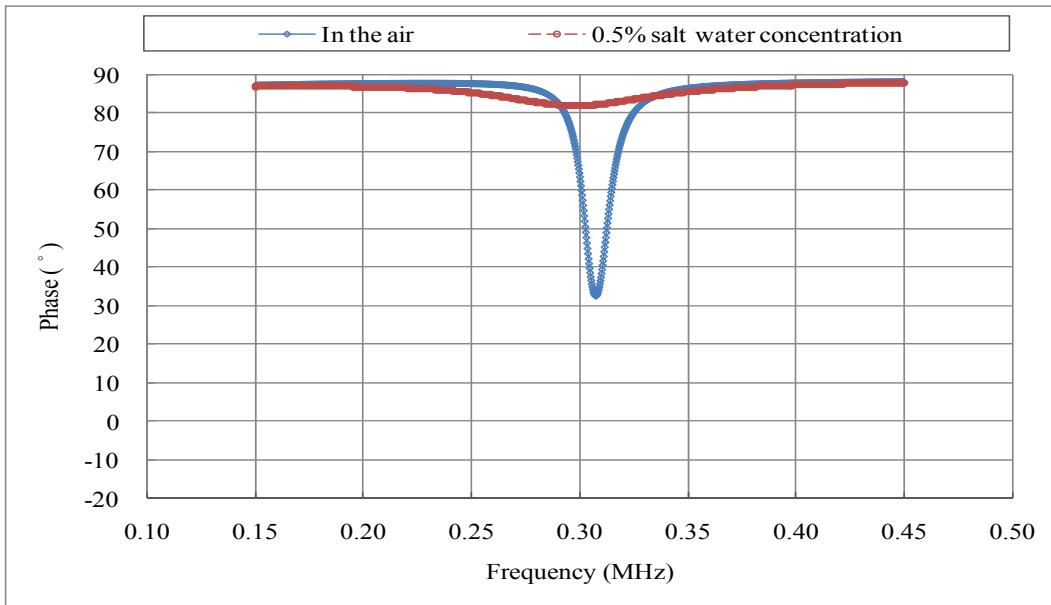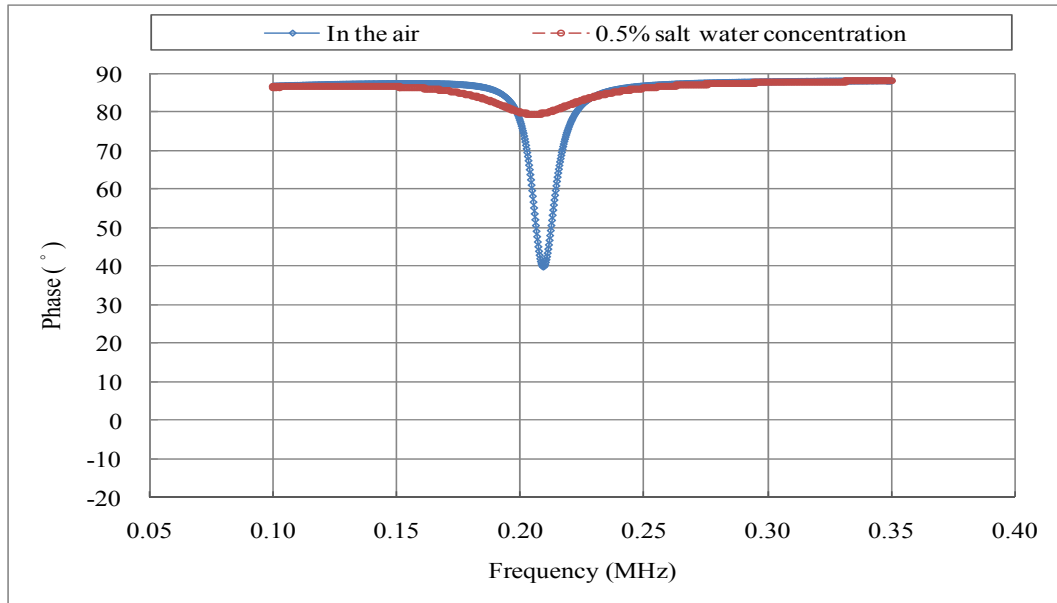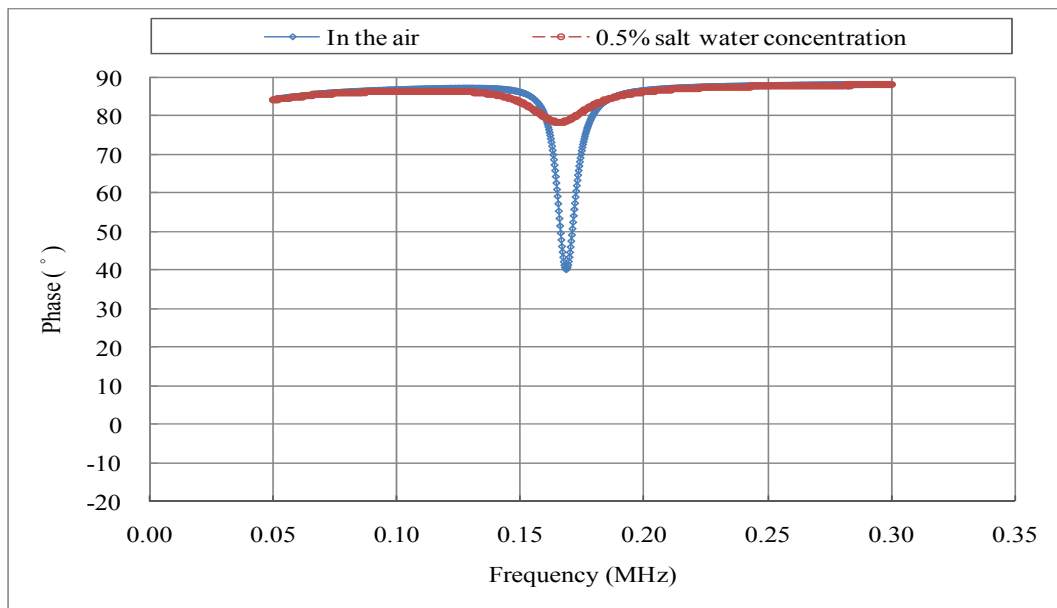
D.1 Capacitor Study
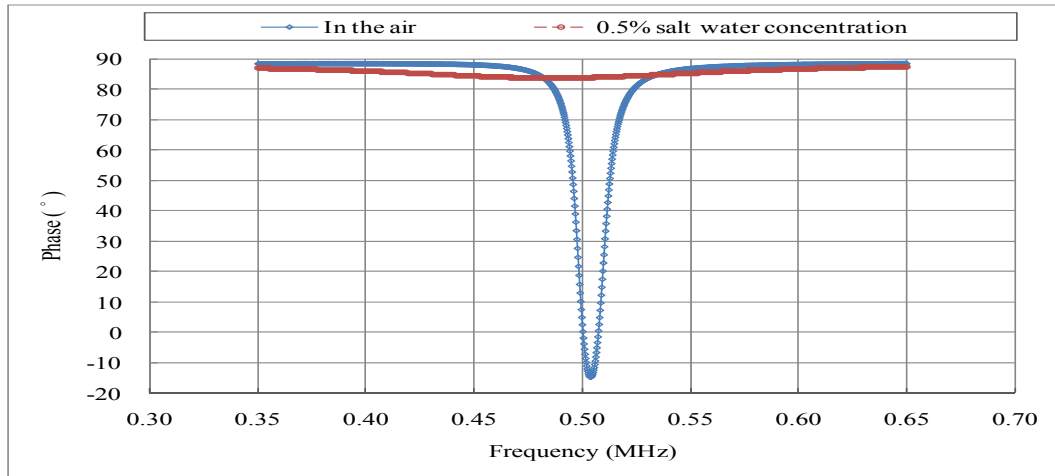
Figure D.1.1. Comparison of conductivity sensor with 33,000 pF (COG) capacitor in air and 0.5% salt water.
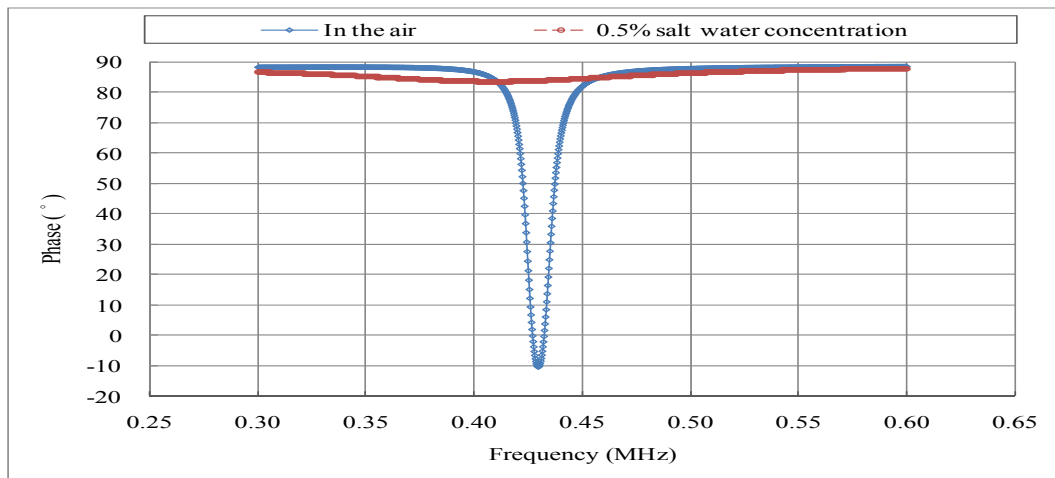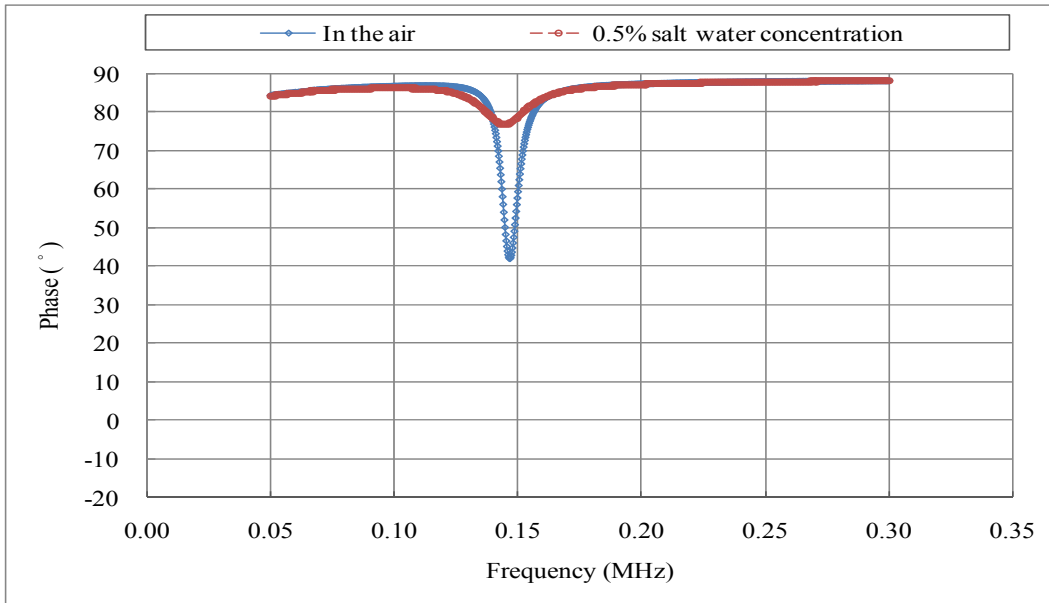

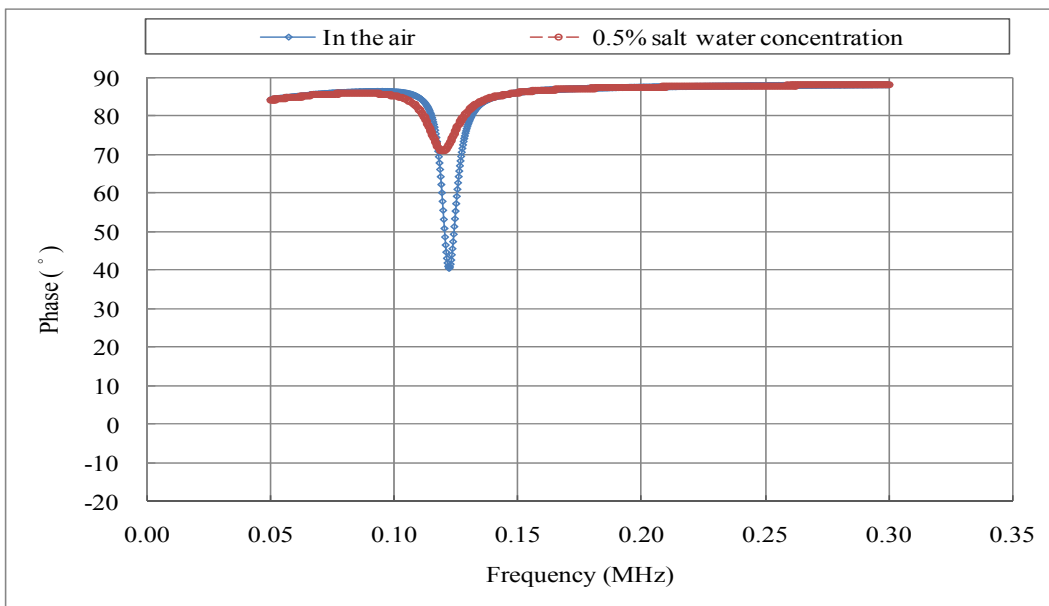*Figure D.1.2. Comparison of conductivity sensor with 47,000 pF (COG) capacitor in air and 0.5% salt water.*
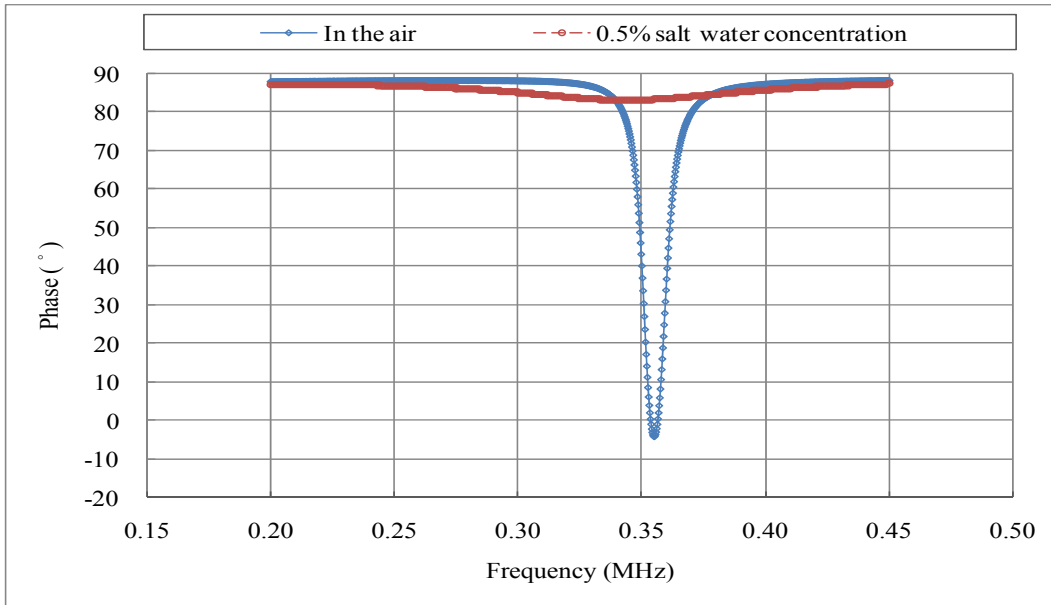
Figure D.1.3. Comparison of conductivity sensor with 68,000 pF (COG) capacitor in air and 0.5% salt water.

Figure D.1.4. Comparison of conductivity sensor with 100,000 pF (X7R) capacitor in air and 0.5% salt water.

Figure D.1.5. Comparison of conductivity sensor with 220,000 pF (X7R) capacitor in air and 0.5% salt water.

Figure D.1.6. Comparison of conductivity sensor with 330,000 pF (X7R) capacitor in air and 0.5% salt water.

Figure D.1.7. Comparison of conductivity sensor with 470,000 pF (X7R) capacitor in air and 0.5% salt water.

Figure D.1.8. Comparison of conductivity sensor with 680,000 pF (X7R) capacitor in air and 0.5% salt water.

D.2 Performance of the Conductivity Sensor with Chloride Copper II Covered Sensing Probe (Copper Probe)
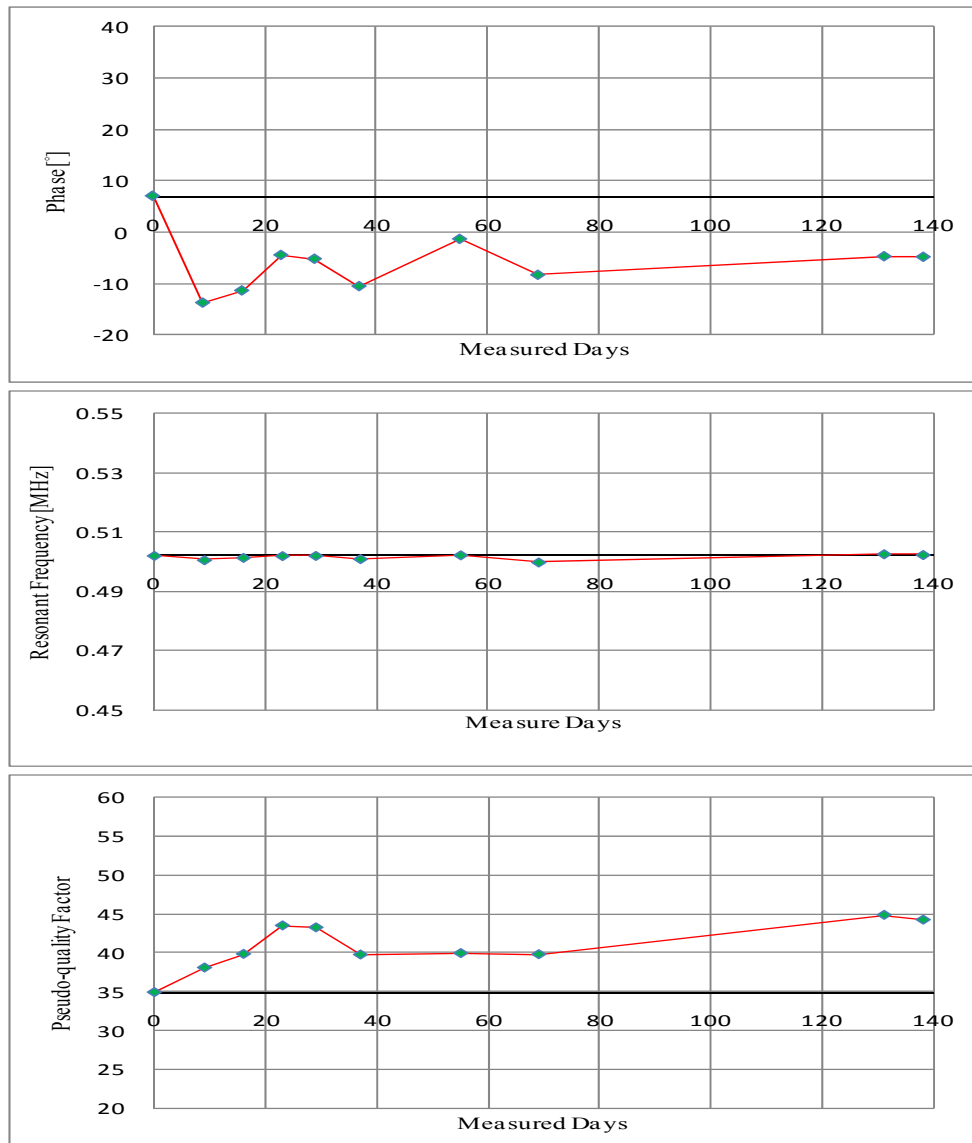
Figure D.2.1. Measured response of conductivity sensor with copper (II) chloride layer on sensing probe (33000 pF capacitor).
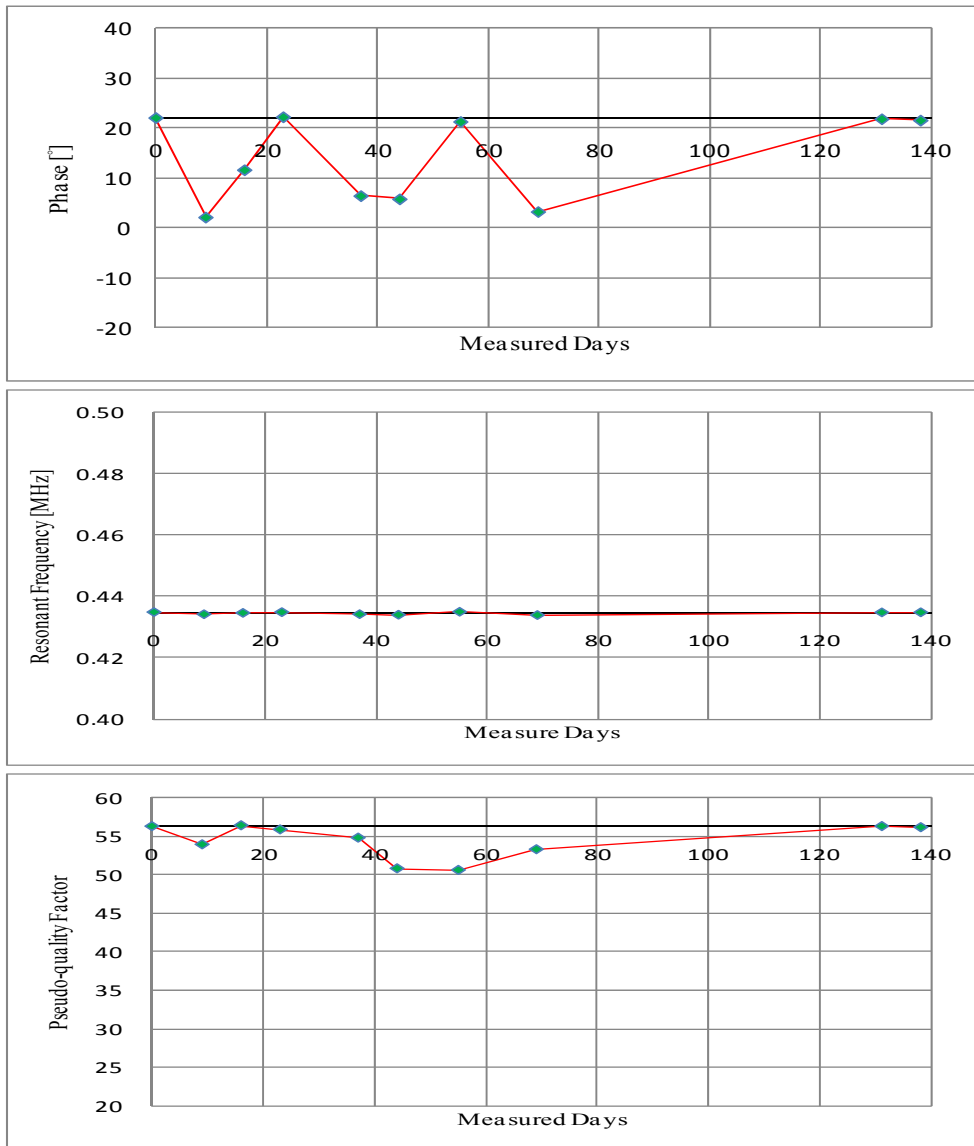
Figure D.2.2. Measured response of conductivity sensor with copper (II) chloride layer on sensing probe (47000 pF Capacitor)
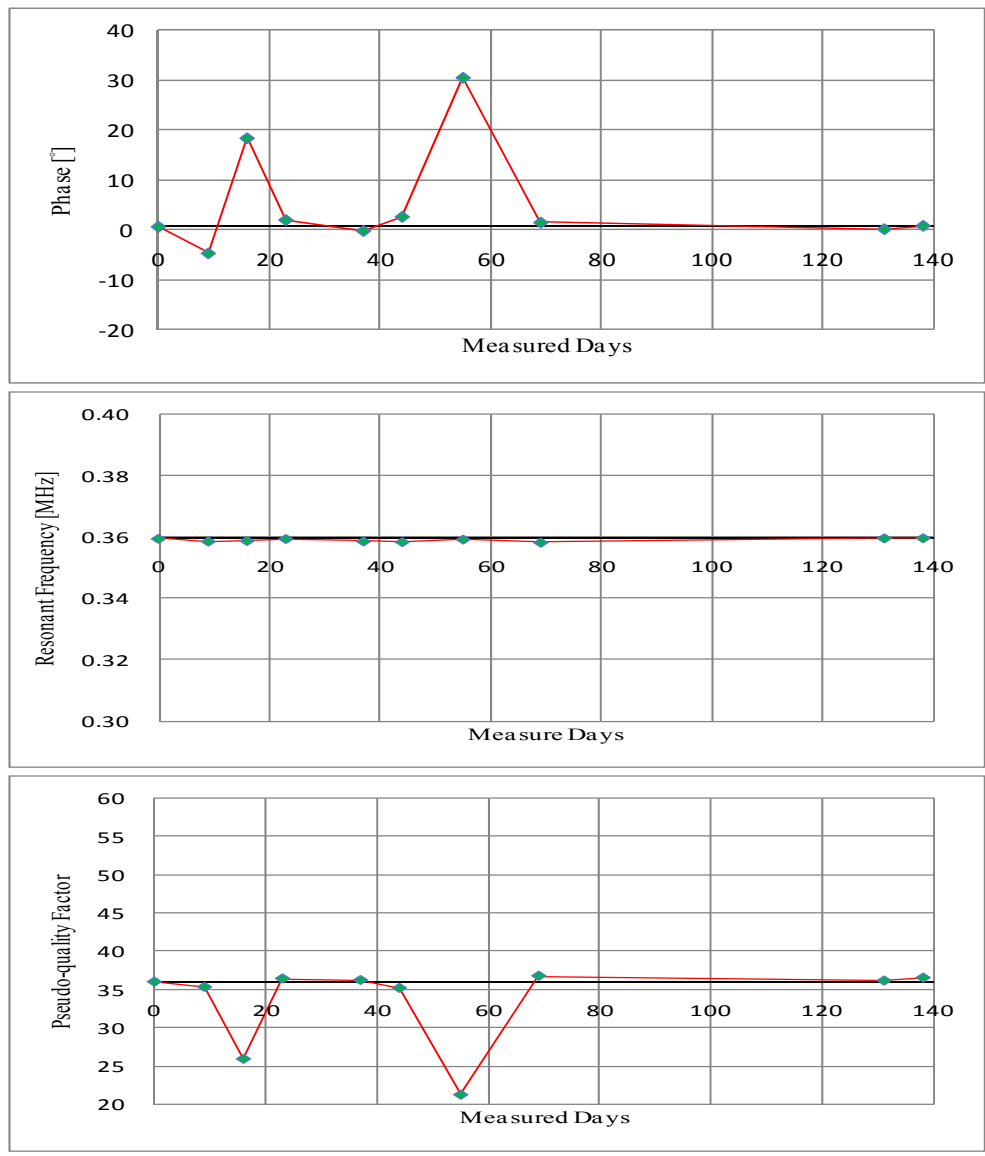
232

Figure D.2.3. Measured response of conductivity sensor with copper (II) chloride layer on sensing probe (68000 pF Capacitor)

D.3 Conductivities Obtained from the Commercial Conductivity Meter and Proposed Formula (Eq. 2.8) in Different Temperatures and Salt Water Concentrations
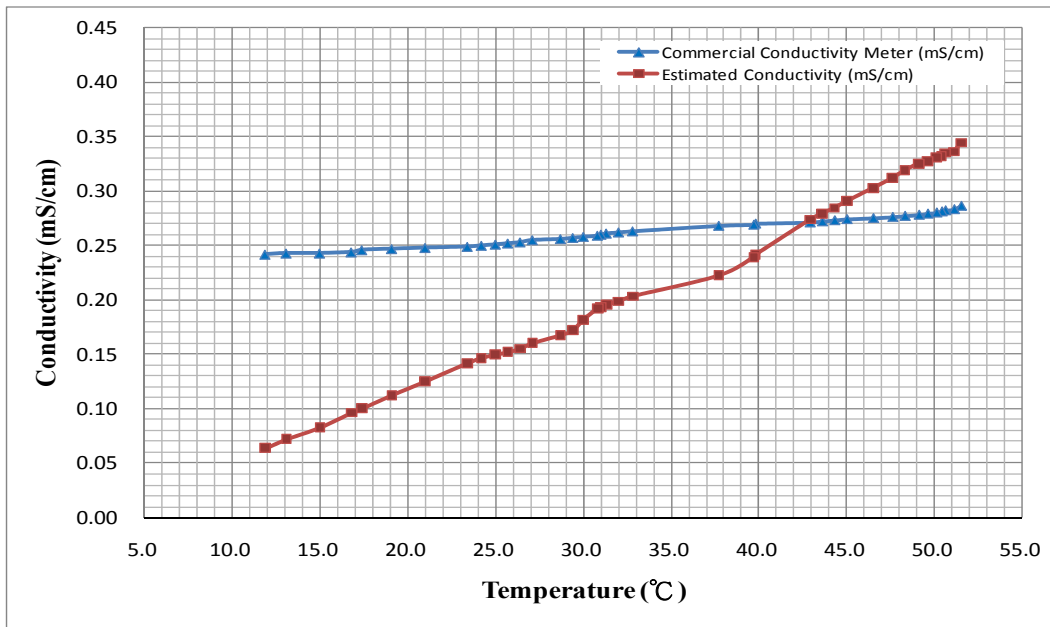

Figure D.3.1. Comparison of conductivity values measured using commercial meter and extracted from passive sensor for tap water at different temperatures
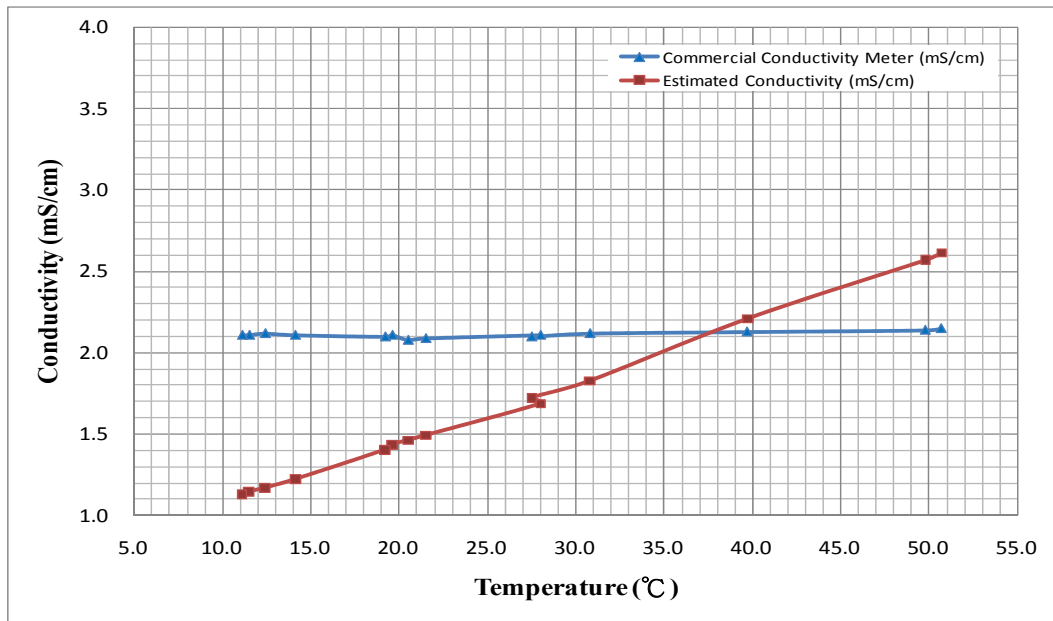
Figure D.3.2. Comparison of conductivity values measured using commercial meter and extracted from passive sensor for 0.1% salt water at different temperatures
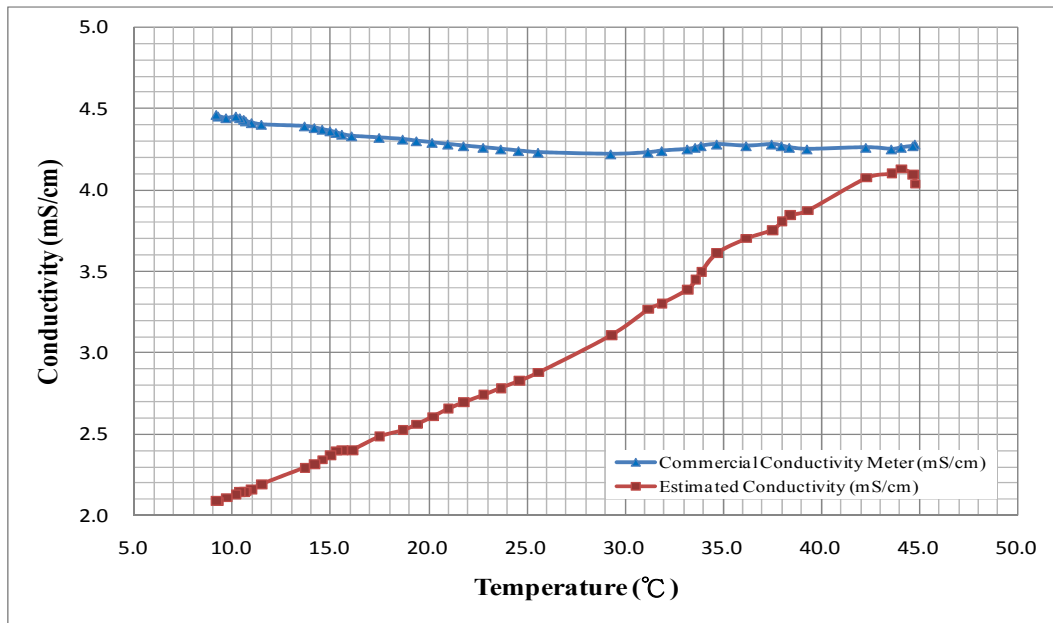

Figure D.3.3. Comparison of conductivity values measured using commercial meter and extracted from passive sensor for 0.2% salt water at different temperatures
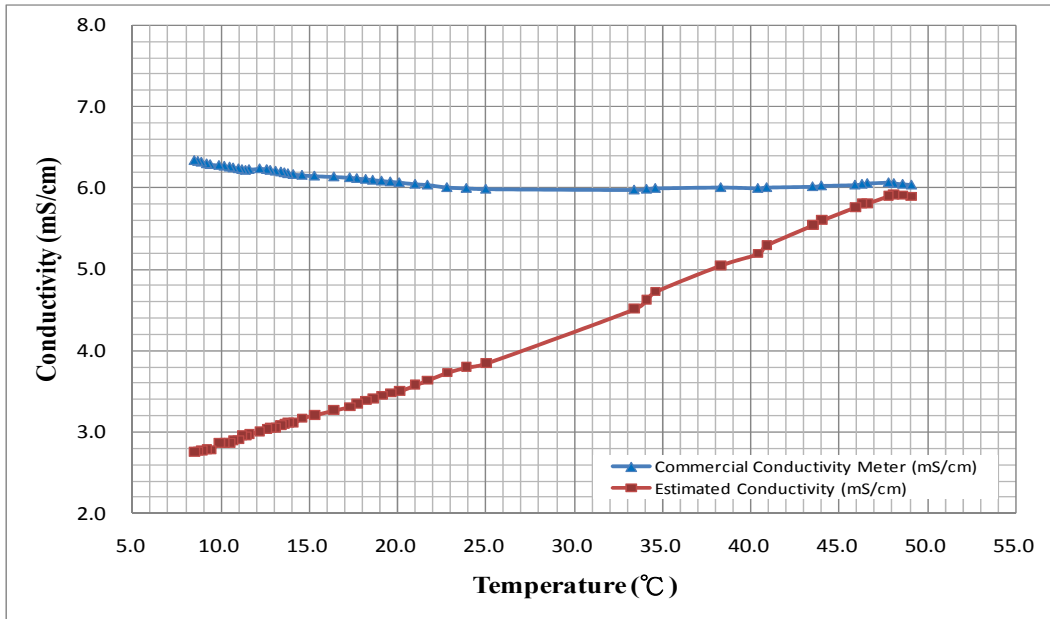
Figure D.3.4. Comparison of conductivity values measured using commercial meter and extracted from passive sensor for 0.3% salt water at different temperatures
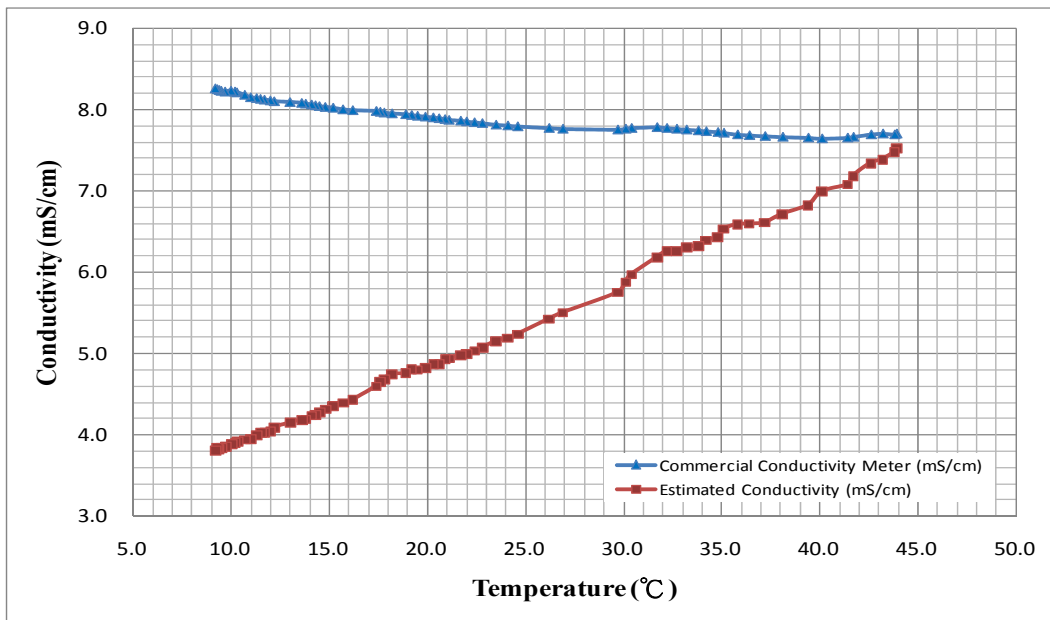

Figure D.3.5. Comparison of conductivity values measured using commercial meter and extracted from passive sensor for 0.4% salt water at different temperatures
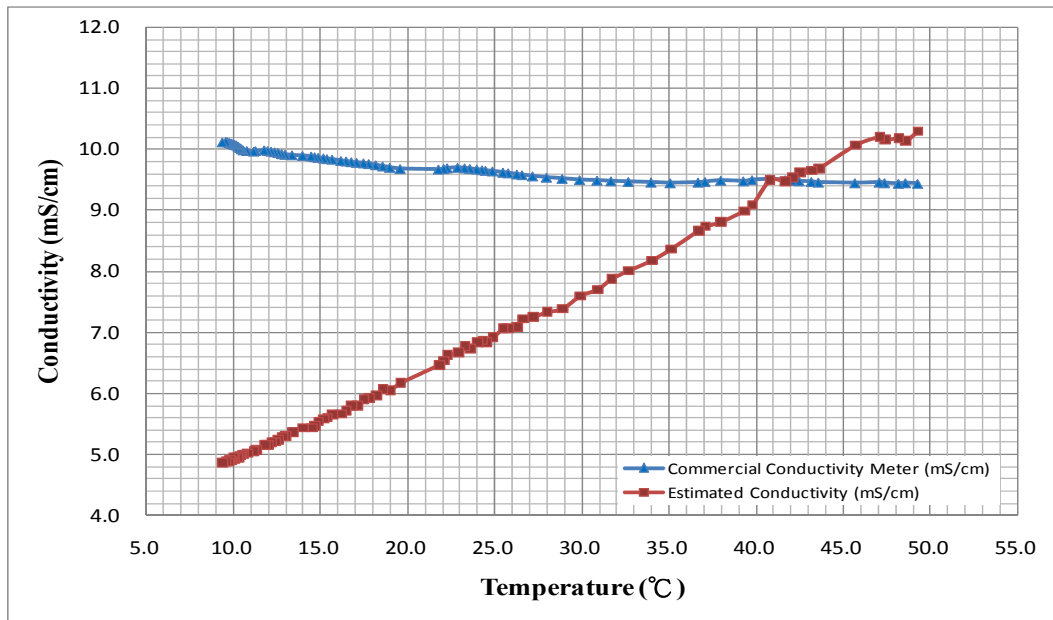
236

Figure D.3.6. Comparison of conductivity values measured using commercial meter and extracted from passive sensor for 0.5% salt water at different temperatures

Figure D.3.7. Comparison of conductivity values measured using commercial meter and extracted from passive sensor for 0.6% salt water at different temperatures
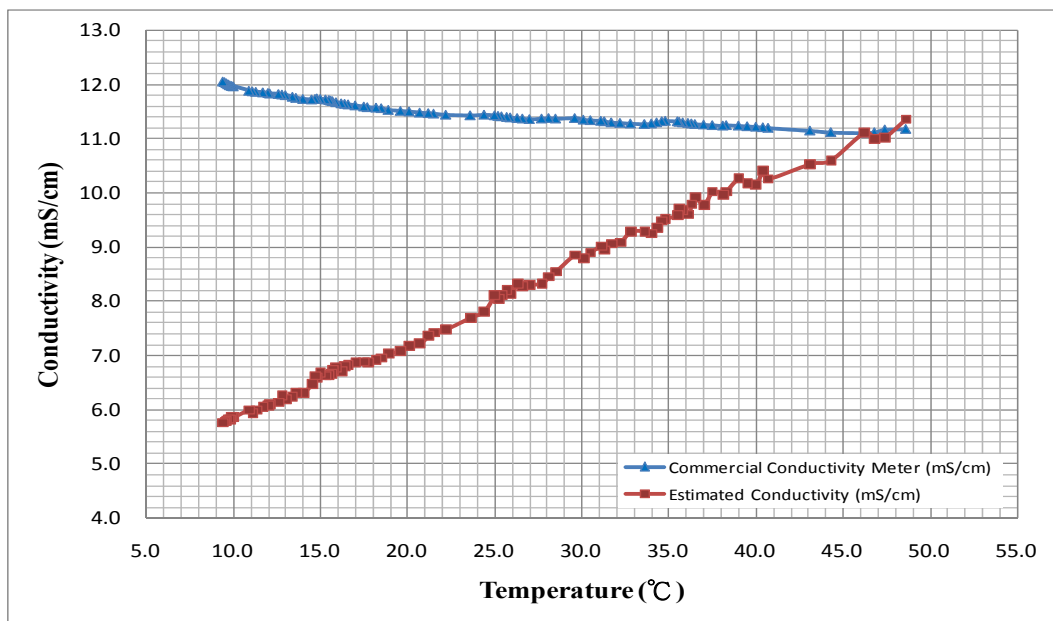
Figure D.3.8. Comparison of conductivity values measured using commercial meter and extracted from passive sensor for 0.7% salt water at different temperatures
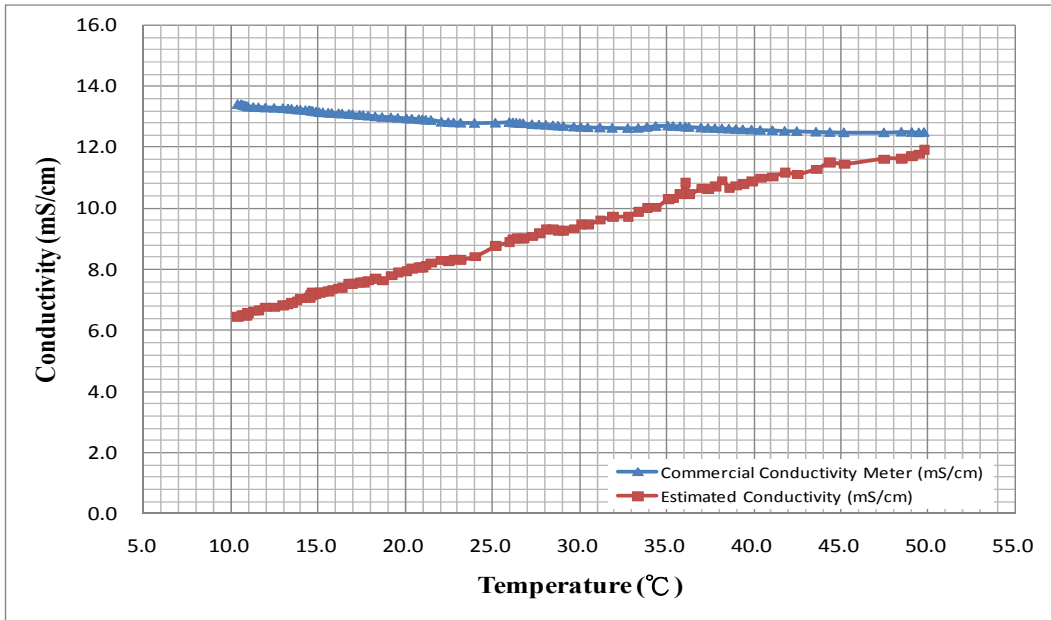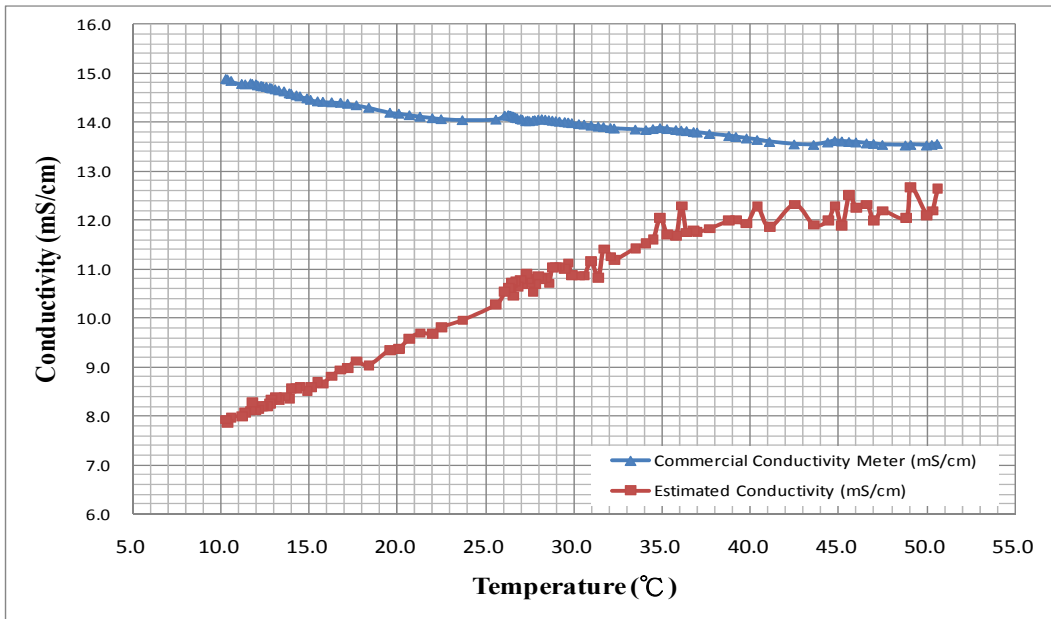

Figure D.3.9. Comparison of conductivity values measured using commercial meter and extracted from passive sensor for 0.8% salt water at different temperatures

D.4 Temperature Compensation Results for the Estimated Conductivities in Different Temperatures and Salt Water Concentrations
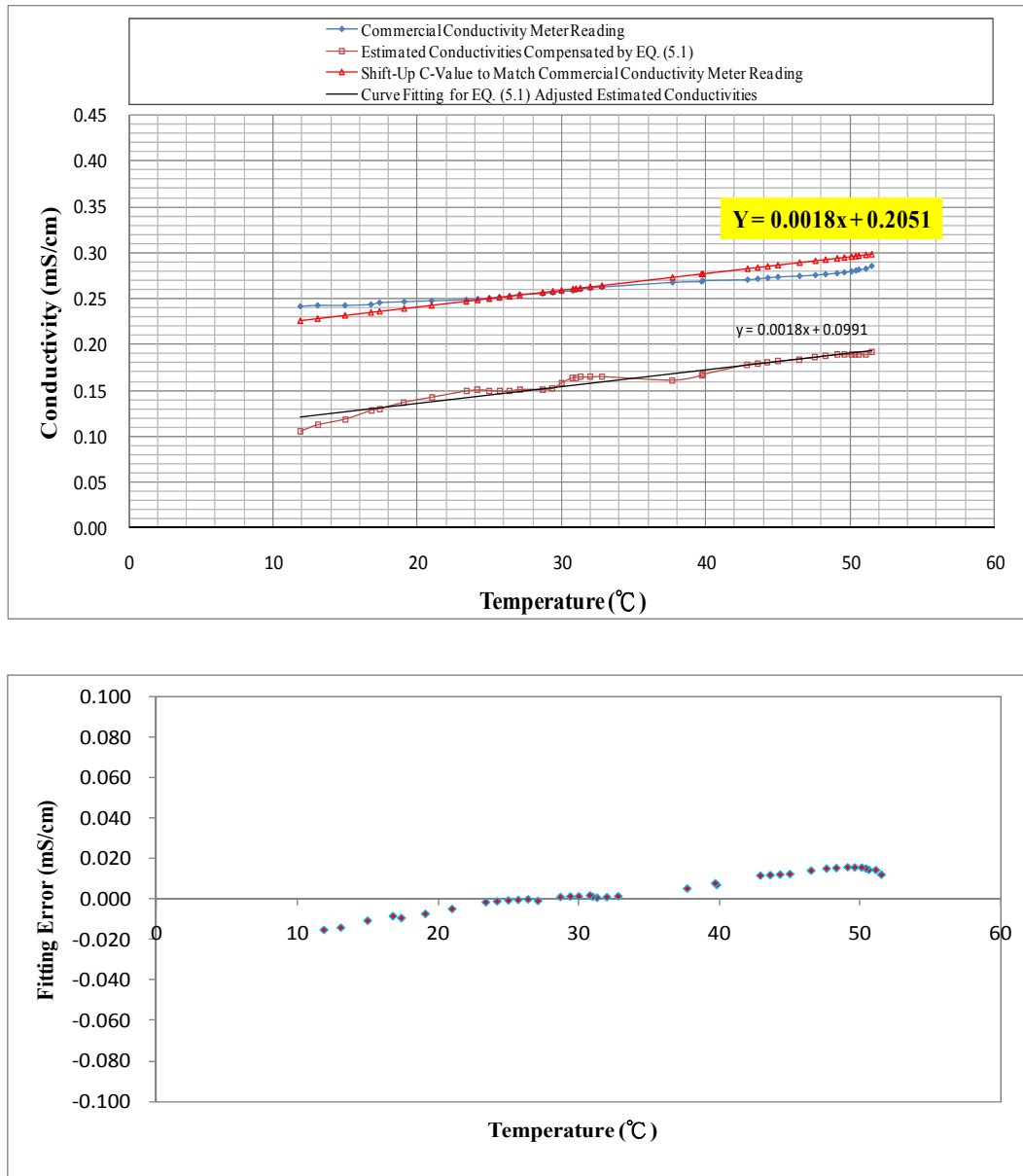

Figure D.4.1. Temperature compensation results and fitting errors for the estimated conductivities in different temperatures in tap water concentration environment

Figure D.4.2. Temperature compensation results and fitting errors for the estimated conductivities in different temperatures in 0.1% salt water concentration environment

Figure D.4.3. Temperature compensation results and fitting errors for the estimated conductivities in different temperatures in 0.2% salt water concentration environment
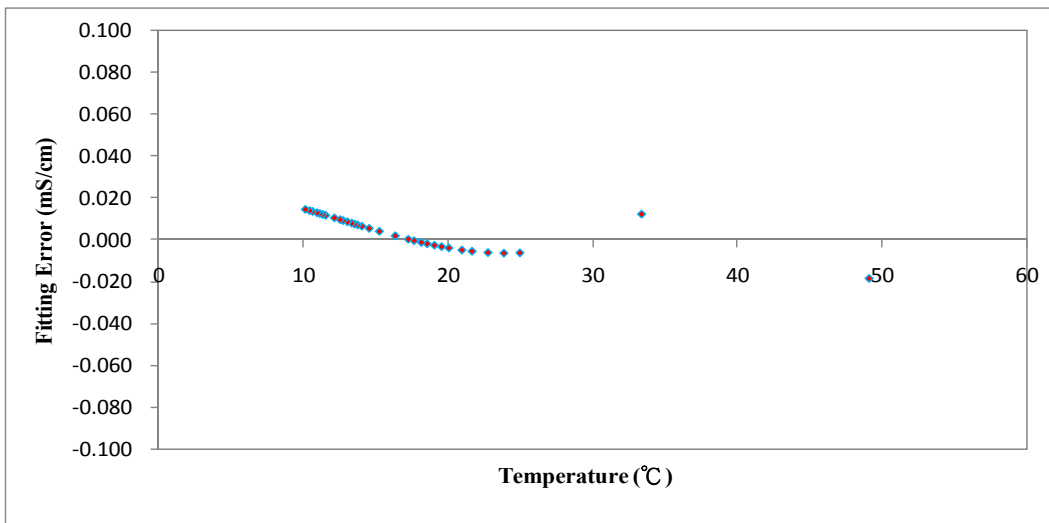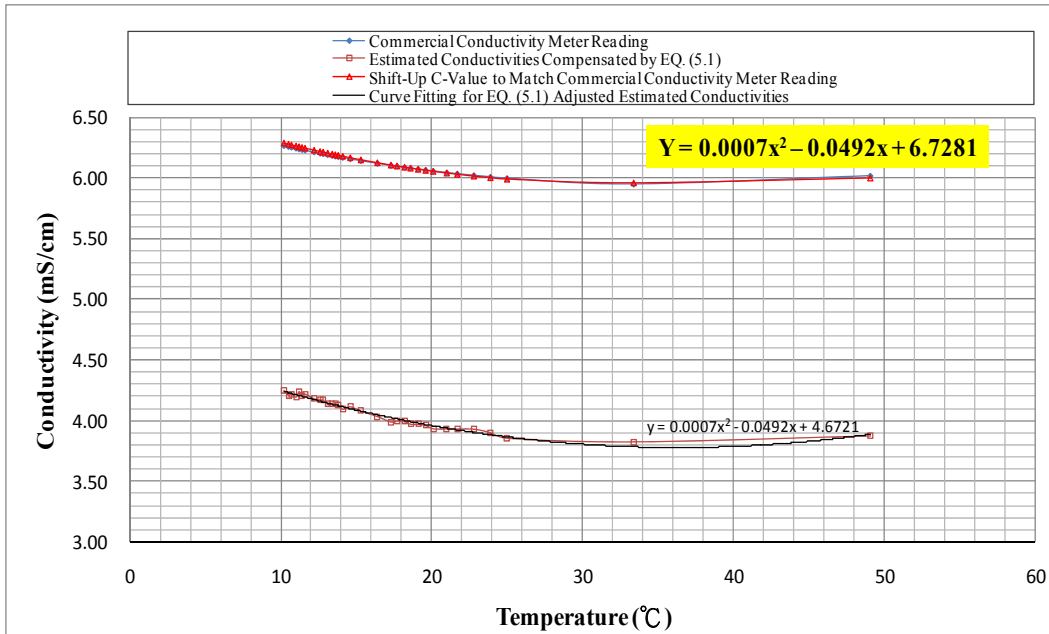
Figure D.4.4. Temperature compensation results and fitting errors for the estimated conductivities in different temperatures in 0.3% salt water concentration environment
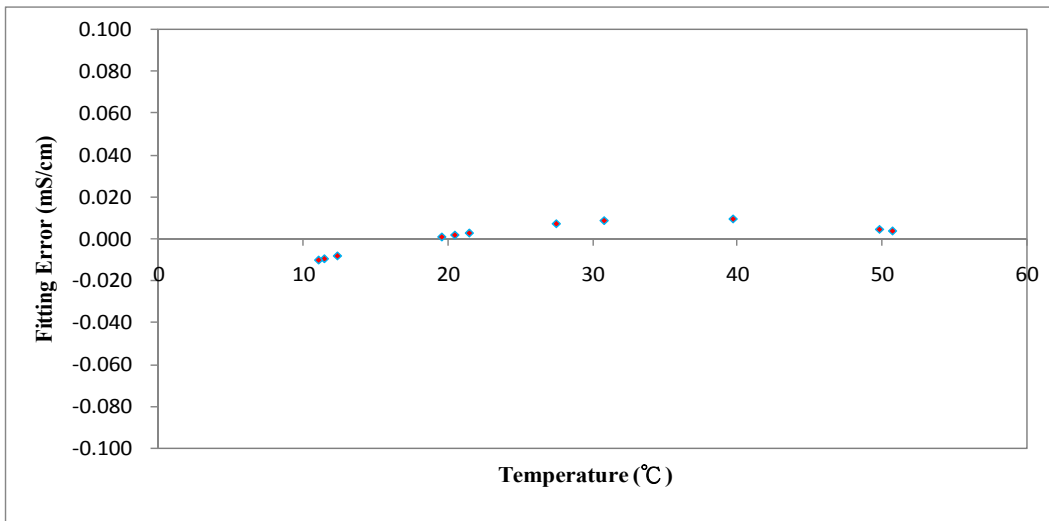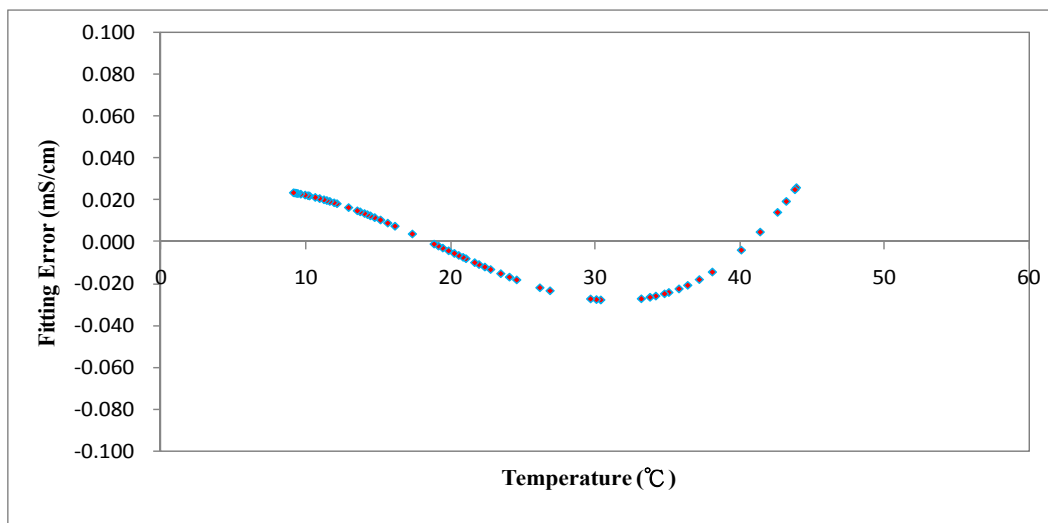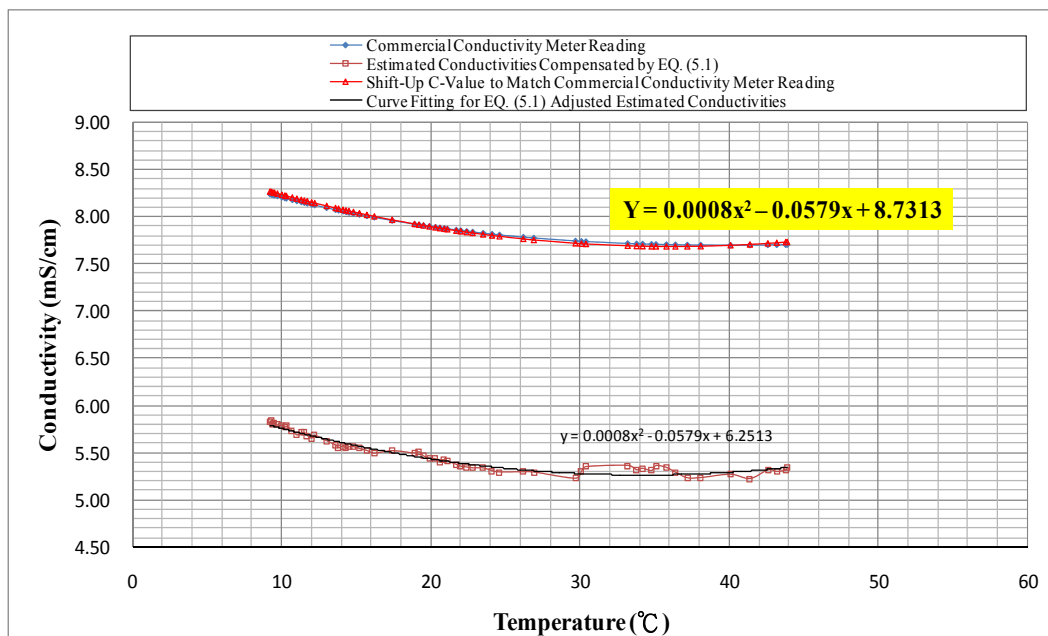
Figure D.4.5. Temperature compensation results and fitting errors for the estimated
conductivities in different temperatures in 0.4% salt water concentration environment
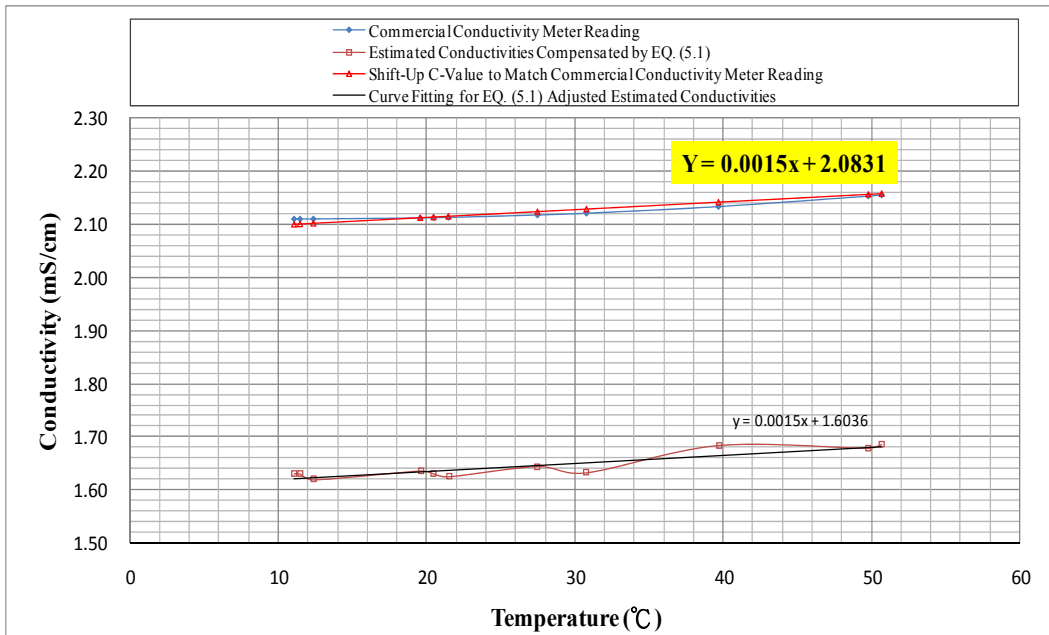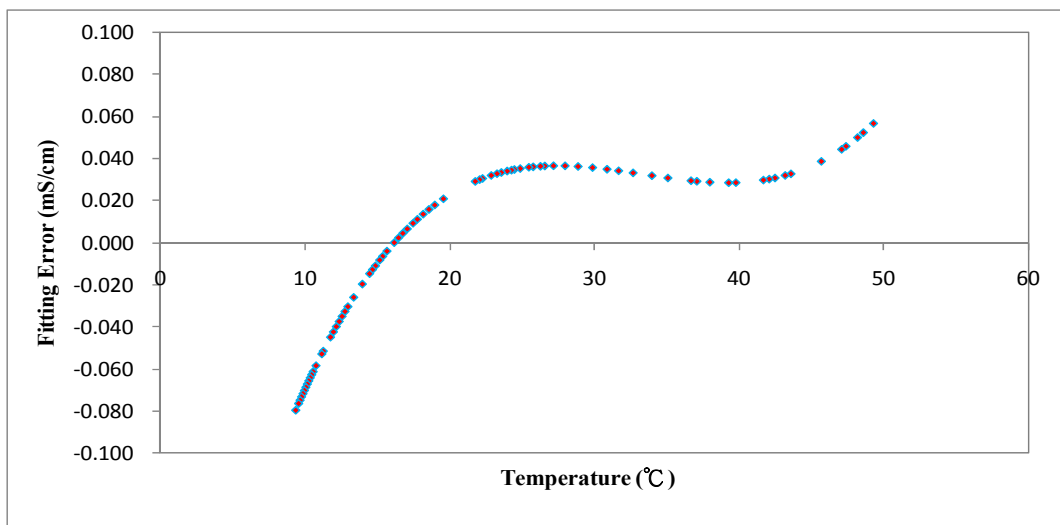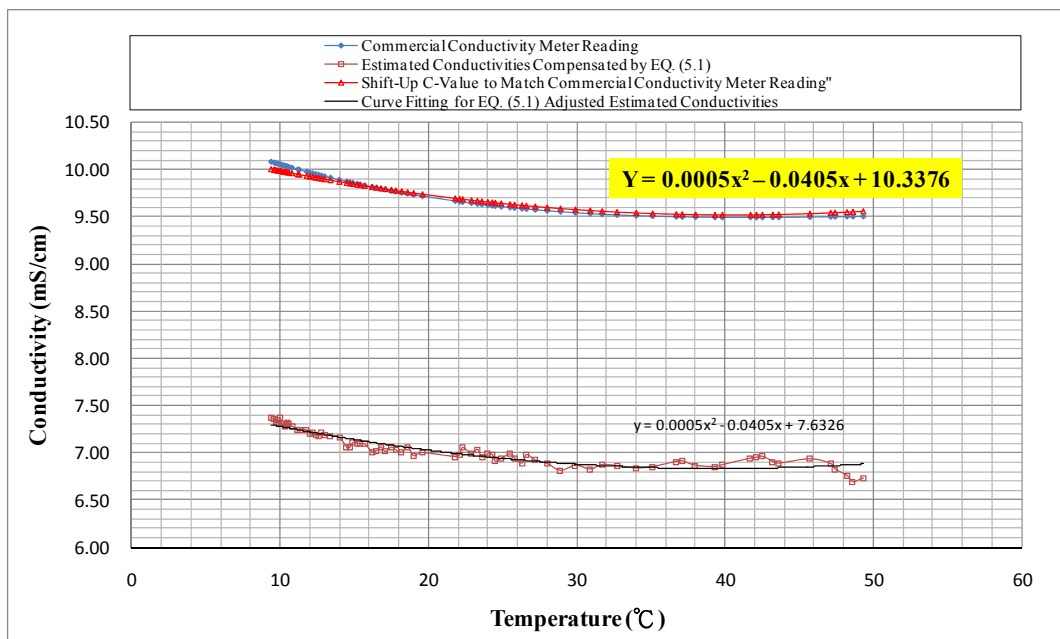
Figure D.4.6. Temperature compensation results and fitting errors for the estimated conductivities in different temperatures in 0.5% salt water concentration environment
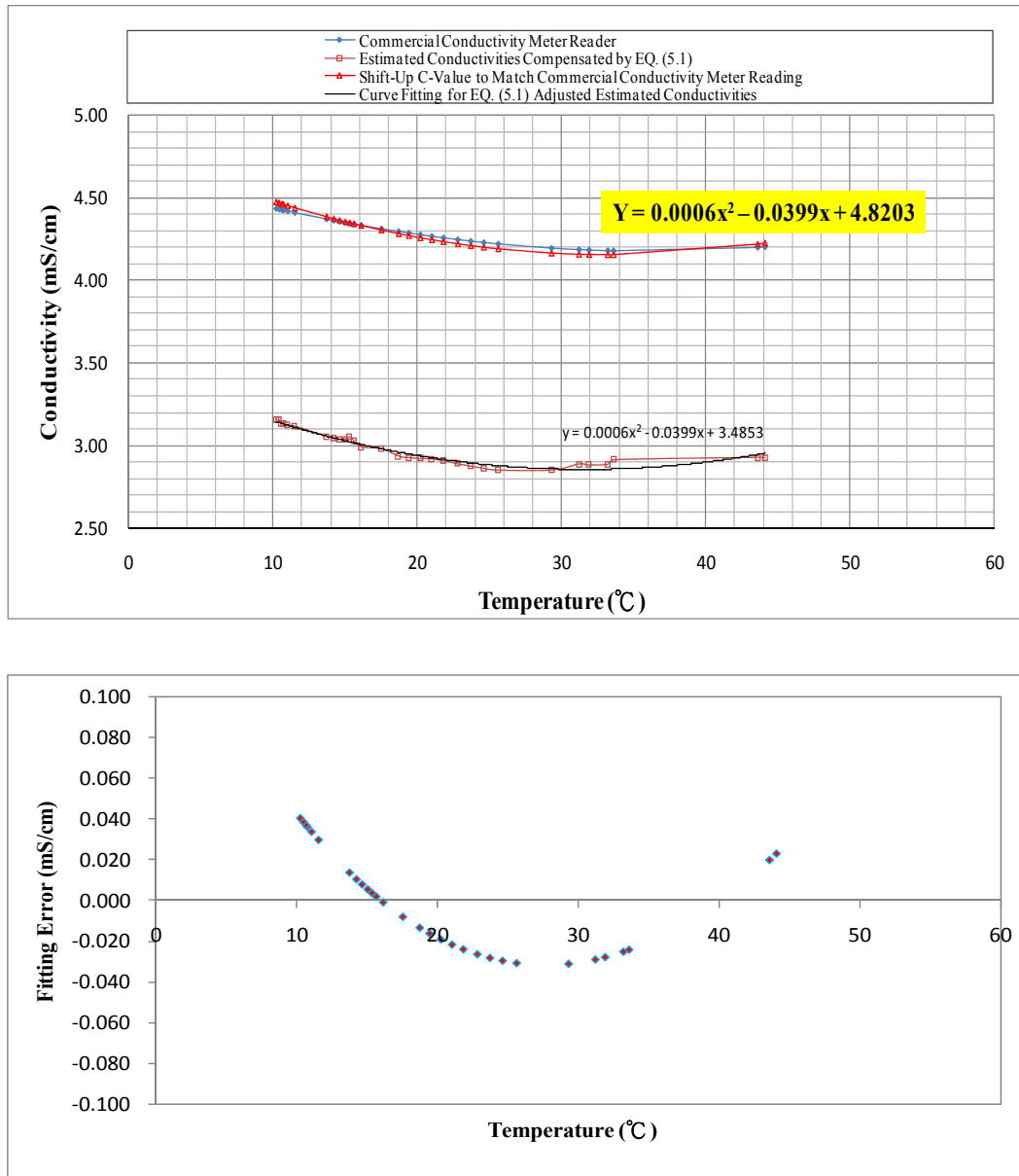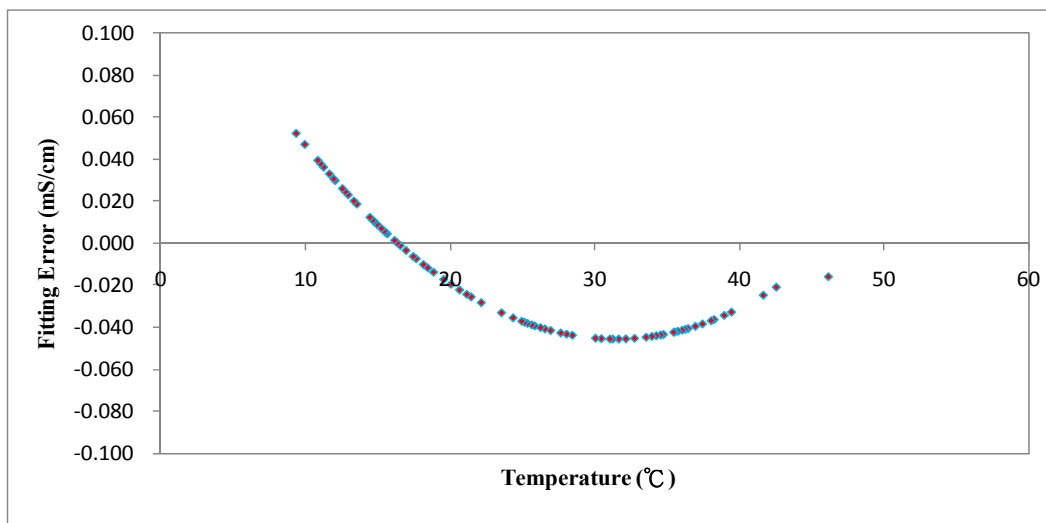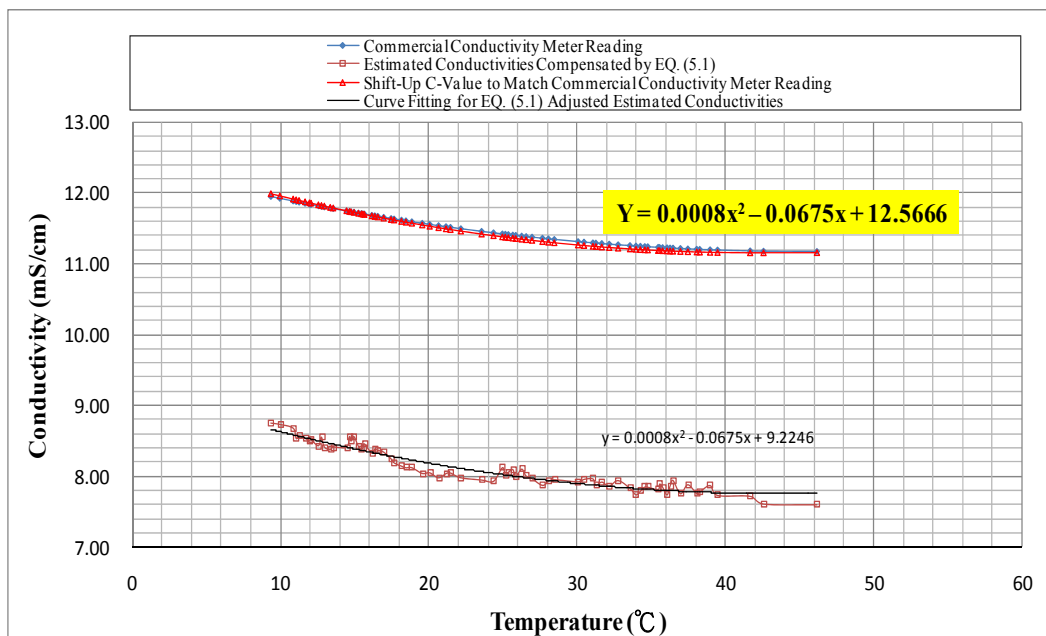
Figure D.4.7. Temperature compensation results and fitting errors for the estimated conductivities in different temperatures in 0.6% salt water concentration environment

Glossary of Terms

CSE   Copper-copper-sulfate

EAS   Electronic Article Surveillance

ECI   Embedded Corrosion Instrument

ESS   Electronic Structural Surveillance

HCP   Half-cell potential measurement

LPR   Linear polarization resistance

RF   Radio Frequency

SCE   Standard Calomel Electrode

References

1. Andringa, M. M. (2003). *Development of a passive wireless analog resistance sensor*. MS thesis, Department of Electrical and Computer Engineering, University of Texas, Austin.

2. Andringa, M. M. (2006). *Unpowered wireless sensors for structural health monitoring*. PhD dissertation, Department of Electrical and Computer Engineering, University of Texas, Austin.

3. ASTM C 876 - 9 (2009). *Standard test method for half-cell potentials of uncoated reinforcing steel in concrete*. West Conshohocken, PA: American Society for Testing and Materials.

4. ASTM C1152 / C1152M - 04e1 (2006). *Standard test method for acid-soluble chloride in mortar and concrete*. West Conshohocken, PA: American Society for Testing and Materials.

5. ASTM G3-89 (2004). *Standard practice for conventions applicable to electrochemical measurements in corrosion Testing*. West Conshohocken, PA: American Society for Testing and Materials.

6. Bertolini, L., Elsener, B., Pedeferri, P., & Polder, R. B. (2004). *Corrosion of steel in concrete: Prevention, diagnosis, repair*. Weinheim: WILEY-VCH Verlag GmbH & Co. KGaA.

7. Broomfield, J. P. (2006). "*Corrosion of steel in concrete: Understanding, investigation & repair* (Second.edition). Taylor & Francis.

8. Davis, W. A., and Agarwal, K. K. (2001). *Radio frequency circuit design*. New York: John Wiley & Sons, Inc.

9. C.J. Newton and J.M. Sykes. (1987). *Cement Conc. Res*. 17(4), 765-776.

10. Denny A. Jones (1995). *Principles and Prevention of Corrosion* (Second edition), Prentice Hall.

11. Dickerson, N. P. (2005). *Wireless corrosion sensors for reinforced concrete structures*. MS thesis, Department of Civil, Architectural and Environmental Engineering, University of Texas, Austin.

12. Dubendorf, V. A. (2003). *Wireless data technologies*. London: John Wiley & Sons, Ltd.

13. Finkenzeller, K. (2003). *RFID handbook: Fundamentals and applications in contactless smart cards and identification* (Second edition). London: John Wiley & Sons Ltd.

14. Grizzle, K. M. (2003). *Development of a wireless sensor used to monitor corrosion in reinforced concrete structures*. MS thesis, Department of Civil, Architectural and Environmental Engineering, University of Texas, Austin.

15. He, X.-Q., Zhu, Z.-Q., Liu, Q.-Y., and Lu, G.-Y. (2009). Review of GPR Rebar Detection. *PIERS Proceedings*, Beijing, China, 804-813.

16. Kelly, R. G., Hudson, J. K., and Ross, R. A. (2002). *Development of a prototype version of an embeddable corrosivity measuring instrument for reinforced concrete*. Final Contract Report (VTRC 03-CR10). Richmond, VA: Department of Transportation in Virginia.

17. Koch, G. H., Brogers, P. H., Thompson, N., Virmani, Y. P., and Payer, J. H. (2002). *Corrosion cost and preventive strategies in the United States*. FHWA Report, FHWA-RD-01-156. Washington, DC: Federal Highway Administration.

18. Horiba, Ltd. (2010). http://www.horiba.com/application/material-property-characterization/water-analysis/water-quality-electrochemistry-instrumentation/ph-knowhow/the-story-of-conductivity/the-fundamentals/temperature-compensation/

19. L. Bertolini, B. Elsener, P. Pedeferri, and R. Polder. (2004). *Corrosion of Steel in Concrete: Prevention, Diagnosis, Repair*. Weinheim: Wiley-VCH, Verlag GmbH & Co. KgaA.

20. Li, D., Conwaya, P. P., and Liua, C. (2008). Corrosion characterization of tin–lead and lead free solders in 3.5 wt.% NaCl solution. *Corrosion Science, 50*(4), 995-1004.

21. Manko, H. H. (2001). *Solders and soldering* (Fourth edition). McGraw-Hill.

22. Mansfield (1981). Recording and Analysis of AC Impedance Data for Corrosion Studies. *Corrosion*, 37(5), 301-307.

23. Pasupathy, Praveenkumar (2010). *Coupled Passive Resonant Circuits as Battery-Free Wireless Sensors*. PhD dissertation, Department of Electrical and Computer Engineering, University of Texas, Austin.

24. Paul A. Tipler and Gene Mosca (2004). *Physics for scientists and engineers* (Vol 2B, Fifth edition.). New York: W. H. Freemen and Company.

25. Paul A. Tipler and Gene Mosca (2008). *Physics for Scientists and Engineers* (Sixth edition). New York: W. H. Freeman and Company.

26. Pla-Rucki, G. F., and Eberhard, M. O. (1995). Image of reinforced concrete: State-of-the-art review. *Journal of Infrastructure Systems*, *1*(2), 134-141.

27. New Civil Engineer Magazine (2006). Poor maintenance blamed for Montreal collapse, Octorber.

28. Pourbaix, M. (1974). *Atlas of electrochemical equilibria in aqueous solutions*. Houston, TX: National Association of Corrosion Engineers (NACE).

29. Puryear, J. M. H. (2007). *Passive, wireless corrosion sensors for reinforced concrete structures*. MS thesis, Department of Civil, Architectural and Environmental Engineering, University of Texas, Austin.

30. Roberge, P. R. (2000). *Handbook of corrosion engineering*. New York: McGraw-Hill.

31. Simonen, J. T., Andringa, M. M., Grizzle, K. M., Wood, S. L., and Neikirk, D. P. (2004). Wireless sensors for monitoring corrosion in reinforced concrete members. *Proceedings of SPIE, Smart Structures and Materials 2004 - Sensors and Smart Structures Technologies for Civil, Mechanical, and Aerospace Systems*, *5391*, 587-596.

32. Song, H.-W., and Saraswathy, V. (2007). Corrosion monitoring of reinforced concrete structures - A review. *International Journal of Electrochemical Science*, *2*(1), 1-28.

33. Tan, A. C. (1989). *Lead finishing in semiconductor devices: Soldering*. Singapore: World Scientific Publishing Co. Pte., Ltd.

34. Tan, A. C. (1993). *Tin and solder plating in the semiconductor industry: a technical guide*. London: Chapman & Hall.

35. Tuutti, K. (1982). *Corrosion of steel in concrete*. Stockholm, Sweden: Swedish Foundation for Concrete Research.

36. Yunovich, M., Thompson, N.G., Vanyos, T. B., and Lave, L. (1998). *Corrosion Cost and Preventive Strategies in the United States (Appendix D: Highway bridges)*, Report FHWA-RD-01-156, Retrieved from, http://www.corrosioncost .com/pdf /highway.pdf/

Curriculum Vitae

Chih-Chieh Chou was born on September 28, 1979 in Taipei, Taiwan to Ting-Fa Chou and Yu-In Tao. Raised in Taipei, Taiwan, Chih-Chieh graduated from Yan-Ping High School in June 1997. He graduated from the Chung Yuan Christian University in June 2001 with a Bachelor of Science in Civil Engineering. Next, Chih-Chieh obtained a Master of Science in Structural Engineering from the National Taiwan University in June 2004. During this period, he worked as a graduate research assistant at the National Center for Research on Earthquake Engineering in Taiwan and conducted research work under the supervision of Dr. Chung-Chun Chang. In August of 2008, Chih-Chieh moved to Austin, Texas to attend graduate school in architectural engineering at the University of Texas at Austin. There, he worked as a graduate research assistant at the Ferguson Structural Engineering Laboratory and conducted research work under the supervision of Dr. Sharon L. Wood. Chih-Chieh graduated from the University of Texas in August of 2010 with a Master of Science in Architectural Engineering. After finishing his work at the University of Texas, he accepted a position with China Engineering Consultants, Inc., in Taiwan.

Permanent Address: 1F., No.359-7, Wuxing St.,

Xinyi Dist., Taipei City 110,

Taiwan (R.O.C.)

This thesis was typed by the author.